DISSERTATION

CLOUD CONDENSATION NUCLEI IN WESTERN COLORADO: OBSERVATIONS AND MODEL PREDICTIONS

Submitted by

Daniel Stewart Ward

Department of Atmospheric Science

In partial fulfillment of the requirements

For the Degree of Doctor of Philosophy

Colorado State University

Fort Collins, Colorado

Summer 2010

COLORADO STATE UNIVERSITY

April 28, 2010

WE HEREBY RECOMMEND THAT THE DISSERTATION PREPARED UNDER OUR SUPERVISION BY DANIEL STEWART WARD ENTITLED CLOUD CONDENSATION NUCLEI IN WESTERN COLORADO: OBSERVATIONS AND MODEL PREDICTIONS BE ACCEPTED AS FULFILLING IN PART REQUIREMENTS FOR THE DEGREE OF DOCTOR OF PHILOSOPHY.

Committee on Graduate work

_____
Jeffrey L. Collett

_____
Richard Eykholt

_____
Sonia M. Kreidenweis

_____
Advisor: William R. Cotton

_____
Department Head: Richard H. Johnson

ABSTRACT OF DISSERTATION

CLOUD CONDENSATION NUCLEI IN WESTERN COLORADO: OBSERVATIONS AND MODEL PREDICTIONS

Variations in the warm cloud-active portion of atmospheric aerosols, or cloud condensation nuclei (CCN), have been shown to impact cloud droplet number concentration and subsequently cloud and precipitation processes. This issue carries special significance in western Colorado where a significant portion of the region's water resources is supplied by precipitation from winter season, orographic clouds, which are particularly sensitive to variations in CCN.

Temporal and spatial variations in CCN in western Colorado were investigated using a combination of observations and a new method for modeling CCN. As part of the Inhibition of Snowfall by Pollution Aerosols (ISPA-III) field campaign, total particle and CCN number concentration were measured for a 24-day period in Mesa Verde National Park, climatologically upwind of the San Juan Mountains. These data were combined with CCN observations from Storm Peak Lab (SPL) in northwestern Colorado and from the King Air platform, flying north to south along the Western Slope. Altogether, the sampled aerosols were characteristic of a rural continental environment and the cloud-active portion varied slowly in time, and little in space. Estimates of the κ hygroscopicity parameter indicated consistently low aerosol hygroscopicity typical of organic aerosol species.

The modeling approach included the addition of prognostic CCN to the Regional Atmospheric Modeling System (RAMS). The RAMS droplet activation scheme was altered using parcel model simulations to include variations in aerosol hygroscopicity, represented by κ. Analysis of the parcel model output and a supplemental sensitivity study showed that model CCN will be sensitive to changes in aerosol hygroscopicity, but only for conditions of low supersaturation or small particle sizes.

Aerosol number, size distribution median radius, and hygroscopicity (represented by the κ parameter) in RAMS were constrained by nudging to forecasts of these quantities from the Weather Research and Forecasting with Chemistry (WRF/Chem) model. The new system was validated against observations from SPL and research flights along the Colorado Front Range, and used to test the sensitivity of CCN in western Colorado to various anthropogenic emissions of aerosols and aerosol precursor gases. Results showed complex interactions between gas and aerosol species that could lead to an increase in CCN even when some emissions are eliminated. Both observations and modeling suggest that, although several large anthropogenic aerosol sources are located within the study region, these sources have a minor impact on the local CCN population.

Daniel Stewart Ward
Department of Atmospheric Science
Colorado State University
Fort Collins, CO 80523
Summer 2010

ACKNOWLEDGEMENTS

The work described in this dissertation received support from many people. I would like to thank Prof. William Cotton for his advice and guidance, and for providing me with the opportunity to be a part of this project. I am also grateful for the support and suggestions of committee members Prof. Sonia Kreidenweis, Prof. Jeff Collett, and Prof. Richard Eykholt, which greatly improved this work. Special thanks are due to every member of the Cotton project group who have created a true learning community and thus contributed to this work. These thanks are extended to former member Will Cheng, for advice and help with WRF/Chem, and especially to former member Prof. Sue van den Heever, a wonderful teacher, for her enthusiasm and encouraging words.

Essential logistical support for the ISPA-III phase in Mesa Verde was provided by George San Miguel of the National Park Service and Ian McCubbin from the Desert Research Institute (DRI). Thanks also to the King Air facility staff at the University of Wyoming (UWYO), particularly Larry Oolman, for leading the ISPA-III research flights. Modeling and data support were freely given by Jeff Snider (UWYO), Christine Wiedinmyer at the National Center for Atmospheric Research (NCAR), Trude Eidhammer (NCAR), and Gannet Haller (DRI). Funding was provided by the National Science Foundation grant ATM-0835421.

This work would not have been possible without the constant love and support from my friends and family. To my daughter, the shining light at the end of the tunnel, this work was very happily done for you. Many thanks to my parents and sisters who are my mentors and have a share in all I do. And even though she thinks aerosols only come out of hair spray cans, this dissertation belongs as much to Jill as it does to me.

Daniel S. Ward

April 2010

TABLE OF CONTENTS

Chapter 1

Introduction

A substantial collection of atmospheric science literature now exists that demonstrates the importance of aerosols for our understanding of cloud microphysical and precipitation processes. By their role as cloud condensation nuclei (CCN) and ice nuclei (IN), aerosols can alter the droplet and ice crystal distributions in clouds. Modifications in the microstructure of clouds affect their interactions with radiation and can lead to changes in the amount and distribution of precipitation with implications for regional and global issues of climate and water resources. These potential impacts have led to the consideration of aerosols as a significant modulator of global climate as reported by the IPCC (Andreae and Rosenfeld, 2008), but also one of the most uncertain (Charlson et al., 2001; Ghan and Schwartz, 2007).

Key questions remain regarding the distribution of CCN across the globe and how best to represent the distribution of CCN numerically, while retaining both accuracy and computational efficiency. This study aims to address some aspects of these questions, first by reporting on new CCN datasets from western Colorado collected as part of the Inhibition of Snowfall by Pollution Aerosols (ISPA) III field campaign. These data are presented and analyzed with the purpose of filling the measurement gaps and providing the first estimation of cold-season, Western Slope CCN climatology. Secondly to address these aims,

a new, innovative way to forecast CCN in a regional model is introduced in which the Regional Atmospheric Modeling System (RAMS) microphysics is coupled to the Weather and Research Forecasting Model with Chemistry (WRF/Chem) aerosol modules. The new modeling system allows for prediction of CCN based on forecasts of aerosol characteristics including number, size and composition, and subsequent feedbacks on the model microphysics and precipitation processes. It is intended as a first step toward online aerosol chemistry in RAMS and an indication of the value of such a system. Together, this model development and the observations of CCN in western Colorado will advance our understanding of how aerosols affect clouds and how human activity may be modifying the system.

The cloud response to variations in CCN is inextricably linked to the dynamics of the cloud system (Levin and Cotton, 2009). In other words, separate cloud types, or cloud regimes, respond differently to increases in CCN number concentrations. As a consequence, understanding the global response to aerosol and cloud interactions, which in modeling studies is necessarily represented by sub-grid scale parameterizations, remains a challenge. This issue was reviewed by Stevens and Feingold (2009) who recommend a regime-specific approach to these investigations. They suggest examination of individual cloud regimes by small-scale, cloud-resolving modeling studies and intense observational campaigns. The knowledge gleaned from small-scale studies can then be applied in large-scale parameterizations and extended to the global scale. This bottom-up method directs resources to particularly susceptible or climatologically important cloud regimes for which the greatest benefits to climate research can be gained (Stevens and Feingold, 2009).

Previous studies show that orographic clouds are particularly susceptible to aerosol effects, perhaps the most susceptible regime yet identified (Levin and Cotton, 2009). Investigations of precipitation climatology in mountainous regions in the western U.S. have

demonstrated a long-term decrease in accumulated precipitation downwind and upslope of urban areas (Givati and Rosenfeld, 2004; Rosenfeld and Givati, 2006). Jirak and Cotton (2006) found similar results along the Colorado Front Range and attributed lower precipitation to increases in pollution from the urban corridor. Case studies of orographic clouds have also attributed lower precipitation production to local anthropogenic aerosol sources (Borys et al., 2000; Borys et al., 2003), and recent modeling studies of these clouds have shown large sensitivity in precipitation to changes in CCN number concentration (Lynn et al., 2007; Saleeby et al., 2009).

Issues of orographic precipitation suppression are of particular significance in western Colorado where water supplies depend largely on the amount of snow produced by orographic clouds (Saleeby et al., 2009). The sharp rise in elevation from west to east along Colorado's Western Slope leads to frequent formation of precipitating orographic clouds. This, in combination with the location of an aerosol and cloud microphysics observing station in the northern Colorado Park Range, makes the Western Slope region an ideal laboratory for studying aerosol-orographic cloud interactions. In fact, a substantial portion of the research on this topic has taken place in northwestern Colorado.

While the observational evidence supports a potentially important aerosol impact on orographic clouds in western Colorado, the scope of the impact remains largely unknown. For example, it has been hypothesized that differences in cloud liquid water content (LWC) may dictate the sensitivity of precipitation to increases in aerosol (Borys et al., 2000). High LWC clouds are more common in southwest Colorado than in northwest Colorado, suggesting a potential difference in the magnitude of aerosol effects. However, the comparison is difficult to make because observational records of droplet-nucleating aerosol do not exist for the majority of the Western Slope.

The difficulty is compounded by the limitation of efforts to simulate aerosol effects on orographic clouds, for the most part, to sensitivity studies. Limited because we know very little about the character of the ambient aerosols flowing into orographic clouds, such as their seasonality, variability in size, number, composition, etc., and cannot reliably forecast these quantities on a case-by-case basis. In a review of existing climate-chemistry models, Zhang (2008) notes that because of the interaction between aerosols and clouds, forecasting aerosol-cloud effects requires a modeling system with both detailed chemistry and microphysics. Yet these coupled models are few due to the challenges of representing the complex systems involved with limited computational resources. The coupled system presented in this dissertation contains strategies for meeting these challenges. As such, although initially motivated by regional water-resource interests, the strategies applied here may have additional applications in global-scale parameterizations. This, according to Stevens and Feingold (2009), is the route the community needs to take toward better understanding of aerosol-cloud interactions in the climate system.

The goals and research outlined above is organized in this dissertation as follows. Chapter 2 gives an overview of previous relevant research as a means of placing the current study in scientific context. In Chapter 3, the first step in the model development, the addition of aerosol composition variations to the RAMS droplet activation scheme, is described. The new RAMS droplet activation code is then applied in sensitivity studies of a mixed-phase orographic cloud in northwestern Colorado, results of which are shown in Chapter 4. Sensitivity studies suggest what the impact of variations in CCN could potentially be, but data describing the ambient CCN are required to assess its true magnitude and nature. Chapters 5 and 6 provide analysis of CCN observations collected in Colorado during the ISPA campaign with the aim of addressing the scope of the impact in this region.

Then, in Chapter 7, the method for coupling WRF/Chem and RAMS is laid out with verification simulations shown in the following chapter. The coupled system is applied to a study of the sensitivity of CCN in western Colorado to emission sources, shown in Chapter 9. Finally, conclusions are offered with a focus on the implications for future studies and suggestions for their direction.

Chapter 2

Background

In the conditions of relative humidity common to our atmosphere, cloud droplets will only form onto particle nuclei, also known as heterogeneous nucleation (Pruppacher and Klett, 1997). These nuclei, or CCN, are omnipresent in the troposphere though in widely variable number concentrations, sizes and compositions. All of these aerosol properties are important for determining whether a nucleated droplet will grow to cloud droplet size, or activate. Furthermore, variations in droplet activation lead to variations in droplet size with subsequent impacts on cloud radiation and precipitation processes. Therefore, the evolution of particles in the atmosphere and their properties are topics that have been extensively researched through observations and numerical modeling. This chapter will review the course of relevant research to provide background and context for the work presented in this dissertation. It also serves the purpose of introducing concepts and terminology that will be important in later chapters.

First, a summary of the physics of droplet activation is given followed by a brief explanation of the role it plays in precipitation processes. Next, a discussion of the sources and major production pathways of CCN is necessary, especially with regard to modeling strategies for these processes. Finally, current droplet activation parameterizations are outlined concluding with an explanation of the current scheme in RAMS. Explanation of

other relevant topics including CCN closure, CCN measurement techniques, and the WRF/Chem model accompany the chapters in which they are applied.

2.1 Droplet activation theory

Methods for observing cloud droplet spectra were being improved in the 1950s and soon thereafter it was discovered in the laboratory (Gunn and Phillips, 1957) and in the ambient air (Squires, 1958) that the microstructure of clouds depends on the concentration of atmospheric particles. That is, because a cloud droplet requires a particle nucleus to form in the atmosphere, the number of cloud droplets that form in a supersaturated environment tends to vary with particle number. Subsequent observations by Squires and Twomey (1966; some of which were collected in the air above Fort Collins), and Twomey and Warner (1967), among others, confirmed that a positive relationship existed between CCN number concentration and cloud droplet number concentration (CDNC). During their analysis of droplet and aerosol measurements, Twomey and Warner (1967) noted that the ratio of measured CCN to CDNC varied with the supersaturation. As they wrote, the theory of droplet growth that, in a sense, determines the CCN number concentration had been used in similar research for some time.

2.1.1 Köhler equations

The Köhler equations, attributed to several papers by H. Köhler from the 1920s and 1930s (as cited by Pruppacher and Klett, 1997), describe droplet growth but also predict, for a given set of conditions, particles that will grow by condensation to cloud droplet size, and those that will not. This can be understood by first considering the equilibrium vapor pressure ($e_{a,w}$) above the surface of a spherical, pure liquid water droplet (see Pruppacher and Klett, 1997, or Seinfeld and Pandis, 2006 for a complete derivation of this theory). The $e_{a,w}$ is equivalent to the saturation vapor pressure above the curved surface. This quantity is expressed by the Kelvin equation:

$$S_{v,w} = \exp\left[\frac{2M_w\sigma_{w/a}}{RT\rho_w a}\right] \tag{2.1}$$

where $S_{v,w}$ is the saturation ratio ($e_{a,w}$/ $e_{sat,w}$), M_w is the molecular weight of water, $\sigma_{w/a}$ is the surface tension of the interface between the water and air, R is the universal gas constant, T is the temperature of the system, ρ_w is the density of water, and a is the droplet radius. The term in the exponent of Eq. 2.1 is always positive. Therefore, the saturation ratio is always greater than one and the vapor pressure above the droplet is always greater than the saturation vapor pressure above a flat-water surface. Also, the equilibrium vapor pressure decreases as the radius of curvature grows. This is known as the Kelvin effect and is illustrated by curve "a" in Figure 2.1. Here the equilibrium vapor pressure above a pure liquid water droplet is shown, assuming an insoluble nucleus of 10nm radius. Not shown but implied, as curve "a" extends beyond the limits of the diagram, is that for a pure water

droplet of a small size to reach equilibrium requires a high saturation ratio in atmospheric terms.

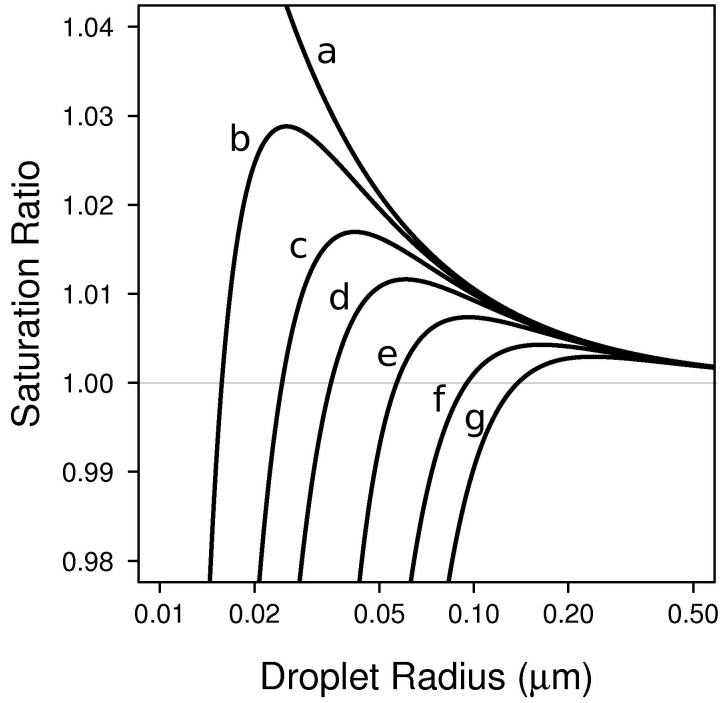

Figure 2.1: Plots of the equilibrium vapor pressure for solution droplets with the following characteristic dissolved nuclei: a) r=10nm, κ=0, b) r=10nm, κ=0.2, c) r=10nm, κ=0.6, d) r=10nm, κ=1.28, e) r=25nm, κ=0.2, f) r=25nm, κ=0.6, g) r=25nm, κ=1.28. Produced with code created by Markus Petters (2007).

If the droplet nucleus is soluble, the equilibrium vapor pressure above a solution must be considered. Mathematically this can be approximated by the introduction of the solute effect to the curvature term described above, completing the Köhler equations:

$$S_{v,w} = \exp\left[\frac{2M_w\sigma_{s/a}}{RT\rho_w a} - \frac{\nu\Phi_s m_s M_w/M_s}{(4\pi a^3\rho_s/3) - m_s}\right] \qquad (2.2)$$

where ν is the ion dissociation factor, Φ_s is the molal osmotic coefficient of the solute, and m_s, M_s and ρ_s are the mass, molecular weight and density of the solute. The solute term is also known as the water activity, a_w:

$$a_w = \exp\left(-\frac{\nu\Phi_s m_s M_w/M_s}{(4\pi a^3\rho_s/3) - m_s}\right) \tag{2.3}$$

and in this equation is an estimate of the hygroscopicity of a droplet solution. Hygroscopicity can be thought of in simpler terms as the measure of a droplet solution's capacity for growing by condensation of water vapor. The impact of the solute term on the equilibrium vapor pressure is illustrated by curve "b" in Figure 2.1 for a somewhat hygroscopic droplet solution. Adding soluble material to the droplet acts to depress the vapor pressure and results in the apparent maximum in the equilibrium vapor pressure curve. Now the distinction can be made between aerosol particles that will activate cloud droplets in a supersaturated environment, or CCN, and those that remain unactivated, known as haze particles. If the supersaturation (SS) exceeds the level of the maximum in the curve, the droplet will grow quickly to cloud droplet size. Otherwise the solution will remain in stable equilibrium as a small haze particle, even in a subsaturated environment. This threshold is known as the critical supersaturation, S_c. For a given S_c, a corresponding critical droplet radius, called the wet critical radius, r_{cw}, is implied. Moreover, for a given S_c and solution hygroscopicity, the radius of the dry particle nucleus required for activation can also be inferred (Petters et al., 2007). This is referred to as the dry critical radius, r_c, and will be used instead of the r_{cw} for these modeling applications.

The term CCN thus refers to a potential state of a particle that is a function of the ambient SS and temperature (see Eq. 2.1) and cannot be conferred to a particle independent

of its environment or predicted environment. Also note that in this discussion it is assumed that all soluble particles exist as solution droplets, meaning they have deliquesced, or taken on water, below 100% relative humidity. Therefore, when the hygroscopicity of a particle is referenced, actually the hygroscopicity of the particle in solution is being described. Petters and Kreidenweis (2008) point out that the assumption of deliquescence in the subsaturated environment does not apply to some aerosol species, particularly some organic species. However, they conclude that these exceptions are rare enough to be neglected in most modeling studies.

2.1.2 Aerosol hygroscopicity

Köhler curves are plotted with increasing solution hygroscopicity in curves 'b', 'c' and 'd'. It can be seen that hygroscopicity is a significant influence on S_c. The two quantities are inversely related, so an increase in hygroscopicity leads to a decrease in S_c. This can be seen in Figure 2.1 curves 'e', 'f', and 'g' plotted for increasing hygroscopicity and a larger particle nucleus with a 25nm radius. Unfortunately, a_w is difficult to assess in a practical way. Hygroscopicity has traditionally been approximated using estimates of ion dissociation and the proportion of soluble material contained in the droplet nucleus. These approximations are not always appropriate for describing hygroscopicity, according to Pruppacher and Klett (1997). Recently Petters and Kreidenweis (2007) introduced a more functional representation of hygroscopicity. They show how the expression for a_w can be simplified to a function of the ratio between dry particle volume (V_a) and water volume (V_w) using a single parameter, κ. In Eq. 2 from Petters and Kreidenweis (2007):

$$\frac{1}{a_w} = 1 + \kappa \frac{V_s}{V_w} \tag{2.4}$$

The κ parameter is determined experimentally for different aerosol species and is listed by Petters and Kreidenweis (2007) for most common aerosol constituents. They also show that the hygroscopicity of particles containing more than one chemical species, known as internal mixtures, can be computed simply as a volume-weighted average κ:

$$\kappa = \sum_i \varepsilon_i \kappa_i \tag{2.5}$$

where ε_i is the volume fraction of each component of the solute. This expression assumes there is no interaction between the different solute ions in solution. Since its introduction, κ has been used to represent hygroscopicity in both observational (e.g. Gunthe et al., 2009; Koehler et al., 2009) and modeling studies (e.g. Reutter et al., 2009; Eidhammer et al., 2009). It offers particular advantages to model parameterizations of aerosol effects, as noted by Petters and Kreidenweis (2007), and was instrumental in the model developments described in the following chapters.

2.2 Aerosol effects on precipitation

Droplet activation occurs on the micro-scale and yet, as a major link between aerosols and cloud microphysics, it influences cloud-scale and larger scale processes. Evidence for the up-scaling impact was uncovered more than 50 years ago in seminal cloud

microphysics experiments by Gunn and Phillips (1957) and Squires (1958). They found that for a constant ambient liquid water content (LWC), environments with high particle numbers supported the formation of many cloud droplets, but they were small, while droplets that formed in cleaner environments were fewer but typically larger. Since the initial measurements were taken, this relationship between aerosol number concentration and droplet size has been demonstrated by in situ studies (e.g., Borys et al., 2000; Chuang et al., 2000) and in satellite observations across scales (e.g., Rosenfeld and Lensky, 1998; Nakajima et al., 2001; Kaufman et al., 2002; Breon et al., 2002).

Much of the observational evidence for this theory was obtained by analyzing the emissions of large ocean-going ships that leave tracks of pollution in the otherwise clean marine atmosphere (Radke, 1989; Ackerman et al., 2000). In one such study off the Washington coast, Ferek et al. (1998) found droplet size distributions in ship tracks that were initially bimodal and evolved to a unimodal distribution after an hour-long aging. They conclude that higher CCN number concentrations inside the ship track led to higher CDNC and mean droplet diameters half the size of those measured in the ambient air. This is, however, not a universal rule since the ratio of CDNC to particle number concentration, known as the activated fraction, depends on aspects of the aerosols and the environment. Moreover, droplet size varies not only with droplet number but also with the water available in the given environment. Even so, as stated by Ramanathan et al. (2001) in a review of aerosols and climate, in most cases an increase in aerosol will lead to a decrease in droplet radius.

2.2.1 Twomey effect

The implications of this finding were realized early but are still studied today. Twomey (1974) first considered the impact a decrease in droplet size would have on cloud albedo. He explains that the optical thickness of a cloud is directly proportional to the cross-sectional area of droplets in that cloud. Subsequent measurements showed that increasing CCN typically leads to greater cloud albedo because of its impact on droplet size (Twomey, 1977). The magnitude of this effect, known as the first aerosol indirect effect, on a global scale is still debated. Kaufman et al. (2002) suggest that the uncertainty surrounding global temperature change due to the indirect effect is 5 to 10 times greater than that of greenhouse gases.

Much of the uncertainty is a result of the poorly understood impacts of aerosols on cloud dynamics and precipitation, which may also lead to cloud system albedo changes. Cloud droplets cannot grow to rain drop size on the time scale of a cloud lifetime by condensation only. Collision and coalescence of the droplets is required in warm clouds to produce rain. When collision-coalescence occurs effectively, rain is produced and the cloud is considered to be colloidally unstable. Small droplets, such as those often observed in polluted clouds, do not collide efficiently and often form colloidally stable clouds. In a study of the smoke from sugar-cane fires, Warner (1968) observed a long-term decrease in precipitation downwind of the aerosol source and no similar decrease at upwind locations. The observed 25% decrease in rainfall was attributed to the impact of the increased aerosol on the colloidal stability of the downwind clouds.

2.2.2 Regime-specific aerosol effects

Warner (1968) restricted his study to small precipitating cumulus, guessing that heavily raining cumulonimbus would not be affected by fluctuations in CCN number. It has since been observed that the interplay between cloud microphysics and dynamics leads to contrasting aerosol effects in different cloud types and even cumulonimbus clouds are impacted. For example, simulations of deep convective clouds by Khain et al. (2004) and Lynn et al. (2005) demonstrated that an initial suppression of precipitation formation by an increase in aerosols leads to more vigorous convection due to an increase in the amount of latent heat released. This may result in an increase in precipitation rate in the polluted system but because of feedbacks onto other dynamics, such as secondary convection, a decrease in total precipitation can still occur (Lynn et al., 2005; van den Heever et al., 2006).

Since Albrecht (1989) wrote about the effect of aerosols on cloud fraction in marine stratocumulus, significant attention has been paid to the aerosol effects that are specific to this cloud regime. Again, the initial effect of increased aerosols in marine stratocumulus clouds is a suppression of precipitation, drizzle in this case (Jiang et al., 2002). However, the dynamical feedbacks of drizzle suppression are complex and not well understood. Two-dimensional simulations of stratocumulus clouds by Feingold et al. (1996) showed that the evaporation of drizzle just below cloud base acts to destabilize the boundary layer, promoting convection below cloud base and leading to enhanced cloud albedo. Conversely, the boundary layer may become more stable if the drizzle reaches the surface. Further model investigations, including large-eddy scale (Stevens et al., 1998) and three-dimensional eddy-resolving simulations (Jiang et al., 2002) confirmed these hypotheses. Adding to the complexity is the largely unknown role of giant CCN (GCCN) in this and other cloud regimes. Feingold et al. (1999) reported on large eddy simulations in which observed

GCCN concentrations could cause a formerly colloidally stable cloud to precipitate. This effect was most pronounced in high CCN environments.

The mechanism by which precipitation can be suppressed in polluted areas is slightly different in mixed-phase, orographic clouds. In these clouds ice crystals coexist with cloud droplets and the main determinant of precipitation efficiency is the rate of collection of droplets by the ice, or riming (Saleeby and Cotton, 2007). Theoretically, the riming efficiency is computed from the size of the collector ice crystal and the size of the cloud droplets being collected, and decreases sharply for droplets with diameters below 10μm (Pruppacher and Klett, 1997). Therefore, an increase in CCN can decrease riming, leading to suppressed precipitation totals on the windward side of the orography and increased accumulated precipitation on the leeward slope as unrimed, slowly falling snow crystals are advected further downstream (Saleeby et al., 2009). This "spillover" effect has also been shown in two-dimensional simulations of warm-phase orographic clouds, although in these cases the precipitation redistribution is attributed to a slowing of the rate of cloud droplet collection or autoconversion (Muhlbauer and Lohmann, 2008; Lynn et al., 2007). The riming efficiency also partly determines the rate of aerosol scavenging by precipitation. Analysis of cloud-water samples collected from orographic clouds by Collett et al. (1993) showed that high riming rates lead to greater removal of aerosols from the atmosphere. Particles in droplet solution that are not scavenged may undergo chemical transformations and be restored as aerosols upon evaporation of the droplets.

2.3 Sources and chemistry of CCN

Extracting the impact of aerosols from the natural dynamical variability of clouds is often challenging (Xue and Feingold, 2006) and to do so requires knowledge of the variability of ambient aerosol properties (Levin and Cotton, 2009). Thus, an enormous amount of research has been published on the sources and properties of atmospheric aerosol. Here only a short discussion is warranted on the major aerosol species with emphasis given to areas where uncertainty is still high.

2.3.1 Sulfate aerosol

Andreae and Rosenfeld (2008) deduced from previous work that sulfate aerosol is the most abundant species (reckoned by number) in the atmosphere today. The majority of sulfate aerosol is anthropogenic, or produced by humans. Ten studies of atmospheric sulfur emissions reviewed by Haywood and Boucher (2000) estimate the global atmospheric sulfate aerosol burden to be between 1.5 and about 3 Tg, while Andreae and Rosenfeld (2008) use a figure of 2.8 Tg. In all the studies, the anthropogenic contribution to global sulfur emissions was greater than the natural contribution. Eighty percent of the world's sulfur emissions in 1990 were estimated to be from fossil fuel use (Smith et al., 2001). Dentener et al. (2006) give an updated estimate of 84% for the year 2000. Other sources that are minor by comparison include biomass burning, volcanic activity, and natural production of dimethyl sulfide (DMS) by marine plankton.

While some sulfate is emitted directly in particle form, known as primary emission, the main source of anthropogenic sulfate aerosol is secondary formation from sulfur dioxide (SO_2) emissions (Haywood and Boucher, 2000). SO_2 forms sulfate aerosol through two main conduits: a gas-phase reaction pathway and a complex set of aqueous-phase oxidation reactions. In the gas phase, SO_2 reacts with the OH radical to produce sulfur trioxide, and then forms sulfuric acid in the presence of water vapor as shown in Seinfeld and Pandis (2006). Gas-phase sulfuric acid has been shown to nucleate new particles when in sufficient concentrations, especially in the presence of gaseous ammonia (Sihto et al., 2006), and will also condense onto existing particles. For typical concentrations of reactants the lifetime of SO_2 with regard to this pathway is on the order of a week, the reaction with the OH radical being the limiting step. Also noted by Seinfeld and Pandis (2006) is that SO_2 has a high rate of dry deposition that is not well represented in models, which, according to Andreae and Rosenfeld (2008), leads to uncertainty in the fraction of SO_2 converted to sulfate.

SO_2 oxidation in the aqueous-phase occurs at a much faster rate than the gas-phase pathway, although new particles are not formed. The chemical pathway and rate of oxidation in aqueous solution varies with pH and temperature. The major oxidants are ozone, peroxides, and oxygen when catalyzed by dissolved Fe(III) or Mn(II), although formaldehyde, and OH radical are considered situationally important. Only peroxides are important at low pH and the other pathways increase in rate with increasing pH. Regardless of pathway, the resulting S(VI) can add to the mass of the droplet nucleus particle upon evaporation of the droplet.

By virtue of its abundance and hygroscopic nature, sulfate aerosol has been used as a surrogate for CCN in earlier studies of continental aerosol effects on clouds and precipitation (Novakov et al., 1994; Leaitch and Isaac, 1994; Boucher and Lohmann, 1995). Still, difficulty representing the dry deposition of SO_2 and aqueous reactions involving sulfur

(often limited by a lack of knowledge of oxidant availability) add uncertainty to model predictions of sulfate aerosol.

2.3.2 Nitrate aerosol

The global atmospheric burden of nitrate aerosol is reported by Andreae and Rosenfeld (2008) to be approximately 0.49 Tg, or somewhat less than one fifth the total mass burden estimated for sulfate aerosol. Because of the comparatively low burden and emissions, nitrates are thought to be less important than sulfates on a global scale (Levin and Cotton, 2009). Locally, nitrates can be proportionally much more abundant (Haywood and Boucher, 2000) and an important component of the CCN population due to its high hygroscopicity (κ=0.67 for ammonium nitrate; Petters and Kreidenweis, 2007). Ammonium nitrate is produced by the gas-phase reaction between basic ammonia and nitric acid. The equilibrium between these three compounds is a strong function of the ambient temperature and humidity. As these ambient quantities decrease, particle phase nitrate will become more abundant. This means that surface observations of nitrate aerosol may often misrepresent the quantity present at cloud base. In addition, ammonium nitrate is only produced in large amounts in low-sulfate, or high ammonia environments because ammonia molecules will preferentially react with the stronger sulfuric acid.

Nitric acid is a product of daytime NOx reactions with the hydroxyl radical and nighttime reactions involving the nitrate radical. These precursors have both biogenic and anthropogenic sources including the burning of fossil fuels and biomass, and lightning as listed by Bauer et al. (2007). Anthropogenic emissions of nitrate aerosol precursors are expected to increase during this century until nitrates rival sulfates in terms of the overall

climate impact (Bauer et al., 2007). Although for modeling purposes nitrate aerosol is typically assumed to take the form of ammonium nitrate, nitric acid has been known to deposit onto large particles such as mineral dust or sodium chloride aerosol (Andreae and Rosenfeld, 2008). Recent measurements of particle nitrate at rural sites by Lee et al. (2008) established that these coarse-mode forms often dominate local nitrate aerosol mass and warrant consideration in current models.

2.3.3 Carbonaceous aerosol

Organic aerosol present perhaps the greatest challenge to our understanding of aerosol impacts on clouds and climate. Analyses of aerosol composition have shown that the majority of particles contain some organic and some inorganic material (Murphy et al., 2006), and by some estimates, the organic material dominates the total mass of atmospheric aerosol (Jimenez et al., 2009). Yet, the variability in sources and chemistry of organic aerosol are such that major simplifications are needed to represent the role of organic compounds in the atmosphere (Kanakidou et al., 2005). Therefore, what follows is a description of recent strategies for modeling organic aerosol and the uncertainties therein that are highly relevant to this study.

Fuzzi et al. (2006) recommend that organic aerosol be classified by source for modeling purposes. In a broad sense these categories are combinations of primary or secondary sources, and anthropogenic or biogenic sources. Primary anthropogenic sources include fossil fuel and biomass burning but also a diverse list of minor sources such as tire dust or meat cooking, especially in urban areas. These activities result in the emissions of hundreds of identifiable carbonaceous compounds in particulate form or as quickly

condensing gases (Rogge et al., 1996). For modeling emissions, observations of site-specific studies, similar to the Rogge et al. (1996) Los Angeles work, are often extended to global inventories using a scaling factor such as population density, or energy consumption (Bond et al., 2004; Dentener et al., 2006). Kanakidou et al. (2005) and Fuzzi et al. (2006) point out large uncertainties in this method of scaling, although it may still be the best method since we lack sufficient observational datasets on the topic. Regional emission inventories, such as the National Emissions Inventory (NEI), do include some specific sources of primary organic aerosol (US EPA, 2009).

Most often in modeling of primary emissions a distinction is made between organic carbon (OC) and light-absorbing carbon, which is roughly the same as elemental carbon (EC), or soot, and emitted largely by diesel combustion (Bond et al., 2004). Some models do not consider any additional primary carbonaceous aerosol complexity (Grell et al., 2005; Easter et al., 2004). This is a limited view from a cloud-modeling perspective since potential differences in hygroscopicity between species are of interest. Nonetheless, current understanding and computer power do not support representation of even a majority of known emitted species and the OC group must be used. Investigations into the hygroscopicity of OC as a group have led to a variety of conclusions about its potential impact on CDNC. In a comprehensive study of this kind, Ervens et al. (2005) tested the sensitivity of CDNC to realistic variations in OC chemical properties. They concluded that for droplet activation OC could be adequately represented with an insoluble and soluble fraction. The insoluble/soluble fraction approach is applied in many current global models including CAM3 (Zhang, 2008), ECHAM/MADE (Lauer et al., 2005) and TOMAS (Pierce et al., 2007).

In addition to primary emissions, secondary formation of organic aerosols is now recognized as a major contributor to atmospheric aerosol mass (Heald et al., 2005; Jimenez

et al., 2009). Secondary organic aerosols (SOA) refer to particulate organic compounds that were emitted into the atmosphere in the gas phase but partitioned to the particle phase following a decrease in volatility, typically a result of oxidation, or a change in atmospheric conditions. The observation of SOA is complicated by semi-volatile organic compounds that might be found in either phase due to slight variations in these conditions and by compounds that are found in both SOA and in direct emissions, such as dicarboxylic acids. We are only beginning to learn about contributions to SOA by aqueous oxidation processes (Kanakidou et al., 2005). In measurements of the composition of fog droplets in California, Collett et al. (2008) showed that organic matter can comprise close to 50% of the total solute material, suggesting cloud processing may be an important contributor to SOA mass.

Only a handful of attempts have been made to model the partitioning between SOA and precursor gases for both biogenic and anthropogenic emissions. Schell et al. (2001) described the development of one such model, the Secondary Organic Aerosol Model (SORGAM). SORGAM predicts precursor gases in a series of classes containing oxidation products of species with similar chemical structure and, therefore, presumed similar oxidation pathways. It also employs a two-product model in which two classes are predicted for the same precursor gas species or group of species containing oxidation products with different volatility. The molecular weights assigned to the different classes were determined somewhat arbitrarily (Schell et al., 2001). The two-product method is also used in the modeling efforts of Chung and Seinfeld (2002) and Kanakidou et al. (2000).

The more recent Model to Predict Multi-phase Partitioning of Organics (MPMPO) predicts partitioning of specific oxidation products but only for three precursor organic gases (Chen and Griffin, 2005). Neither system truly satisfies the need for SOA hygroscopicity information as SORGAM does not predict specific species, and no hygroscopicity data exist for the majority of species predicted in MPMPO. Also, none of the

aforementioned models include contributions from the oxidation products of isoprene, even though these are likely to add considerable mass to ambient aerosols (Hodzic et al., 2009). At the time of publication of Levin and Cotton (2009), they noted that no estimates of the contribution of SOA to the total CCN population had yet been published. In the brief time since, Pierce and Adams (2009) estimated the contribution on a global scale using TOMAS, a sectional aerosol microphysics model. They predict that about 20% of the global CCN mass consists of SOA but stress the extreme uncertainty in the emissions of precursor gases and condensation rates that led to their conclusion.

2.3.4 Dust and sea-salt aerosols

Dust and sea-salt (NaCl) are observed in far fewer numbers in the atmosphere than sulfates, nitrates, or organic aerosol but dominate the global mass burden because of their comparatively large size. Dust particles are considered wind-generated although emissions also depend on soil moisture and are geographically limited to specific source regions (Ginoux et al., 2001). Modeling the flux of dust into the atmosphere has proved challenging because of the variability in source strength and scarcity of validation datasets, although the application of satellite observations has furthered efforts (Laurent et al., 2008).

Pure mineral dust particles are not considered a major contributor to CCN number concentrations due to their small number burden and generally low hygroscopicity. Koehler et al. (2009) tested the droplet growth characteristics of dust from several sources. They found that hygroscopicity differed between source regions but recommend a value of κ=0.03 for modeling purposes. Still, dust may be co-emitted with hygroscopic material or over time may become coated with more hygroscopic material by coagulation or

condensation and thereby be more likely to act as CCN or GCCN (Levin et al., 1996; Perry et al., 2004; Fan et al., 2004; Twohy et al., 2009). Dust particles have also been shown to act as efficient ice nuclei and therefore can have a multi-faceted impact on clouds, especially mixed-phase clouds (Demott et al., 2003; van den Heever et al., 2006; Wiacek et al., 2010).

Emission of sea-salt particles in modeling also relies on wind speed-dependent empirical formulas. Physically, sea-salt is emitted by the bursting of bubbles on the ocean surface or, at higher wind speeds, the shearing of droplets off of wave crests. Production of sea-salt particles is particularly potent in shoal areas with breaking waves (Clarke et al., 2006). These mechanisms produce sea-salt particles with sizes spanning four orders of magnitudes but typically at low number concentrations (O'Dowd et al., 1997). Recent work on sea-salt emission functions has suggested that the introduction of significant wave height (SWH) into the equations may improve emission predictions in high wind speeds (Witek et al., 2007).

In contrast to dust, sodium chloride is extremely hygroscopic (κ=1.28) (Petters and Kreidenweis, 2007). Sea-salt aerosol is observed far inland from oceans in different forms (Lee et al., 2008) but its contributions to CCN populations are greatest in remote, marine locations (Pierce and Adams, 2006). Sea-salt particles are also an important source of GCCN because of the wide range spanned by their sizes.

2.4 Aerosol processes

Particle nucleation events, in which new particles are formed from low volatility gas precursors, are still under investigation. Evidence now exists for a role of organic acids in the nucleation of new particles (Dusek et al., 2010), although it is likely that the organic

compounds assist in nucleation with sulfuric acid rather than form pure organic particles (Zhang et al., 2004). Still, CCN measurements collected during nucleation events by Dusek et al. (2010) show a substantial organic mass fraction in new particles and a corresponding decrease in new particle hygroscopicity. In aerosol models, nucleation schemes are often unrealistically simplified such as in the Modal Aerosol Dynamics Model for Europe (MADE) (Ackermann et al., 1998), or non-existent as in SORGAM, citing the lack of knowledge concerning organics and nucleation (Schell et al., 2001). Chapman et al. (2009) note that nucleation schemes that incorporate organic compounds are still in the development stage.

Processes acting on pre-existing particles and particle distributions over time can alter their sizes and compositions and hence, their CCN activity. These processes are regularly known together as aerosol aging and incorporate condensation, coagulation and cloud processing. All three result in the addition of mass, often of a different chemical nature, to existing particles. Petters et al. (2006) review the impact of an additional aging process known as chemical aging whereby oxidation reactions on the surface of organic aerosol change their water activity. From their laboratory measurements they conclude that chemical aging is likely an insignificant control on aerosol hygroscopicity when compared to other aging processes.

Condensation refers to the gas-particle partitioning of low volatility gases onto existing particles. Partitioning depends on the volatility of the compound as well as its concentration in the atmosphere. Condensation often produces combinations of different chemical compounds, or internal mixtures. Internal mixtures can also result from cloud processing of aerosol. Sulfate and organic acids produced in the aqueous phase within a cloud droplet are deposited onto the droplet nucleus upon droplet evaporation. If the droplet is situated in a colloidally unstable cloud, it may combine with other droplets to form a precipitation hydrometeor. And if the hydrometeor falls to the ground, it will

remove its nucleus mass from the atmosphere and the mass of any other particles it collected during its fall. This is known as wet deposition and is challenging to simulate since it is connected to cloud microphysics. Aerosols are also removed from the atmosphere by gravitational settling, or dry deposition. The rate of settling increases with particle size and, therefore, is most important for coarse mode aerosols. Model estimates vary in their assessments of deposition processes (Textor et al., 2006), which often lead to disagreements in total aerosol burden estimates (Andreae and Rosenfeld, 2008).

Particles may combine, or coagulate, as a result of atmospheric collisions. Collisions are most likely to occur between particles of very different sizes so while particle distribution mass is conserved during coagulation, total number decreases and the size distribution becomes skewed toward the larger particle sizes. Moreover, as with condensation, internal mixtures can be created by coagulation.

Model representations of aerosol mixing state vary, as do judgments of its impact on cloud microphysics. Cubison et al. (2008) investigated the importance of the representative mixing state in modeling CCN activation in an urban setting. They found that CCN prediction was improved compared to observations by assuming externally mixed aerosol and conclude that using an internal mixture for modeling can lead to both over and under-predictions of CCN. Medina et al. (2007) conducted analogous predictions of CCN during a field project in the northeast United States. They also attributed error in their predictions to the simplifying assumption of internally mixed aerosol. In contrast, a similar experiment from the same field project found that knowledge of the aerosol mixing state was not necessary to predict CCN in this particular remote location (Ervens et al., 2007).

In general, aerosol populations are thought to exhibit the characteristics of externally mixed aerosol near sources and become more internally mixed with aging (McFiggans et al., 2006). This is often used to justify the assumption of internally mixed

aerosol in CCN predictions at remote locations (Dusek et al., 2006; Andrejczuk et al., 2008; Ward et al., 2010). McFiggans et al. (2006) review observational studies of aerosol mixing state and find that neither an external or internal mixture truly defines atmospheric aerosol. Instead, the majority of aerosols fall somewhere in between, in a quasi-internal mixture.

Many recent studies find that aerosol composition is partially dependent on size. Size-differentiated composition measurements near Houston, Texas, showed nucleation-size, or Aitken, mode aerosol that were dominated by organic compounds but an accumulation mode containing mostly sulfate mass. Both Medina et al. (2007) and Furutani et al. (2008) were able to improve their predictions of CCN when size-varying aerosol composition was taken into account. Complex mixing states receive representation in few regional or global models, perhaps because the impact of mixing state on aerosol hygroscopicity is unclear. A notable exception is the GATOR-GCMOM global-urban scale model that simulates the transition of aerosol from an external mixture soon after emissions to a quasi-internal mixture with aging (Jacobson et al., 2007). Other major coupled models use exclusively either an internal or external mixture (Zhang, 2008), assuming simplicity to increase computational efficiency as is done with many of the complexities of atmospheric aerosol reviewed in this section.

2.5 Modeling of droplet activation

According to Levin and Cotton (2009), the field of aerosol modeling has evolved somewhat apart from the field of cloud microphysics modeling, with coupled models being a relatively new development. Yet, aerosols and clouds interact in the atmosphere, meaning to model one effectively, the interaction with the other must also be considered. The bulk of

this interaction occurs where droplets and ice crystals form on particles, leading to possible in-cloud chemistry, deposition or evaporation. Thus, an accurate droplet activation scheme is essential for simulating a more complete aerosol and cloud system.

Droplet activation has long been studied by simulating single aerosol-laden air parcels within an updraft (McFiggans et al., 2006). These parcel models solve the Köhler equations of droplet growth within the rising air parcel, returning a precise model estimate of the CDNC. Parcel models have been applied to the question of the effects of aerosol composition on droplet activation (e.g. Ghan et al., 1998; Antilla and Kerminen, 2007; Reutter et al., 2009). In one of the first examples of these studies, Lee et al. (1980) even used an empirically derived hygroscopicity factor to account for aerosol composition observed at different locations. However, to avoid the computational expense of implementing a parcel model within a microphysical scheme, larger-scale numerical models use droplet activation parameterizations. Early parameterizations, such as Feingold and Heymsfield (1992) and Cotton et al. (1992), computed the CDNC using the power law relationship developed by Twomey (1959). The drawbacks of this approach, as reckoned by McFiggans et al. (2006), are implicit aerosol composition (implied but not expressed directly) and unrealistic representation of the aerosol size distribution. The power law approach has been revisited in recent work by Khvorostyanov and Curry (2008) who have updated the Twomey (1959) relationship to include the effects of some aerosol chemical properties. Chuang and Penner (1995) introduced a parameterization that used lognormal aerosol size distributions and was subsequently applied in the ECHAM GCM cloud droplet scheme (Lohmann et al., 1999). Still, this parameterization used implicit aerosol composition, which cannot truly capture the variations in aerosol hygroscopicity observed in the atmosphere (Nenes and Seinfeld, 2003).

2.5.1 Parameterizations

Several cloud droplet activation parameterizations have since been developed that explicitly define aerosol chemistry, although often for a limited number of chemical species (Abdul-Razzak and Ghan, 2000; Nenes and Seinfeld, 2003; Ming et al., 2006; Segal and Khain, 2006; Kivekas et al., 2008; Hsieh et al., 2009). All of these cited parameterizations are based approximately on Köhler theory and represent composition with estimates of the combination of the Van't Hoff factor, molecular weight of the solute and the insoluble fraction (Eq. 2.2). The use of these factors makes consideration of internally mixed aerosol chemistry challenging.

Nenes and Seinfeld (2003) introduced an advanced droplet activation parameterization that has the option of inputting a size-dependent composition. It has shown utility in estimating the impact of surface-active compounds that can alter the droplet surface tension beyond the effect described by Köhler theory (Fountoukis and Nenes, 2005). A more recent incarnation of this parameterization included the effect of entrainment on droplet activation for global models (Barahona and Nenes, 2007). The binned, or sectional, aerosol size distribution used in this parameterization and comprehensive set of equations does, however, require a sacrifice of computational efficiency (Nenes and Seinfeld, 2003). Some previous researchers have simplified their formulations by assuming an invariant aerosol composition. For example, the original incarnation of the Abdul-Razzak and Ghan (2000) cloud droplet parameterization was limited to an aerosol population composed of a soluble ammonium sulfate fraction and an

insoluble fraction. Segal and Khain (2006) also use only soluble sodium chloride aerosol in their parameterization, citing a small sensitivity of CDNC to aerosol composition compared to that of aerosol number as justification.

Whether these simplified parameterizations are sufficient for cloud modeling remains a subject of discussion. Rissman et al. (2004) tested an updated version of the Abdul-Razzak and Ghan (2000) for CDNC sensitivity to aerosol chemistry, especially organics in marine stratocumulus conditions. They found large variations in the sensitivity to aerosol chemistry that were dependent on the other model initial conditions including aerosol mean radius, number concentration and soluble organic mass fraction. For some situations, they determined that the CDNC was more sensitive to changes in aerosol chemistry than to the ambient vertical velocity (based on observed values of these parameters). For similar stratocumulus conditions, Meskhidze et al. (2005) determined that on average, CDNC was 2-3 times more sensitive to vertical velocity than to aerosol composition. In cumulus clouds, the sensitivity to aerosol composition was found to be less important (Meskhidze et al., 2005).

2.5.2 Droplet activation in RAMS

A slightly different approach to droplet activation is used in the Regional Atmospheric Modeling System (RAMS) (Cotton et al., 2003). Saleeby and Cotton (2004) showed that parcel model output of CDNC, which is used for validation of the majority of the parameterizations referenced above, could be accessed directly by the model microphysics using a lookup table system. The tables consist of the parcel model activated fraction results for a large range in atmospheric conditions. As these conditions are encountered in

RAMS, the appropriate activated fraction value is found and applied to the model aerosol number concentration. This scheme retains the computational efficiency of a traditional parameterization and yet always returns the parcel model computation as if the parcel had been simulated online. The main drawback of the RAMS droplet activation parameterization is a lack of flexibility with regard to range in atmospheric and aerosol conditions chosen to construct the lookup tables.

The Saleeby and Cotton (2004) parameterization has been applied in several cloud-scale modeling studies since its introduction (e.g. van den Heever et al., 2006; van den Heever and Cotton, 2007; Cheng et al., 2009; Saleeby et al., 2009). However, similar to several of the aforementioned parameterizations, only a limited number of aerosol composition arrangements can be considered. The next chapter will describe the introduction of the κ parameter into the RAMS droplet activation parameterization and add to the discussion about the importance of aerosol composition in such parameterizations.

Chapter 3

Aerosol hygroscopicity in the RAMS droplet activation scheme

The RAMS cloud droplet activation scheme previously allowed for only a soluble ammonium sulfate and insoluble fraction aerosol composition (Saleeby and Cotton, 2004). Furthermore, the proportion of soluble to insoluble aerosol in the former setup is fixed during a simulation. While this setup showed some ability in precipitation forecasting (Saleeby and Cotton, 2005), questions remain regarding the impact of aerosol chemistry on RAMS predictions of CDNC and how these impacts may feed back into additional model microphysics and precipitation production. In fact, these questions have been central in the debate over the importance of including detailed aerosol chemistry in coupled models. In this chapter the addition of hygroscopicity as an independent variable in the activation scheme is described. New lookup tables are constructed using the output from a parcel model that simulates droplet growth based on the κ parameter. The results of the parcel model simulations will be used to add constructively to the debate about the importance of aerosol composition, with recommendations for future modeling studies.

3.1 Parcel model description

The parcel model used for simulating droplet activation was introduced by Heymsfield and Sabin (1989) and Feingold and Heymsfield (1992), and has been described thoroughly by Saleeby and Cotton (2004). The parcel model follows a simulated air parcel as it is lifted at an initial updraft velocity and becomes supersaturated with respect to water. Initially (time, t = 0), the parcel contains a prescribed distribution of dry aerosol. The distribution is assumed to be lognormal with geometric standard deviation, $\sigma_g = 1.8$ and the total number concentration is divided into bins with assigned representative radii. The model then puts the aerosol-laden parcel through a high humidity, but unsaturated, environment in which it is assumed that all the particles deliquesce and reach an equilibrium size. With aerosol deliquesced but unactivated, the parcel begins its simulated ascent, rising 2.5m per timestep. While being lifted, activation of haze particles and the growth of droplets in each size bin along with expressions for the change in temperature, pressure, air density and liquid water content with time are solved iteratively. After reaching its maximum supersaturation (S_{max}), the parcel is lifted a further 50m to provide ample time for activated droplets to grow.

The percentage of the initial particle number that activate in the parcel model depends on a number of input variables that describe the initial aerosol and environmental conditions. To limit the number of combinations of initial settings, Saleeby and Cotton (2004) restricted the independent variables to four: temperature T, updraft velocity w, total particle, or condensation nuclei (CN), number concentration N_{cn}, and the aerosol distribution number median radius r_g, and assumed a constant aerosol composition of ammonium sulfate or sodium chloride with a constant insoluble fraction. We have extended this scheme to include aerosol hygroscopicity as a fifth independent variable.

The incorporation of aerosol hygroscopicity was made possible by modifications made to the original Heymsfield and Sabin (1989) parcel model by Eidhammer et al. (2009). Their model development work included the introduction of the hygroscopicity parameter (κ) (Petters and Kreidenweis, 2007) into the saturation ratio formula for liquid droplets. The research reported here includes only one aerosol mode characterized by a single value of κ for each simulation. The representation of complex combinations of aerosol species is simplified by using κ but an internal mixture of aerosol is still assumed for this analysis. As in previous studies (e.g., Ervens et al., 2007; McFiggans et al., 2006; Rissman et al., 2004), the possible inaccuracy of ignoring quasi-internal or external mixing states is noted here but also noted are the difficulties in modeling such aerosol.

With the Eidhammer et al. (2009) changes in place, the parcel model was run for all combinations of initial T, w, N_{cn}, and r_g used in Saleeby and Cotton (2004) and for 23 values of κ between 0.00001-1.28. All initial values are given in Table 3.1. These values were

Table 3.1: Initial values for parcel model simulations.

T (°C)	-30	-20	-10	0	10	20	30		
N_{cn} (cm^{-3})	10	31.6	100	316	1000	3600	1e5		
w (m/s)	0.01	0.032	0.1	0.316	1.0	3.16	10	31.6	
r_g (μm)	0.01 0.24	0.015 0.36	0.02 0.48	0.03 0.64	0.04 0.96	0.06 1.28	0.08	0.12	0.16
κ	1e-5 0.4 0.85	1e-4 0.45 0.9	0.001 0.5 1.0	0.01 0.55 1.1	0.1 0.6 1.28	0.2 0.65	0.25 0.7	0.3 0.75	0.35 0.8

selected to span typical observed magnitudes of aerosol hygroscopicity in both urban and remote locations. Andreae and Rosenfeld (2008) reported typical continental values of κ = 0.2 to 0.4 with few observations below 0.1, and 1.28 is the reported value for NaCl (Petters and Kreidenweis, 2007). The initial pressure, 600mb, and initial relative humidity, 99%, were kept the same for all model runs. S_{max} achieved in the parcels, and the resulting activated droplet number concentration, N_d, were recorded.

In general, the sensitivity of droplet activation to changing κ has been shown to decrease with increasing κ (Petters and Kreidenweis, 2007). For this reason, several of the high-κ parcel model results can be disregarded for the construction of look-up tables while maintaining sufficient resolution of the potential impacts on activated fraction. Lookup tables for the following ten values of κ were included in the RAMS droplet nucleation scheme: 0.00001, 0.01, 0.1, 0.2, 0.25, 0.35, 0.45, 0.6, 0.9, and 1.28. When intermediate values of κ occur in the course of a simulation, N_d is determined by linear interpolation between the activated fraction for the adjacent higher and lower κ lookup tables.

The updated scheme has the new ability to simulate the different CCN activity of any combination of internally mixed aerosol while not requiring any additional computation time. A clear disadvantage, however, is that the lookup tables are created for one aerosol mode with a constant composition and are not easily modified. Particle composition that is a function of particle size is not represented, although recent studies, such as Cubison et al. (2008), have shown that variations in composition with size could be important for assessing CCN activity. Abdul-Razzak and Ghan (2000; 2002) included multiple-mode capability in their droplet activation parameterization (Abdul-Razzak et al., 1998). They use a sectional representation of particle distributions, each with an associated composition, to capture any complex combination of aerosol size and chemical makeup. The drawback of a

binned scheme is the additional computational expense required to run it compared to simplified, bulk aerosol parameterizations.

3.2 Supersaturation regime analysis

As κ is increased in the parcel model, the simulated particles become more hygroscopic and equivalent particle sizes will activate at lower supersaturations. Thus, increases in κ allow for particles with incrementally smaller sizes to reach the critical threshold and a larger portion of the aerosol distribution to activate. Recently, Reutter et al. (2009) reported the results from a parcel model study in which they found that the relationship between an increase in κ and an increase in N_d was not constant, but varied with changes in the ratio of the initial updraft speed to the initial particle number (w/N_{cn}). They suggest that this ratio can be used to define environmental regimes in which droplet activation has similar sensitivity to changes in aerosol composition. Conditions with low values of w/N_{cn} were classified as updraft-limited ($w/N_{cn} <\approx 10^{-4}$ $ms^{-1}/(cm^{-3})$) and high values as aerosol-limited ($w/N_{cn} >\approx 10^{-3}$ $ms^{-1}/(cm^{-3})$) with a transition regime between these two extremes (10^{-4} $ms^{-1}/(cm^{-3}) <\approx w/N_{cn} <\approx 10^{-3}$ $ms^{-1}/(cm^{-3})$). The median radius of the input lognormal aerosol size distribution was held fixed. They found that changes in composition had an insignificant effect on droplet activation in the aerosol-limited regime and a moderate impact on droplet number concentrations for updraft-limited conditions.

The w/N_{cn} quantity is especially useful for classifying different parcel model environments, as it is an able predictor of the model S_{max}. In the simulations described in this dissertation, the S_{max} (averaged over all initial r_g and T) was highly correlated with w/N_{cn} in a positive sense (linear correlation coefficient r = 0.93) between values of w/N_{cn} = 10^{-6} $ms^{-1}/(cm^{-3})$ and $w/N_{cn} = 10^{-1}$ $ms^{-1}/(cm^{-3})$.

In Reutter et al. (2009), as in previous studies (e.g., Feingold, 2003; Rissman et al., 2004; McFiggans et al., 2006), a sensitivity parameter was defined to describe the effects of perturbations in aerosol or environmental characteristics on droplet number concentrations or droplet effective radii. Here the convention of Reutter et al. (2009) is adopted. They defined the sensitivity parameter as the logarithmic change in droplet number concentration N_d with the logarithmic change in a specified chemical or physical parameter X_i:

$$S(X_i) = \frac{\partial \ln N_d}{\partial \ln X_i} \tag{3.1}$$

Figure 3.1a shows how changes in aerosol composition affect CCN activity as w/N_{cn} increases in the parcel model, for an initial r_g = 0.06 μm. The dependent variable, S(κ) (equation 3.1), was computed using the method shown by Feingold (2003) and summarized as follows. Parcel model predictions of N_d are plotted against κ on a log-log plot. A linear relationship is fitted to the plot using regression and the resulting slope of the line is understood to be S(κ) for the specified range in κ and given initial conditions. Reutter et al. (2009) use this approach but plot values of N_d for each initial κ that have been averaged over the all the initial conditions and name the modified parameter $\overline{S}(\kappa)$. In the current simulations, several combinations of initial w and N_{cn} result in the same value of w/N_{cn}, meaning multiple values of S(κ) occur at the same w/N_{cn}. Additionally, several values of S(κ) are computed at the same w/N_{cn} but for different initial T. These are averaged to give the single value of S(κ) at each w/N_{cn} shown in Figure 3.1a. The range in κ for this portion of the analysis, 0.2 to 0.5, was chosen to incorporate the typical hygroscopicity values for continental aerosol. It extends the range suggested by Andreae and Rosenfeld (2008) for

continental airmass modeling (0.2 to 0.4) to include the majority of observations compiled by Hudson (2007) in continental regions, reported as κ = 0.33 +/- 0.15 by Andreae and

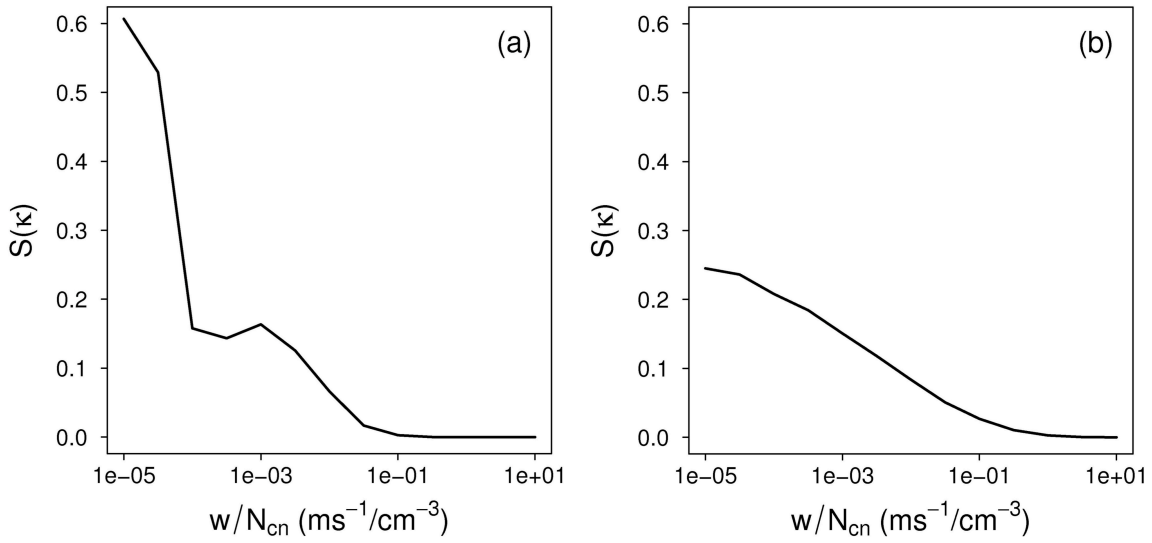

Figure 3.1: The sensitivity of the droplet number to κ, S(κ), computed from parcel model output, as a function of the ratio w/N_{cn}, for κ = 0.2 to 0.5. The sensitivities were averaged over all initial values of T. Results are shown for (a) input aerosol size distributions with r_g = 0.06 μm, and (b) averaged over all initial values of r_g.

Rosenfeld (2008). The particular range chosen is unimportant for this application since we are concerned mostly with relative magnitudes of the sensitivity parameter.

The updraft and aerosol-limited regimes are clearly discerned in Figure 3.1a and compare well to the Reutter et al. (2009) regime designations, also based on r_g = 0.06 μm, despite some differences between our analysis and that of Reutter et al. (2009). They used a broader range of κ, from 0.001 to 0.6, and focused on high updraft and high particle number conditions, characteristic of pyrocumulus clouds. For the current simulations, the change in κ from 0.2 to 0.5 leads to the highest values of S(κ) for w/N_{cn} less than 10^{-4} $ms^{-1}/(cm^{-3})$, defined as the updraft-limited regime. When the model is initialized as aerosol-limited ($w/N_{cn} > 10^{-3}$ $ms^{-1}/(cm^{-3})$), S(κ) is small and diminishes to near zero with increasing w/N_{cn}. In this regime, as noted by Reutter et al. (2009), the parcel reaches a S_{max} great

enough to activate nearly 100% of the particles in the given distribution at all values of κ and for all initial values of w. Thus, compositional effects are rendered insignificant in these highly supersaturated model environments.

Next, this analysis is extended to a range of size distributions by comparing the results of simulations with different initial r_g. Fifteen values of r_g between 0.01 μm and 1.28 μm were used to initialize the parcel model. Figure 3.1b shows the same quantities as in Figure 3.1a, but averaged over the range of initial r_g. The resulting curve exhibits the same three-regime structure as in Figure 3.1a, but the divisions between the regimes are no longer distinct. The sharp decrease in S(κ) between the updraft-limited and transition regimes has been reduced, and some sensitivity to the change in κ extends well into the aerosol-limited regime.

A better demonstration of the effect of changing the size distribution is given in Figure 3.2, which displays the change in S(κ) with increasing r_g while holding w/N_{cn} constant. Previous studies have evaluated S(κ) and sensitivity to other measures of composition as a singular value representative of the entire initial parameter space (e.g., Rissman et al., 2004; Reutter et al., 2009). This figure shows that S(κ) varies significantly within that parameter space, in this case with respect to r_g. In the aerosol-limited regime (Figure 3.2a), S(κ) is small for r_g = 0.06μm but increases to S(κ) = 0.35 below that size. For these small aerosol, composition affects CCN activity even in the aerosol-limited regime. A similar trend is apparent for the transition regime shown in Figure 3.2b, although the high S(κ) values are shifted to higher median radii. Finally, for the updraft-limited regime illustrated in Figure 3.2c, the highest sensitivity extends to even larger median radii, tapering off above r_g = 0.15μm. In all Figure 3.2 plots, the sensitivity to changes in κ varies significantly within the w/N_{cn} regimes. Altogether, the results in this figure show that

w/N_{cn}, or supersaturation-based regimes, cannot fully predict the compositional dependence of CCN activity independently of the r_g.

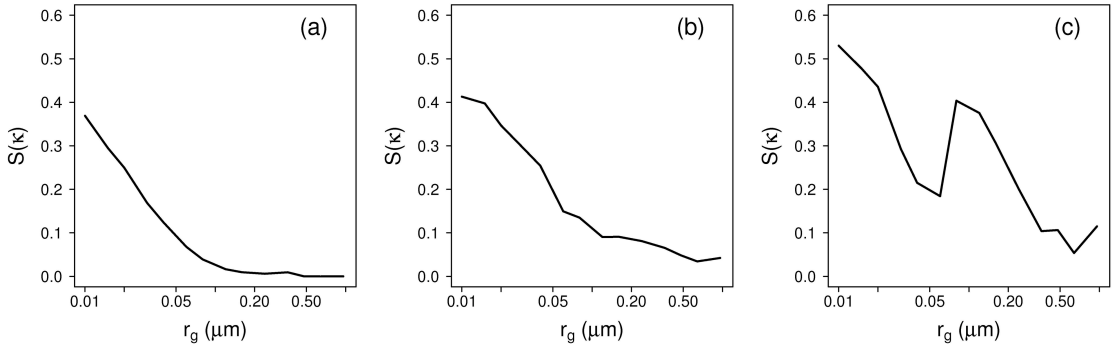

Figure 3.2: S(κ) computed from parcel model output for κ = 0.2 to 0.5 as a function of the choice of initial r_g. The sensitivities were averaged over all initial values of T. Each panel displays output from simulations initialized with a single value of w/N_{cn} set to (a) 1e-02, (b) 1e-03, and (c) 1e-04 ms^{-1}/cm^{-3}.

3.3 Relationship between r_g and S(κ)

The analysis of the w/N_{cn} regimes and the sensitivity parameter imply a role of the size distribution in predicting the dependence of CCN activity on aerosol composition. In their review of droplet activation theory, McFiggans et al. (2006) state that CCN activity is determined by the number of particles and the gradient of the size distribution, at the critical radius (r_c) or range in r_c under investigation. They note that this idea can be attributed to Twomey (1959) whose power-law representation of CCN clearly demonstrates the influence of size distribution parameters over activated fraction. This influence can be shown for lognormal representations of aerosol size distributions as well.

Figure 3.3 illustrates the impact of the initial size parameter r_g on S(κ). The two input aerosol distributions are assumed to have κ = 0.2, and the effect of changing this to κ =

0.5 is evaluated. The shifts in critical dry size for this κ change, corresponding to a selected S_c (chosen as S_c = 0.165%), are indicated. For the distribution with r_g = 0.10 μm, S(κ) = 0.14

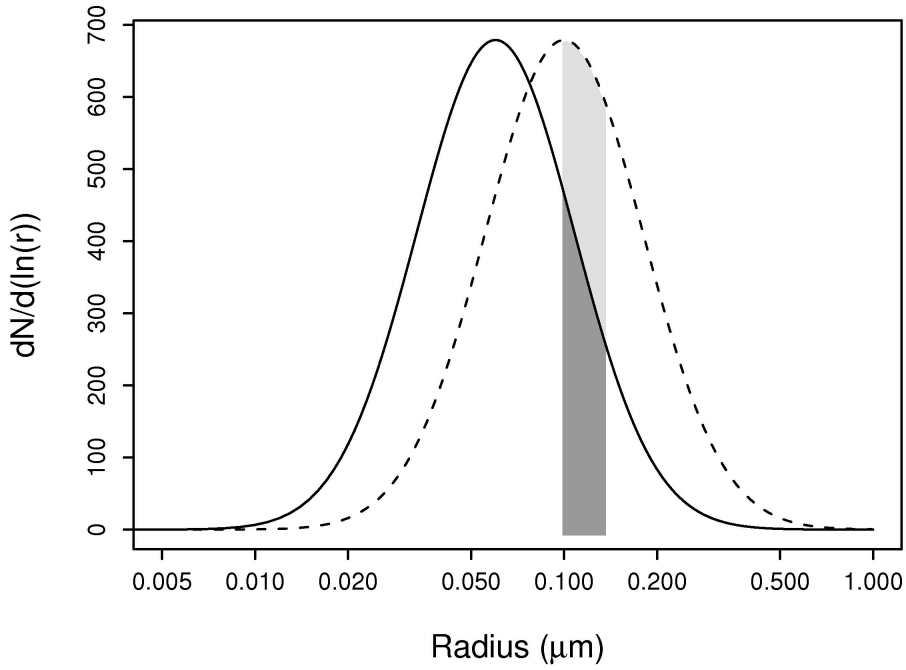

Figure 3.3: Representation of the initial lognormal distributions of aerosol used in the parcel model for r_g = 0.06 μm (solid) and r_g = 0.10 μm (dashed). Each distribution assumes N_{cn} = 1000 and σ_g = 1.8. The shaded region shows the additional number of particles that would activate in each distribution if κ were increased from 0.2 to 0.5 in an environment with S_{max} = 0.165%.

(here, S(κ) is computed simply by differencing the logarithm of N_d at each κ and dividing by the logarithm of the fixed fractional change in κ, see equation 3.1), but the value of this parameter increases to 0.59 for r_g = 0.06 μm due to the shift of the distribution median relative to the r_c of the given supersaturated environment. Of course, in the parcel model, critical supersaturation would not be identical when κ is modified, even for the same updraft velocity, tending to somewhat dampen out these differences (Rissman et al., 2006).

As suggested in Figure 3.3, the variability of the compositional-dependence of N_d is explained, in large part, by the location of the r_c on the size distribution function of an aerosol population. For the lognormal size distribution function, the relative location of r_c can be represented by the percentage of particles in the size distribution smaller than the stated r_c. This percentage can be expressed by evaluating the normalized cumulative size distribution function at radius $r = r_c$:

$$N(r_c) = \frac{1}{2} + \frac{1}{2} erf\left\{\frac{\ln(r_c / r_g)}{\sqrt{2}\ln\sigma_g}\right\} \tag{3.2}$$

where erf is the error function and $N(r_c)$ is the fraction of particles smaller than r_c for the given size distribution parameters r_g and σ_g. Moderate variations in the prescribed value of σ_g, which in these simulations is kept constant, have been shown to play only a minor role in CCN activity by Antilla and Kerminen (2007).

To determine $N(r_c)$ a cumulative distribution function was created for each initial value of r_g used in the parcel model and $\sigma_g = 1.8$. Then, r_c was computed using Eq. (10) from Petters and Kreidenweis (2007) for every combination of initial N_{cn}, w, T, and r_g, but for the fixed range in κ, 0.2 to 0.5. The S_{max} reached in each simulation was used as the S_c required for calculating r_c. The final r_c was taken as the average between the r_c for initial $\kappa = 0.5$ and the r_c for initial $\kappa = 0.2$, for each combination of the other initial conditions. The span of particle size between r_c computed for $\kappa = 0.5$ and $\kappa = 0.2$ (in Figure 3.3, the width of the shaded region along the x-axis) is not constant but varies with the environmental supersaturation and with κ itself. As shown by Petters and Kreidenweis (2007), the change in r_c for a fixed range in κ increases with decreasing supersaturation.

The r_c, computed as explained above for every combination of N_{cn}, w, T, and r_g, was used to solve the cumulative size distribution function with the corresponding r_g. The resulting $N(r_c)$ values are positively correlated with $S(\kappa)$, which is consistent with an increase in r_c relative to r_g leading to an increase in the sensitivity of CCN activity to changes in κ. The computed Pearson linear correlation coefficient, r = 0.82, suggests that the predictive ability of $N(r_c)$ is strong for the entire range of varied initial conditions, including median radius. Therefore, for a fixed r_g, $S(\kappa)$ can be predicted from r_c or, for a known κ range, from S_c as shown by Reutter et al. (2009). However, the inverse is also true. For a fixed S_c and a known κ range, the sensitivity to changes in κ depends on the initial r_g.

This result is, perhaps, intuitive, but it is also instructive. It suggests that for cloud regimes with characteristic supersaturations the importance of aerosol composition for droplet nucleation can be anticipated if basic aerosol size and source data are known. Of course, it is important to remember that these conclusions are derived from simulations that assumed a perfect internal mixture of aerosol and known uni-modal size distribution function, conditions that do not apply universally.

The analysis of the parcel model results can act as a guide to understanding how the RAMS droplet activation parameterization will perform in various conditions. This will be examined in the next chapter in an application of the new lookup tables to an orographic cloud case study.

Chapter 4

Orographic cloud sensitivity study

As an initial application of the κ-based lookup tables, and to test the role of the particle size distribution and aerosol hygroscopicity, sensitivity simulations were carried out centered around a mixed-phase orographic cloud case study for which aerosol size and droplet activation data were known. Previous modeling studies on this topic have shown a redistribution of orographic precipitation resulting from variations in the initial model total particle number concentration (N_{cn}) (Muhlbauer and Lohmann, 2008; Lynn et al., 2007). The spillover effect, described in Chapter 2, has also been demonstrated by Saleeby et al. (2009) for changes in CCN number concentration in winter orographic clouds. They also showed that the impact of the redistribution of precipitation could, over time, substantially reduce the amount of water resources available to the Western Slope. With these simulations the aim is to determine the importance of the model aerosol size and hygroscopicity on these same cloud systems by applying the expanded droplet nucleation scheme to a case observed during the Inhibition of Snowfall by Pollution Aerosols (ISPA) II field campaign in February 2007. Aerosol size and droplet activation data collected during this study provided representative values for the initialization of RAMS in these simulations.

The sensitivity study was run with RAMS, which in addition to housing the new droplet activation parameterization is well suited for simulating mixed-phase cloud systems owing to a sophisticated bin-emulating, bulk microphysics package (Saleeby and Cotton,

2008). Recently this was enhanced by the inclusion of a binned method for representing the riming process that was shown to improve the prediction of riming efficiencies (Saleeby and Cotton, 2008). RAMS predicts the cloud droplet distribution mixing ratio and number concentration (Saleeby and Cotton, 2004) and also predicts two moments of the distributions for rain, hail, pristine ice, snow, aggregates and graupel (Cotton et al., 2003).

4.1 Experimental design

An orographic snowstorm that occurred over the Park Range in northwestern Colorado during February 11-12, 2007 was chosen as the case for this sensitivity study. Orographic clouds in this region form with westerly or northwesterly flow, which induces the greatest uplift over the north-south running topography. In the absence of a frontal system, this flow is often forced by the presence of a mid-level ridge to the west and a developing lee trough to the east, together setting up a strong cross-barrier pressure gradient over the Park Range (Rauber et al., 1986). The February 11-12, 2007 storm formed under these conditions. It was characterized by a sustained period of high LWC, especially after 00Z on February 12, and persistent precipitation of heavily rimed snow crystals (Saleeby et al., 2009). It has been hypothesized by Borys et al. (2000) that higher LWC mixed-phase orographic clouds are more sensitive to changes in CCN number concentration (N_{ccn}). Also, Saleeby et al. (2009) found that mixed-phase orographic storms that contain large supercooled droplet sizes, therefore riming efficiently, are more susceptible to the impacts of increasing N_{ccn}. For these reasons, the February 11-12, 2007 storm provides an excellent test case for examining the effects of a variable aerosol population.

4.1.1 ISPA-II observations

To represent realistic variations in aerosol in these simulations, observations from the ISPA field campaign were used as the basis for the model initializations. Aerosol number concentration and size distribution data were collected from January 6, 2007 to February 28, 2007 using a scanning mobility particle sizer (SMPS) and an aerodynamic particle size spectrometer (APS) located at the Desert Research Institute (DRI) Storm Peak Laboratory (SPL). SPL is located at an elevation of 3210m above mean sea level atop the southern extent of the Park Range and is often above cloud base during winter orographic storms (Borys and Wetzel, 1997). The SMPS measured particle diameters between 0.0087 and 0.34 μm and the APS measured the larger particles with diameters between 0.49 and 20.5 μm. Total N_{cn} was estimated as the sum of particles observed by the SMPS and APS. In addition to the aerosol size distribution, N_{ccn} was measured at supersaturations of 0.1%, 0.2%, 0.3%, 0.4% and 0.6%, as reported by Saleeby et al. (2009), using the Droplet Measurement Technologies (DMT) CCN-100 (Roberts and Nenes, 2005). Observations from the SMPS and APS consistently showed particle counts between N_{cn} =500 and N_{cn} =3000 cm^{-3} (for aerosol larger than the SMPS detection limit of r=0.00435 μm) most often distributed uni-modally with distribution peaks smaller than r=0.05 μm. The dominant Aitken-size mode (with respect to number) is most characteristic of a rural continental airmass as defined by Seinfeld and Pandis (2006).

For the purpose of obtaining realistic initial values for r_g to initialize the aerosol field in RAMS, a single lognormal mode was fit to the aerosol size distribution samples from ISPA using the method of maximum likelihood. A time series of the resulting r_g is shown in

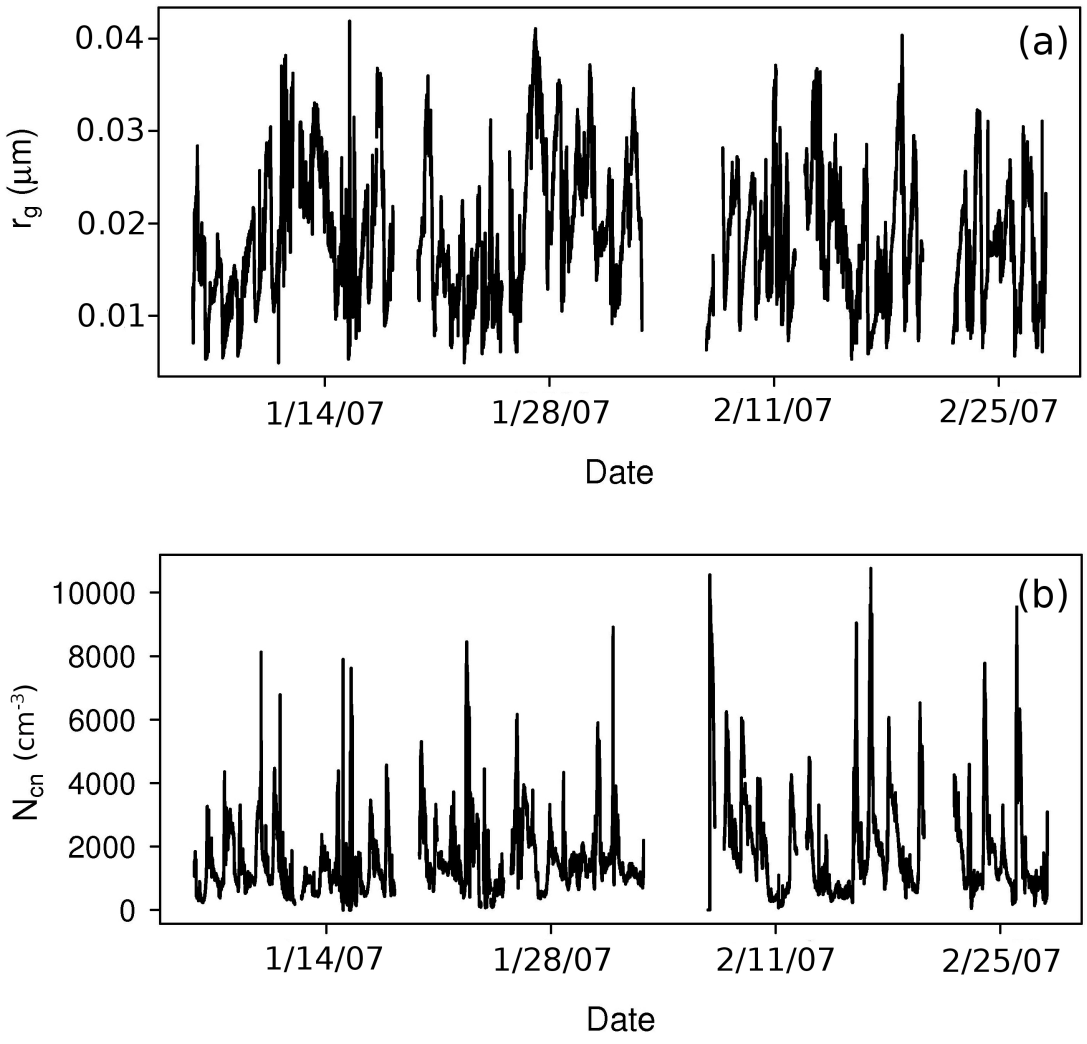

Figure 4.1: Time series of a) r_g and b) N_{cn} estimated from observations collected during the ISPA campaign at SPL in 2007. Note that r_g is estimated by fitting a single lognormal mode to the aerosol size distribution data. N_{cn} was derived from the sum of all aerosol observed by the SMPS and APS.

Figure 4.1a plotted with N_{cn} (Figure 4.1b) at five-minute intervals. For the entire ISPA field study, the estimated average r_g=0.018 μm and varied little with 10th and 90th quantile values of r_g=0.010 μm and r_g=0.028 μm. Total aerosol number, as measured by the SMPS and APS, showed more variation with a range of N_{cn} = 461 to 10,762 cm^{-3}. The N_{cn} for the entire study period had a mean of N_{cn}=1681 cm^{-3} but a median of N_{cn}=1290 cm^{-3}. Some of the samples exhibit a second mode with a peak near r=0.05 μm containing a relatively small proportion of the aerosol number, also characteristic of the rural continental airmass. In these instances the fitted distribution will underestimate the number of larger particles that, due to their size, are more likely to activate droplets. However, because this second mode contains so few particles, it does not appear in the sampled size distribution when this is averaged over the entire study period. For the simple purpose of producing an estimated r_g for model initialization, the single mode r_g will be used.

With the combination of size-differentiated aerosol and droplet activation data, it is possible to estimate the κ value of each ambient aerosol sample if an internal mixture is assumed. At a fixed supersaturation, the critical diameter that separates the particles that grow into cloud droplets from those that don't implies a single value of κ for internally mixed aerosol. With N_{ccn} known, the critical diameter (and subsequently κ) can be estimated from the aerosol size distribution samples. This method is similar to that used in CCN closure experiments in which, typically, an aerosol hygroscopicity is assumed and used to predict N_{ccn}. Previous studies of this kind have suggested that variations in aerosol composition are the greatest source of error in achieving CCN closure (e.g. Cantrell et al., 2001; Rissman et al., 2006; Bougiatioti et al., 2009). Here, CCN closure is presumed and this assumption is used to back out aerosol hygroscopicity. The CCN data sampled during ISPA at 0.3% supersaturation were used in this analysis. The DMT-CCN counter uses a temperature differential to create the necessary supersaturated environment.

Measurements taken when the temperature differential was not stabilized were neglected. The remaining data were averaged over 5-minute periods and compared to a single corresponding SMPS and APS observation. The results of this analysis show very little variation in κ estimated from the SPL measurements. For the entire field campaign, the average estimated κ was 0.14 with 10^{th} and 90^{th} quantile values of κ=0.08 and κ=0.18. Past research in the Park Range area has found that sulfate aerosol plays a major role in local orographic cloud microphysics (e.g. Borys et al., 2000; Borys et al., 2003), but the ISPA measurements show a low hygroscopicity aerosol population, perhaps indicative of a dominant organic component.

4.2 RAMS setup

RAMS was set up, as in Saleeby et al. (2009), on four horizontal grids with two-way nesting. The grid arrangement and other important model parameters are given in Table 4.1. RAMS uses a sigma-z terrain-following vertical coordinate system set up, in this case, with 40 vertical levels. To increase the vertical resolution in the boundary layer, the lowest model level has a vertical grid spacing of 75m. This is stretched by a ratio of 1.12 for subsequent levels until reaching a maximum spacing of 750m. The North American Regional Reanalysis dataset was used to initialize the meteorological fields as well as nudge the lateral and model top boundary meteorology at 5-minute intervals. Model aerosol number concentration was initialized in a horizontally-homogeneous, vertically-decreasing profile with a surface concentration of N_{cn}=1500 cm^{-3}. This value is slightly higher than the median concentration observed at SPL during ISPA. It was prescribed assuming that, since the rg observed during ISPA was near the lower detection limit of the SMPS instrument, the

Table 4.1: Settings used for all RAMS sensitivity simulations.

Setting	All grids	Grid 1	Grid 2	Grid 3	Grid 4
Microphysics	Two-moment bulk as in Saleeby et al. (2009) (Meyers et al., 1997)				
Turbulence closure	Horizontal: TKE - based on Smagorinsky (1963) Vertical: Mellor and Yamada (1982)				
Radiation	Two-stream (Harrington, 1997)				
Surface boundary	LEAF-2 (Walko et al., 2000)				
Top boundary	Rigid lid with damping layer				
Cumulus Parameterization		Kain and Fritsch (1993)	None	None	None
Grid points (X x Y)		62 x 50	54 x 50	97 x 82	114 x 114
Horizontal spacing		60km	15km	3km	0.75km
Center latitude (°N)		40.0	40.3	40.2	40.46
Center longitude (°W)		106.0	106.5	106.4	106.75

Aitken mode contained a portion of particles that were not large enough to be observed. Above the model level 150m above ground, the initial aerosol number concentration decreases linearly to the model level 4000m above ground. Above 4000m a low, free-tropospheric number concentration N_{cn}=100 cm^{-3} is assumed. The formation of ice crystals by homogeneous and heterogeneous freezing, as well as secondary ice production are

treated as described by Saleeby et al. (2009) with a vertically-decreasing profile of ice nuclei (IN) number concentration. Pristine ice crystal formation is predicted by the following formula in RAMS:

$$N_{pris} = N_{IN} F_M \tag{4.1}$$

Here N_{pris} is the number of pristine ice crystals formed, N_{IN} is the number of ice-forming nuclei available, and F_M is a factor from Meyers et al. (1992) based on the ice supersaturation.

Twenty-one simulations were run with varied initial r_g and κ. The initial values of r_g and κ remained constant throughout the entire respective simulation. The values of these parameters are shown in Table 4.2 for all simulations. Note that here we employ the entire range in κ that is available in the droplet nucleation look-up tables and no longer restrict the analysis to typical continental values. All simulations were run for a duration of 42 hours beginning at 00:00Z February 11, 2007 and ending at 18:00Z February 12, 2007. This time period captured the length of the storm system which began at around 06:00Z on February 11 and began to dissipate by 18:00Z on February 12.

Table 4.2: RAMS sensitivity simulation names and initial values for r_g and κ.

Initial	κ	0.00001	0.01	0.1	0.2	0.4	0.6	1.28
r_g (μm)								
0.010		A1	A2	A3	A4	A5	A6	A7
0.020		B1	B2	B3	B4	B5	B6	B7
0.040		C1	C2	C3	C4	C5	C6	C7

4.3 Sensitivity simulations results

It is expected that the riming efficiency, and resulting precipitation distribution, would be modulated by variations in the CCN number concentration flowing into the orographic cloud (Saleeby et al., 2009). How then do adjustments in aerosol hygroscopicity change the N_{ccn} for the particular orographic cloud conditions? A first check is shown with vertical profiles of initial model N_{ccn} at a supersaturation of 0.6% in Figure 4.2. N_{ccn} is

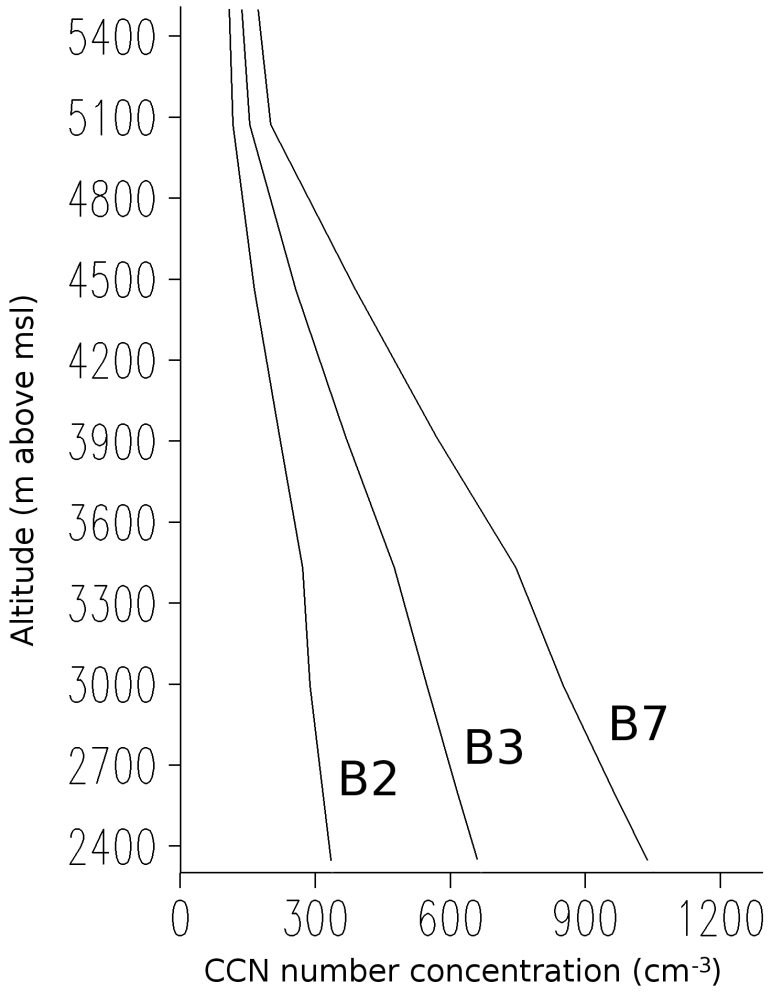

Figure 4.2: Vertical profiles of CCN diagnosed from RAMS simulations B2, B3, and B7 for conditions of 0.6% supersaturation and T = 25˚C. The profiles were taken from 40.5˚N and 107.0˚W at 30 simulation minutes after the model initialization.

predicted at prescribed values of supersaturation by the inclusion of the separate updraft look-up table in the RAMS droplet nucleation scheme. The look-up table is comprised of the updraft speeds required to reach the prescribed supersaturation in the parcel model given the simulated T, N_{cn} and r_g. In this case, T is set to a constant 25˚C for diagnosis of model CCN to approximate the temperature in the SPL CCN instrument. The vertical profiles in this case were diagnosed at a model grid point upwind of SPL for the B-simulations in which r_g=0.020 μm, about the observed average value for the ISPA campaign. The majority of particles in simulation B7 would activate droplets at the prescribed supersaturation of 0.6% but this number decreases with decreasing κ. For simulations A1, B1 and C1 (not plotted) fewer than 5 cm^{-3} particles would activate droplets in RAMS at this supersaturation, even near the surface boundary. These quantities may seem unrealistically low, even for a remote atmospheric environment, but Cotton et al. (1986) reported that CDNC of 5 cm^{-3} were observed in Park Range orographic clouds during a field project in the mid 1980s.

The simulated orographic flow strengthened as the model progressed into February 12 and reached peak intensity by 12:00Z on that day with updraft speeds generally greater than 1 m/s along the windward side of the Park Range and exceeding 2 m/s in many locations. These conditions, along with the prescribed N_{cn}=1500 cm^{-3} put this case into the aerosol-limited regime as defined by Reutter et al. (2009), although areas with weaker updrafts would be classified into the transitional regime. Apart from predictions of sensitivity to κ in these regimes, the aerosol-limited regime is characterized by high supersaturation. As a result, in some locations more droplets are activated in the model orographic cloud than were predicted for a supersaturation of 0.6% in Figure 4.2. As air

parcels enter the high updrafts forced by the topography, even the non-hygroscopic aerosol case (κ=0.00001) produced CDNC values in excess of 700 cm^{-3} (Figure 4.3a). The vertical cross-sections in Figure 4.3 are shown at a latitude of 40.455˚ and at 12:00Z on February 12, during the peak intensity of the storm. The differences between the CDNC in simulations B1 and B7 are significant. The high-κ simulation, B7 (Figure 4.3c), generates between one and two hundred more droplets per unit volume at its maximum and a larger area with CDNC values greater than 700 cm^{-3} than that shown in Figure 4.3a for the low-κ case. Also

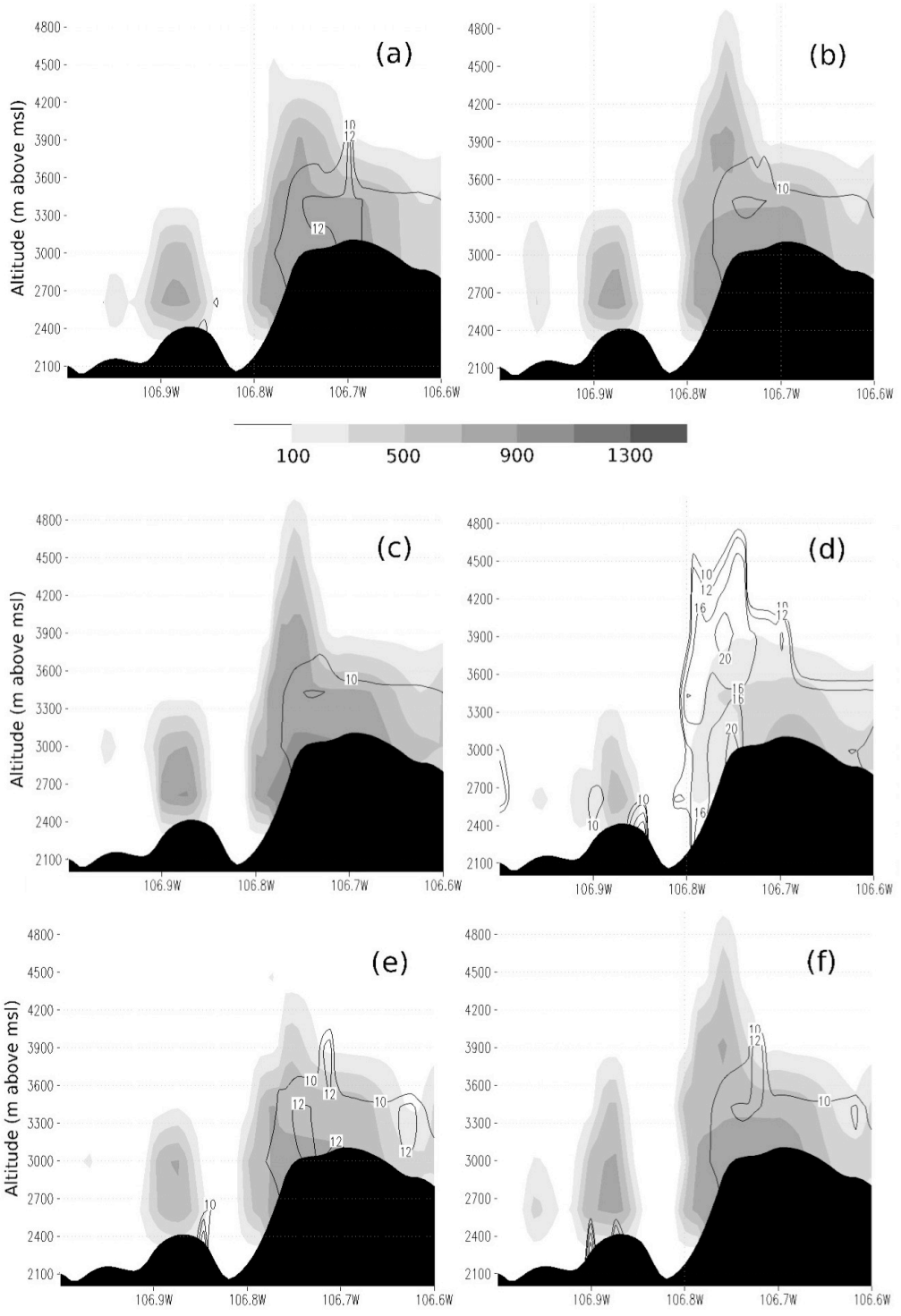

Figure 4.3: Vertical cross-sections of CDNC (shaded; cm^{-3}) and mean droplet diameter (contoured; μm) for RAMS simulations a) B1, b) B4, c) B7, d) A1, e) A4, f) A7. Only mean droplet diameters above 10μm are contoured. The cross-section was taken at 40.455°N and terrain is blacked out.

important to note are the smaller mean droplet diameters produced in simulations B4 (Figure 4.3b) and B7 when compared to B1.

The differences in mean droplet diameter for the range in κ are greater for the simulations in group A shown in Figure 4.3d-f. Large regions of mean droplet diameters near or below 10μm are predicted in simulation A7 (Figure 4.3f) whereas Figure 4.3d shows, in general, mean droplet diameters in excess of 10μm and areas of much larger droplets for A1. For A4, shown in Figure 4.3e, the CDNC and mean droplet diameter fields are more similar to those of high-κ conditions than low-κ conditions. This is evidence that the greatest sensitivity to κ in these simulations occurs below κ=0.2.

4.3.1 Spillover

Increasing the value of κ from near zero to 1.28 led to changes in the distribution of precipitation across the topographical barrier for all simulation groups. As shown in previous work, an increase in the CDNC leads to a decrease in windward precipitation and an increase in leeward precipitation, known as the spillover effect (Muhlbauer and Lohmann, 2008; Saleeby et al., 2009). To illustrate this effect, the difference between total precipitation in simulations A1 and A7 is shown in Figure 4.4 along with the same plot for B1 and B7, and C1 and C7. The location of the continental divide is plotted to show the approximate location of the ridge of the topography. In Figure 4.4a, a strong spillover effect is apparent. Precipitation is increased on the windward (western) side of the ridge for the low extreme in κ when compared to the high extreme and decreased on the leeward

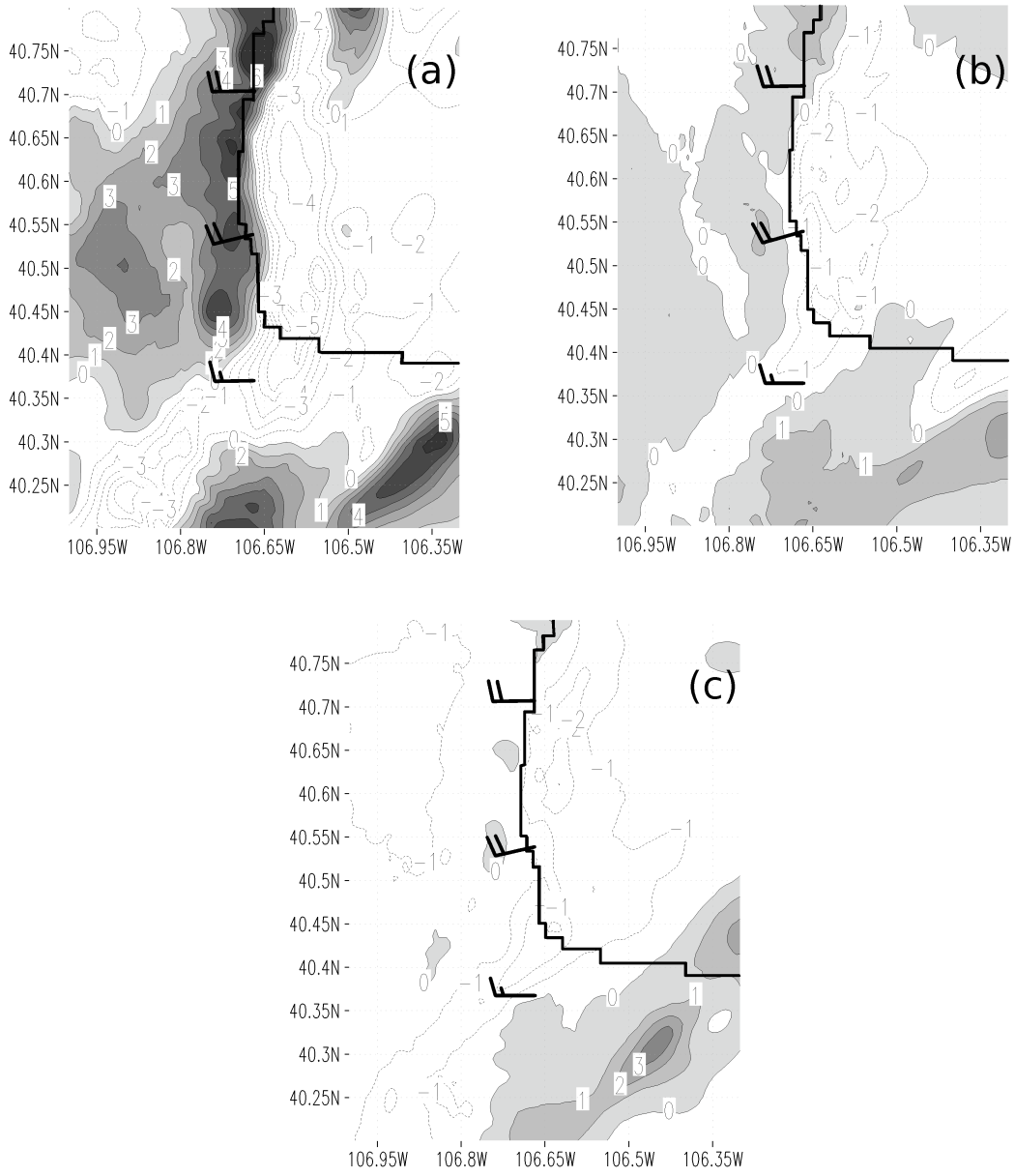

Figure 4.4: The simulated difference in total storm-period precipitation (mm) between a) A1-A7, b) B1-B7, c) C1-C7 is shown. Positive values (indicating, for example, areas that received more total precipitation in A1 than in A7) are shaded. Negative values are contoured with dotted lines. The continental divide is marked by the solid black line and the mean wind speed (kts) and direction for the lowest 1km and averaged over the entire simulation time period are plotted with wind barbs.

(eastern) side. The magnitude of the difference, between 4 to 5mm along the Park Range, accounts for about 10% of the total storm precipitation in this region, similar to that shown by Saleeby et al. (2009) for a change in initial N_{cn} from 300 cm^{-3} to 1100 cm^{-3}. Of course, this is only theoretical since a range in κ such as that used to initialize A1 and A7 is not likely to be observed at SPL. When the precipitation fields are compared for the simulations based on the 10th and 90th quantiles in κ estimated from the ISPA project (considered to be A3, B3, C3, and A4, B4, C4), the differences are trivial.

When r_g is increased in the model, as in the B and C simulations, the scale of the precipitation differences is diminished. For r_g increased to r_g=0.02μm (Figure 4.4b), the differences between the high-κ and low-κ simulations are only about half of those shown for the smaller r_g. In Figure 4.4c, the sensitivity to the change in κ is even smaller and almost no enhancement of windward precipitation is shown. The diminishing sensitivity can be explained by the relationship between κ-dependence and the relative positions of r_c and r_g, as shown in Sect. 3.2. As the aerosol size distribution moves to larger sizes, r_g will necessarily increase with respect to r_c. In the model, this leads to weaker CCN sensitivity to changes in κ and therefore, less impact on the simulated orographic cloud.

The ratio of leeward precipitation to total orographic precipitation was proposed by Jiang and Smith (2003) as a measure of the spillover effect. This spillover ratio was also used by Muhlbauer and Lohmann (2008) and is applied here as a single number indicator of the impact of the varied aerosol parameters. The leeward precipitation in this case was computed as the sum of all precipitation that fell during the storm period to the east of the continental divide, west of 106.3˚W, and between 40.4˚N and 40.8˚N, per unit area. Total orographic precipitation was defined as precipitation, per unit area, that fell between those same latitudes and between 106.3˚W and 107.0˚W. The spillover ratios for all simulations are shown in Table 4.3. As expected from the analysis in Figure 4.4, the spillover ratio

Table 4.3: Spillover ratio values for all RAMS sensitivity simulations.

Simulation Group	Number	1	2	3	4	5	6	7
A		0.366	0.389	0.398	0.398	0.400	0.400	0.401
B		0.391	0.400	0.399	0.399	0.399	0.400	0.402
C		0.398	0.402	0.401	0.402	0.403	0.402	0.404

changed the most for the A group of simulations. In all simulation groups, the spillover ratio was apparently most sensitive to variations in the lowest values of κ.

4.4 Conclusions

In summary, the simulated orographic snowstorm case from the study period showed some sensitivity, evident as increased spillover precipitation, to extreme changes in the model aerosol hygroscopicity as represented by the κ parameter. The differences in precipitation amount and distribution were similar to those seen in simulations of the same case by Saleeby et al. (2009) in which only N_{cn} was varied. However, the lack of variability of κ and r_g, as estimated from SPL observations, suggest only a small role for these quantities in this environment. Therefore, for the purpose of modeling cloud physics in these high supersaturation clouds and for rural continental aerosol populations, consideration of the variability of aerosol composition might be safely neglected. Particle number, however, should not be disregarded as shown by Saleeby et al. (2009). Still, this conclusion and the new lookup tables alone cannot answer remaining questions about the ambient CCN at SPL or other locations. They suggest what the impact of variable aerosol properties could be on winter orographic clouds. The next two chapters present

observations of CCN upwind (climatologically) of the Rocky Mountains in Colorado as a step toward determining the actual impact of ambient aerosol on the regional precipitation.

Chapter 5

CCN observations from Mesa Verde National Park

In this chapter, observations from the initial phase of the ISPA-III field campaign will be presented. The goals of this phase were twofold: first, to provide a dataset of CCN from a location typically upwind of the San Juan Mountains. It has been hypothesized that high-LWC orographic storms, that are more common in the San Juan Mountains than in the Park Range, are especially susceptible to spillover from increased CCN. The second goal was to determine if the variability in CCN could be explained by local or regional weather patterns. This could give insight into important sources of droplet activating aerosol in the region and possibly provide a basis for anticipating high or low CCN events during winter season orographic storms in the San Juan Mountains. CCN data were collected continuously from 9/22/09 to 10/16/09.

5.1 Instrument site

Mesa Verde National Park (MVNP) was chosen as the sampling site for this project. The site is located to the southwest of the higher elevations in the San Juan Mountains at an

elevation of 2190m above mean sea level (msl). Figure 5.1 shows the location of the sampling site (MEVE) with reference to the surrounding topography. The local ecosystem consists mainly of juniper and pinyon pine trees and the topsoil contains loess, a fine, red-colored silt (MVNP, 2005). It is a location that endures frequent forest fires especially during the summer, although none burned on the mesa during this project.

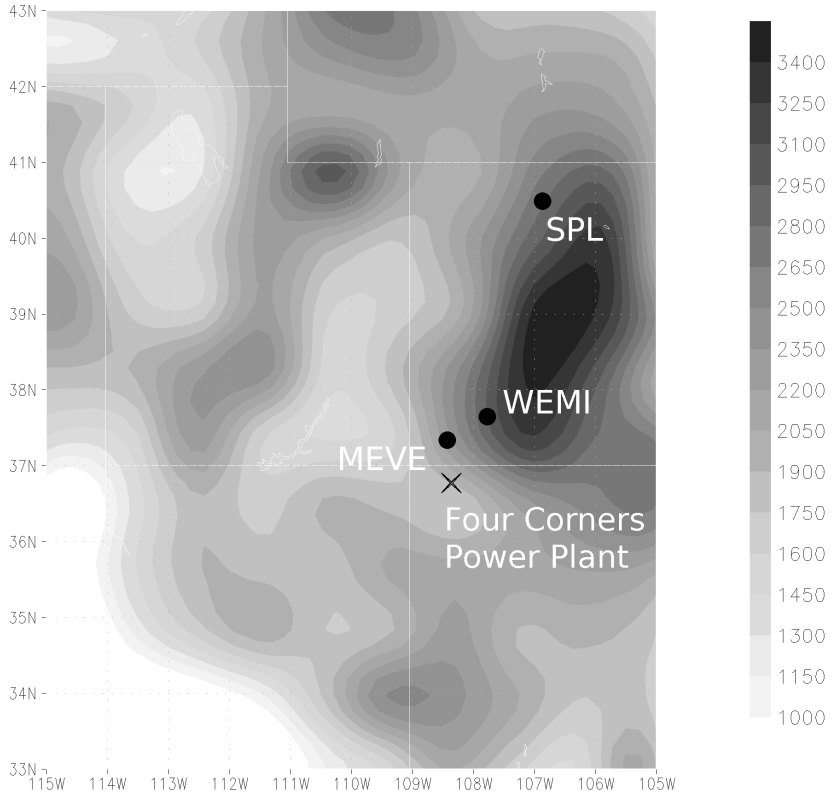

Figure 5.1: The locations of the Mesa Verde observations site (co-located with the MEVE IMPROVE site) and the WEMI IMPROVE site are plotted on the local topography in meters above msl. Storm Peak Laboratory in the Colorado Park Range is indicated by "SPL" and the location of the Four Corners Power Plant is marked with a black "X".

5.1.1 Climatology

Mesa Verde is located in a region of low population density and the typical airmass in the region is of continental origin (Hobbs et al., 1980). The main local industry is agriculture. Most of the agricultural activity takes place in small areas to the north of MVNP and to the east in the Mancos River Valley. The US EPA (2009) emissions inventory reports substantial ammonia emissions in these areas, although these are restricted to a 50km by 50km region with very little emitted on Mesa Verde itself. Despite the rural setting, there are several large point sources of particles and gas precursors that are local to the observation site. The most important of these, potentially, is the Four Corners power plant located about 100km south-southeast of Mesa Verde. Four Corners is one of the largest coal-firing power plants in the country and one of the larger sulfur emitters (US EPA, 2009). Together with two additional power plants located between the Four Corners plant and Mesa Verde, these sources are responsible for SO_2 emissions in excess of 10 tons per day on average and the emission of large amounts of NOx (US EPA, 2009). Decreased visibility was often observed in the direction of these sources, which stand at a lower altitude than the sampling site. Other substantial power plant aerosol sources, the Navajo and Page plants, are located to the west and southwest of Mesa Verde but are more distant than Four Corners.

The sampling site is co-located with the Interagency Monitoring of Protected Visual Environments (IMPROVE) network collection site MEVE1. Atmospheric aerosol samples are collected at IMPROVE sites on four separate filters for 24-hour periods once every three days. Three filters only collect particles with diameters less than 2.5μm (or $PM_{2.5}$). The mass ratios of collected particulate species are determined by several different analysis

techniques (Hyslop and White, 2008). Hyslop and White (2008) placed an additional sampler at several IMPROVE sites to assess the precision of some aspects of the collection and analysis techniques. They found discrepancies of 18-115% between collocated instruments in the determination of organic carbon and elemental carbon and 10% for soil particles, or dust. It is important to note that sulfate and nitrate aerosol are assumed to exist as ammonium sulfate and ammonium nitrate but mass measurement of ammonium is not conducted. Also, these data do not provide information about particle number concentration. Here, IMPROVE data will be used only to gain a general sense of long-term total aerosol mass concentration and composition and not for any purpose requiring high levels of precision.

Figure 5.2 shows the contribution to total $PM_{2.5}$ by IMPROVE estimated species at MEVE averaged from 1999-2008 for the dates of the ISPA observations. Since the IMPROVE

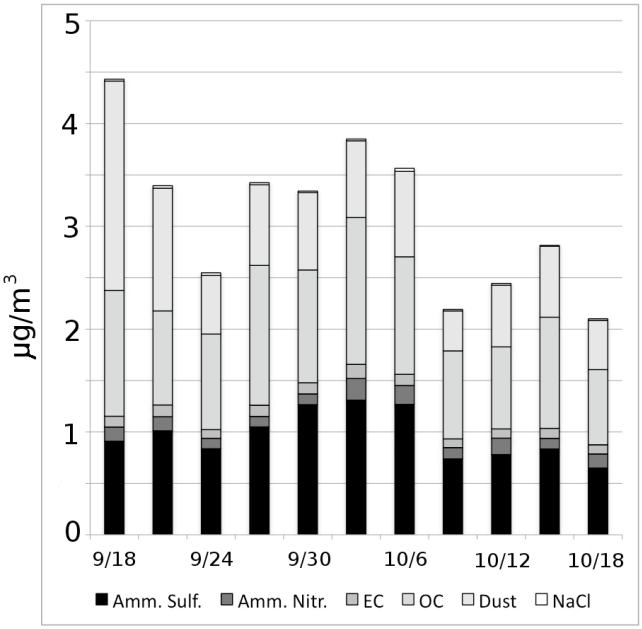

Figure 5.2: $PM_{2.5}$ composition as measured by the IMPROVE program at MEVE1 and averaged for ten years, 1999-2008.

sampling day is every three days, the averages are for the three days centered on the date shown in the figure. For example, the 9/18 average represents samples collected on 9/17, 9/18 or 9/19. Figure 5.2 shows an average aerosol mass concentration of about 3 μg/m^3 during the September-October time period making MEVE one of the cleaner locations in the network, but typical for a site in the Rocky Mountains (Debell, 2006). The analysis shows similar sulfate and organic aerosol mass with only small contributions from nitrate aerosol and elemental carbon. There is also substantial fine mode dust aerosol mass indicated. The IMPROVE site WEMI is located to the northeast of MEVE and also at a higher elevation (2750m msl). Average mass concentrations for 1999-2008 at WEMI are shown in Figure 5.3. The mass concentrations of sulfate, nitrate and organic aerosols are very similar at the two sites but less fine mode dust is collected this time of year at WEMI.

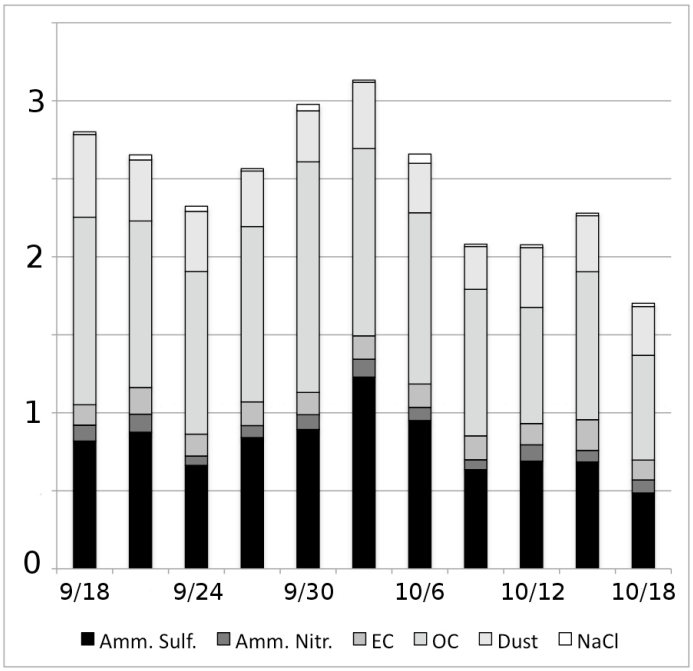

Figure 5.3: PM2.5 composition as measured by the IMPROVE program at WEMI1 and averaged for ten years, 1999-2008.

5.2 Instrument setup

To sample aerosols at MNVP two instruments were deployed: a Droplet Measurement Technologies (DMT) CCN-100 counter and a TSI 3010 condensation particle counter (CPC). These were setup inside a climate controlled building at the Mesa Verde Research Center. An inlet was installed on the building specifically as an intake for the CCN-100 and CPC. The main inlet was constructed out of 4" diameter aluminum tubing with a sheltered opening at a height of 4.15m above the ground and 3.1m above the CCN-100 inlet manifold. At the bottom of the main inlet a fan was installed to maintain flow from the top of the tubing. Flow was directed from the main inlet to each instrument by a combination of 0.3m 3/8" copper tubing and flexible 12mm OD tubing (0.4m for CCN-100, 0.7m for CPC). The copper tubing is used to navigate the necessary change in flow direction from vertical (main inlet) to horizontal (inlet manifolds on the CCN-100 and CPC). To diminish the loss of particles by impaction on the tubing walls the copper tubing was bent only slightly in two locations and the remainder of the required 90° turn was accomplished with the flexible tubing. The access opening of the copper tubing was tapered. The instrument shed was collocated with a meteorological observation tower that recorded wind speed and direction, temperature, dewpoint temperature, solar radiation, and precipitation.

The DMT CCN-100 is a continuous-flow instrument that creates a controlled supersaturated environment within which particles can grow to droplet size. It was developed by Roberts and Nenes (2005) and has been used in many field programs and laboratory studies since its introduction (e.g. Medina et al, 2007; Petters et al., 2007; Ervens et al., 2007; Cubison et al., 2008; Quinn et al., 2008; Gunthe et al., 2009). Supersaturation is produced and maintained in the CCN-100 by imposing a tightly controlled temperature

gradient on the sheath/sample flow within a moist growth chamber. While the flow rates are kept constant the SS can be set higher or lower by increasing or decreasing the temperature gradient. Particles enter the growth chamber at slightly above the ambient temperature, flow up the temperature gradient through the supersaturated environment in the center of the chamber and either reach stable equilibrium or grow into cloud droplet size. An optical particle counter (OPC) detects droplets that have reached a threshold size and reports these as CCN. The threshold droplet diameter was set to 2μm for the ISPA measurements. There is a risk at this size that a few of the smallest particles will activate but not have time to reach the threshold at the SS settings that were used (Roberts and Nenes, 2005). The decision to use 2μm was made to ensure consistency between this dataset and previously collected datasets at SPL. The CCN-100 was operated at a 10:1 sheath to sample flow ratio and at two values of SS: 0.3% and 0.5%. It was set to alternate between the two SS every 15 minutes, running continuously for the entire project period taking one measurement per second.

The CCN-100 used at Mesa Verde was calibrated on 9/14/09 at the DMT facility in Boulder, Colorado. The SS in the instrument is calibrated by sampling a distribution of particles for which the CCN activity is known, usually ammonium sulfate. The instrument-set SS is then compared to the theoretically determined SS and adjusted for accuracy. Intrinsic instrumental uncertainty is less than 10% for the conditions expected during this project (Roberts and Nenes, as cited by Quinn et al., 2008).

The CPC detects total particle number (within the detectable size range) in a similar way. The sample flow passes through a region in the instrument that is saturated with butanol vapor and then down a temperature gradient to cause the vapor to condense onto the particles. The resulting droplets are counted by an OPC and divided by the flow volume to compute a particle number concentration. This system works with a large sample flow

rate, which makes observing particles in very clean environments practical for a range in particle sizes. It was shown by Mertes et al. (1995) that the lower detection limit of the CPC could be decreased to d=5nm particles by increasing the temperature difference between the saturation and condensation regions. This detection limit is defined as the diameter at which 50% of the particles will activate and become detectable. At Mesa Verde, the CPC was run with the recommended temperature differential which results in a lower detection limit of approximately d=10nm. The particles and CCN observed by these instruments will be described next.

5.3 Data analysis

The time series of N_{ccn} and N_{cn} for the entire project are shown in Figures 5.4 and 5.5. The high-frequency data (one observation per second for the CCN-100 and one observation per 10 seconds for the CPC) were smoothed using a 30-minute running average. Of course, a 30-minute average of the N_{ccn} at a specific SS includes only 15 minutes of data. For this averaging an assumption is made that the CCN-100 is sampling similar ambient air during the 30-minutes when the instrument cycles once through each SS. Data that met certain criteria were flagged and set as missing. This was done any time the temperature gradient in the CCN-100 was not stabilized, which occurs between every change in instrument SS and sometimes lasts between 1-2 minutes. Other flagging criteria, including sharp changes in the air pressure and a significant change in the flow rate through either instrument, were not encountered. An attempt was made to eliminate observations that may have been contaminated by exhaust from nearby vehicles. Surges in N_{cn} that exceeded five standard deviations from the mean (computed from the 24-hour period in

question) and lasted less than two minutes were removed from the dataset. Thirteen such events were identified, all occurring between the hours of 7:55am and 5:00pm and all on weekdays. Corresponding CCN observations were disregarded, although the surges in that dataset were not as extreme. Since the events were short-lived, their removal had a minimal impact on the dataset as a whole.

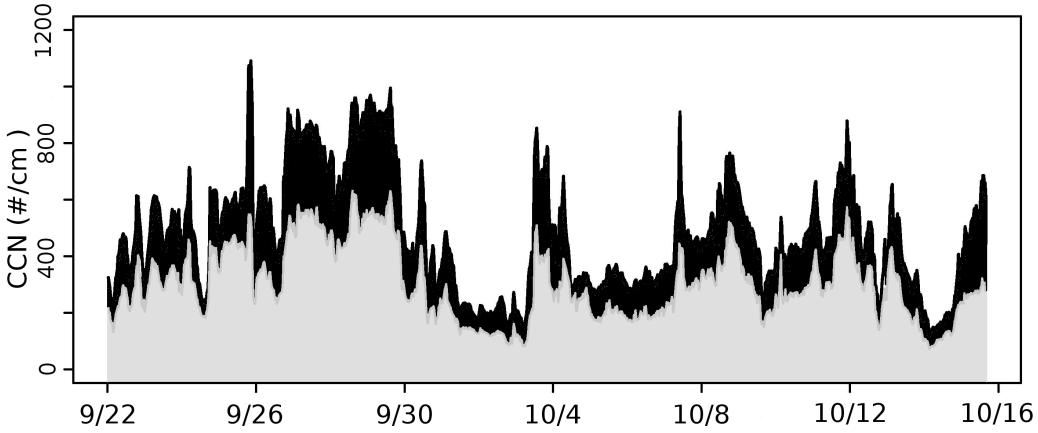

Figure 5.4: Time series of CCN number concentration observed at MVNP during the ISPA field project. CCN at SS=0.3% is shown in grey and CCN at SS=0.5% is shown in black.

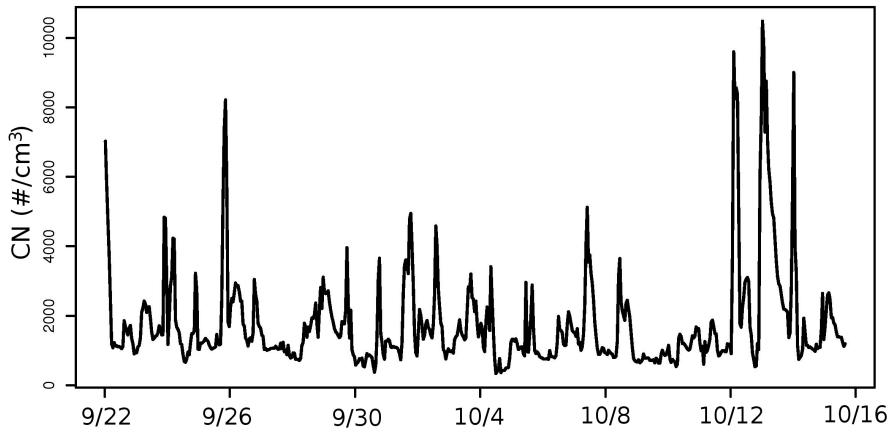

Figure 5.5: Time series of CN number concentration observed at MVNP during the ISPA field project.

Figure 5.4 shows the time series of N_{ccn} at both SS values for the entire project. The average N_{ccn} at SS=0.3% was 302 cm^{-3} and at SS=0.5% was 481 cm^{-3} (Table 5.1). Episodes of similar N_{ccn} that lasted for one to several days are evident in the time series. The N_{cn}, shown in Figure 5.5, appears to vary on much shorter timescales. To further this comparison, the lag autocorrelations of each time series are given in Table 5.1. The CCN time series exhibits

Table 5.1: Statistical information for physical quantities observed at MVNP. These represent the entire time series from 9/22-10/16. Lag quantities are autocorrelations for lags of 1, 10 and 24 hours. N' is the effective sample size computed using equation 5.1. Labels are as follows: CCN3 = N_{ccn}(SS=0.3%); CCN5 = N_{ccn}(SS=0.5%); ACT3 = N_{ccn}(SS=0.3%)/N_{cn}; ACT5 = N_{ccn}(SS=0.5%)/N_{cn}; and C3/C5 = N_{ccn}(SS=0.3%)/N_{ccn}(SS=0.5%).

	Units	Mean	Min	Max	StDv	Lag 1	Lag 10	Lag 24	N'
Temp	˚C	54	31	82	10.6	0.96	0.06	0.74	11
Dpt	˚C	22	-5	48	10.5	0.96	0.63	0.26	11
RH	%	32	9	98	16.9	0.95	0.26	0.46	14
Wind Speed	Mph	6	1	16	2.8	0.77	0.11	0.27	74
N_{cn}	cm^{-3}	1773	336	10944	1427	0.94	0.25	0.07	33
CCN3	cm^{-3}	302	72	631	128	0.98	0.78	0.61	10
CCN5	cm^{-3}	481	123	1090	204	0.98	0.75	0.57	10
C3/C5	-	1.6	1.14	2.38	0.17	0.84	0.45	0.22	101
ACT3	-	0.23	0.01	0.72	0.14	0.95	0.58	0.44	32
ACT5	-	0.37	0.02	0.97	0.21	0.95	0.60	0.51	28

a high autocorrelation, especially relative to that for the CN time series. According to VanReken et al. (2003) this is an indication that the largest particle number variations occur for particles that are either too small or non-hygroscopic to activate droplets at the prescribed SS.

A direct comparison of the observed CN and CCN is given by the activated fraction, shown in Figure 5.6 against the instrument SS. The average values of activated fraction are well below 0.5. This is an indication that the majority of particles counted by the CPC are

either too small or too non-hygroscopic to activate at the instrument SS. These values for activated fraction compare well to observations of, presumably, aged continental aerosols collected by Gunthe et al. (2009) in the Amazon rain forest. In contrast, Bougiatioti et al. (2009) found activated fraction values well above 0.5 even at SS=0.4%. They sampled at a marine location where the aerosol is likely to be larger and consist principally of sea-salt.

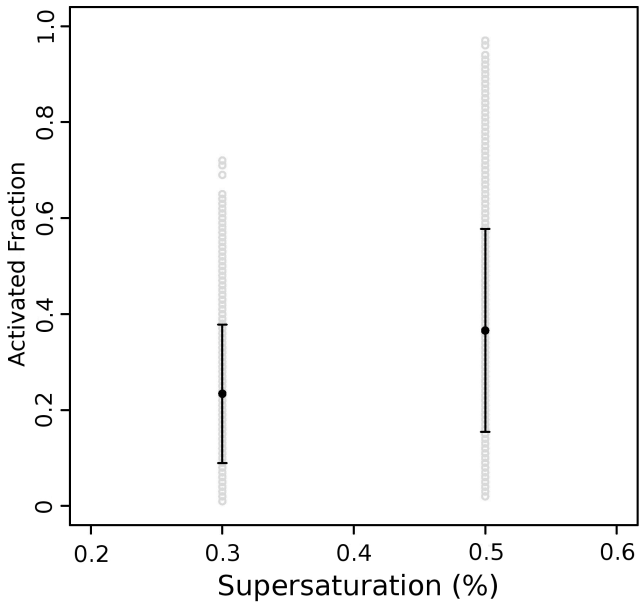

Figure 5.6: Activated fraction for the entire field project plotted against the SS set in the CCN-100 instrument. The mean at each SS is marked with the closed circle and error bars represent one standard deviation from the mean.

The activated fraction is shown as a time series in Figure 5.7 for SS=0.5% along with the time series of the ratio between CCN counted at SS=0.5% and at SS=0.3%. These CCN ratios have, in the past, been used to make inferences about the aerosol composition (Bougiatioti et al., 2009). However, it is not possible to confirm these inferences without direct size distribution or aerosol composition measurements. In this dataset, the CCN(0.5%):CCN(0.3%) ratio is inversely related to the activated fraction for the entire project period as suggested in Figure 5.7 and confirmed by the regression coefficients given

in Table 5.2. Although, the correlation is not statistically significant at the 95% rejection level, and accordingly the relationship is not consistent enough to lead to additional conclusions.

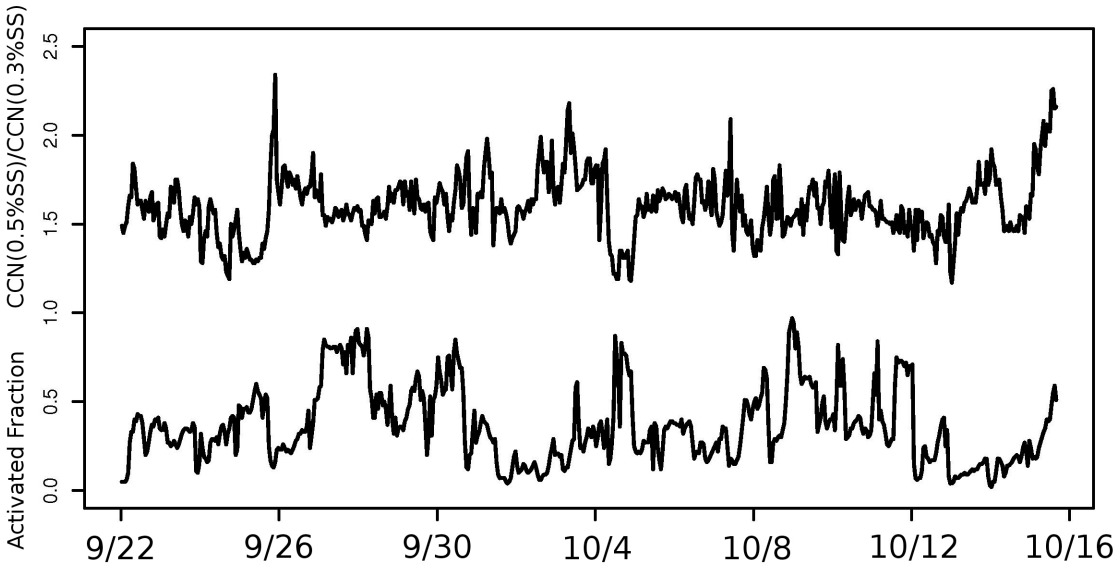

Figure 5.7: Time series of the activated fraction for SS=0.5% (always less than 1.0) and of the ratio of N_{ccn} at SS=0.5% to N_{ccn} at SS=0.3% (always greater than 1.0).

Table 5.2: Regression coefficients for observed quantities at MVNP. Relationships that are significant at the 95% confidence level for a two-tailed student t test are bolded. Labels are the same as in Table 5.1.

	Temp	Dpt	Wind Spd	N_{cn}	CCN3	CCN5	C3/C5	ACT3	ACT5
Temp	-	0.24	1.2	.002	.04	0.03	3.76	14.7	11.1
Dpt	0.23	-	0.15	.0011	.02	0.02	-13.2	8.6	3.9
Wind Spd	0.08	0.01	-	.0001	.0008	.0008	0.71	0.72	0.61
N_{cn}	27	20.4	32.3	-	1.14	0.94	933	-5457	-3773
CCN3	5.7	2.98	1.71	.01	-	**0.60**	-109	461	323
CCN5	9.7	3.9	4.2	.02	**1.54**	-	119	608	467
C3/C5	0.001	-0.004	0.003	.0001	-.0002	.0001	-	-0.41	-0.16
ACT3	0.003	0.002	0.002	-.0001	.0006	.0003	-0.293	-	**0.668**
ACT5	0.005	0.002	0.004	-.0001	.0009	.0005	-0.245	**1.44**	-

5.3.1 Composite analysis

To further address the goals of this project it is of interest to learn whether the observed CCN varies with the surface wind. This could provide insight into the location of important local sources of CCN at MVNP if we assume that the surface wind is representative of the local direction of aerosol transport. A composite analysis was carried out as a means of finding a relationship, if one exists, between the observed wind and CCN and CN at MVNP.

Surface wind was recorded every hour also at the MVNP Research Center and at a height of approximately 3m above ground. Observations of N_{cn} and N_{ccn} were sorted by the corresponding surface wind direction into the following groups: N, W, S, E (315˚ to 44˚, 225˚ to 314˚, 135˚ to 224˚, 45˚ to 134˚) and NW, SW, SE, NE (270˚ to 359˚, 180˚ to 269˚, 90˚ to 179˚, 0˚ to 89˚). The mean N_{ccn} in each bin of the first group is shown in Figure 5.8 with error bars indicating one standard deviation above and below the mean. The CCN at both SS averaged highest for easterly surface winds and averaged 15-20% lower for northerly winds. The northerly wind bin contained about 40% of the observations while the remaining bins each contained about 20% of the observations. While easterly winds were associated with the most CCN, they also contained the lowest activated fraction of the group (Figure 5.9). This suggests that large amounts of particles were carried to the site on easterly winds, but they were less likely to activate droplets either due to small size or low hygroscopicity.

The composite analysis for the second group of wind direction bins is shown in Figures 5.10 and 5.11. Here the highest and lowest mean N_{ccn} were observed with southeasterly and northeasterly prevailing winds, respectively. The southeasterly bin also contained a low activated fraction when compared to the other bins, although it was nearly

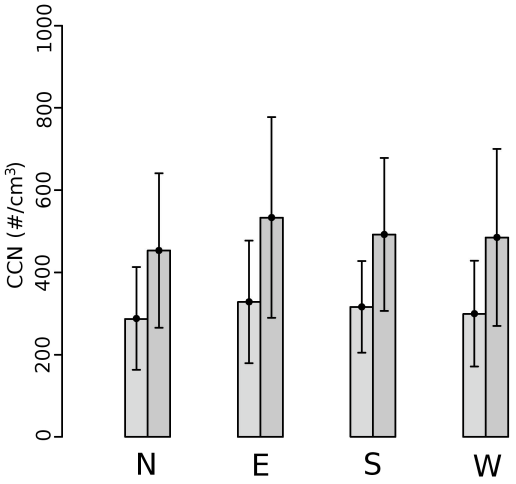

Figure 5.8: Average N_{ccn} at SS=0.3% (light grey) and N_{ccn} at SS=0.5% (dark grey) binned by the prevailing wind direction (N, E, S, W). Error bars represent one standard deviation from the mean.

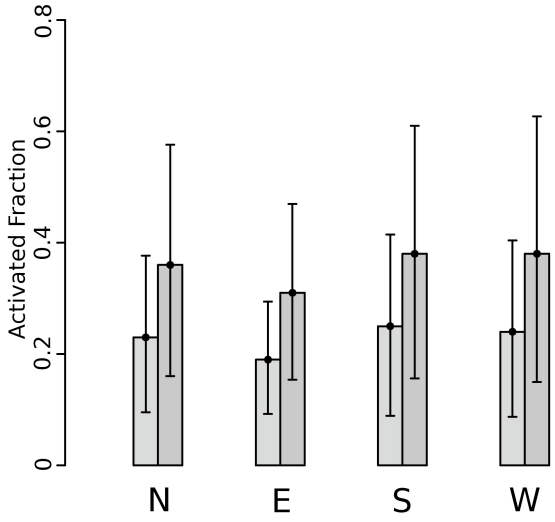

Figure 5.9: Average activated fraction at SS=0.3% (light grey) and at SS=0.5% (dark grey) binned by the prevailing wind direction (N, E, S, W). Error bars represent one standard deviation from the mean.

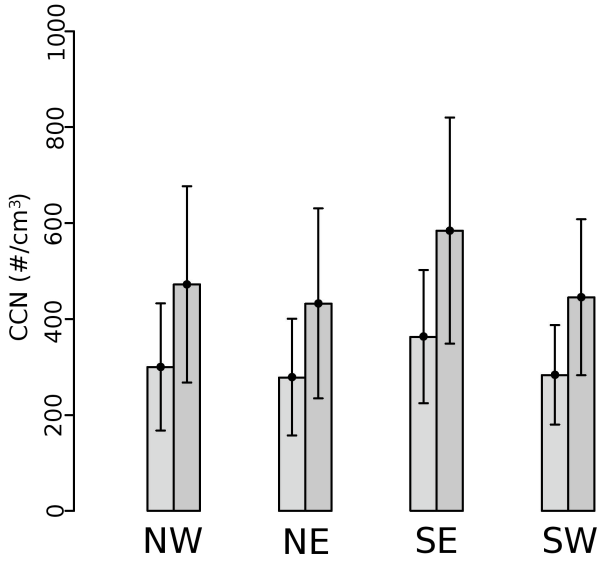

Figure 5.10: Average N_{ccn} at SS=0.3% (light grey) and N_{ccn} at SS=0.5% (dark grey) binned by the prevailing wind direction (NW, NE, SE, SW). Error bars represent one standard deviation from the mean.

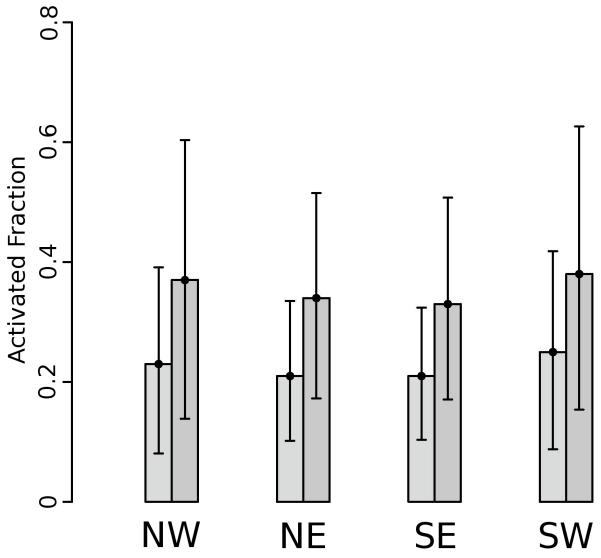

Figure 5.11: Average activated fraction at SS=0.3% (light grey) and at SS=0.5% (dark grey) binned by the prevailing wind direction (NW, NE, SE, SW). Error bars represent one standard deviation from the mean.

identical to the activated fraction for the northeasterly bin. When the groups were broken down further into 45-degree wind direction bins, the highest average N_{ccn} occurred in the 90˚ to 135˚ range. Major local pollution sources do lie to the southeast of the observation site as mentioned earlier in this chapter, but it is important to point out that none of the mean N_{ccn} or activated fractions are different from their respective population means at a 95% confidence level. Clearly shown in the figures is the fact that the mean N_{ccn} for each bin falls within just one standard deviation from the means in all other bins. This rules out the possibility of making connections between local surface wind and observed CN and CCN that could be applied to cases outside the time period of this project.

An identical analysis was performed for various ranges in observed wind speed. Similarly, the variance in N_{ccn} and N_{cn} within each chosen wind speed bin was too large to identify significant differences in means between the bins. Some recent studies have

suggested that surface-site aerosol composition relates, albeit weakly, to the local low-level wind (Medina et al., 2007; Bougiatioti et al. 2009). In fact, source apportionment by trajectory analysis depends on this relationship (Stohl, 1998; Engstrom and Magnusson, 2009). These studies follow air parcels back in time from the observation site to identify the location of their origin. In the case of the MVNP observations, if a relationship between surface wind and aerosol properties exists it is masked by the variability of the surface wind in the composite analysis. The surface wind direction and speed can be influenced by near-site objects such as trees and buildings, or local topography including the mesa itself, and in this case may not be representative of the local aerosol transporting winds.

5.3.2 Regression analysis

Previous research shows that differences in the observed regional meteorology can explain some of the variability in aerosol properties observed on board aircraft or at surface sites (e.g. VanReken et al., 2003; Medina et al., 2007; Quinn et al., 2008; Furutani et al., 2008; Bougiatioti et al., 2009). Traditionally these distinctions are made using trajectory analysis and are often limited to labeling observations as marine-source or continental-source, as in VanReken et al. (2003), Furutani et al. (2008), and Bougiatioti et al. (2009). Moreover, it is difficult to test whether the relationship between the computed trajectories and observed aerosols would apply generally to future cases. In this section regression analysis will be used to investigate a more broadly applicable relationship between the large-scale wind and MVNP CCN and CN number concentrations. As with the previous section, the results of this analysis could give insight into the location of important sources of aerosol, both local and distant, for the MVNP CCN population.

The 700mb and 500mb geopotential height fields from the North American Regional Reanalysis (NARR) dataset (Mesinger et al., 2006) were used. Wind speed and direction at these pressure levels can be estimated by making the geostrophic assumption. This assumption holds well at 500mb and at 700mb except near the highest terrain, such as the Rocky Mountains in Colorado, where friction in the surface layer disrupts the geostrophic balance. Examining the wind and height at these pressures offers two main advantages over the surface wind composite analysis described above. First, obstacles at the surface that introduce turbulence into the wind flow do not impact the 700mb or 500mb wind. Second, the horizontally gridded fields provide wind information over a large area, improving upon the single horizontal data-point used for the composite analysis. NARR data are output on a 349x by 277y polar-stereographic grid with a horizontal grid spacing of about 32km in the lower latitudes. The data are available in 3-hr increments. Output from 9/23/09 00:00 GMT to 10/16/09 00:00 GMT was used to construct the time series of the geopotential height fields.

In preparation for analysis, the 700mb and 500mb geopotential height fields were weighted by the cosine of the latitude. This essentially equalizes the influence of each grid point on the basis of grid-box area. The 24-hr time mean was removed from all grid points. Missing data were removed from the dataset before analysis. Next, the time series of N_{cn} and N_{ccn} from MVNP were averaged over 3-hr time periods, centered on the corresponding NARR output time. The time series were standardized and the 24-hr time mean was removed from each. Then, the 500mb and 700mb geopotential height time series were regressed onto the time series of N_{ccn} and N_{cn}. The resulting regression maps were plotted and the correlations at each grid point were computed. The correlations are used to test whether the regression relationship is significant and could be applied to cases outside of the ISPA observation period, or if it is specific to this case and not representative of the

potential population of regression coefficients at each grid point. The latter is the null hypothesis. The correlations were checked for significance against the null hypothesis using a two-tailed student t test. An effective sample size was calculated for the test using equation 5.12 from Wilks (1995):

$$n' \cong n\frac{1-\rho_1}{1+\rho_1} \qquad (5.1)$$

where ρ_1 is the lag-1 autocorrelation coefficient, n is the sample size and n' is the effective sample size, or the equivalent number of independent samples. The effective sample size is used to correct for the persistence in the CCN dataset. The high persistence in the CCN datasets, given by the autocorrelations in Table 5.1, reduces the effective sample size to 10. The result is the same when n' is computed using the lag-1 autocorrelation for the 3-hr standardized dataset. The CN time series varies on a shorter timescale and, therefore, has a higher effective sample size, n'=33. This is limited in the regression analysis to one independent sample per day (n'=23), the assumed sample size for the NARR datasets. Significance was tested at the 95% confidence level.

Figure 5.12 shows the regression of the 700mb height field onto the CCN (SS=0.3%) time series. This is the pattern of 700mb heights that explains the most variance in the CCN(SS=0.3%) time series. The pattern includes positive regression coefficients over the central and western United States, as well as over the northern Pacific. High pressure in these regions was associated with high N_{ccn} at MVNP during this project. The dashed line indicates areas that would be statistically significant for an effective sample size of n'=23, or one independent sample per day. None of the regression coefficients tested significant using the computed n'=10.

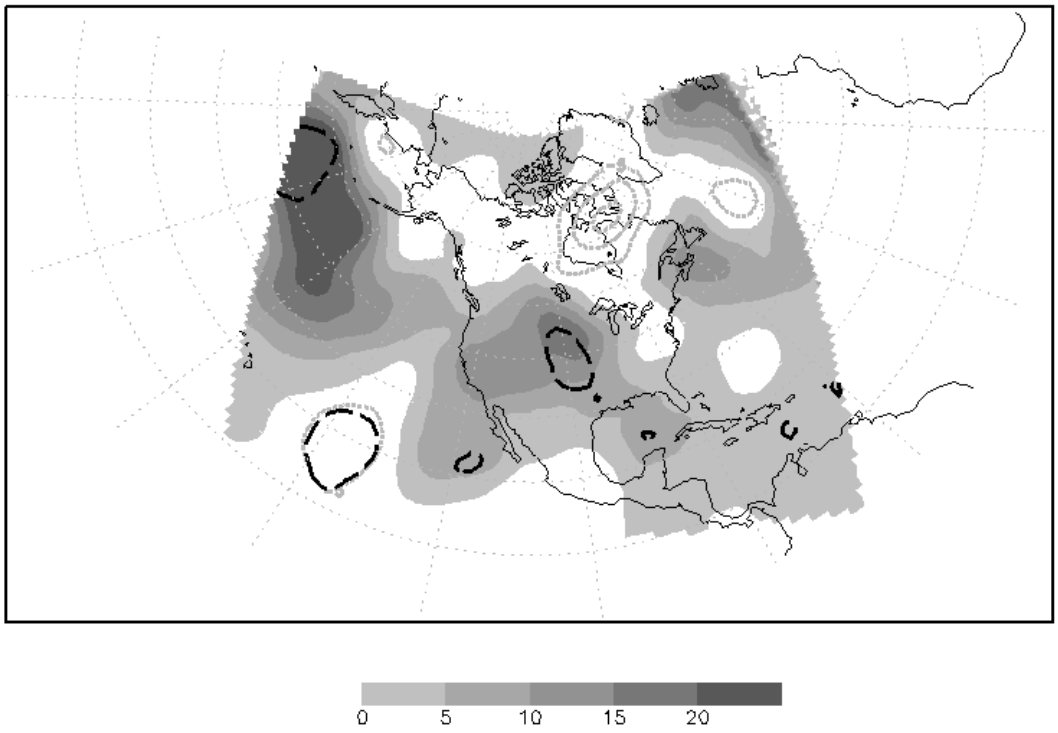

Figure 5.12: Regression of 700mb geopotential height onto the time series of N_{ccn} sampled at MVNP with SS=0.3%. Units are geopotential meters (gpm) per standard deviation of N_{ccn}. Regions where the correlation between N_{ccn} and height is significant at the 95% confidence level assuming n'=23 are outlined with a dashed line.

The pattern is, not surprisingly, similar for CCN (SS=0.5%) as shown in Figure 5.13. However, for the regression onto the CN time series (Figure 5.14) a large region of low pressure off the west coast of the United States is associated with higher N_{cn} at MVNP. A large portion of the low pressure is statistically significant. The regression coefficients in the MVNP vicinity are not significant but the pattern, with negative regression coefficients to the west and positive to the east, suggests that south wind at 700mb was associated with high CN concentrations at MVNP.

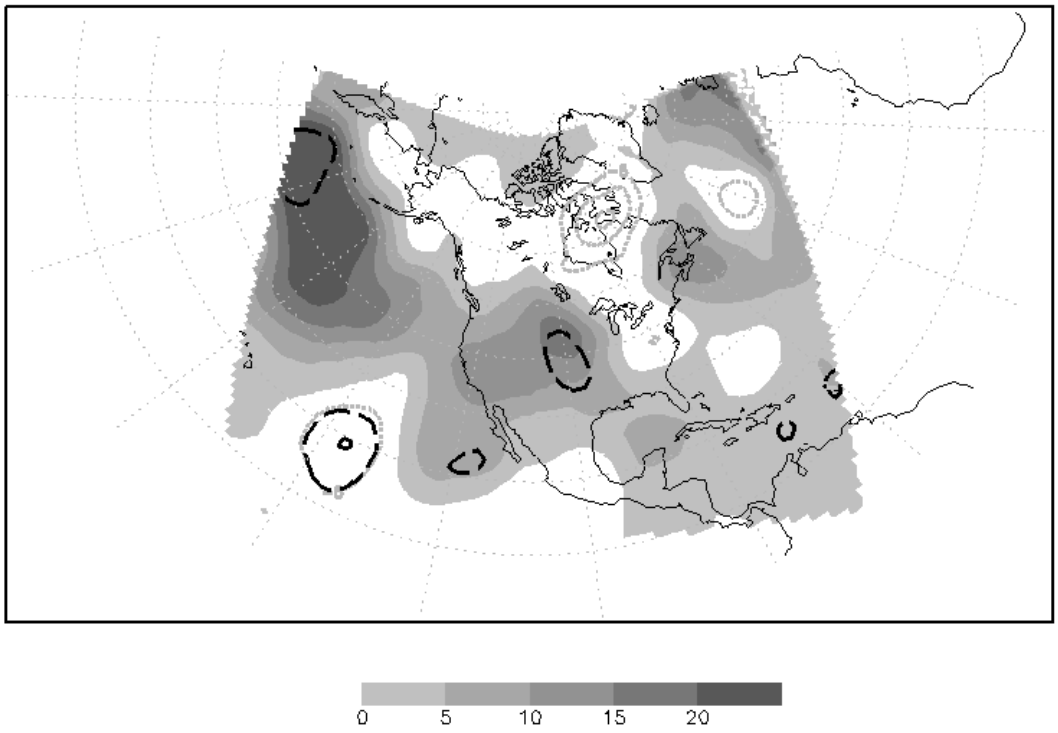

Figure 5.13: Regression of 700mb geopotential height onto the time series of N_{ccn} sampled at MVNP with SS=0.5%. Units are geopotential meters (gpm) per standard deviation of N_{ccn}. Regions where the correlation between N_{ccn} and height is significant at the 95% confidence level assuming n'=23 are outlined with a dashed line.

At 500mb, the regression pattern is similar to that at 700mb with positive coefficients over the western United States and over the northern Pacific (Figures 5.15, 5.16). Again, this means that high pressure in these areas was connected to high N_{ccn} at MVNP and low pressure connected to low number concentrations. In this case, the maximum regression coefficient over the western U.S. was located further west than at 700mb. It was also higher in magnitude, but this is likely due to the higher variance of the 500mb geopotential height. No areas were found to be statistically significant for n'=10.

The regression of 500mb heights onto the CN time series, shown in Figure 5.17, was also similar to that for 700mb.

In summary, the regression analysis indicated that high values of N_{ccn} observed at MVNP were associated with high pressure locally and further west. N_{cn} varied most with the pressure pattern off the west coast of the U.S. and Canada. The fact that the regression coefficients were not statistically significant assuming 10 independent samples of CCN indicates a high likeliness that the height pattern was unduly influenced by one or more specific events. Therefore it would not be appropriate to extend these conclusions to future cases.

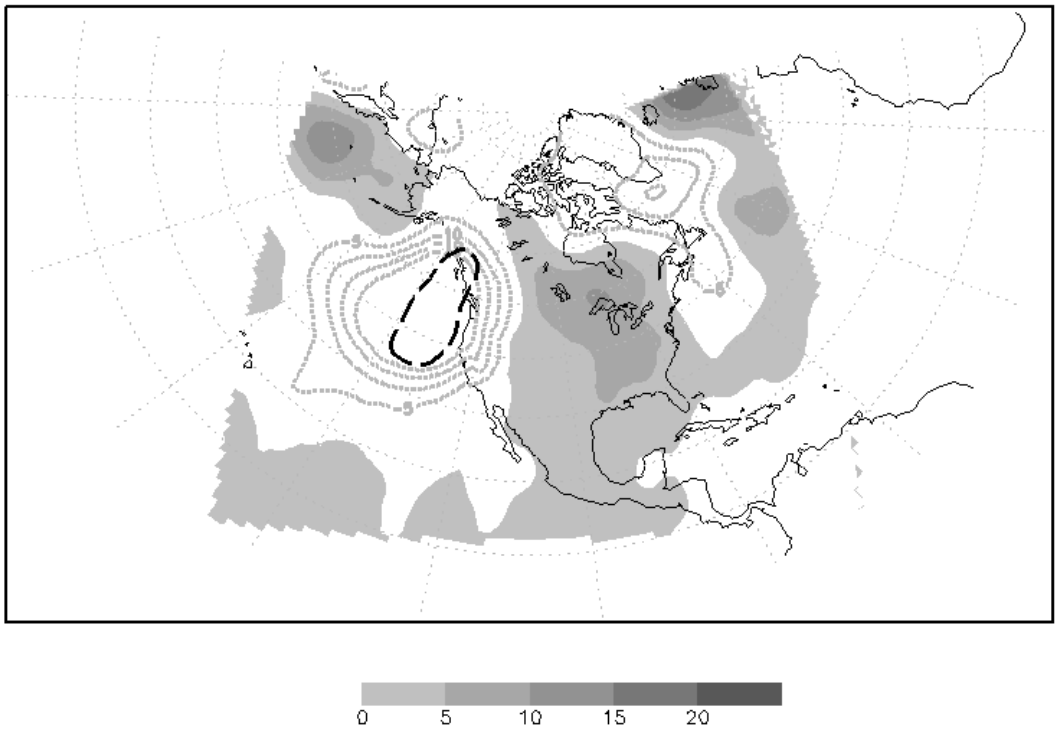

Figure 5.14: Regression of 700mb geopotential height onto the time series of N_{cn} sampled at MVNP. Units are geopotential meters (gpm) per standard deviation of N_{cn}. Regions where the correlation between N_{cn} and height is significant at the 95% confidence level assuming n'=23 are outlined with a dashed line.

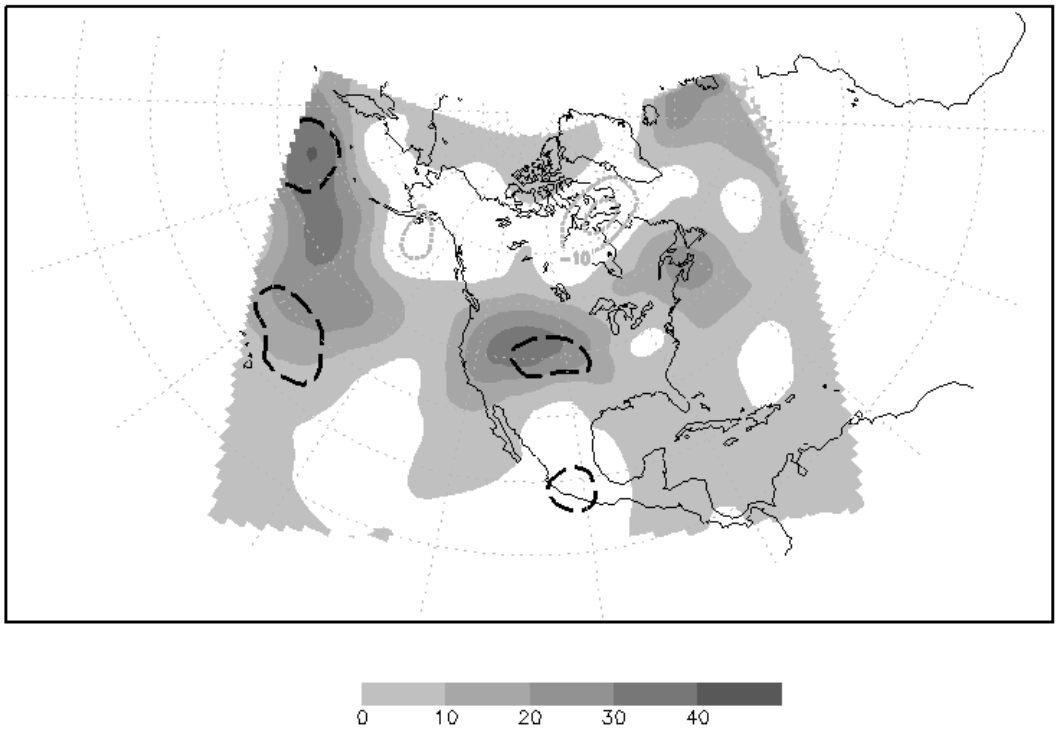

Figure 5.15: Regression of 500mb geopotential height onto the time series of N_{ccn} sampled at MVNP with SS=0.3%. Units are geopotential meters (gpm) per standard deviation of N_{ccn}. Regions where the correlation between N_{ccn} and height is significant at the 95% confidence level assuming n'=23 are outlined with a dashed line.

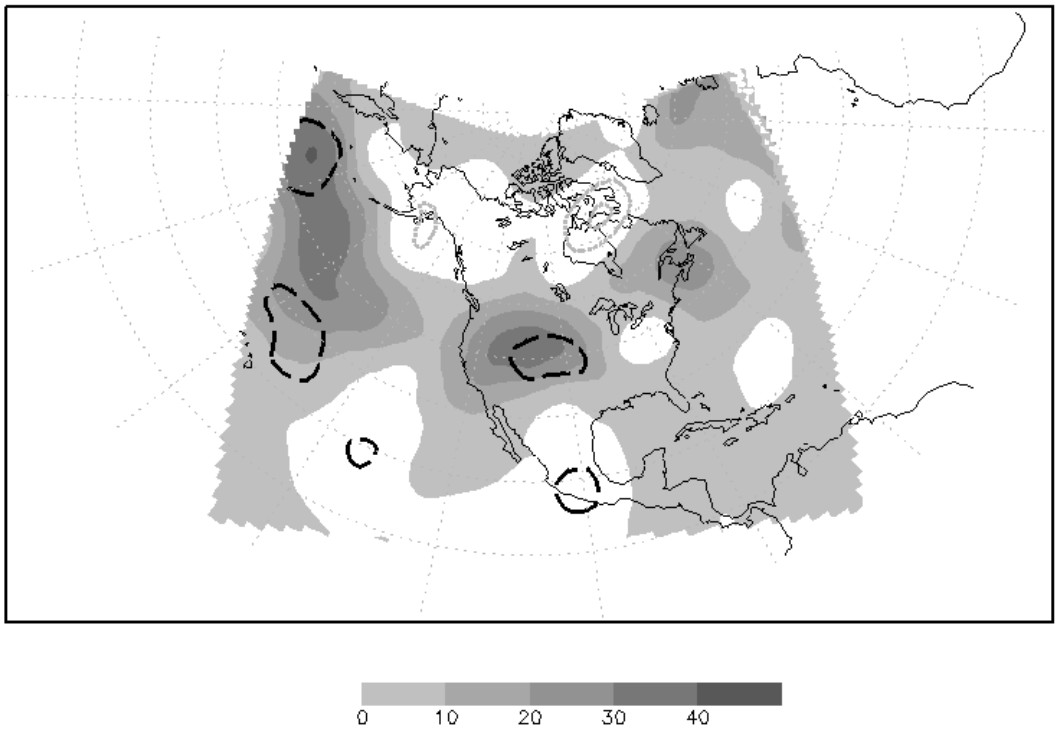

Figure 5.16: Regression of 500mb geopotential height onto the time series of N_{ccn} sampled at MVNP with SS=0.5%. Units are geopotential meters (gpm) per standard deviation of N_{ccn}. Regions where the correlation between N_{ccn} and height is significant at the 95% confidence level assuming n'=23 are outlined with a dashed line.

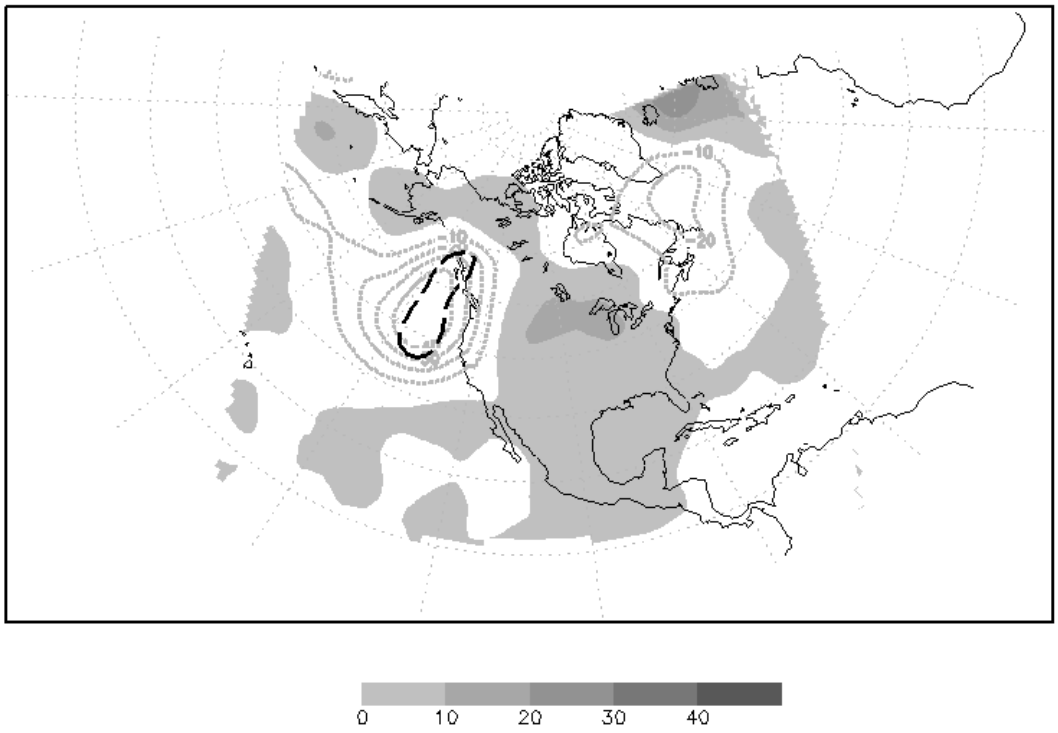

Figure 5.17: Regression of 500mb geopotential height onto the time series of N_{cn} sampled at MVNP. Units are geopotential meters (gpm) per standard deviation of N_{cn}. Regions where the correlation between N_{cn} and height is significant at the 95% confidence level assuming n'=23 are outlined with a dashed line.

5.4 Synopsis

CCN number concentration data were collected with a DMT CCN-100 at a site in MVNP. These were supplemented with N_{cn} and meteorological data, all measured continuously for a period of 24 days. The N_{ccn} observations varied within a range of about one order of magnitude and rarely exceeded 1000cm^{-3} at SS=0.5%. The average N_{ccn} at the surface site was 302cm^{-3} at SS=0.3% and 481cm^{-3} at SS=0.5%. These values show that the MVNP environment is clean when compared to observations in the northeastern and southeastern United States that typically average 2-3 times greater than the MVNP measurements (Medina et al., 2007; Ervens et al., 2007; Hudson, 2007; Quinn et al., 2008). The N_{ccn} observations at MVNP were remarkably episodic, with high or low events lasting for one to several days. This limited the effective sample size to about 10 events for regression analysis.

The MVNP measurements are comparable in magnitude to N_{cn} and N_{ccn} at SPL collected in January and February of 2007 as reported by Saleeby et al. (2009) and Ward et al. (2010). The N_{ccn} observed at MVNP is on average somewhat higher, although this is not unexpected given the difference in seasons. Also, SPL should be expected to be somewhat cleaner because of its high altitude and disconnection from the more polluted surface layer below. The MVNP aerosol may be considered, by geographic proximity to SPL, to also be characteristic of rural continental airmasses, although typically size distribution information would be used to make this distinction. CDNC and CCN observed at Elk Mountain in southern Wyoming also fall within the 200-400 cm^{-3} range although no SS is specified for these measurements (Politovich and Vali, 1983). Eltgroth and Hobbs (1979) measured ambient N_{cn} in excess of 3500 cm^{-3} on three separate days in 1977. Although,

they sampled air closer to the Four Corners power plant and these observations are more than 30 years old.

At MVNP in 2009, it is unclear whether the large, local aerosol sources impacted the measurements of N_{ccn} and N_{cn}. Observed spikes in N_{cn} were not always accompanied by similar spikes in N_{ccn}. This could be evidence of the influence of a nearby combustion source introducing a large number of small particles into the environment (Medina et al., 2007), or producing enough SO_2 to cause an aerosol nucleation event in the area. The composite analysis and regression analysis both suggested that the highest N_{cn} at MVNP during this project were associated with southerly and southeasterly wind both at the surface and aloft, perhaps signaling advection of particles from the vicinity of the power plants. In either case, the N_{ccn} dataset did not exhibit these same apparent connections to the local sources. If effluent from Four Corners and other local power plants were contributing particles to MVNP they were likely freshly formed and, therefore, too small to activate droplets.

The potential impact of local lofting of dust aerosol on the N_{cn} and N_{ccn} measurements has heretofore been left unaddressed, but decreased visibility, presumably due to dust aerosol, was observed during high wind events. One such event occurred on 9/30/09 as a cold front boundary approached MVNP from the northwest leading to southwest winds at the observation site. Instantaneous wind speeds of 15-20m/s were observed ahead of the front and estimated visibility decreased to less than 1.5km on a clear sky day. The measured N_{cn} dropped to below 400 cm^{-3} during the period of strongest winds while the N_{ccn} rose until the activated fraction at SS=0.5% neared 0.9. This could have been due to sampling of a dust mode with few particles of large size dominating the samples, but is more likely a result of decreased inlet efficiency during the high wind event. Smaller quantities of fine-mode soil aerosol were collected at the IMPROVE site WEMI1, which indicates that dust collected at MEVE1 does not have a similar impact on N_{ccn} closer to the

main area of interest, the San Juan Mountains. In the absence of detailed aerosol chemistry time series at MVNP, aerosol size distribution or size-selected CCN measurements would be required to estimate the hygroscopicity of the MVNP CCN and the impact of dust on the CCN activity. In general, N_{ccn} at MVNP is characteristic of a remote site and did not exhibit large or abrupt variations.

Chapter 6

CCN observations from the King Air

CCN data have been collected in northwestern Colorado at SPL (Saleeby et al., 2009), and nearby at Elk Mountain (Politovich and Vali, 1983), and now in southwestern Colorado (see Chapter 5). About 350km separate these sites from north to south, a stretch through which much of the aerosol flowing into the central Rocky Mountains of Colorado will pass on the prevailing westerlies that are common to the region. In December of 2009, sixteen low-altitude transects of this region, also known as the Western Slope, were made during 8 flights from Laramie, WY to Cortez and Montrose, CO. Vertical profiles were carried out at the northern and southern ends of transects near SPL and Cortez, CO. On-board measurements of N_{cn}, aerosol size distribution, and N_{ccn} at three different values of SS were made on all transects. These data will contribute to the cold-season climatology of CCN transported into the Colorado mountains. The instruments and aircraft platform used in this phase of the ISPA field campaign will be described in this chapter. Then, the data collected along the horizontal transects and vertical profiles will be presented and, finally, the method of analysis known as CCN closure will be explained and applied to this dataset.

6.1 The King Air observational platform

The King Air 200T is a twin-propeller turboprop aircraft operated by the University of Wyoming in Laramie, WY, for tropospheric research. On-board instruments measure cloud physics parameters, atmospheric radiation and atmospheric state quantities. For the ISPA flights the main interest was sampling of aerosols and their CCN activity. For this reason a CPC was operated aboard the aircraft as well as a Particle Measuring Systems passive cavity aerosol spectrometer probe (PCASP) for differentiating particle sizes and a static-diffusion, thermal-gradient CCN counter.

6.1.1 Instruments

The University of Wyoming (UWYO) CCNC-100A measures N_{ccn} by subjecting ambient aerosols to an environment that is supersaturated with respect to water and counting particles that activate droplets. The counter itself consists of a circular chamber with ports for sample intake and exhaust, temperature-controlled plates on top and bottom, and a photodetector. The theory and operation of this instrument is described by Delene and Deshler (2000), Snider et al. (2003), and Snider et al. (2006). The method for creating a supersaturated environment in the CCNC-100A is similar to that for the DMT continuous flow diffusion chamber in that a sharp temperature gradient across a small space is used to establish and control the SS. In the CCNC-100A, aerosols do not flow continuously through the region of maximum SS. Instead they are admitted into the chamber, which is then sealed off from the ambient air and flow. Particles are allowed to diffuse within the

chamber while being exposed to the supersaturated environment. Particles with S_c below the instrument SS will grow to droplet size. The abundance of droplets is monitored with the photodetector that measures the amount of light scattering caused by the droplets in the chamber. The photodetector voltage is proportional to the number of large particles (droplets) present in the chamber and, therefore, an indicator of N_{ccn}.

The detection stage lasts for 20 seconds during which a steady SS is maintained within the chamber (Snider et al., 2006). Together with the time needed to flush the old sample out of the chamber, admit the new sample, and achieve the steady state SS, CCN measurements are expected at a frequency of once every 30-35 seconds (Delene and Deshler, 2000; Snider et al., 2006). In operation, the frequency of measurement was about once every 40 seconds.

The temperature gradient within the chamber is monitored by thermocouples and the nominal SS (SS_{nom}) is computed from the reported temperature gradient and chamber-top temperature. Water vapor is supplied to the chamber by wetted pads that are re-moistened every 1-2 hours. Snider et al. (2006) report that the activation behavior of particles in the CCNC-100A is characteristic of a SS below the SS_{nom}. They define an effective SS (SS_{eff}) to describe this behavior. The reasons for the departure are not entirely understood but through experimentation, Snider et al. (2006) defined a technique for computing S_{eff}. Thus, the SS_{nom} values of 0.4%, 0.8% and 1.6% set during the December flights correspond to SS_{eff} values of about 0.27%, 0.54% and 1.08%. It is assumed in the following analysis that the SS_{eff} represents the true SS experienced by particles within the chamber. Overall uncertainty in the CCN count has been estimated to be ±40% (Snider and Brenguier, 2000) and, more recently, ±30% (Snider et al., 2006). These estimates do not include detector error associated with the random positions of droplets within the

supersaturated chamber. Estimating this error will be explained below since it also applies to the PCASP detection methods.

The PCASP is an optical particle counter, measuring the forward scattered light from particles passing through a laser beam (Snider and Petters, 2008). The scattering is relative to particle size (assuming particles are spherical) so particles intercepted by the PCASP beam can be separated into size bins. Reliable sizing can be done for particles with diameters larger than 0.135μm. Thirty bins are defined above this size with the upper limit at a particle diameter of 3μm. It is assumed that particles are classified into size bins by their dry diameter. However, hygroscopic particles deliquesce, or take on water, at relative humidity (RH) well below 100%. To ensure that the PCASP sampling environment is dry enough to rule out wetted particles, heaters are installed at the inlet. Moreover, typical ambient RH during the December flights was well below the RH=40% quality threshold recommended by Snider and Petters (2008). The sample flow rate is not constant but averages about 1 cm^3/s. The bin number concentration is defined as the count rate divided by the flow rate for each sample.

Both CCNC-100A and PCASP use photodetectors that detect only a fraction of particles in each sample. For example, the CCNC-100A chamber fills with activated droplets during the detection stage, but only those droplets that cross the detector beam are counted. The count is considered representative of the entire population, but the droplets are randomly arranged. At the time of detection, they may be arranged such that a larger (or smaller) than representative number lie in the path of the detector beam. Snider et al. (2006) point out that the many arrangements of particles can be represented using a Poisson distribution. Then the average error, known as Poisson error, can easily be estimated for each PCASP size bin using the following expression from Snider et al. (2006):

$$\sigma_i = \frac{\sqrt{C_i}}{V \cdot \log\left(D_i / D_{i-1}\right)} \qquad (6.1)$$

where C_i is the count rate for bin i, V is the sample volume, and D represents the diameter limits of size bin i. Thus, the Poisson error is proportional to the square root of the particle count and will increase for higher number concentrations, but increase in proportion relative to the total count as the number concentration gets smaller (Snider and Brenguier, 2000).

6.1.2 Flight plan

Clear-air aerosols were targeted for measurement during the King Air flights with the goal of sampling in different large-scale flow regimes. Eight days during the project period (Dec. 1 to Dec. 19) were considered clear enough to collect a complete cloud free dataset along the Western Slope. Flight days were separated into three flow regimes based on the general direction of the wind at 700mb and 500mb in the western United States. Composite images of 500mb heights for each regime are shown in Figures 6.1-6.3. First, the westerly regime is shown in Figure 6.1 and was characterized by zonal flow from the west coast through Colorado. The remaining flights were conducted on days with a 500mb ridge to the west of Colorado and a trough to the east. The amplitude of the ridge/trough pattern dictated whether flow through western Colorado was northwesterly (Figure 6.2) or northerly (Figure 6.3). Distant sources of particles to the southwest, such as the southern California urban areas, were of interest but unfortunately no episodes of southwest flow were observed.

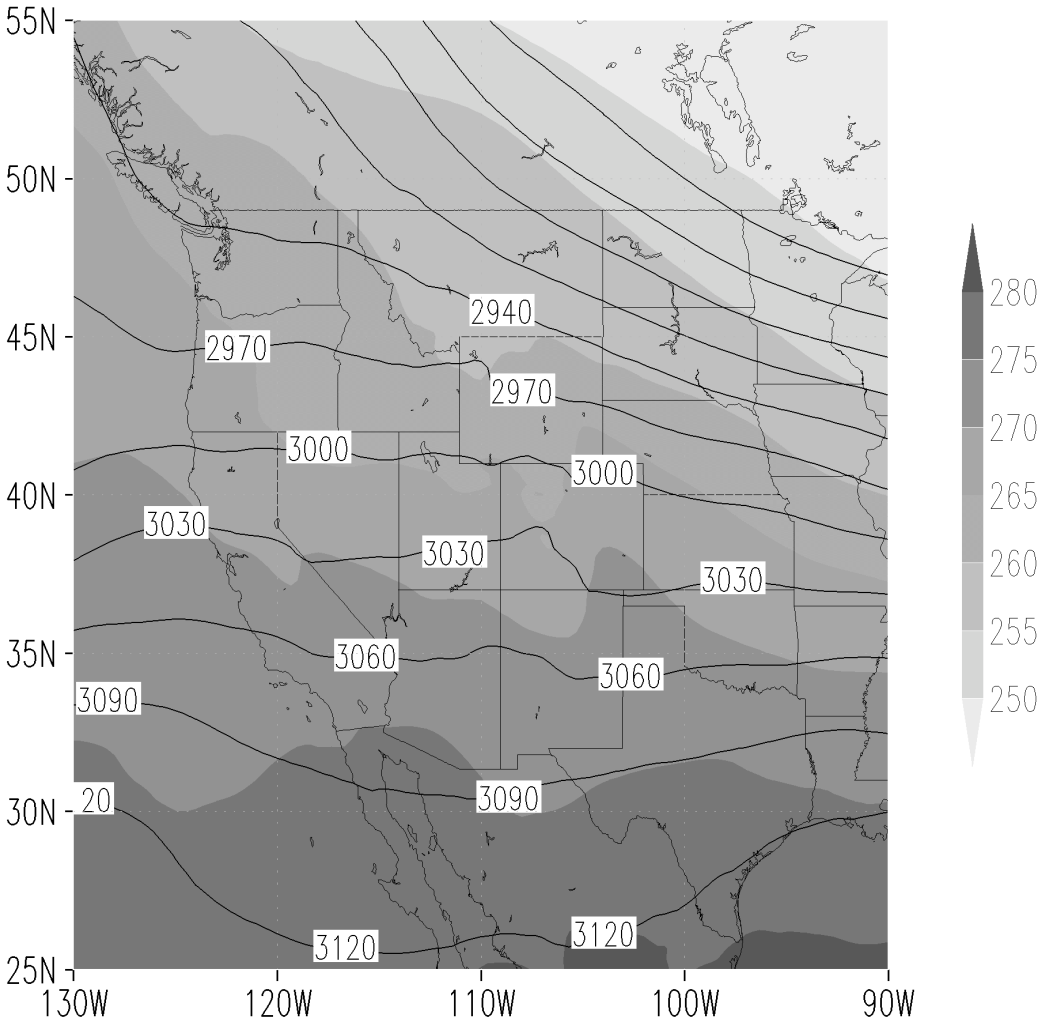

Figure 6.1: Composite of 700mb geopotential height and temperature for westerly flow regime cases. Temperature is in degrees Celsius and height is in meters.

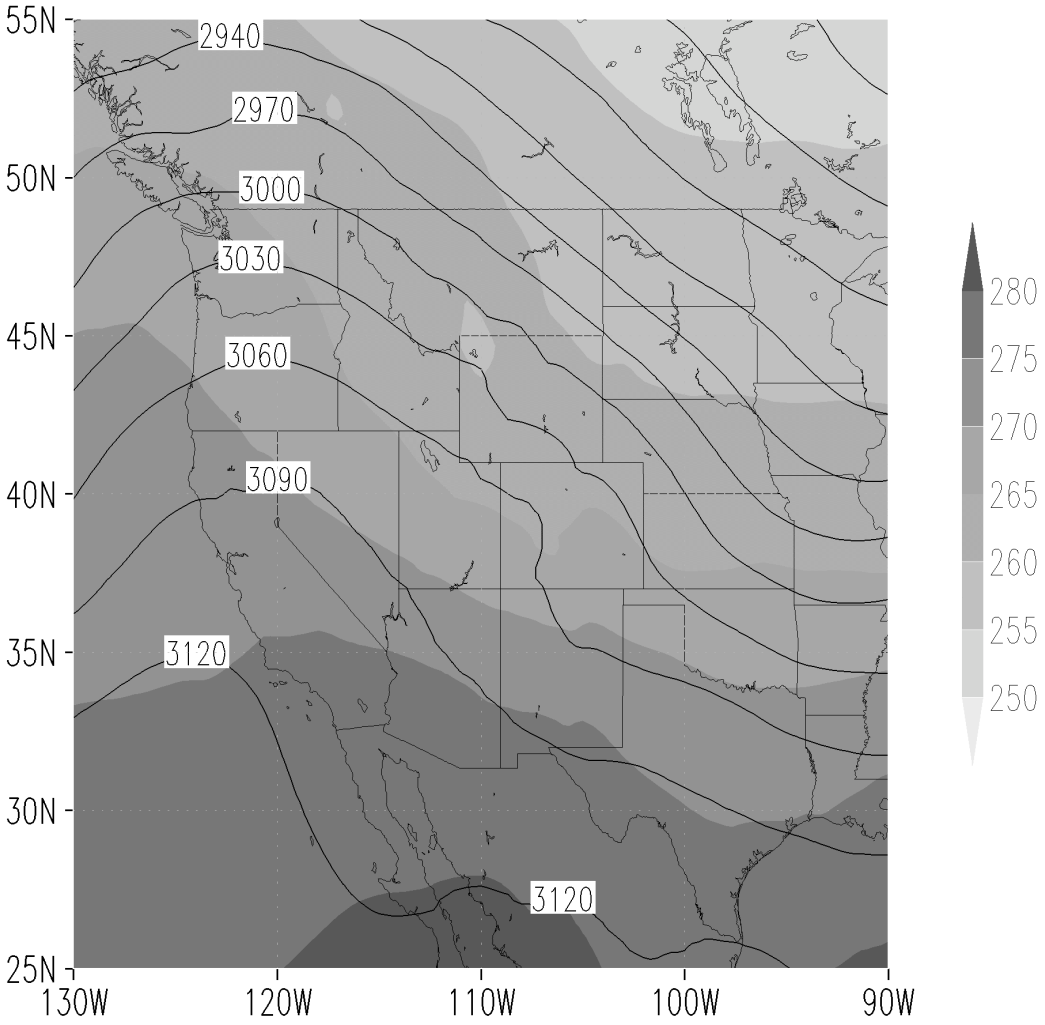

Figure 6.2: Composite of 700mb geopotential height and temperature for northwesterly flow regime cases. Temperature is in degrees Celsius and height is in meters.

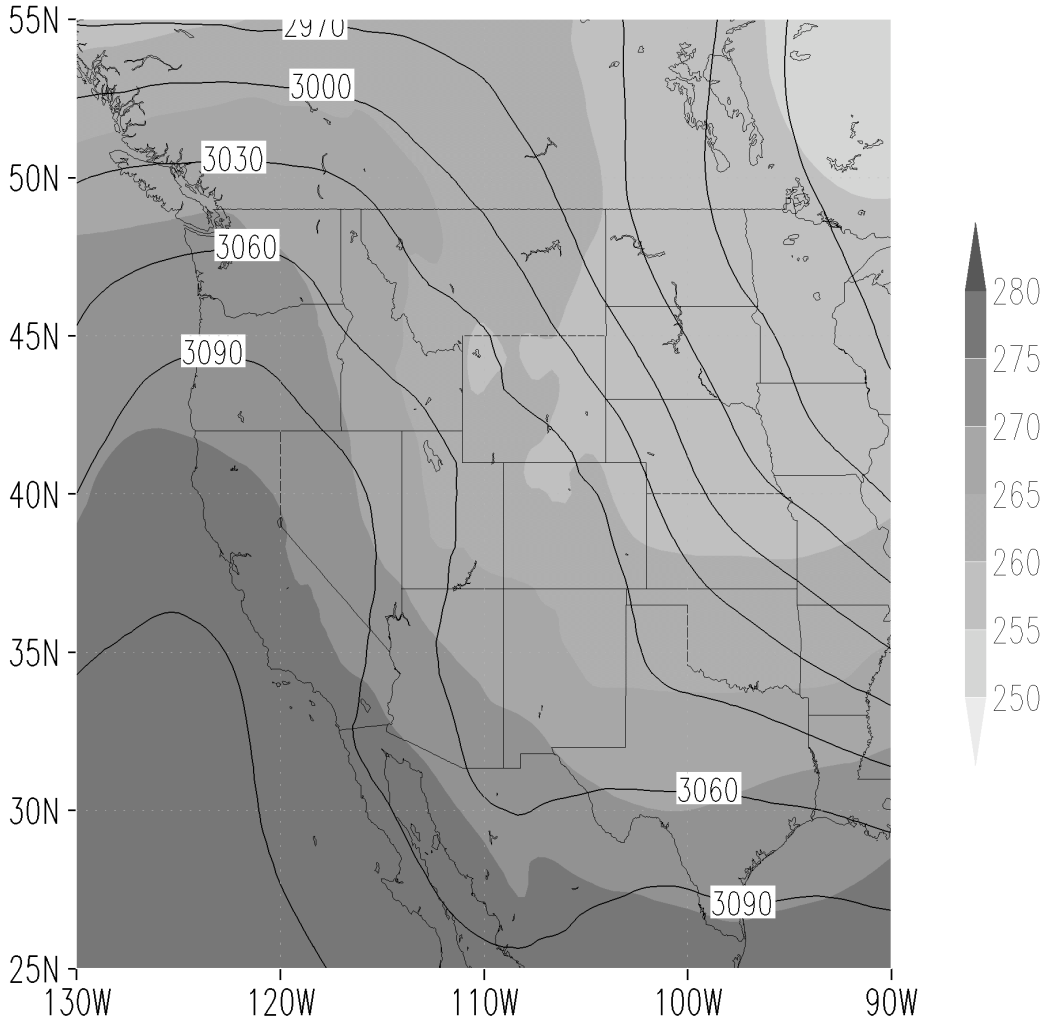

Figure 6.3: Composite of 700mb geopotential height and temperature for northerly flow regime cases. Temperature is in degrees Celsius and height is in meters.

Dates and other information about each flight are given in Table 6.1. As indicated in Table 6.1, two separate flight plans were used. The first is given in Figure 6.4 and was used for the westerly and northwesterly regimes. Vertical profiles were taken just west of Steamboat Springs and over Cortez. These were done in "vertical stacks" where the aircraft flies at a constant altitude for 40-60km then turns 180 degrees and abruptly rises, repeating

Table 6.1: Flight dates and information about the flight paths, flow regimes, and data observed for all King Air flights in December, 2009.

Flight	Date	Launch time (UTC)	Duration (hours)	Flight Plan #	Stacks (AM,PM)	Flow Regime
F1	12/3/09	17:05	4.7	2	Steamboat Springs (SB), Nucla (Nc)	N
F2	12/5/09	16:06	5.6	1	SB	W
F3	12/10/09	16:25	5.3	1		NW
F4	12/11/09	17:27	6.0	1	SB, Cortez (Cz)	W
F5	12/15/09	16:01	6.0	1	SB, Cz	W
F6	12/17/09	16:07	6.0	1	SB, SB	NW
F7	12/18/09	16:47	6.3	1	Cz, SB	NW
F8	12/19/09	15:59	5.8	2	SB, Nc	N

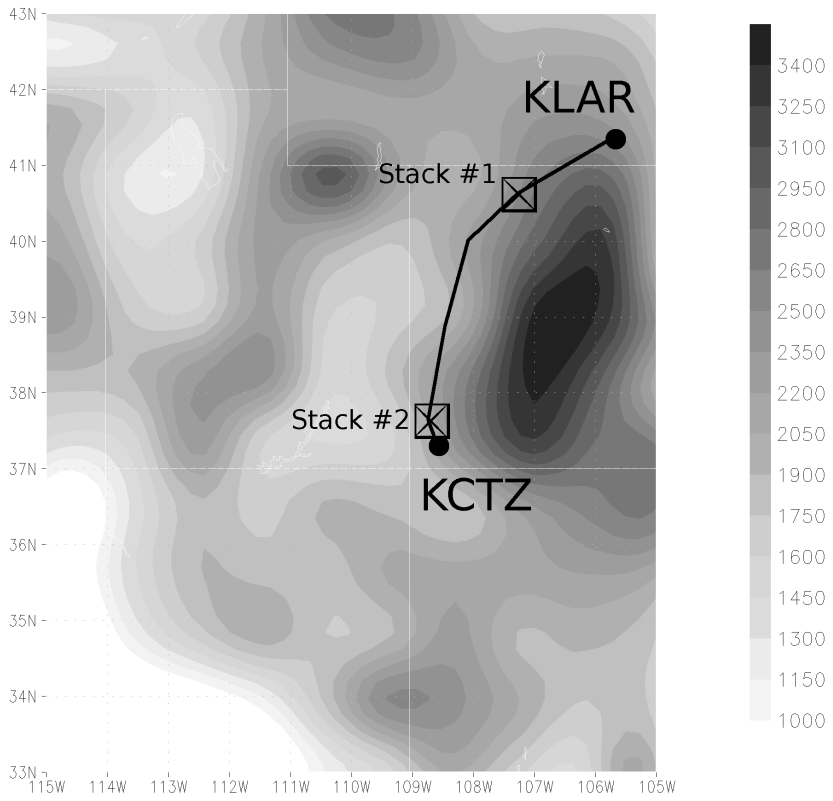

Figure 6.4: The basic flight path for flight plan #1. Stack #1 is at Steamboat Springs, CO and Stack #2 is at Cortez, CO. The Laramie and Cortez airports are marked. Topography is shaded with units of meters.

the 40-60km leg at a higher altitude and in the opposite direction. The stacks included 5 altitudes, the lowest between 250-500m above ground level (agl) and increasing about 500m on each leg with some variation. Flight plan #2 is shown in Figure 6.5 and was used during northerly wind events. It differed mainly in the location of the southern stack, which was moved north to sample flow into the San Juan Mountains better in this regime. The north to south transects were similar in both flight plans. These were flown at constant height above mean sea level meaning the distance above ground level varied, but in general this was less than 1000m above ground level (agl). The flight leg between Laramie and the

northern stack was necessarily run at higher altitudes and was used for instrumental setup. Data from this leg are not included in the analysis.

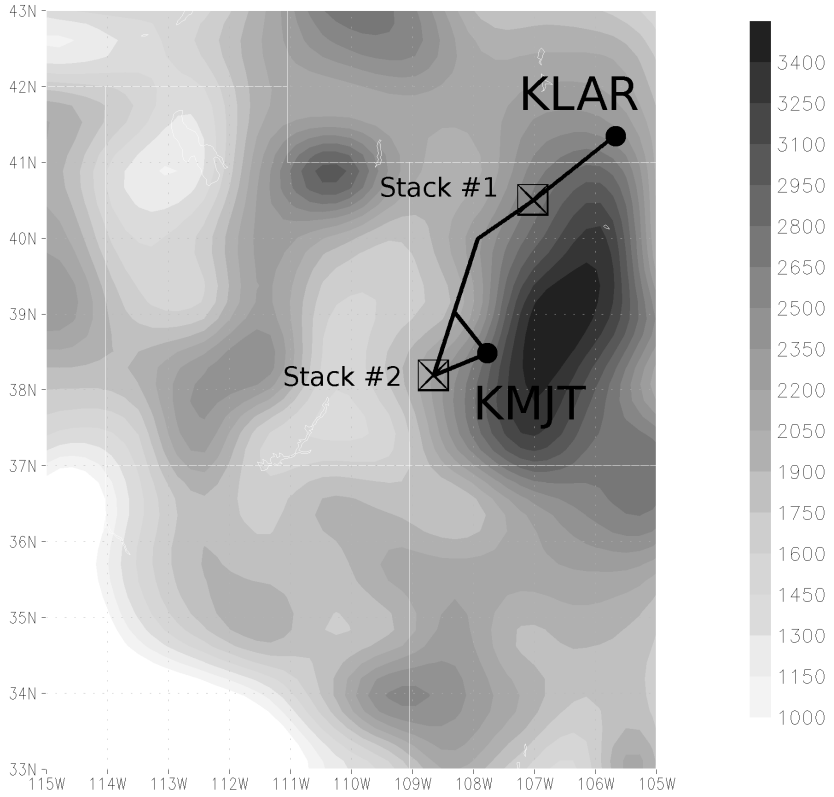

Figure 6.5: The basic flight path for flight plan #2. Stack #1 is at Steamboat Springs, CO and Stack #2 is at Nucla, CO. The Laramie and Montrose airports are marked. Topography is shaded with units of meters.

6.2 CCN observations

The N_{ccn} data collected on these flight paths underwent a check for quality of the photodetector voltage output. If the voltage exceeded established minimum or maximum

values, or if there were too few voltage data points to create a normal noise profile, the voltage, and interpreted N_{ccn}, were set to missing. PCASP aerosol size distribution bins and CPC particle number were averaged over 20-second time periods (20 observations), beginning ten seconds before the CCN instrument chamber opened and ending ten seconds after it was opened. The averaged values were then matched with the N_{ccn} computed from the aerosol that entered the chamber.

N_{ccn} is plotted against SS_{eff} for all valid data points except those collected during the vertical profiles in Figure 6.6. The mean observed N_{ccn} indicate a clean atmosphere with only a few observations of $N_{ccn} > 200cm^{-3}$ at the lowest $SS_{eff.}$ This plot also illustrates the expected increase in N_{ccn} with increasing SS_{eff} that has been represented using the power law relationship from Twomey (1959). The dataset is separated into large-scale flow regimes, as defined in Figures 6.1-3, and the composite plots are given by Figure 6.7, 6.8, and 6.9. The mean N_{ccn} was similar for the northerly (Figure 6.9) and northwesterly regimes (Figure 6.8), although the latter was less variable. The westerly regime (Figure 6.7) was cleaner in general, with a mean N_{ccn} of about $50cm^{-3}$ at SS_{eff}=0.27%.

To test for spatial trends in the N_{ccn} along the horizontal transects, the SS_{eff}=0.27% data were binned by latitude. The latitude bins were averaged and plotted for all transects in Figure 6.10. N_{ccn} averaged higher in the northern portion of the flights, but the difference was slight. In general, N_{ccn} varied little along the Western Slope. The latitude bin-average N_{cn} is also plotted on Figure 6.10 (on a different scale) to show the variation in activated fraction. Values of activated fraction were low in magnitude across the entire flight track, although higher in the southern portions than in the north. Only 5-10% of particles counted by the CPC were cloud active, on average. The implications are that greater than 90% of the ambient particles along the flight track were too small or non-hygroscopic to activate

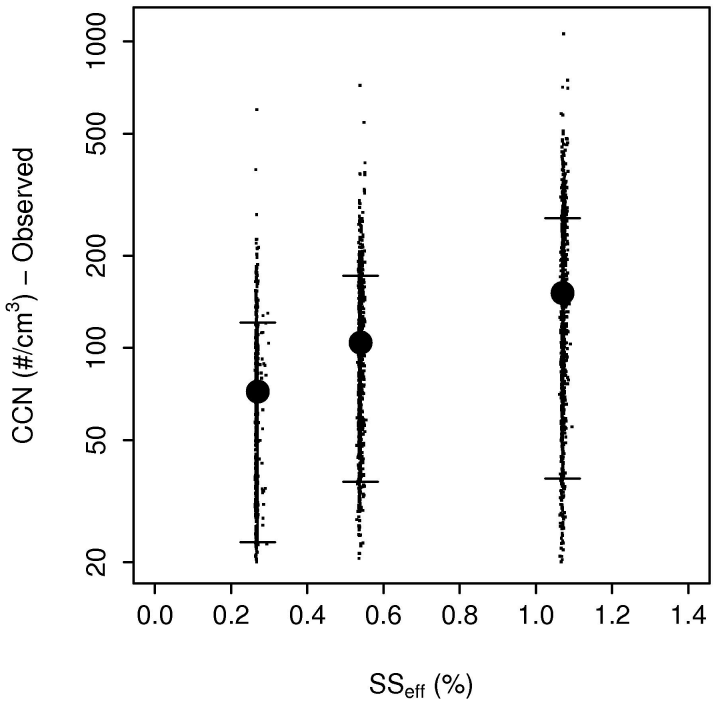

Figure 6.6: N_{ccn} plotted against SS_{eff} for all horizontal transects. The mean N_{ccn} is marked with the filled circle and the error bars represent one standard deviation from the mean.

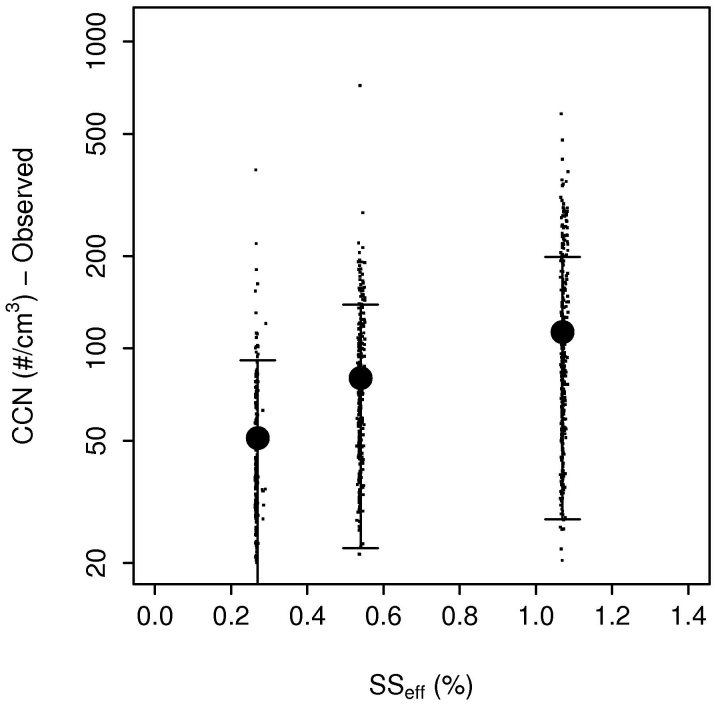

Figure 6.7: Same as in Figure 6.6 but for westerly flow regime cases.

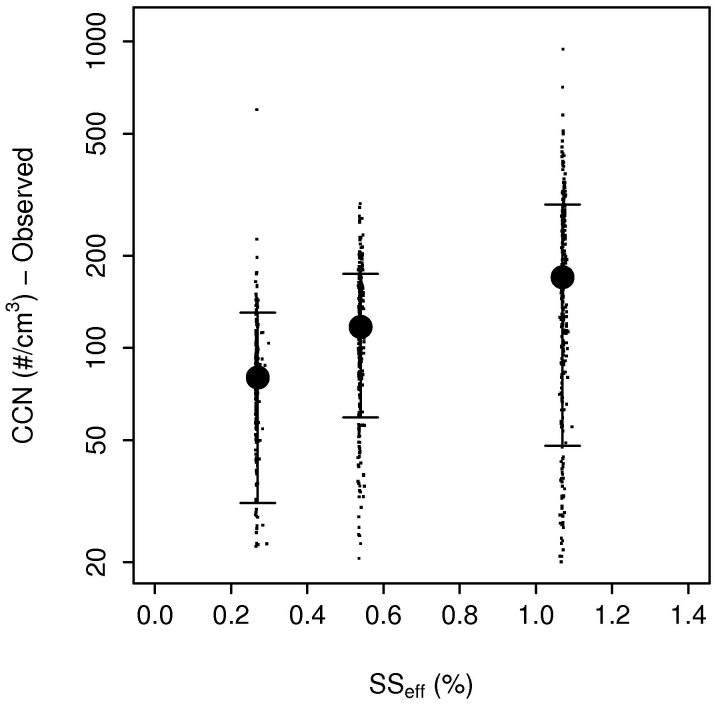

Figure 6.8: Same as in Figure 6.6 but for northwesterly flow regime cases.

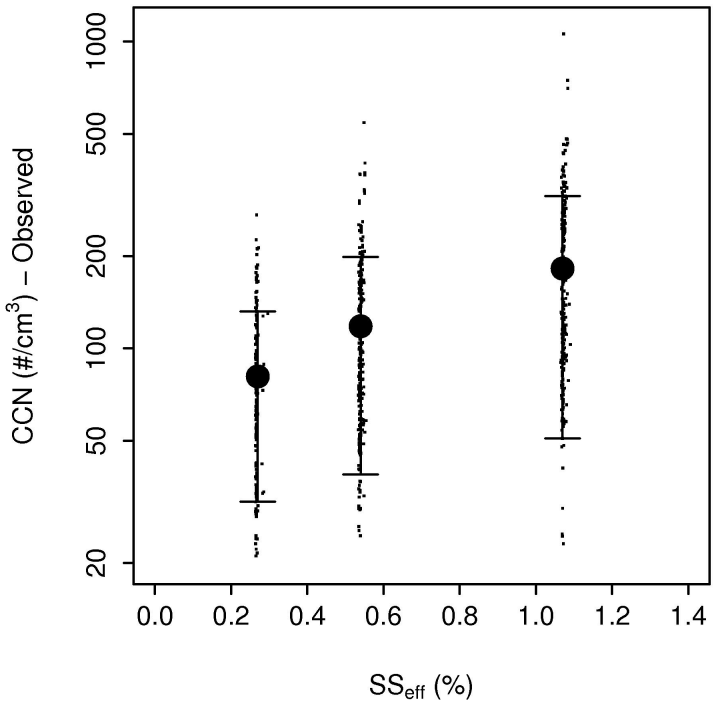

Figure 6.9: Same as in Figure 6.6 but for northerly flow regime cases.

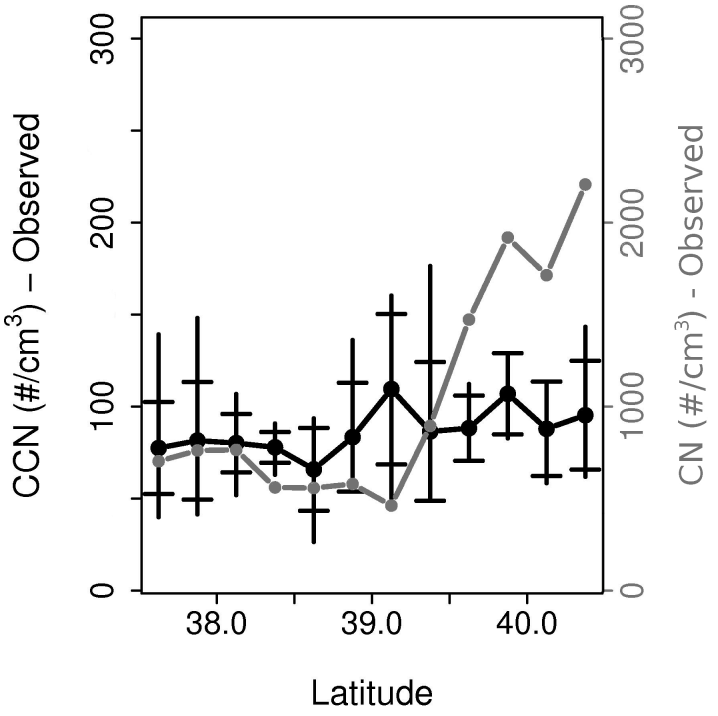

Figure 6.10: N_{ccn} (SS_{nom} = 0.4%) and N_{cn} plotted against latitude for all horizontal transects. The data were binned by latitude and averaged. The N_{ccn} is plotted in black. The capped error bars represent one standard deviation from the mean for each latitude bin and the range in values in each bin is represented with the uncapped error bar. Bin averaged N_{cn} is plotted in grey and uses the scale on the right-hand side.

droplets at SS_{eff}=0.27%. Values of activated fraction were about twice as high on average at MVNP for SS=0.3%.

Data collected during the vertical stacks also exhibit a low activated fraction. Profile data are collected in stacks to accommodate the operation of the CCNC-100A, which can be disrupted by sharp changes in ambient air pressure. During the ascent between stack altitudes, the CCNC-100A chamber is left open and particle detection is delayed. A distance of 40-60km was flown at each stack leg to collect several data points at each SS_{nom} at a constant altitude, and legs were repeated if necessary. The data were averaged over each altitude, disregarding horizontal variations in sampling along the flight leg. For the purpose

of plotting these data, any stack leg with less than 3 valid data points was set to missing. The altitude of the stacks sometimes varied between profiles, usually because clouds were encountered at target altitudes. The approximate ground levels at the three locations are 2100m msl for Steamboat Springs, 2000m msl for Cortez and 1850m msl for Nucla.

The vertical profiles are given in Figures 6.11-17 for all stacks. They are set in order by date and time flown and show N_{ccn} for all three SS_{nom} settings and also N_{cn}. On occasion the N_{ccn} plotted for a lower SS_{eff} exceeds that plotted for a higher SS_{eff}. Recall that the CCNC-100A makes one observation every 40 seconds. Over a 40km or 60km flight leg, the CCNC-100A is sampling proximate air parcels at each SS_{nom}, but not the same air parcels. Therefore it is possible to bias measurements at a particular SS. In general, the King Air 200T flew through higher numbers of particles and cloud-active particles in the lowest level of the stack compared to the highest level. This difference was most pronounced on the F7 and F8 flights for both northern and southern stacks (Figures 6.16 and 6.17). Still, the N_{ccn} average at SS_{eff}=0.27% never exceeded 200cm^{-3} even at the lowest altitudes. Activated fraction did not vary considerably with height for the majority of profiles.

On the F1 and F5 flights (figures 6.11 and 6.14), N_{ccn} and N_{cn} did not decrease constantly with altitude. Instead, a relative clean layer was observed on these days with slightly higher N_{ccn} and N_{cn} in the altitudes above the clean layer. During the F1 stacks the clean layer was evident in both the northern and southern profiles and at similar altitudes. For F5, the clean layer was more pronounced in the southern stack and difficult to discern in the northern stack.

Very similar trends in N_{ccn} and N_{cn} with height were observed between the northern and southern stacks for F1, F6, F7 and F8. In general, the magnitudes of N_{ccn} and N_{cn} were also similar on these days, all of which were characterized by northerly or northwesterly flow. This suggests that the King Air 200T was sampling within the same, or similar

airmasses. While this may not come as a surprise for north and south stacks under northerly flow, it is an important point to make. Aerosol measurements have been more abundant in northwestern Colorado in comparison to southwestern Colorado. It now appears that, especially under north and northwesterly winds, the northern measurements can be used to estimate N_{ccn} in the southern locations. In contrast, the vertical profiles for the westerly flow flights F4 and F5 do not appear to be as consistent from north to south. Differences in aerosol sources to the west of the Colorado mountains may lead to these inconsistencies with westerly winds.

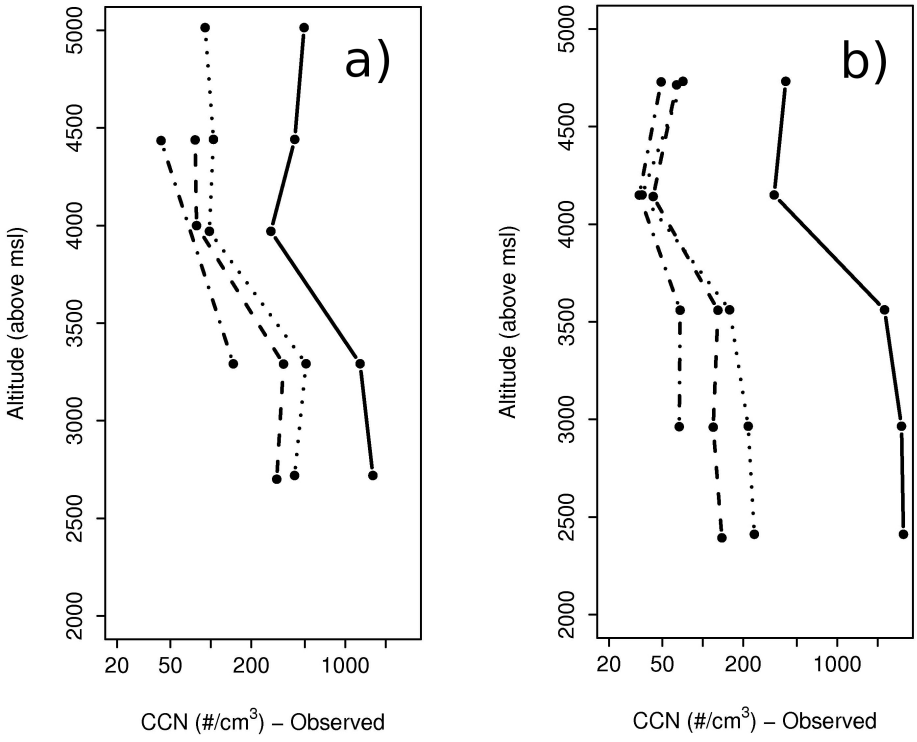

Figure 6.11: Vertical profiles collected during F1 at Steamboat Springs (a) and Nucla (b). The plotted values are N_{cn} (solid), N_{ccn} at SS_{nom}=1.6% (dotted), N_{ccn} at SS_{nom}=0.8% (dashed), N_{ccn} at SS_{nom}=0.4% (dash-dot).

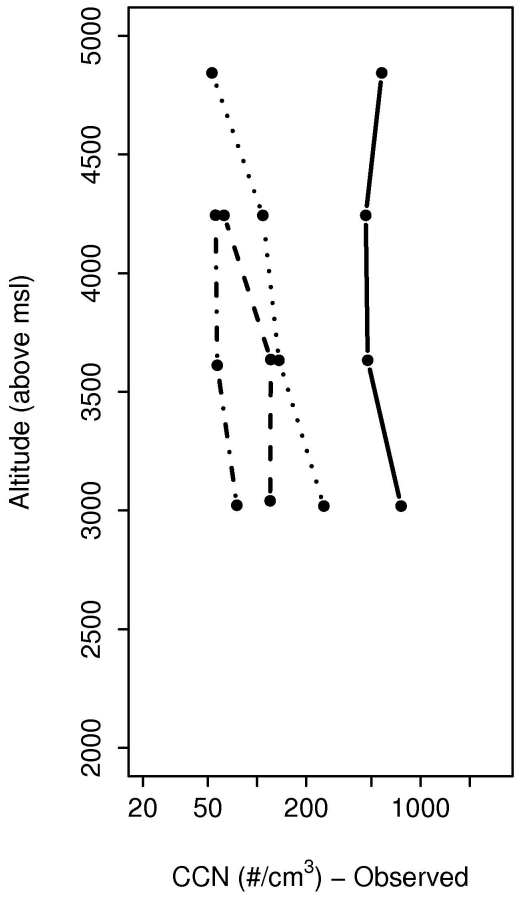

Figure 6.12: Vertical profile collected during F2 at Steamboat Springs. The southern stack was not performed on this day due to cloudiness. The plotted values are N_{cn} (solid), N_{ccn} at SS_{nom}=1.6% (dotted), N_{ccn} at SS_{nom}=0.8% (dashed), N_{ccn} at SS_{nom}=0.4% (dash-dot).

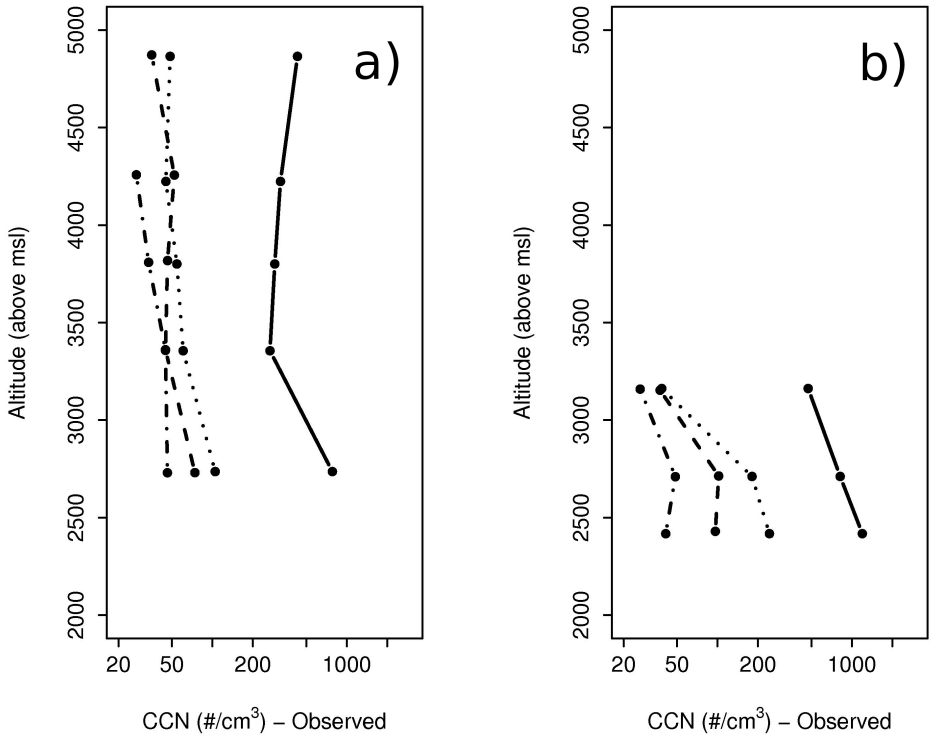

Figure 6.13: Vertical profiles collected during F4 at Steamboat Springs (a) and Cortez (b). The plotted values are N_{cn} (solid), N_{ccn} at SS_{nom}=1.6% (dotted), N_{ccn} at SS_{nom}=0.8% (dashed), N_{ccn} at SS_{nom}=0.4% (dash-dot).

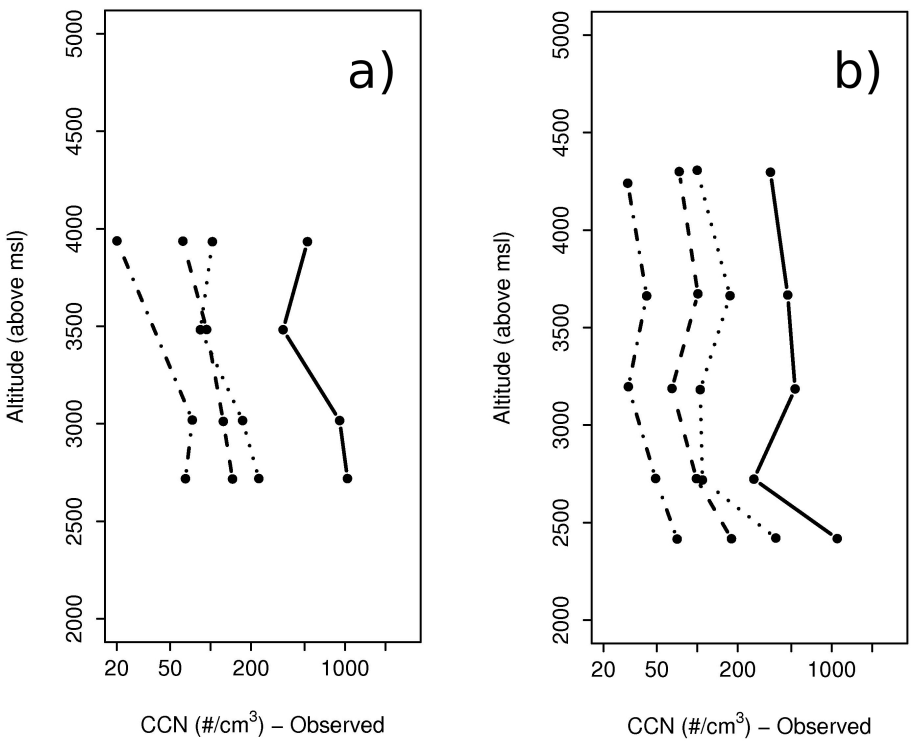

Figure 6.14: Vertical profiles collected during F5 at Steamboat Springs (a) and Cortez (b). The plotted values are N_{cn} (solid), N_{ccn} at SS_{nom}=1.6% (dotted), N_{ccn} at SS_{nom}=0.8% (dashed), N_{ccn} at SS_{nom}=0.4% (dash-dot).

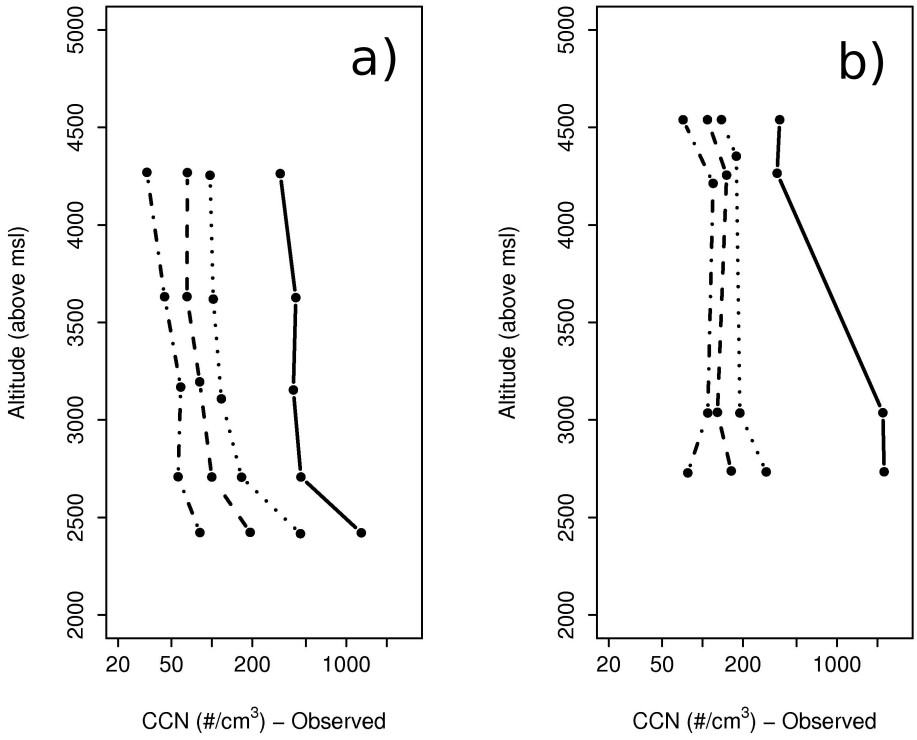

Figure 6.15: Vertical profiles collected during F6 at Steamboat Springs in the morning (a) and afternoon (b). The plotted values are N_{cn} (solid), N_{ccn} at SS_{nom}=1.6% (dotted), N_{ccn} at SS_{nom}=0.8% (dashed), N_{ccn} at SS_{nom}=0.4% (dash-dot).

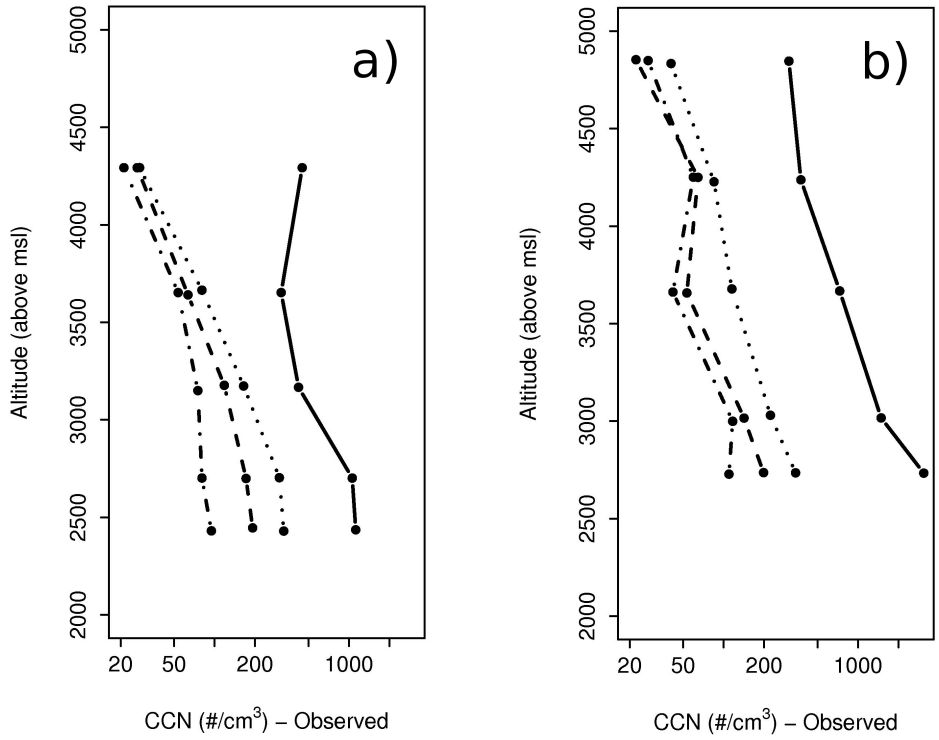

Figure 6.16: Vertical profiles collected during F7 at Cortez (a) and Steamboat Springs (b). The plotted values are N_{cn} (solid), N_{ccn} at SS_{nom}=1.6% (dotted), N_{ccn} at SS_{nom}=0.8% (dashed), N_{ccn} at SS_{nom}=0.4% (dash-dot).

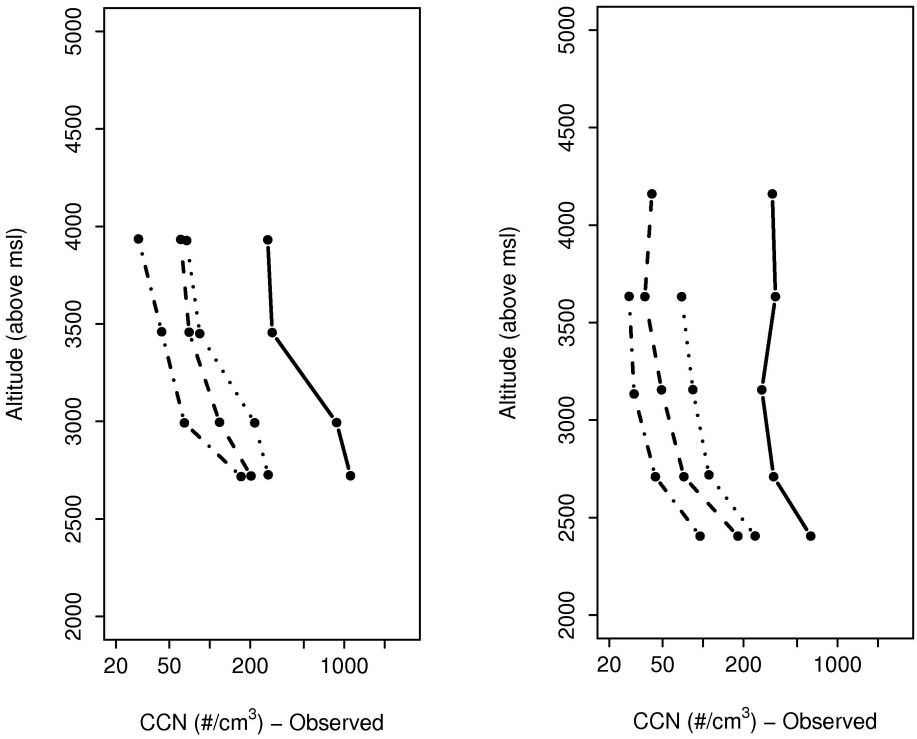

Figure 6.17: Vertical profiles collected during F8 at Steamboat Springs (a) and Nucla (b). The plotted values are N_{cn} (solid), N_{ccn} at SS_{nom}=1.6% (dotted), N_{ccn} at SS_{nom}=0.8% (dashed), N_{ccn} at SS_{nom}=0.4% (dash-dot).

6.2.1 CCN closure studies

CCN closure is regarded as one of the most effective techniques for evaluating the character of ambient CCN-active aerosol and assessing our ability to predict their CCN activity. A CCN closure study, as explained by VanReken et al. (2003), is an attempt to match observed CCN number concentrations with those predicted using one of several

methods, usually involving knowledge of the aerosol size distribution, composition, or both. Only when CCN number concentration is predicted nearly perfectly is closure achieved. Squires and Twomey (1961) and Twomey and Warner (1967) published two of the earliest studies along these lines, although their goal was not to show whether CCN could be predicted but instead to find out whether CCN could be used to predict CDNC. In the process they showed that CCN were related to CDNC observed in the low-levels of nearby clouds.

More recent closure studies use Kohler theory to model N_{ccn} at a fixed SS. Covert et al. (1998) describe one of the first attempts at CCN closure using this method. They measured N_{ccn} with a static diffusion, thermal gradient instrument at a coastal site in southern Australia. Simultaneous observations of aerosol size and hygroscopic growth were made. For each sample the critical dry size for droplet activation was computed from the Kohler equations using the hygroscopic growth information and temperature and SS set in the CCN counter. The number of observed particles larger than the critical size is counted and regarded as the prediction of N_{ccn} used to test for closure. Covert et al. (1998) found that N_{ccn} was, on average, overpredicted but only by about 20%. Subsequent studies have achieved a wide range of results with respect to CCN closure. Chuang et al. (2000) systematically, and substantially, underpredicted CCN in marine aerosol samples. The majority of their error probably resulted from instrument bias but they also note the importance of the treatment of aerosol composition in CCN prediction.

In contrast, a CCN closure study in south Florida reported by VanReken et al. (2003) found excellent agreement between measured and predicted N_{ccn} while assuming all particles were composed of pure ammonium sulfate. While they speculated that the simplified representation of aerosol composition might apply in other environments, this was not the case for rural continental aerosol sampled by Medina et al. (2007). They

observed CCN and size-dependent aerosol composition at a site in southern New Hampshire for 7 days in August. By including a size-dependent insoluble fraction parameter, based on the observations, in their CCN model, they realized substantial improvement in CCN predictions relative to CCN measurements.

Recent attempts have also focused on measuring aerosol hygroscopicity as the key to achieving CCN closure (Ervens et al., 2007; Quinn et al., 2008; Furutani et al., 2008; Bougiatioti et al., 2009). Broekhuizen et al. (2006) and Cubison et al. (2008) both show evidence that CCN closure can be improved with knowledge of size-dependent composition. Cubison et al. (2008) also found that assumptions about the aerosol mixing state (internal or external) can adversely impact CCN predictions. They sampled aerosol near Los Angeles, California in an urban airmass. For this case, assuming an external mixture of aerosol increased the accuracy of the CCN predictions. The assumption of externally mixed aerosol was also used by Stroud et al. (2007) to improve CCN closure at a polluted site in North Carolina. Incidentally, they used the University of Wyoming CCNC-100A instrument for their measurements. The work of Stroud et al. (2007) aptly reflects the current state of CCN closure studies by pointing out that inadequate understanding of aerosol composition effects on hygroscopicity and instrument inaccuracies are the main barriers to achieving CCN closure.

6.2.2 CCN closure aboard the King Air

As in the studies outlined above, to predict N_{ccn} for the King Air horizontal transects, information about the aerosol size distribution and composition are needed. To compute

the critical size for each sample, the temperature and SS are set equal to the conditions in the CCNC-100A. Size distribution data are given by the PCASP.

Since composition measurements were not taken during this project, a reasonable estimate of aerosol hygroscopicity must be used instead. This estimate is, unfortunately, constrained by the detection limits of the PCASP. The PCASP lower size limit for reliable measurements was given as 0.135μm earlier in this chapter. However, even at SS_{eff}=0.27% and the average temperature of the CCNC-100A, a particle with the hygroscopicity of ammonium sulfate corresponds to a critical diameter of 0.07μm. Therefore, if the value of κ for ammonium sulfate were used to predict N_{ccn}, an unmeasured portion of the aerosol size distribution would exist above the critical size. These particles would go uncounted and N_{ccn} could be underpredicted considerably. Only less hygroscopic particles would possess a critical size larger than 0.135μm. To ensure that the computed critical size will fall within the detection range of the PCASP at SS_{nom}=0.4% (SS_{eff} approximately 0.27%), a value of $\kappa \leq 0.125$ must be assumed. A value of κ=0.1 is used for this study. This is equivalent to assuming the sampled aerosol have a low hygroscopicity, more characteristic of organic aerosol species than sulfates or nitrates, although κ=0.1 does fall within the range estimated for SPL during ISPA-II (see Chapter 4).

Using the estimated κ, a critical diameter is computed using the forms of the Köhler equations given in Petters and Kreidenweis (2007). This is done separately for each sample since the SS_{eff} and average chamber temperature vary from sample to sample. Particles in size bins greater than the critical size, as counted by the PCASP, are summed. The sum is regarded as the predicted N_{ccn}. Note, due to the limitations of the PCASP size range, only CCN measurements at SS_{nom}=0.4% were used in this analysis.

Figure 6.18 shows the predicted N_{ccn} plotted against the measured N_{ccn} for all horizontal transects. Error bars depict the estimated uncertainty for the CCNC-100A

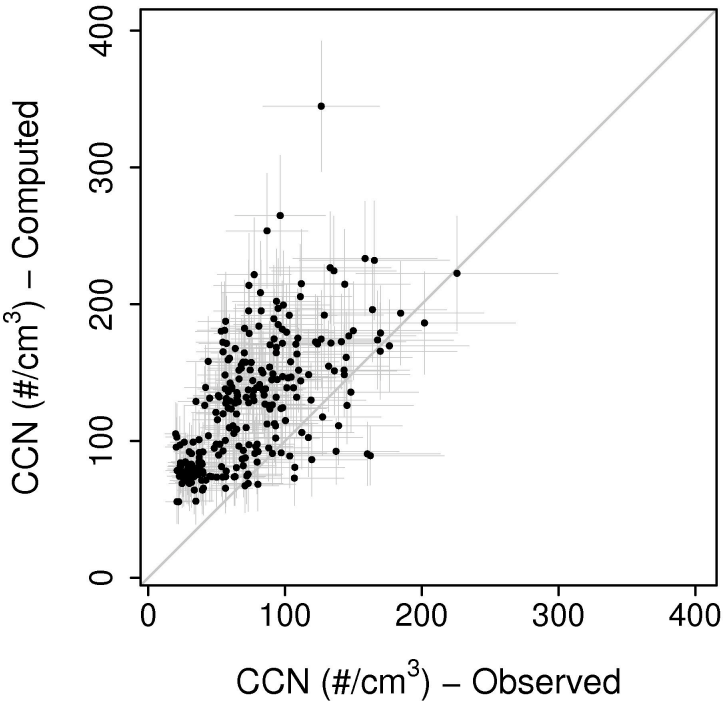

Figure 6.18: Observed vs. predicted N_{ccn} for all horizontal transects. Horizontal error bars represent the Poisson error in the CCN detection added to 30% instrument error as estimated by Snider et al. (2006). Vertical error bars represent the Poisson error in the PCASP detection. The 1:1 relation line is plotted.

measurements and the PCASP counts (expressed in the predicted N_{ccn}). For the CCNC-100A, the uncertainty is considered the sum of the Poisson error and 30% additional instrument uncertainty as estimated by Snider et al. (2006). The PCASP uncertainty is shown as the sum of the Poisson error for each size bin used for N_{ccn} prediction. Despite the low prescribed value of κ, the majority of data points were over-predicted. Instrument bias aside, this indicates that the sampled aerosol had very low hygroscopicity ($\kappa < 0.1$, in general). There is no specific reason to expect instrument bias, but as Stroud et al. (2007) note, this should not be ruled out for these instruments. Figure 6.18 also shows substantial spread of the data points. The assumptions made concerning the aerosol composition and mixing state probably contributed to the spread and, clearly, instrument uncertainty played

a large role. Overall, N_{ccn} was predicted within a factor of three when compared to the measurements. The results of this analysis are consistent with the observation of very low activated fraction that was made using the CPC.

Figures 6.19-21 show the same CCN closure plot for data separated by flow regime. The noted differences in magnitude of N_{ccn} between regimes are also apparent in these images. Remarkably consistent N_{ccn}, mainly between 30-50cm^{-3}, were observed under westerly flow and these were just as consistently overpredicted (Figure 6.19). Observations under northwesterly flow show the largest average deviation from the plotted 1:1 relation line (Figure 6.20). This could indicate a change in aerosol mixing state or average composition sampled during these flights, but it cannot be said for certain. No regime showed a preference for underprediction of N_{ccn}.

As in Chapter 4, κ for each sample can be backed out from the Petters and Kreidenweis (2007) version of the Köhler equations if internally mixed aerosols are assumed. The estimated κ is similar to the effective κ, κ_t, used by Gunthe et al. (2009). Here the terminology, κ_t, will be adapted for the estimated κ. Again, this also requires the assumption that aerosol chemistry is the sole cause of inaccurate CCN predictions, although PCASP error likely plays an additional role. These computations could only be carried out for SS_{nom}=0.4%.

The κ_t for the transect flight legs are shown as a scatter plot in Figure 6.22. For samples with a greater measured CCN than total PCASP particle count, κ_t can be considered greater than 0.125, but a more exact value cannot be computed. These samples are marked with triangles in Figure 6.22. The κ_t varied within a small range above κ_t=0.03 and averaging about 0.07 (without considering the κ_t>0.125 samples). These values fall below the typical range for κ in observations of continental airmasses summarized by Andreae and

Rosenfeld (2008) and average lower than the κ estimated at SPL during ISPA-II (0.14, see Chapter 4).

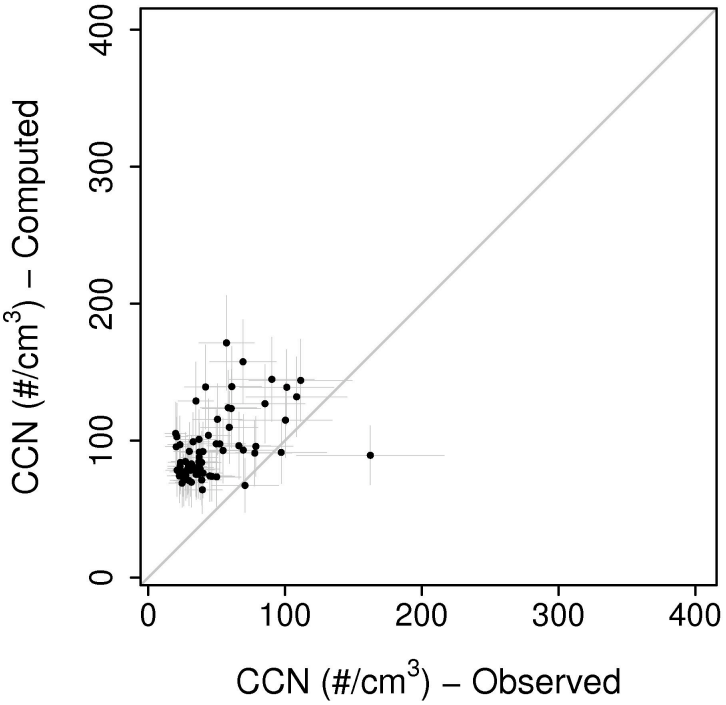

Figure 6.19: Same as Figure 6.18 but for westerly flow regime cases.

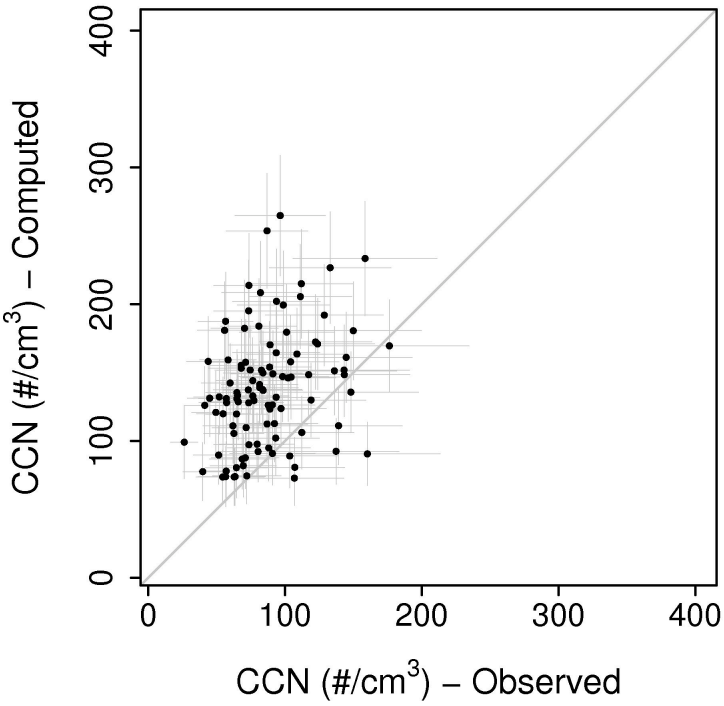

Figure 6.20: Same as Figure 6.18 but for northwesterly flow regime cases.

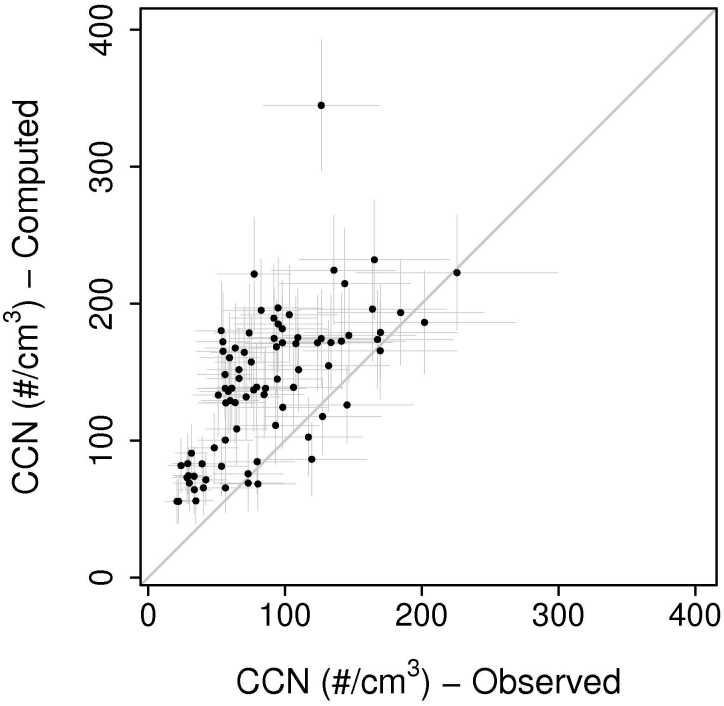

Figure 6.21: Same as Figure 6.18 but for northerly flow regime cases.

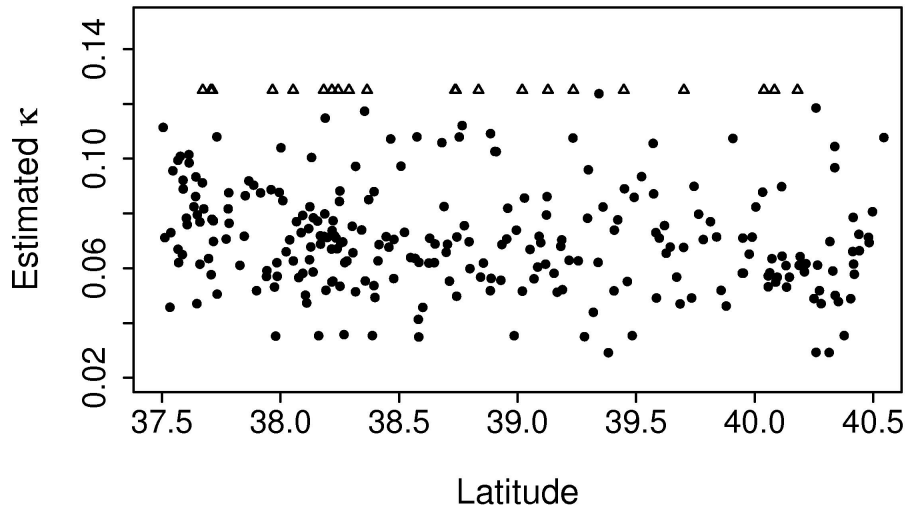

Figure 6.22: A scatterplot of κ_t vs. latitude for all horizontal transects. Valid points are plotted with filled circles. The points at which κ_t is greater than 0.125 are plotted with empty triangles.

6.3 General Western Slope CCN characteristics

In combination with observations from MVNP and SPL, the beginnings of fall and winter season CCN climatologies now exists for the Western Slope. The N_{ccn} and activated fractions are consistent with remote continental, aged aerosol. These characteristics were true from SPL, south to MVNP, and somewhat consistent in time as well as space. This result suggests that variability of CCN in this region may be less important than originally thought. This has implications for studies of aerosol effects on orographic clouds in this region. CCN flowing in to the San Juan Mountains and other locations along the Western Slope can be estimated by the available measurements from northwestern Colorado, at least for particular wind regimes and seasons. This may also be encouraging from a modeling perspective. The lack of variability associated with CCN along the Western Slope could

justify simplified representations of aerosols in numerical simulations, provided the simplifications are based on averaged observed quantities.

The low aerosol hygroscopicity estimated from these observations was particularly noteworthy. Values of κ less than 0.1 are indicative of a dominant organic or insoluble aerosol component and a minor contribution from the more hygroscopic inorganic species. This is inconsistent with observations from the IMPROVE network site at Mount Zirkel (MOZI) in the Colorado Park Range. The composition of the $PM_{2.5}$ aerosol sampled at MOZI in December from 1999-2008 averaged more than 50% sulfate and nitrate by mass. This is corroborated by the analysis of Borys et al. (2000) who found substantial sulfate and nitrate mass in cloud water samples collected at SPL during the winter. Richardson et al. (2007) used an aerosol mass spectrometer (AMS) and other methods to measure aerosol composition at SPL during April and May of 2004. They also found high proportions of inorganic compounds that dominated the total aerosol mass except during dust events. In light of these observations, it is likely that the estimated hygroscopicity values in this study are biased low either due to flawed instrumentation or the method of estimation. Studies using similar CCN closure methods have often resulted in overpredictions of CCN (Covert et al., 1998; VanReken et al., 2003). A more successful method for predicting N_{ccn} from aerosol size distribution information was introduced by Petters et al. (2007) but this method requires size-selection of particles during sampling.

Many questions remain unanswered, especially concerning the sources of the CCN, CCN composition, and variations with season. Current modeling technology is beginning to allow for a more comprehensive approach to these problems, the source apportionment problem in particular. In the next chapter, the coupling of the WRF/Chem aerosol modules to RAMS meteorology and microphysics will be described. Within the coupled system, it will be possible to simulate the evolution of a particle from emission to droplet activation

and bring us closer to answering source apportionment questions for the Colorado Rocky Mountains.

Chapter 7

Coupling of WRF/Chem and RAMS

Aerosols in the atmosphere interact with each other and undergo complex chemical and physical transformations. For these reasons, it is difficult to characterize the sources and sinks of potentially cloud-active particles with *in situ* observations. Andreae and Rosenfeld (2008) write, "...a meaningful analysis of the sources and burdens of cloud-active particles must take the form of a comprehensive atmospheric model that contains emissions of precursor gases and primary aerosol species, and accounts for transport, transformations and sink terms of precursor gases as well as the interactions of the various aerosol components." Comprehensive models of this kind are only beginning to be developed. Perhaps the most advanced example of a multi-scale aerosol and cloud microphysics model is the GATOR-GCMOM, which was described by Jacobson et al. (2007). GATOR-GCMOM uses a sectional representation of aerosols with size-differentiated composition, includes important aqueous-phase oxidation pathways, and is one of the only models containing online aerosol-microphysics interactions. The main disadvantage of such a system is the computation time required to simulate all these processes. As computational efficiency increases with advances in technology, it will become feasible to apply these comprehensive models to many scientific questions.

The initial steps toward the creation of a coupled system to examine the variability of atmospheric CCN have been taken with the supplementing of RAMS microphysics with WRF/Chem aerosol forecasts. WRF/Chem rivals the inclusiveness of the GATOR-GCMOM system with respect to aerosol chemistry processes, but is comparatively deficient in treatment of microphysical processes and their interactions with aerosols (Jacobson et al., 2007). By incorporating the WRF/Chem aerosol forecasts into RAMS, the aim is to overcome these deficiencies and form a more complete system for modeling CCN. To achieve this goal, accurate forecasts of aerosol number, size, and hygroscopicity from WRF/Chem need to be supplied to the RAMS droplet activation scheme. The important elements of this model development, the WRF/Chem modules and the method of coupling to RAMS are explained in this chapter.

7.1 The WRF/Chem modeling system

WRF is a non-hydrostatic, atmospheric model that has been developed collaboratively at several institutions. While it is described as a single entity, WRF could be more accurately described as a framework for the combining of separately developed numerical modules. WRF offers a choice between numerical schemes for many different processes, even several options for the dynamical core of the meteorology, giving users the flexibility to tailor the model code to their research needs. The modular nature of WRF allows it to be used in a number of research applications and also allows for easier development by separate research groups (Fast et al., 2006).

Atmospheric chemistry was introduced into WRF several years ago by fitting existing chemical mechanisms into the WRF framework, creating WRF/Chem (Grell et al.,

2005). In the latest version of WRF/Chem, version 3.0, separate modules treat emission of anthropogenic aerosols and precursor gases, emission of biogenic precursor gases, gas-phase oxidation, aerosol dynamics, and secondary organic aerosol formation. The abilities and limitations of the modules used to provide aerosol forecasts to RAMS are described in the next section.

7.1.1 RACM

Gas-phase chemistry was treated with the Regional Atmospheric Chemistry Model (RACM) developed by Stockwell et al. (1997) as an upgrade to the Regional Acid Deposition Model, version 2 (RADM2; Stockwell et al., 1990). Both mechanisms are available for use in WRF/Chem but only RACM treats the gas-phase oxidation of the important biogenic aerosol precursor gases alpha-pinene and limonene. McKeen et al. (2007) note that the neglect of these gas-phase species probably leads to underestimates of SOA when using RADM2.

Chemical mechanisms for regional-scale modeling are often compared in the literature by the number of species and number of reactions they include. While this may not be the true measure of utility (Arteta et al., 2006), for the record RACM includes 77 chemical species (17 stable inorganic species, 4 short-lived, inorganic intermediates, 32 stable organic species and 24 organic intermediates) and 237 photolytic, thermal, and oxidation reactions. Inorganic gas-phase chemistry is treated similarly in these and other chemical mechanisms but they often differ with their treatment of organic chemistry. In RACM, organic species with similar oxidation pathways and functional groups are arranged together in groups, a common strategy for dealing with the many organic compounds present in the atmosphere (e.g. Chapman et al., 2009, Lamarque et al., 2010). The grouping

of organic species corresponds to the speciation of anthropogenic (16 species groups) and biogenic (3 species groups) emissions in the National Emissions Inventory (NEI) that is also used in this project, making RACM a convenient choice in this respect.

All of these reactions are important in the production of cloud-active aerosol since many species need to undergo oxidation in the gas-phase before partitioning to the particle-phase. Reactions involving species that are not known to partition are still necessary to simulate as they determine the availability of oxidants in the model atmosphere.

7.1.2 MADE/SORGAM

RACM models strictly gas-phase processes. To simulate aerosol processes and the transition between the gas and particle phases, an aerosol dynamics module is used. As with the chemical mechanism, WRF/Chem offers several choices for aerosol dynamics. The current version includes modal representation aerosol options (Grell et al., 2005) as well as an option for a sectional representation (Fast et al., 2006). The sectional aerosol module, named the Model for Simulating Aerosol Interactions and Chemistry (MOSAIC), is described by Fast et al. (2006). The sectional scheme offers more realistic representations of aerosol size distributions (Zhang et al., 2002), but is computationally expensive. Fast et al. (2006) point out that only MOSAIC's eight size bins for aerosol require 112 prognostic variables to describe the aerosol composition and number. The most sophisticated modal option for aerosol dynamics in WRF/Chem is the Modal Aerosol Dynamics Model for Europe (MADE; Ackermann et al., 1998).

Aerosols in MADE are represented by two lognormal size distributions, corresponding to an Aitken mode and an accumulation mode. The two modes overlap and

interact through coagulation. The MADE Aitken and accumulation modes describe only submicron diameter particles. Supermicron particles are included in WRF/Chem by the addition of an interactive coarse mode (Schell et al., 2001).

Particles are added to the lognormal modes either by direct emission or by secondary formation. New particle formation in MADE is treated solely by the Kulmala et al. (1998) parameterization of sulfuric acid nucleation. The Kulmala et al. (1998) parameterization uses the predicted T, RH, and sulfuric acid vapor concentration to determine a nucleation rate for particles in the sulfuric acid/water system. New particles are assigned to the Aitken mode with a diameter of 3.5nm and the size distribution parameters are adjusted to retain the lognormal shape of the distribution. Nucleation of other species, or including other species, is not included in MADE.

Simulated particles in MADE grow by condensation and coagulation. Low vapor-pressure gas-phase species condense onto existing particles at a rate determined by the vapor pressure of the species over the aerosol surface. The Kelvin effect, a result of the curvature of the aerosol surface, is parameterized by a size-dependent growth factor in this scheme to simplify the computation of the condensational growth rate (Ackermann et al., 1998; Binkowski and Shankar, 1995). Condensation of organic mass is included by the introduction of the Secondary Organic Aerosol Model (SORGAM) into the MADE framework (Schell et al., 2001). The low volatility organic predicted in RACM are assigned to eight product groups in SORGAM. These are the reaction products of aromatic precursors (two-product model assumed), alkanes, alkenes, α-pinene (two-product) and limonene (two-product). The molecular weights and vapor pressures for these groups of species are approximations since each group contains many unspecified compounds and our knowledge of the characteristics of these compounds is often lacking (Schell et al., 2001). Where a two-product model is assumed, reaction products of the same precursor class are

given two separate vapor pressures. This accounts for some of the variation in reaction products. The organic gas precursors condense onto existing particles at a rate determined by the gas-phase concentration, characteristic vapor pressure, and availability of aerosol surface area to condense onto. Any new particle mass is kept in its original product group under a similar variable name.

Recent work suggests a potentially large contribution to SOA mass from isoprene reaction products (e.g. Heald et al., 2008; Carlton et al., 2009). Heald et al. (2008) estimate the contribution from isoprene to be 78% of global SOA, but the gas-phase and aqueous-phase isoprene to SOA pathways that are thought to be important are also poorly understood (Carlton et al., 2009). SORGAM is not set up to manage the gas-particle partitioning of the products of isoprene oxidation, even though isoprene chemistry is predicted in RACM. Therefore, the MADE/SORGAM module could underestimate SOA yields in situations where isoprene products are abundant. Heald et al. (2005) suggest that numerical models generally under-predict organic aerosol mass when compared to observations, and inadequate treatment of isoprene is likely a contributing factor.

Aerosol mass can be added to existing particles by condensation but the particle number remains the same. During coagulation of particles, the aerosol mass is conserved but the particle number decreases. Throughout, the lognormal shapes of the size distributions are maintained (Binkowski and Shankar, 1995).

Interspecies coagulation occurs in MADE regardless of the particle composition, meaning internal mixtures of multiple species are created. To limit the number of variables, and computation time, that would be required to follow the various internal mixtures, MADE essentially assumes all particles contain the same proportions of the different species. In other words, a perfect internal mixture of all aerosol mass is assumed. With this assumption of a perfect internal mixture, MADE only needs to predict one aerosol number

and size distribution containing all species. Alternative modal schemes that prognose particle number and size separately for each species have been developed (e.g. Lohmann et al., 1999; Lohmann and Diehl, 2006), but these are necessarily restricted to intraspecies coagulation and the assumption of total externally mixed aerosols. Neither assumption, of a pure internal or external mixture, applies universally in the atmosphere (McFiggans et al., 2006) and in some cases an external mixture has been shown to perform best (Cubison et al., 2008). But according to a review of recent observations by McFiggans et al. (2006), aerosols in locations removed from large particle formation areas (such as urban centers) are most likely to be at least somewhat internally mixed.

The significance of this assumption cannot be overstated since the evolution of aerosols size, number and composition are determined within this module. The accuracy of N_{ccn} forecasts in RAMS, therefore, is largely dependent on the skill of MADE/SORGAM.

7.1.3 Limitations of this module setup

The MADE/SORGAM and chemical mechanism modules within WRF/Chem predict the major known components of ambient CCN using a modal representation of aerosols, which minimizes the required computation time. This setup has shown skill at predicting anthropogenic aerosol mass, particularly in polluted areas such as the northeastern United States (e.g. McKeen et al., 2007; Grell et al., 2005) but McKeen et al. (2007) found that WRF/Chem forecasts of $PM_{2.5}$ exhibited a low bias in rural areas. The bias was attributed to the inadequate treatment of secondary organic aerosol formation and the lack of consideration of some biogenic precursor gases. In areas where organic aerosols dominate the total aerosol mass, such as some rural areas, the bias would be most pronounced. This

is of concern for the study of aerosols in western Colorado, which is largely rural. Even though this study focuses on the winter season, and biogenic aerosols are unlikely to factor greatly into the total aerosol mass, it should be noted that overall organic aerosols are likely to be underpredicted in WRF/Chem for simulations in western Colorado.

The modal representation of aerosol size distribution reduces computation time but also precludes our ability to simulate complex size distributions and size-dependent composition. These complexities affect the cloud-active fraction of a predicted aerosol population as shown by Abdul-Razzak and Ghan (2002) and mentioned in previous chapters. The simplified lognormal representation is not expected to result in model bias but it will result in less accurate CCN predictions whenever the ambient aerosol deviates from the idealized size and composition.

A third and possibly most important limitation of this module setup in WRF/Chem is the lack of aqueous-phase sulfate production. Recent evidence suggests that the majority of global sulfate aerosol mass is produced in the aqueous phase (Kanakidou et al., 2005). To simulate the aqueous oxidation, basic online interaction between aerosols and cloud droplets is required. Work has begun in WRF/Chem to link the aerosol modules, in this case MOSAIC, with the WRF/Chem microphysics using the Abdul-Razzak and Ghan (2002) droplet activation parameterization (Chapman et al., 2009). Chapman et al. (2009) were able to estimate the quantity of sulfate produced in cloud droplets using this scheme and an aqueous chemistry module. On the whole, they found that sulfate aerosol was overpredicted, although this was ascribed to over-emission of SO_2.

The model comparison results of McKeen et al. (2007) also showed that sulfate can be overpredicted when aqueous reactions are included in the model framework. As part of the comparison study they ran WRF/Chem using MADE/SORGAM and found that, without aqueous chemistry, $PM_{2.5}$ sulfate was underpredicted. The gas-phase only oxidation

pathway for sulfate production was too slow to account for the observed sulfate amount. Similarly, the underprediction of sulfate production should be expected in the WRF/Chem aerosol output coupled to RAMS. This may be less important for regions in the intermountain western United States, like western Colorado, that are typically dry in the winter. Simulations in wetter mountainous regions like the Cascades or Sierra Nevadas, where aerosol effects on orographic precipitation have also been observed (Rosenfeld and Givati, 2006), may result in even larger underprediction than shown by McKeen et al. (2007). Although, it's difficult to make any general claim, as sulfate production in either phase will probably vary substantially from case to case and can be produced in a distant location and transported long distances.

7.1.4 Anthropogenic emissions

WRF/Chem can be initialized with constant background concentrations of aerosol precursor gases and oxidant species for basic idealized simulations. For more realistic representations of ambient aerosols, gas and aerosol emissions data are input regularly into the model domain in subsequent model time steps. Emissions data for the continental United States are available at high horizontal resolution for both anthropogenic and biogenic emissions.

The National Emissions Inventory (NEI) maintained by the Environmental Protection Agency (EPA) includes anthropogenic emissions for the continental United States as well as southern Canada and northern Mexico (at larger grid spacing). The most recent version of this inventory, NEI-2005, is used in this study.

NEI data are provided in two sets: point emissions and area emissions. Point emissions are released by fixed sources and include power plants, refineries, and other industrial sites. The EPA monitors these sources continuously and as a consequence, detailed emissions data are available. Additional information regarding the height of emitting stacks and effluent characteristics are included in the NEI. In WRF/Chem a plume-rise algorithm computes the appropriate model level for emission of effluent flowing from high stacks or with an initial vertical velocity.

Area sources are derived from measurements of emissions from sources such as automobiles, ships, agriculture, and urban activities. Observed values of emissions from these activities are extended across the entire country onto a 4km by 4km grid by applying scaling factors such as traffic density for car emissions, land-use data for agricultural emissions and population density for urban emissions. All area sources emit at the lowest model level. The NEI does not include biomass burning emissions.

Emissions in the NEI have been compiled for the following gas species: SO_2, CO, NOx, NH_3, and grouped volatile organic compounds (VOC). The VOCs are further divided into 41 separate organic species. The proportion of each VOC species is determined by the source type. In addition to these gas emissions, primary aerosol $PM_{2.5}$ emissions are included and divided into 5 categories by composition. The categories are sulfate, nitrate, organic, elemental carbon, and unspeciated aerosol. Primary PM_{10} aerosol emission estimates are also included but not separated by composition.

All emissions from both point and area sources are inventoried on an hourly basis. For example, if traffic density increases in the morning hours, or if a power plant is typically shut down at night, the effects of these activities on emissions are included in the NEI. Hourly emissions represent particles and precursor gases released on a July weekday for area emissions, and an August weekday for point emissions. This could lead to inaccuracies

for estimates of non-summer emissions that vary with seasonally-dependent anthropogenic activities.

7.1.5 Biogenic emissions

The NEI does not consider natural emissions of aerosol precursor gases from vegetation, although these comprise a substantial fraction of global VOCs and are potentially a large source of particles (Heald et al., 2008). The emission of biogenic aerosol precursor gases is dependent on atmospheric conditions that vary on timescales much shorter than seasons. For example, isoprene emissions are connected to the process of photosynthesis and as a consequence, are dependent on solar radiation. Furthermore, emissions of isoprene and many other natural VOCs increase with increasing temperature (Seinfeld and Pandis, 2006). Biogenic VOC emissions also depend to varying degrees on the ambient humidity and wind speed, and are emitted at different rates by different species of vegetation (Guenther et al., 2006). Recently, the Model of Emissions of Gases and Aerosols from Nature (MEGAN; Guenther et al., 2006), a biogenic emissions module that accounts for these complexities, was introduced into the WRF/Chem framework. Some aspects of the interactions between MEGAN and other relevant modules within WRF/Chem are still under development, but emissions of monoterpenes and limonene, needed for biogenic SOA production in SORGAM, are operational.

MEGAN uses a simple formula for computing emission rates of various biogenic VOCs (Guenther et al., 2006). First, the emission rate for standard environmental conditions and for the particular compound and vegetation type in question is extracted from an inventory. This rate is then adjusted for deviations from those standard conditions

as reported by the model. Computation of the various environmental parameters needed for MEGAN emissions is carried out online in WRF/Chem. Finally, the emission is scaled by a canopy factor that accounts for the complexity of interactions between the emitted compounds and the forest canopy. The canopy factors are not well understood and introduce uncertainty into the inventory, even though they are based on a detailed inventory of leaf area index and foliage conditions that are climate-dependent.

7.2 Forecasts of κ

The WRF/Chem modules described in the previous section simulate the emission and gas to particle formation of aerosol mass for fourteen separate species, all of which contribute to model CCN. In-atmosphere dynamics that modify the particle number and size distribution are also represented using MADE. To review, this system predicts aerosol mass for each species and one aerosol size distribution median radius and particle number concentration containing all species at every grid point. The size and number information can be used directly by the RAMS droplet activation scheme, but a single-value representation of the particle composition using the κ parameter is still required. Here, the assumption of internally mixed aerosol in WRF/Chem is especially helpful.

To compute single-parameter composition for the model aerosol, κ is weighted by the volume of each component in the internal mixture and averaged according to Eq. 2.5. This computation requires values of ρ for each WRF/Chem aerosol species or species group to convert the predicted aerosol mass to volume. In addition, a value of κ must be assigned to each component to compute the weighted average. Values for both ρ and κ can be found

for specific species in the literature but several of the WRF/Chem species are not so easily defined.

For example, in MADE/SORGAM the reaction products of aromatic compounds are represented by two product groups. These groups presumably contain several different species with various values of ρ and κ. To simplify the many possible combinations of species, common products of aromatics for which the κ is known were chosen to represent the hygroscopicity of the whole group. For aromatics, phthalic and homophthalic acid were used. The proportions of the representative species were, in general, derived from measurements of Los Angeles area aerosol mass reported by Seinfeld and Pandis (2006). Table 7.1 contains the representative species selected for each model group and the reference for each selection.

Determining the proportions of ammonium-nitrate, ammonium-sulfate, and non-ammoniated nitrate and sulfate for computation of κ requires some calculation. The interactions of these compounds in the atmosphere, in both the particle and gas phases, are complex and require a thermodynamic model to describe them (Seinfeld and Pandis, 2006). MADE/SORGAM predicts sulfate, nitrate and ammonium/ammonia (NH3) interactions using the Model for an Aerosol Reacting System (MARS) as described by Binkowski and Shankar (1995). Aerosol mass is output separately into sulfate, nitrate or ammonium categories using this system. However, for computation of κ, the mass of the specific compounds produced by these interactions is needed. For instance, sulfate aerosol has a different hygroscopicity in its ammoniated form than when it exists as sulfuric acid. How much of the sulfate aerosol mass exists as ammonium-sulfate and how much as sulfuric acid?

Seinfeld and Pandis (2006) suggest a simple method for determining the proportions of ammonium-nitrate, ammonium-sulfate, and non-ammoniated nitrate and

sulfate. NH_3 favors neutralization of sulfate over nitrate when both are available. In light of this, Seinfeld and Pandis (2006) recommend assuming that all NH_3 reacts first with sulfate. Any remaining NH_3 is available to form ammonium nitrate. This simple approach is used to compute κ from the MADE/SORGAM output. One mole of ammonium aerosol is combined with two moles of sulfate aerosol to form one mole of ammonium-sulfate. If there is ammonium aerosol leftover, it is combined with nitrate aerosol in a 1:1 mole ratio. In cases where there is an insufficient amount of ammonium to neutralize all the sulfate or nitrate, non-ammoniated, "extra" sulfate and nitrate are considered to be sulfuric acid and calcium nitrate, respectively. These alterations of the model aerosol speciation are used simply for diagnosing κ and do not impact the MADE/SORGAM aerosol predictions.

Finally, κ and ρ must be defined for the two MADE/SORGAM aerosol groups with unspecified composition. Primary anthropogenic aerosol was assigned a κ=0.3 to represent typical continental, internally-mixed aerosol following the conclusions of Andreae and Rosenfeld (2008). This category includes emissions of soot (black carbon), industrial dust and small amounts of sulfate and nitrate particles. The primary organic aerosol group is more difficult to characterize. Seinfeld and Pandis (2006) report that primary organic aerosol collected from the Los Angeles urban area consisted mainly of alkanoic acids and dicarboxylic acids such as those shown in Table 7.1 under variable names ORGARO1, ORGARO2, and ORGALK. The κ values of these species groups were averaged to give the κ for primary organic aerosol. Values of ρ and κ for all model species and species groups are given in Table 7.2 along with associated references.

Table 7.1: A list of the prognostic aerosol mass variables in MADE/SORGAM and a description of the species each variable group includes. For the purpose of computing a constant value of κ for each composition variable, each variable is broken down into representative species with known κ.

Model species	Description	Representative species	Reference (Rep. species)
SO4	Sulfate aerosol mass	Sulfuric acid*	Seinfeld and Pandis (SP) (2006)
NO3	Nitrate aerosol mass	Calcium nitrate*	SP (2006)
NH4	Ammonium aerosol mass	Ammonium sulfate* Ammonium nitrate*	SP (2006)
ANTHA	Unspecified primary anthrop. aerosol mass	Internally mixed, continental aerosol	Andreae and Rosenfeld (2008)
ORGARO1	Reaction products of aromatic compounds (1)	Phthalic acid	SP (2006)
ORGARO2	Reaction products of aromatic compounds (2)	Homophthalic acid	SP (2006)
ORGALK	Reaction products of alkanes	Diesel exhaust Palmitic acid** Stearic acid	SP (2006)
ORGOLE	Reaction products of alkenes	Oleic acid** Adipic acid Glutoric acid Malonic acid Succinic acid	SP (2006)
ORGBA1	Reaction products of α-pinene (1)	Products of α-pinene	SP (2006)
ORGBA2	Reaction products of α-pinene (2)	Products of α-pinene	SP (2006)
ORGBA3	Reaction products of limonene (1)	Limonic acid	Virkkula et al. (1999)
ORGBA4	Reaction products of limonene (2)	Limononic acid	Virkkula et al. (1999)
ORGPA	Unspecified primary organic aerosol mass	Alkanoic acids Dicarboxylic acids	SP (2006)
EC	Elemental carbon aerosol mass	Diesel exhaust	Weingartner et al. (1997)
SEAS	Sea-salt aerosol mass	Sodium chloride	SP (2006)
SOILA	Mineral dust aerosol mass	Saharan dust	Koehler et al. (2009)

* The abundance of these species is determined by the availability of ammonium aerosol
** These species are given twice the proportional weight compared to the other species in the group in keeping with their observed proportions as reported by Seinfeld and Pandis (2006). This is done solely for the purpose of computing a representative value of κ for the grouped species.

Table 7.2: A list of the prognostic aerosol mass variables in MADE/SORGAM with the representative values of κ and ρ assigned to each. References for each assigned quantity are also given.

Model species	κ	Reference (κ)	ρ (g/cm^3)	Reference (Rho)
SO4	0.90**	Petters and Kreidenweis (PK) (2007)	1.80	MOSAIC (Fast et al., 2006)
NO3	0.51	Sullivan et al. (2009)	2.50	MOSAIC (Fast et al., 2006)
NH4 (sulfate)	0.61	PK (2007)	1.77	Svenningsson (2006)
NH4 (nitrate)	0.67	PK (2007)	1.72	Svenningsson (2006)
ANTHA	0.3	Andreae and Rosenfeld (2008)	1.65	-
ORGARO1	0.051	PK (2007)	1.49	Pang et al. (2006)
ORGARO2	0.094	PK (2007)	1.49	Pang et al. (2006)
ORGALK	0.005*	Virkkula et al. (1999) Raymond and Pandis (2002)	0.86	Pang et al. (2006)
ORGOLE	0.19	PK (2007)	1.46	Pang et al. (2006)
ORGBA1	0.10	Petters et al. (2009)	1.00	MOSAIC (Fast et al., 2006)
ORGBA2	0.10	Petters et al. (2009)	1.00	MOSAIC (Fast et al., 2006)
ORGBA3	0.08*	Virkkula et al. (1999) VanReken et al. (2005)	1.00	MOSAIC (Fast et al., 2006)
ORGBA4	0.08*	Virkkula et al. (1999) VanReken et al. (2005)	1.00	MOSAIC (Fast et al., 2006)
ORGPA	0.073	PK (2007)	1.49	Pang et al. (2006)
EC	0.02*	Weingartner et al. (1997)	1.7	MOSAIC (Fast et al., 2006)
SEAS	1.28	PK (2007)	2.17	Svenningsson (2006)
SOILA	0.04	Koehler et al. (2009)	2.6	MOSAIC (Fast et al., 2006)

* Figure was estimated from graphical data in the given reference
** This value for sulfuric acid was given by mistake in Petters and Kreidenweis (2007). The correct value has been found to be between 0.68-0.74 by Markus Petters, as cited by Shantz et al. (2008).

7.3 Method of coupling to RAMS

WRF/Chem forecasts of aerosol number concentration, mass, size distribution median radius, and κ, computed using the values in Table 7.2 and equation 2.5, were introduced into RAMS using an internal nudging scheme. At each RAMS grid point, and at a

user-specified time interval, the four aerosol quantities are updated, or nudged, using the following formula:

$$P_{new}(x,y,z,t) = P_{old}(x,y,z,t) + \left[P_{nud}(x,y,z,t) - P_{old}(x,y,z,t)\right] * n_{fac} \quad (7.1)$$

where P_{old} is the value of a generic variable prior to being updated by the nudging value P_{nud}, and P_{new} is the updated variable. The nudging factor, n_{fac}, is used to scale the magnitude of the nudging and prevent large jumps in variable values during the nudging timestep. The aforementioned aerosol quantities are nudged for RAMS coarse mode and accumulation mode aerosols. WRF/Chem predicts aerosol number and mass for Aitken mode aerosols as well but only one mode may be passed through the RAMS droplet activation lookup tables and, because of their small sizes, these aerosols are not likely to be as important in CCN prediction as accumulation mode aerosols. Coarse mode aerosols are not passed through the lookup tables but are assumed activated at a 100% rate in a supersaturated environment.

WRF/Chem and RAMS use different vertical coordinate systems so a linear interpolation scheme was setup to accommodate the vertical level change. In between nudging time steps, particles in RAMS are advected by the model wind but no aerosol dynamics or chemical processes, including emissions, are treated. Therefore, it is recommended that aerosol variables within RAMS be tightly constrained by the WRF/Chem forecasts using a high nudging factor (n_{fac}=0.2) and high nudging frequency of every 5 minutes.

Differences in meteorology and cloud processes between WRF/Chem and RAMS predictions could lead to inconsistencies in the aerosol fields, a clear disadvantage of running the aerosol code offline with respect to RAMS. This becomes especially important

in precipitating regions where aerosol scavenging occurs. Wet deposition is not represented in the version of WRF/Chem described above, which could lead to underestimates of total deposition rates in some areas and overestimates of the aerosol burden. Therefore, even if RAMS correctly removes particles from the atmosphere during a precipitation event, the nudging constrains the aerosol to possibly inaccurate WRF/Chem output. Under the current offline setup, the only strategy available for minimizing this potential error is to avoid simulations with widespread precipitation upwind of the region of interest.

7.3.1 Treatment of dust and sea-salt aerosols

Dust and sea-salt aerosols play a locally important role in aerosol/cloud interactions especially by acting as GCCN and IN. Currently, WRF/Chem does not treat emissions of dust or sea-salt, even though MADE/SORGAM includes variables to accommodate these species. Emissions of these compounds have recently been included in RAMS using the dust source model of Ginoux et al. (2001) (added to RAMS by Smith, 2007) and wind-speed dependent sea-salt emission formulas from O'Dowd et al. (1997).

Making the accumulation mode dust and sea-salt particles cloud-active is an area of future work. These aerosols will have different size distribution median radii than the WRF/Chem predicted aerosols, typically larger. But the droplet activation scheme is not set up to predict droplet number on multiple aerosol distributions at one time. To send multiple size distributions though separately at the same model time and space would require neglecting competition for water vapor between the aerosol populations. Ghan et al. (1998) tested the effects of competition between distributions of sulfate and sea-salt

aerosols using a parcel model. They found a complex response in the droplet activation to parameter variations in the competing modes. Adding coarse mode sea-salt reduced the activated droplet number because of a decrease in the SS_{max}, while adding accumulation mode sea-salt increased the activated droplets simply by increasing the number of particles available. More recent parcel model simulations by Segal et al. (2007) suggest that the importance of this effect for determining SS_{max} and droplet activation is overestimated. They report that the addition of large CCN to an existing distribution of smaller CCN had only a minor impact on CDNC due to competition effects. The impact was, in any case, secondary to the effect of the increase in the droplet collision rate caused by the presence of the large CCN.

For this work, dust and sea-salt are not microphysically active in RAMS. Number concentrations of these aerosols in western Colorado in the wintertime are typically small when compared to the number concentration of the WRF/Chem aerosols, perhaps making the neglect of dust and sea-salt CCN acceptable. For future simulations in locales where dust or sea-salt are important contributors to the CCN number, the effects of competition need to be parameterized in the RAMS droplet activation scheme.

7.4 Summary

To summarize, modules within the WRF/Chem framework were used to form a system for modeling aerosol evolution in the atmosphere beginning at emission by anthropogenic or biogenic sources. Emissions of aerosols and aerosol precursor gases are described by the NEI and MEGAN emission inventories. RACM treats the gas-phase chemistry that converts emissions into low-volatility products that can form aerosol mass.

The gas-particle partitioning, as well as physical processes such as aerosol coagulation and deposition, are included in MADE/SORGAM. Aerosols are separated into 3 lognormal distributions and predicted as a single population on number and size. Aerosol mass is predicted for 14 species and species groups within this system. The κ parameter is computed as a volume-weighted average of all 14 aerosol components and assuming an internal aerosol mixture.

The value of κ is then passed to RAMS along with the aerosol number and median radius. Internal nudging connects the WRF/Chem output to RAMS aerosol variables, which are transported on the RAMS model wind and passed to the droplet activation code.

The end result is a system for predicting CCN and CDNC in RAMS based on model estimates of aerosol properties, including composition. There are several limitations in this scheme as described, but the design improves on the existing method of predicting CDNC in RAMS. The existing method, as mentioned in Chapter 3, consists of user-prescribed aerosol number and size. The aerosol size and composition remain fixed throughout the simulation and the particle number field evolves only through transport and deposition. By integrating the WRF/Chem output and RAMS, even offline, CDNC predictions for the first time in RAMS represent the temporal and spatial variability of the ambient aerosol. As stated by Gustafson et al. (2007), "…a prescribed CCN distribution allowing for vertical and temporal fluctuations does substantially better in simulating cloud properties and radiative effects than does a prescribed uniform and constant CCN distribution."

In the next chapter, results from the new WRF/Chem and RAMS modeling system are presented and compared to CCN observations to demonstrate the improvement over the existing scheme.

Chapter 8

Validation of RAMS and WRF/Chem CCN prediction

Validation, as the term is used here, refers to the comparison of numerical predictions to observations of similar quantities as a means of evaluating model performance. These evaluations are an important part of the testing of a new modeling system. The WRF/Chem system described in the previous chapter has not undergone validation on a consistent basis due to its modular nature and the number of module options available to users. With WRF/Chem, research is often carried out with the combination of modules that suits the individual needs of the researcher and may not be comparable to other studies that used a different combination within the same model.

On the other hand, the various modules within WRF/Chem have all been individually validated to some extent. For example, three major validation studies of WRF/Chem (Grell et al., 2005; Fast et al., 2006, Zhang, 2008) have opted to run an alternative chemical mechanism to RACM, which is used in the current study. But RACM has been evaluated extensively outside of the WRF/Chem framework. It was introduced by Stockwell (1997) and was used by Arteta et al. (2006) as a reference mechanism for

evaluation of a simplified scheme embedded in RAMS. Questions remain about the performance of RACM in conjunction with the other WRF/Chem modules, but like those other modules RACM has been evaluated as a stand-alone model.

It is, therefore, not the purpose of the work presented in this chapter to evaluate the WRF/Chem aerosol forecasts directly as this has been done in the past, albeit in a piecemeal sense. Instead the aim of the following chapter is validation of the new aspects of the WRF/Chem and RAMS system. This will include addressing several questions about the prediction of CCN, such as when and under what conditions does the model perform best when compared to observations? What situations are associated with under or over forecasting of CCN and what appears to be the underlying cause? Answers to these questions can be combined to define conditions under which the new modeling system is valid for future simulations. That is the chief purpose of this validation.

RAMS forecasts of CCN will be evaluated against two different datasets of CCN observations. First, the evolution of the model CCN field in time will be compared to a time series of N_{ccn} from SPL. Secondly, aircraft measurements of CCN along the Front Range collected during the Ice in Clouds Experiment – Layer Clouds (ICE-L) field campaign will be used to test the ability of the model to predict vertical variations in CCN. This is one of the first attempts to compare predictions of CCN from a regional-scale model of this kind directly to observations. As Andreae and Rosenfeld (2008) write, coupled, or to use their term, integrated aerosol and microphysics models are only now beginning to be developed and validation of such models is in its early stages.

8.1 Storm Peak Lab time series case

The application of the new model system in this study centers on western Colorado locations. For that reason it is of interest to test the performance of the code in this region. Previous validation work using WRF/Chem, McKeen et al. (2007) in particular, suggest that organic aerosol mass will be underpredicted in the western Colorado due to its rural setting. Also, since large sources of sulfur dioxide are local to the region of interest, the production of sulfate aerosol may proceed too slowly in conditions that favor aqueous phase sulfate formation. A late winter, relatively cloud-free case was selected to minimize the potential impacts of aqueous production of sulfate. Cases for which the region's sky was completely cloud-free did not occur during the period for which CCN data were available. Although, cloud events at SPL can be considered an opportunity to test the model near clouds even if poor performance is expected.

Observations of CCN number concentration were collected at SPL from April 1-14, 2008. A DMT CCN-100 was operated continuously at five values of SS (0.1%, 0.2%, 0.3%, 0.4%, 0.6%) and rotated SS settings every 5 minutes. These data were supplemented with particle number measurements and size distribution data from an SMPS that covered a range of particle diameters between 0.0087 and 0.34 μm.

For model validation, the most cloud-free portion of the measurement period, from 00:00 GMT April 1 to 00:00 GMT April 5, was selected. 500mb height winds were generally westerly during the first half of the four-day time period shifting to southwest and finally northwest by April 4th with the passage of an upper level trough on April 3rd. 500mb heights that demonstrate these patterns are shown in Figures 8.1 to 8.4. Data from the NARR dataset were used to plot these figures which correspond to 00:00 GMT on each day in the time period. The NARR cloud fraction product is also plotted in Figures 8.1 to 8.4.

The cloud fraction shows the percentage of each grid box that contained cloud at any level at the specific time plotted. For these purposes, the cloud fraction product better defines days when the region was cloud-free since the plotted clouds could be at any level.

Figures 8.1 and 8.4 show cloud-free conditions (cloud fraction < 30%) at SPL and for several hundred kilometers upwind at 500mb. At 00:00 GMT on April 2nd, the NARR data indicate scattered clouds within a large area at SPL and to the west (Figure 8.2). And at 00:00 GMT on April 3rd, a small area of high cloud fraction is apparent just to the west of SPL (Figure 8.3). These clouds were associated with a surface cold front that passed SPL from the northwest to southeast at 03:00 GMT on April 3rd. No precipitation fell at SPL during the four-day test period.

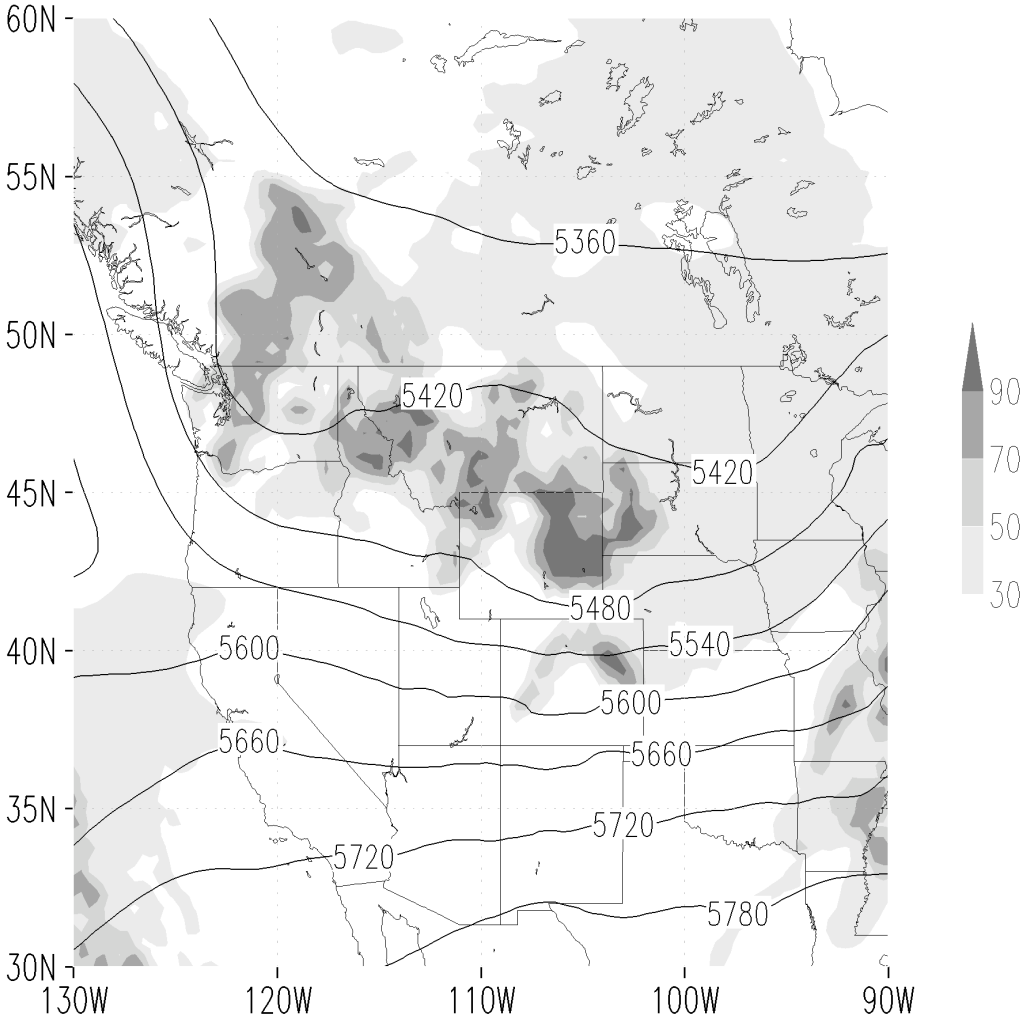

Figure 8.1: 500mb geopotential height (contours; gpm) and grid cell cloud fraction (shaded; %) from the NARR dataset for 00:00 GMT April 1, 2008.

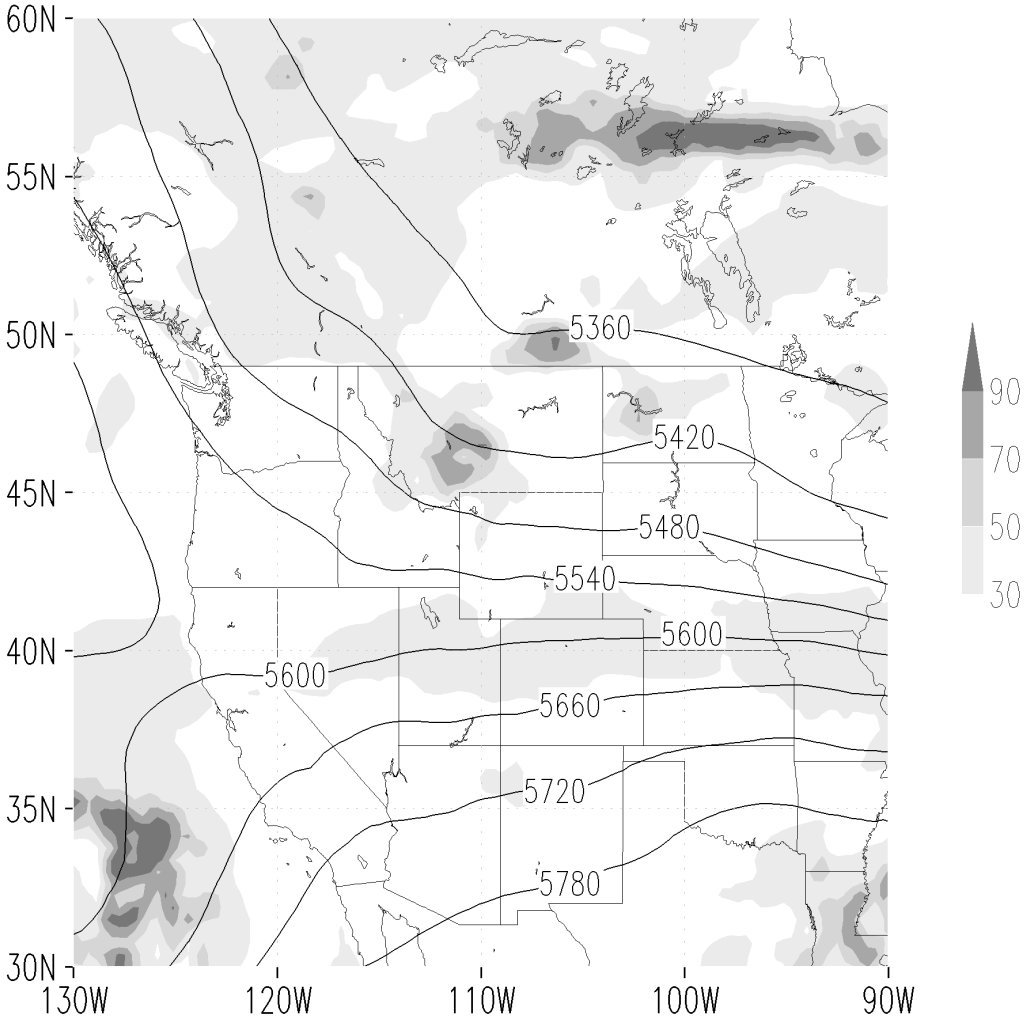

Figure 8.2: 500mb geopotential height (contours; gpm) and grid cell cloud fraction (shaded; %) from the NARR dataset for 00:00 GMT April 2, 2008.

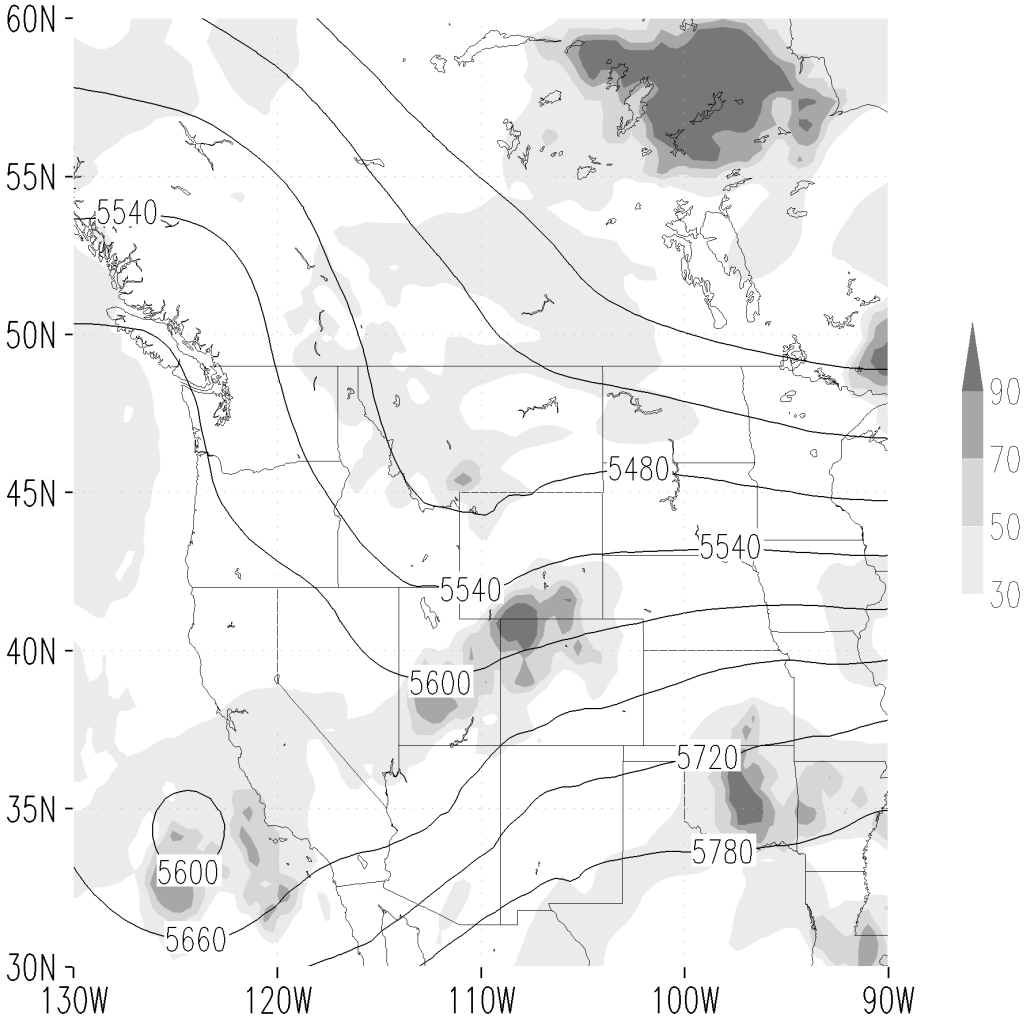

Figure 8.3: 500mb geopotential height (contours; gpm) and grid cell cloud fraction (shaded; %) from the NARR dataset for 00:00 GMT April 3, 2008.

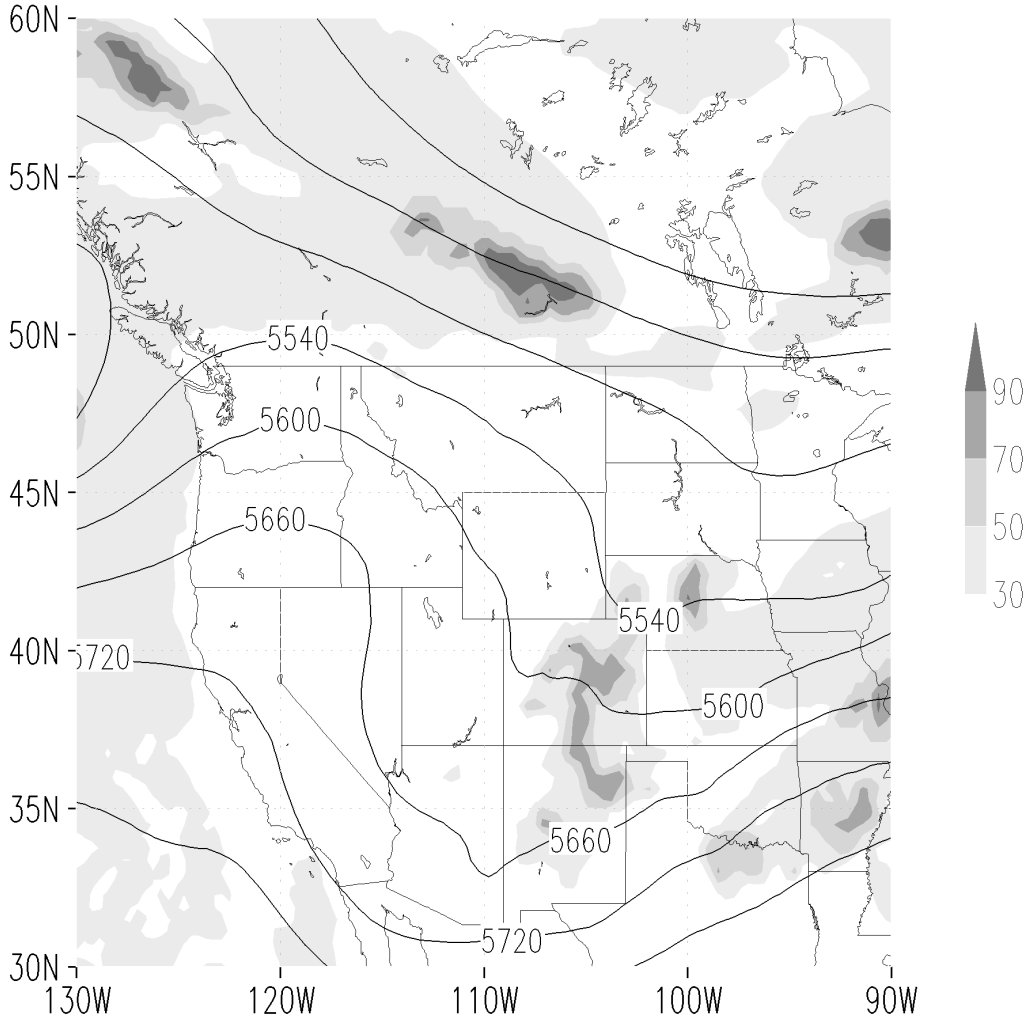

Figure 8.4: 500mb geopotential height (contours; gpm) and grid cell cloud fraction (shaded; %) from the NARR dataset for 00:00 GMT April 4, 2008.

8.1.1 Model setup

To simulate CCN at SPL during this case, both WRF/Chem and RAMS were run for 120 hours from 00:00 GMT on March 31, 2008 to 00:00 GMT on April 5, 2008. Identical

horizontal, polar stereographic grids were used in both models with a grid spacing of 6km in the region of interest surrounding SPL. To achieve this grid spacing over SPL, a two-grid system was set up. The outer grid was set to a horizontal grid spacing of 24km. The location and extent of both grids are shown in Figure 8.5 and grid specifics are given in Table 8.1. WRF/Chem and RAMS use different vertical coordinates but the vertical spacing

Table 8.1: Horizontal grid settings for both case study simulations. These apply to both WRF/Chem and RAMS.

Setting	SPL Grid 1	SPL Grid 2	ICE-L Grid 1	ICE-L Grid 2
Grid points (X x Y)	100 x 85	100 x 90	120 x 100	90 x 100
Horizontal spacing	24km	6km	16km	4km
Center latitude (˚N)	40.0	40.0	39.0	40.5
Center longitude (˚W)	112.0	108.5	109.0	103.5

was set up similarly in each for these simulations. RAMS was set up on 35 vertical levels with a minimum spacing of 100m at the surface. The spacing is stretched by a factor of 1.1 for each subsequent level until reaching a maximum spacing of 2000m. WRF/Chem was run with 27 vertical levels, dictated by the pre-processing program. These levels rise linearly with pressure and in this way they are stretched, similar to the levels in RAMS, with higher vertical resolution in the planetary boundary layer (PBL).

Other WRF/Chem settings of interest are given in Table 8.2. Transport within the PBL is parameterized in WRF/Chem with one of several available schemes. The PBL transport parameterization developed by Hong and Pan (1996), sometimes referred to as the Yung Sun University (YSU) scheme (McKeen et al., 2007), was used for this study. McKeen et al. (2007) found that the YSU scheme decreased model bias in $PM_{2.5}$ amounts when compared to results using a different scheme. Biomass burning and emissions of DMS were inactive for these simulations.

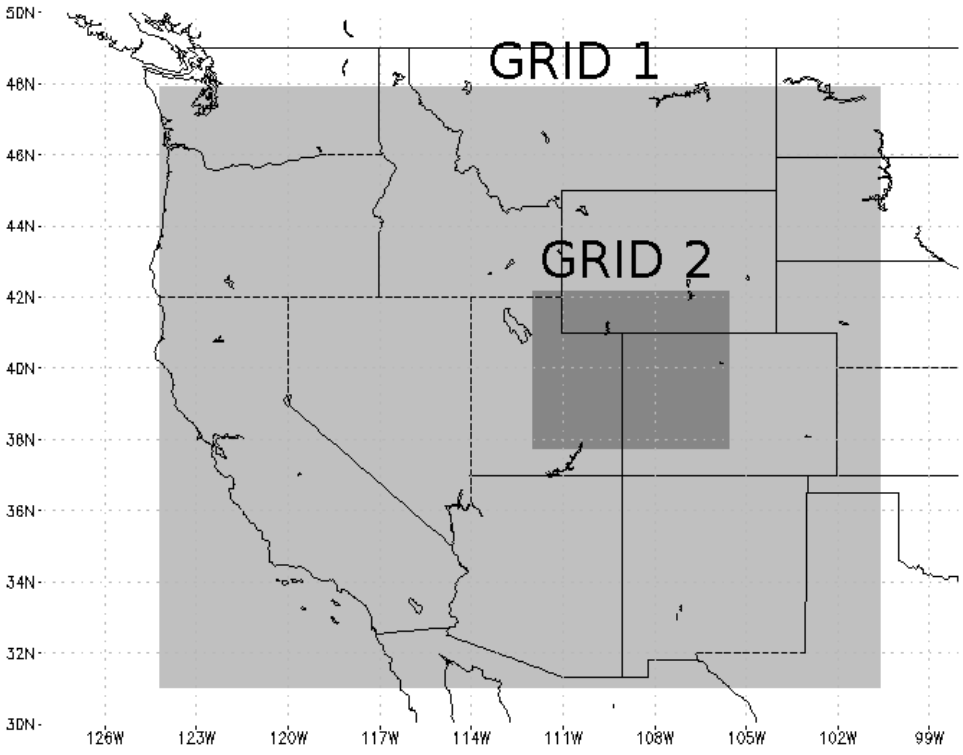

Figure 8.5: Grid setup for the SPL case study simulations. This setup was used both for WRF/Chem and for RAMS.

RAMS was set up with parameters similar to those used in Chapter 4. These are listed in Table 8.3. Instead of using constant aerosol κ and size distribution median radius, as well as user prescribed N_{cn}, as in Chapter 4, these variables are nudged to the WRF/Chem predictions. Note that RAMS is initialized and nudged with the NARR dataset instead of the high resolution (40 km) meteorological data from the Eta model analysis used with WRF/Chem. CCN were output from RAMS at SS=0.3%, 0.4%, 0.6% and 1.0% at a temperature of 25˚C.

Table 8.2: Important settings used in WRF/Chem to provide the aerosol forecasts for the RAMS simulations described in this chapter.

Setting	Description
Dynamical core	Advanced Research WRF (ARW) (Grell et al., 2005)
Microphysics	Single-moment, bulk microphysics; Lin et al. (1983) scheme
Radiation	Shortwave: Dudhia scheme (Dudhia and Moncrieff, 1989) Longwave: RRTM (Mlawer et al., 1997)
Surface boundary	Monin-Obukhov (Janjic) scheme
Top boundary	Rigid lid with damping layer
Time step	20 seconds
Meteorological nudging	Eta analysis dataset
PBL	YSU scheme (Hong and Pan, 1996)
Chemical mechanism	RACM (Stockwell, 1997)
Aerosol option	MADE/SORGAM (Schell et al., 2001)

Table 8.3: Important settings used in RAMS for all simulations in this chapter

Setting	Description
Microphysics	Two-moment bulk as in Saleeby et al. (2009) (Meyers et al., 1997) Single cloud droplet mode
Turbulence closure	Horizontal: TKE - based on Smagorinsky (1963) Vertical: Mellor and Yamada (1982)
Radiation	Two-stream (Harrington, 1997) Aerosol radiative feedback (Stokowski, 2005)
Surface boundary	LEAF-2 (Walko et al., 2000)
Top boundary	Rigid lid with damping layer
Time step	10 seconds on Grid 1, 2.5 seconds on Grid 2
Meteorological nudging	NARR dataset, nudging at lateral and top boundary at 15-minute intervals

8.1.2 Model results compared to observations

After RAMS ran through the 120-hour simulation time, CCN predictions were extracted from the point on the inner grid nearest to the latitude and longitude of SPL. The surface elevation at this grid point was 404m below the reported elevation of SPL. RAMS output from vertical level 4 (396m agl) was considered the best approximation to the lab location and elevation. While the lab is at the surface, its location on a mountaintop means that it often samples free tropospheric air (Borys and Wetzel, 1997) and the above-surface model level should be more representative of free tropospheric air.

A time series of the CCN predicted by RAMS at the SPL location is plotted with the observed CCN at SPL in Figure 8.6. Measurements and predictions at SS=0.4% are shown. RAMS captured the timing of the high CCN event that occurred at and after 00:00 MST on April 3rd, but in general, RAMS overpredicted CCN at SPL during this case with an average N_{ccn}=492 cm^{-3} compared to the observed average N_{ccn}=305 cm^{-3}. The most extreme example of the overprediction occurred on April 2nd. Near 00:00 MST on April 2nd, RAMS predicted a high CCN event with N_{ccn} nearly 6 times higher than the observed N_{ccn} of approximately 200 cm^{-3}. The predicted event is short-lived with N_{ccn} returning to more reasonable values after about 6 hours. During this event, RAMS (nudged from WRF/Chem) forecasted high particle numbers of above 4000 cm^{-3}, which compare well to the average observations at that time (as counted by the SMPS; see Figure 8.7) but the event occurred 2-3 hours later in the model than was observed. Moreover, the predicted activated fraction was greater than 30% during this event, compared to the observed activated fraction of about 10% (Figure 8.8). In fact, Figure 8.8 shows a general high bias in the model activated fraction.

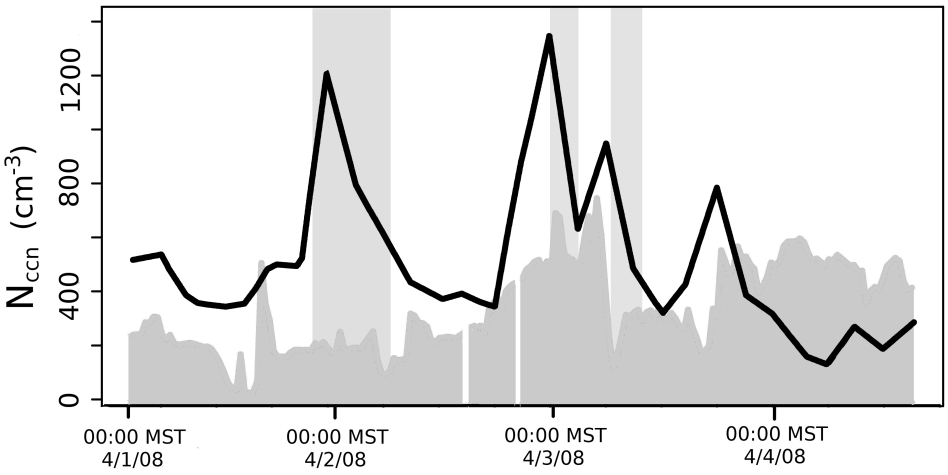

Figure 8.6: Time series plot of N_{ccn} observed at SPL (shaded) and predicted by RAMS (solid line) in units of cm^{-3}. Times when SPL measured a RH in excess of 96% are shaded in light grey to represent possible in-cloud events.

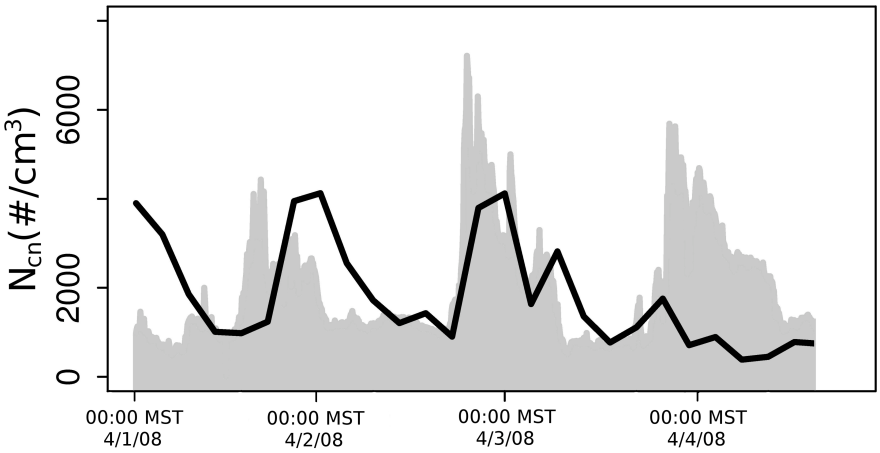

Figure 8.7: Time series plot of N_{cn} observed at SPL (shaded) and predicted by RAMS (solid line) in units of cm^{-3}.

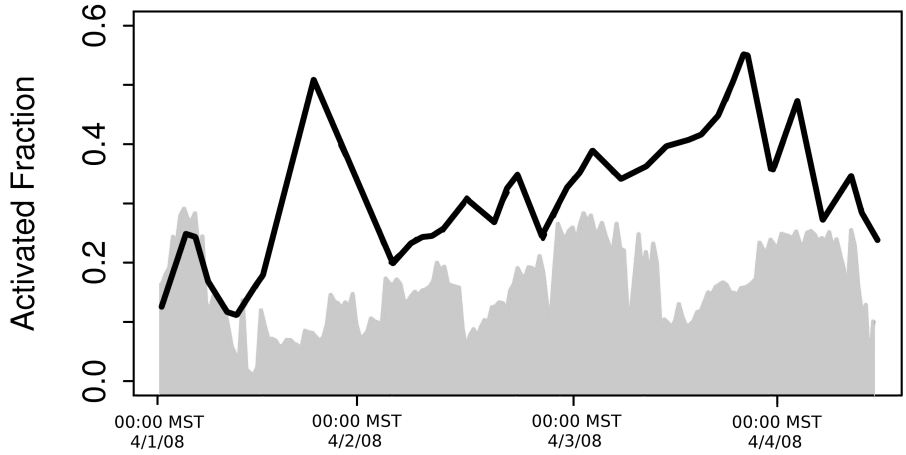

Figure 8.8: Time series plot of activated fraction observed at SPL (shaded) and predicted by RAMS (solid line). The N_{ccn} measured and predicted at SS=0.4% was used in computation of the activated fraction.

Since we prescribe the T and SS for model prediction of Nccn and assume these replicate the CCN-100 instrument conditions, the high bias must be a result of overestimating r_g and/or κ. Of course, the discrepencies between model and observations likely result in part from the assumptions made in the model setup, such as the simplified lognormal size distribution representation. Since the purpose of this validation is to identify model biases that can be used to qualify future use of this modeling system, it would be instructive to investigate how the coupled models performed with regards to prediction of r_g and κ.

Figure 8.9 shows the timeseries of r_g for model predictions and observations. The observed r_g was computed using the method of maximum likelihood as done in Chapter 4. Here, only the SMPS size-differentiated aerosol measurements were used. The resulting size distributions were remarkably similar to those observed during January and February of 2007 (see Chapter 4), especially considering the much shorter time period analyzed in

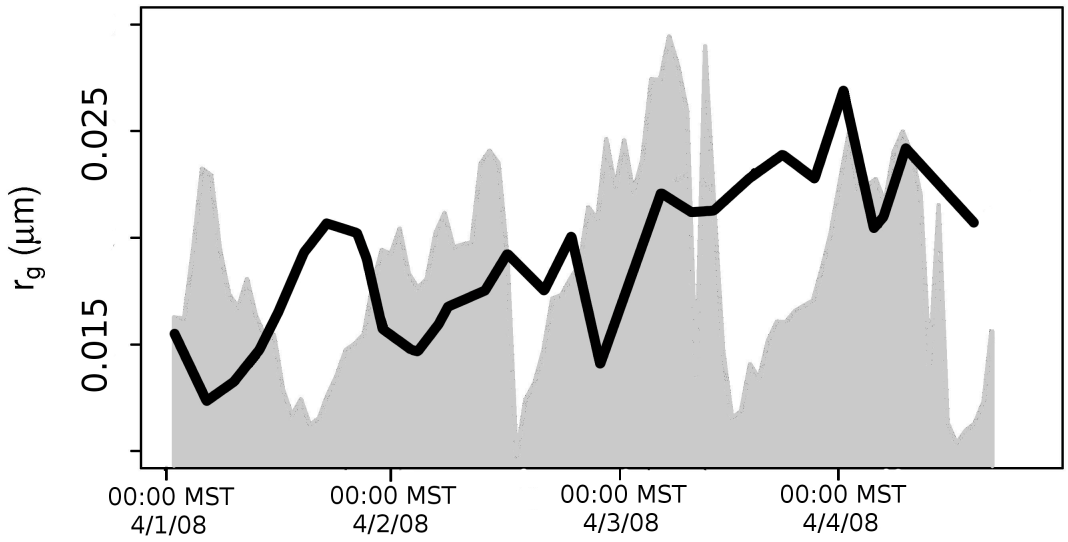

Figure 8.9: Time series plot of r_g estimated from the SMPS observations at SPL (shaded) and predicted by RAMS (solid line) in units of microns.

this case. The average size distribution was characterized by a single Aitken size mode with an estimated average r_g=0.018 μm. The two timeseries in Figure 8.9 correspond very little and are not well correlated but there does not appear to be any bias in r_g for this case. The average RAMS r_g=0.019 μm was nearly equivalent to the observed r_g.

To examine possible bias in model predicted aerosol hygroscopicity, κ was estimated from the observations using the reverse CCN closure method described in Chapter 4 and in Ward et al. (2010). The time series of the estimated κ is plotted with the RAMS κ output in Figure 8.10. Here a high bias in κ is clear, the model κ averages about 60% higher than the observed. This could help explain the consistently high activated fraction produced by RAMS and WRF/Chem for the SPL case, but what is driving the high κ values? To investigate the source of the κ bias, the WRF/Chem output of aerosol mass concentration for individual species was examined.

Different species are plotted by fraction of the total $PM_{2.5}$ mass in Figure 8.11. Note that this output is direct from WRF/Chem since the individual species are not forecast in

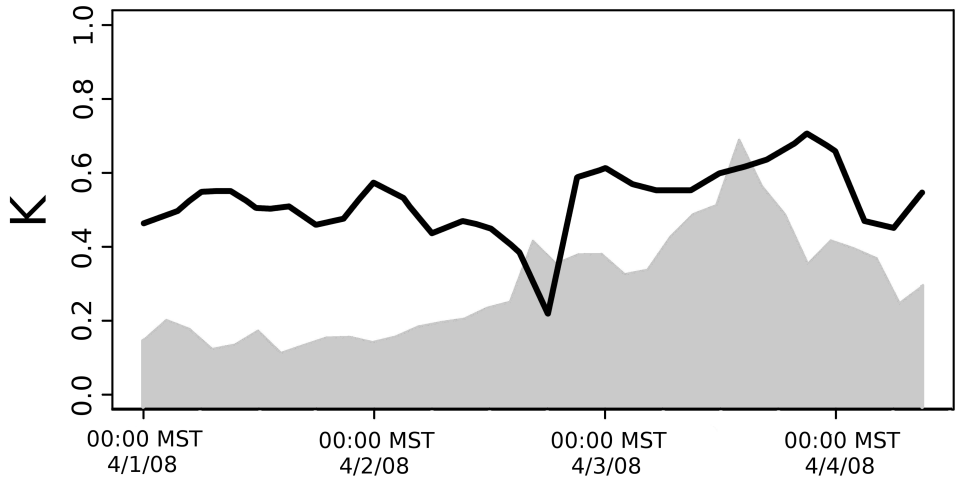

Figure 8.10: Time series plot of κ estimated from the SMPS observations at SPL (shaded) and predicted by RAMS (solid line).

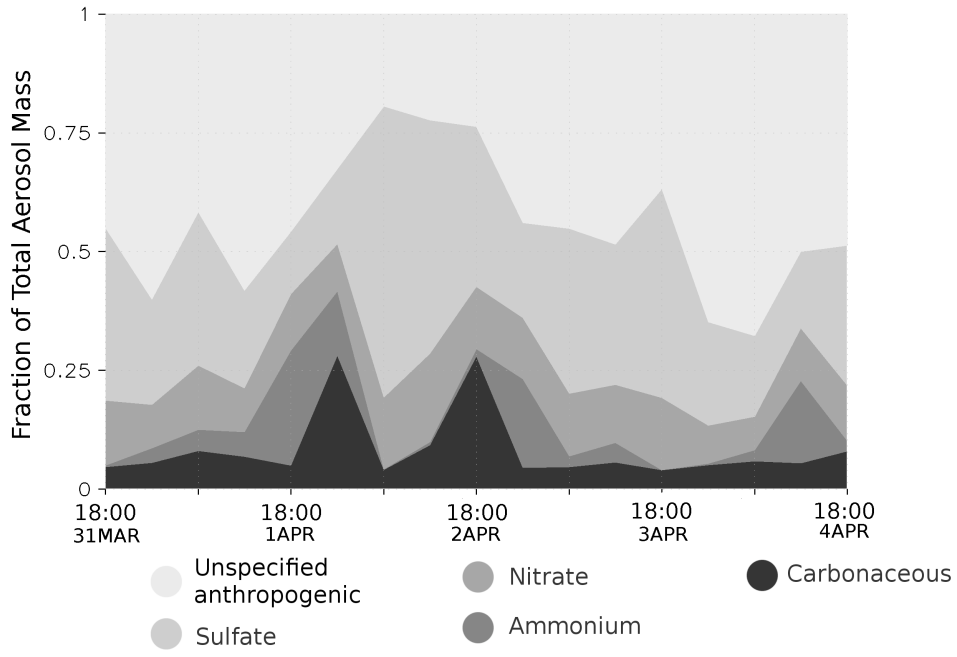

Figure 8.11: Time series plot of aerosol mass fraction for the various species predicted by WRF/Chem. The proportion of species is compared to the total accumulation mode aerosol mass to compute the mass fraction. Note that this plot uses WRF/Chem output directly and that the times are in MST.

RAMS. All carbonaceous species are shown as one category because they made up such a small portion of the total aerosol mass. Instead, the predicted aerosol mass concentration consists largely of sulfate and unspecified primary anthropogenic aerosol. The unspecified category accounted for an average of 50% of the total aerosol mass concentration for this case (Figure 8.11). Together, the domination of the unspecified aerosol and inorganic aerosol explain the high predicted κ. Whether the dominance of these compounds is realistic for SPL during this case can be addressed by comparing the WRF/Chem speciation to IMPROVE measurements from the nearby Mt. Zirkel site.

Particles were sampled at the Mt. Zirkel IMPROVE site for 24 hours beginning at midnight local time on April 2, 2008. Results of the analysis are given in Table 8.4 and show a higher ratio of carbonaceous aerosol to inorganic aerosol mass fraction when compared to the WRF/Chem output. A higher organic mass fraction would act to decrease the model κ in this case.

Table 8.4: Composition of $PM_{2.5}$ aerosol mass analyzed by the IMPROVE project. The aerosol samples were collected for the 24-hour period beginning at 00:00 MST at the Mt. Zirkel IMPROVE site near SPL. The estimated hygroscopicity of this composition, using representative species from Chapter 7, would be approximately κ=0.3.

Species	**Mass Concentration ($\mu g/m^3$)**	**Mass fraction**
Ammonium nitrate	0.75	0.17
Ammonium sulfate	1.1	0.25
Elemental carbon	0.08	0.02
Organic carbon	0.57	0.13
Sea-salt	0.09	0.02
Soil-derived	1.76	0.41

The IMPROVE composition analysis suggests the presence of large amounts of dust aerosol on April 2nd (Table 8.4). Recall that dust is not microphysically active in these simulations, meaning it does not contribute to the online computation of κ. Yet, dust mass and number concentrations are predicted in RAMS so its potential impact on the model κ can be estimated. During the validation period, RAMS predicts a significant dust event in the SPL and Mt. Zirkel area. Dust number concentration above 200 cm^{-3} were predicted on April 1st and steadily decreased to about 50 cm^{-3} by 00:00 MST April 4th. Using the RAMS dust aerosol mass information, κ was recomputed offline to represent the hygroscopicity of an aerosol internal mixture that included dust. The resulting time series is shown in Figure 8.12. Values of κ decreased due to the presence of dust and its low hygroscopicity. The decrease is more drastic during the beginning of the period when dust mass was greatest. The assumption of internally mixed aerosols is probably inaccurate here since the dust number concentration was relatively small compared to the WRF/Chem internally mixed aerosol and the dust particles are in general much larger. Still, the exclusion of dust from the online computation of κ contributed to the high bias in κ during this case.

It is of interest to note that SPL was likely in-cloud at the time of the April 2nd model overprediction. Time periods during which the RH measured at SPL was greater than 96%, indicative of the presence of cloud, are shaded in Figure 8.6. It is possible that the neglect of cloud-active aerosol and wet scavenging in WRF/Chem contributed to the overprediction of N_{cn} during the April 2nd event.

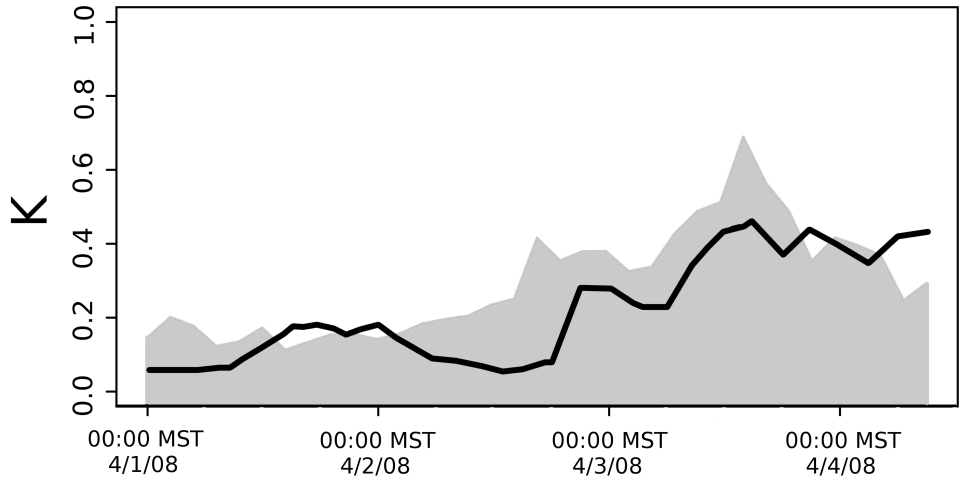

Figure 8.12: Time series plot of κ estimated from the SMPS observations at SPL (shaded) and predicted by RAMS with the impact of predicted dust mass on κ included (solid line).

8.1.3 Constant κ simulation

Since RAMS exhibited a high bias with respect to κ within the SPL simulation, it was rerun with an identical setup but with a constant value of κ=0.3. The purpose of this simulation was to test the sensitivity of the CCN prediction to changes in κ. The time series of N_{ccn} at SS=0.4% near SPL is shown in Figure 8.13 for the constant κ simulation. As expected with the generally lower κ, the simulation resulted in lower N_{ccn} than when κ was nudged with WRF/Chem output (see Figure 8.6). The trends in CCN remain the same between both simulations but the magnitudes more closely match the observations with the constant κ. Of course, this result is case-specific.

The analysis in Chapter 3 showed that the sensitivity of N_{ccn} to changes in aerosol hygroscopicity, represented by κ, increases with decreasing SS and with decreasing r_g

(using the single lognormal mode size distribution). The model output presented in this chapter can be used to test this premise. The sensitivity of N_{ccn} to changes in κ is again expressed using the Feingold (2003) sensitivity parameter S(κ) as in Eq. 3.1. The time series of this quantity is plotted for CCN predicted on all four simulated values of SS at the grid point nearest to SPL (Figure 8.14). S(κ) increases as SS decreases, which is consistent with the Chapter 3 analysis, as well as the results of Ervens et al. (2007) and Reutter et al. (2009).

The sensitivity parameter fluctuates with time with a peak near 00:00 MST on April 3rd and minima closer to the end of the time series. The relationship between S(κ) and r_g proposed in Chapter 3 suggests that the fluctuations could be due to changes in model r_g. In fact, the S(κ) (for SS=0.4%) is inversely correlated with the model r_g time series (Pearson correlation coefficient, r=-0.58). The relationship can be seen in the scatterplot of model r_g vs. κ sensitivity (Figure 8.15).

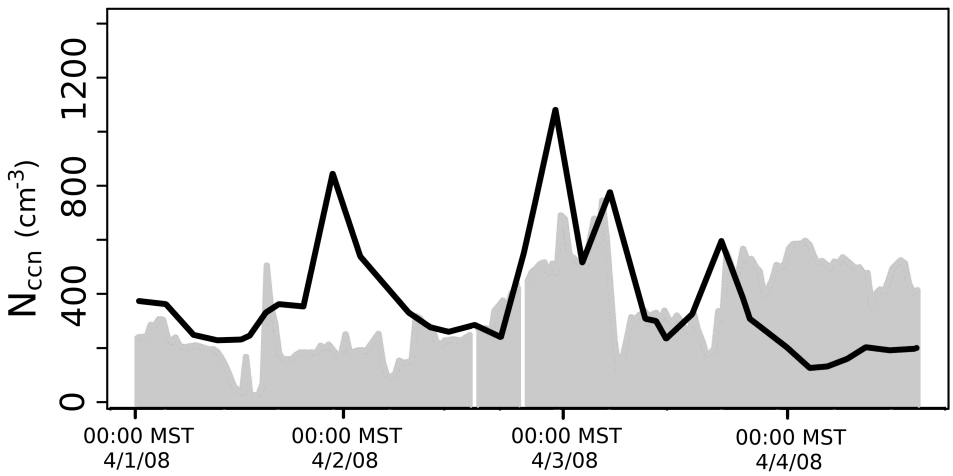

Figure 8.13: Time series plot of N_{ccn} observed at SPL (shaded) and predicted by RAMS (solid line) in units of cm^{-3} for a simulation in which κ was held constant at κ=0.3.

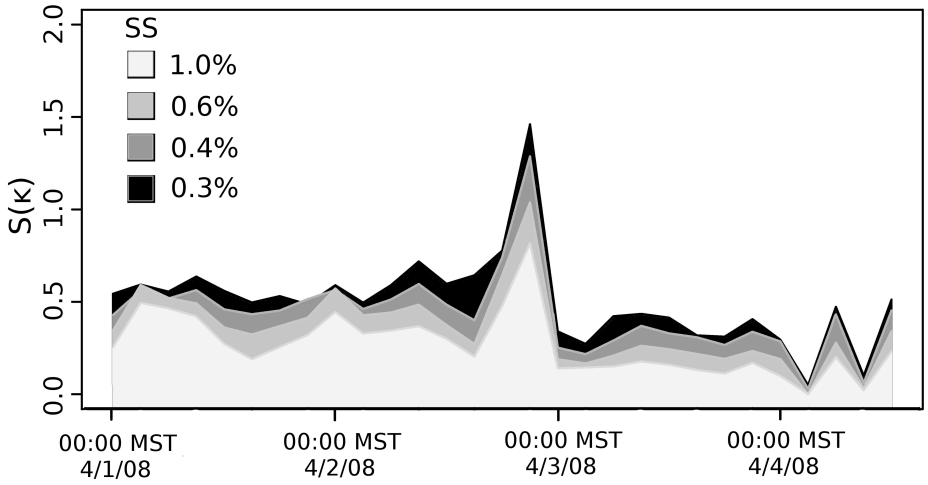

Figure 8.14: Time series of the sensitivity parameter S(κ) computed from the differences between RAMS forecasts of N_{ccn} and κ for the WRF/Chem nudged κ and constant κ simulations.

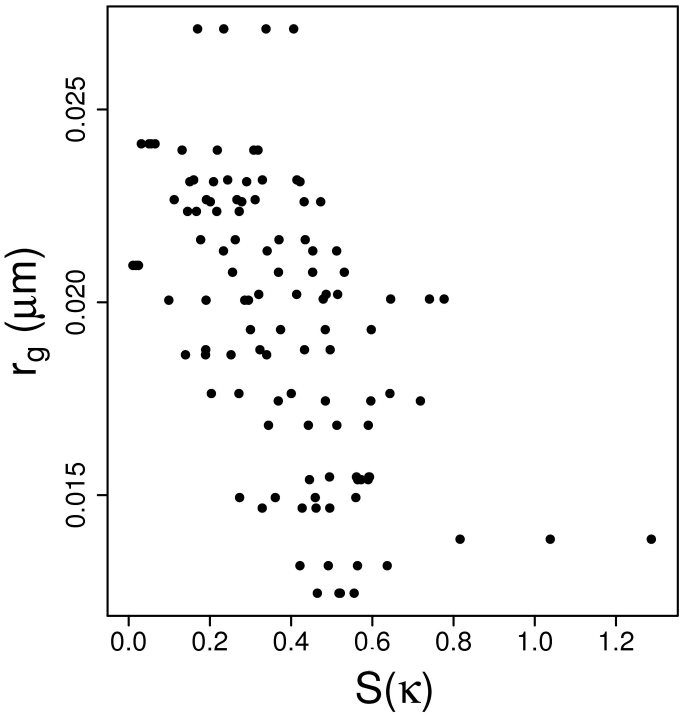

Figure 8.15: Scatterplot of S(κ) as computed for Figure 8.14 vs. the time corresponding r_g from the WRF/Chem nudged κ RAMS simulation.

8.1.4 Comparison to old CCN scheme

To compare the new, nudged CCN forecasting scheme with the old prescribed scheme, an additional two-grid simulation was run without the benefit of the WRF/Chem aerosol forecasts. Initial particle number concentration was set to 3000 cm^{-3} and κ and r_g remained constant throughout the simulation at κ=0.3 and r_g=0.04μm. In all other respects this simulation was identical in set up to the simulation described in the previous chapter.

The time series of N_{ccn} at SS=0.4% using the old scheme is shown in Figure 8.16. The variability in N_{ccn} that was observed at SPL is not captured using the prescribed aerosol quantities. On the other hand, the high bias introduced by the WRF/Chem aerosol forecasts for this case is not an issue when using the old scheme.

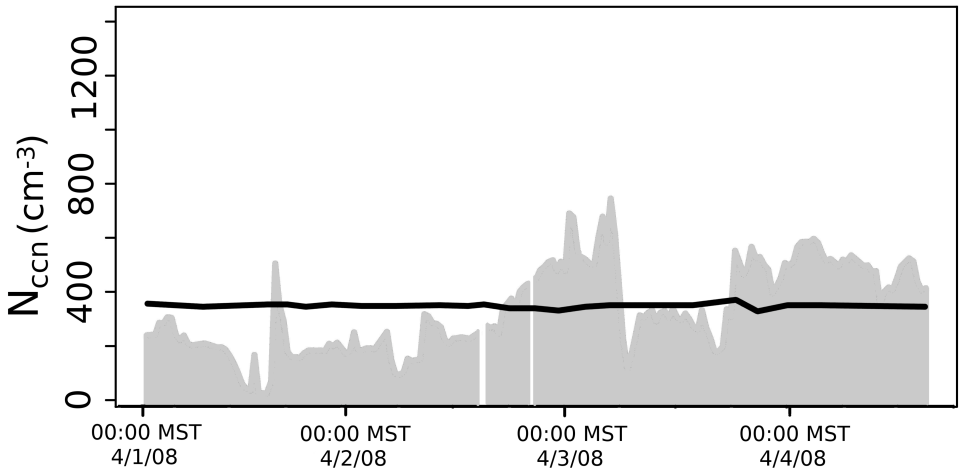

Figure 8.16: Time series plot of N_{ccn} observed at SPL (shaded) and predicted by RAMS (solid line) in units of cm^{-3} for a simulation in which the old aerosol scheme was used. Aerosols were initialized with a number concentration of 3000 cm^{-3}, κ=0.3 and r_g=0.4μm.

8.2 ICE-L vertical profiles case

In November of 2007, CCN were counted aboard the National Center for Atmospheric Research (NCAR) C-130 aircraft along the Colorado Front Range during the ICE-L field campaign. The main focus of this field project was clouds containing ice but on November 30th several "missed approach" vertical profiles were flown in clear skies at Cheyenne, WY, Greeley, CO and Fort Collins-Loveland, CO, airports. This flight pattern is the preferred method for measuring vertical profiles in the lower atmosphere. In the ISPA-III flights the chamber-style CCN counter required the steady air pressure of the level flight stacks, but the continuous flow ICE-L instrument does not have this restriction. The missed approaches measure the vertical variation of a quantity while minimizing the horizontal displacement of the measurements.

CCN data were collected during a total of six missed approaches from the November 30th ICE-L flights between 19:00 GMT and 21:00 GMT. A thermal gradient, continuous diffusion CCN counter was installed on the aircraft to record instantaneous CCN number concentration. The instrument is similar in design to the DMT CCN-100 but was designed for use on aircraft and was introduced by Hudson (1989). N_{ccn} was measured at five values of SS (0.3%, 0.4%, 0.6%, 1.0%, 1.5%). The flight tracks for all missed approaches are shown in Figure 8.17 along with the 300m agl CCN concentration predicted by RAMS at SS=0.4%. The upward portions of the missed approaches, which begin at the marked airports, were used in this analysis. Figure 8.17 also shows the location of a plume of CCN from the RAMS forecast extending northward from the Denver urban area. South wind at the surface veered with height, becoming southwesterly at 700mb, driven by the position of a short-wave ridge relative to the Front Range. This is shown in the 700mb height and temperature maps for 12:00 GMT (Figure 8.18) and 18:00 GMT (Figure 8.19) on November 30, 2007. A

surface high pressure center associated with this ridge was moving east from the Front Range at this time, leaving light south wind at the surface from Denver to Cheyenne and cool, moist but not saturated, air in the lower levels. This is illustrated in Figure 8.20, which is a plot of potential temperature (θ) and RH on a vertical cross-section through 104.8°W longitude.

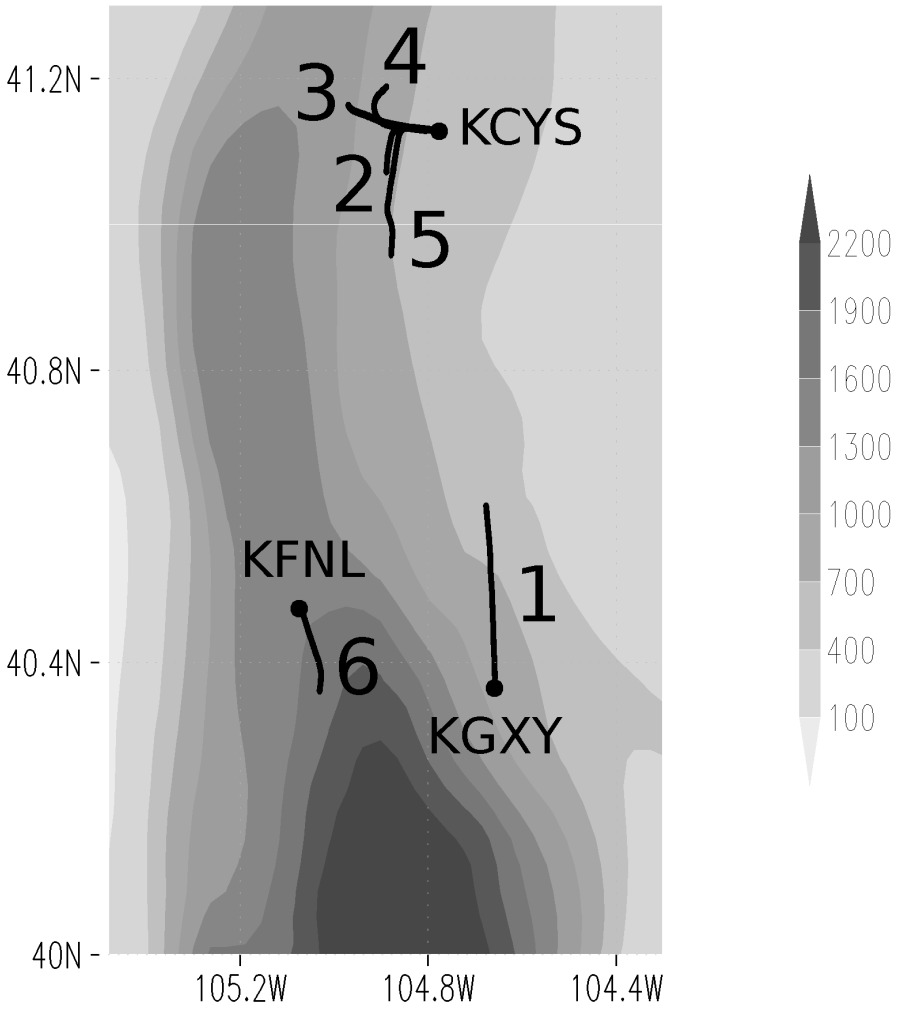

Figure 8.17: Flight tracks for all 6 missed approach vertical profiles taken during ICE-L on November 30th, 2007. The airports where each missed approach was conducted are marked. The flight tracks are plotted on the N_{ccn} field (cm^{-3}) as predicted by RAMS for 19:00 GMT on November 30th at a height of 200m agl.

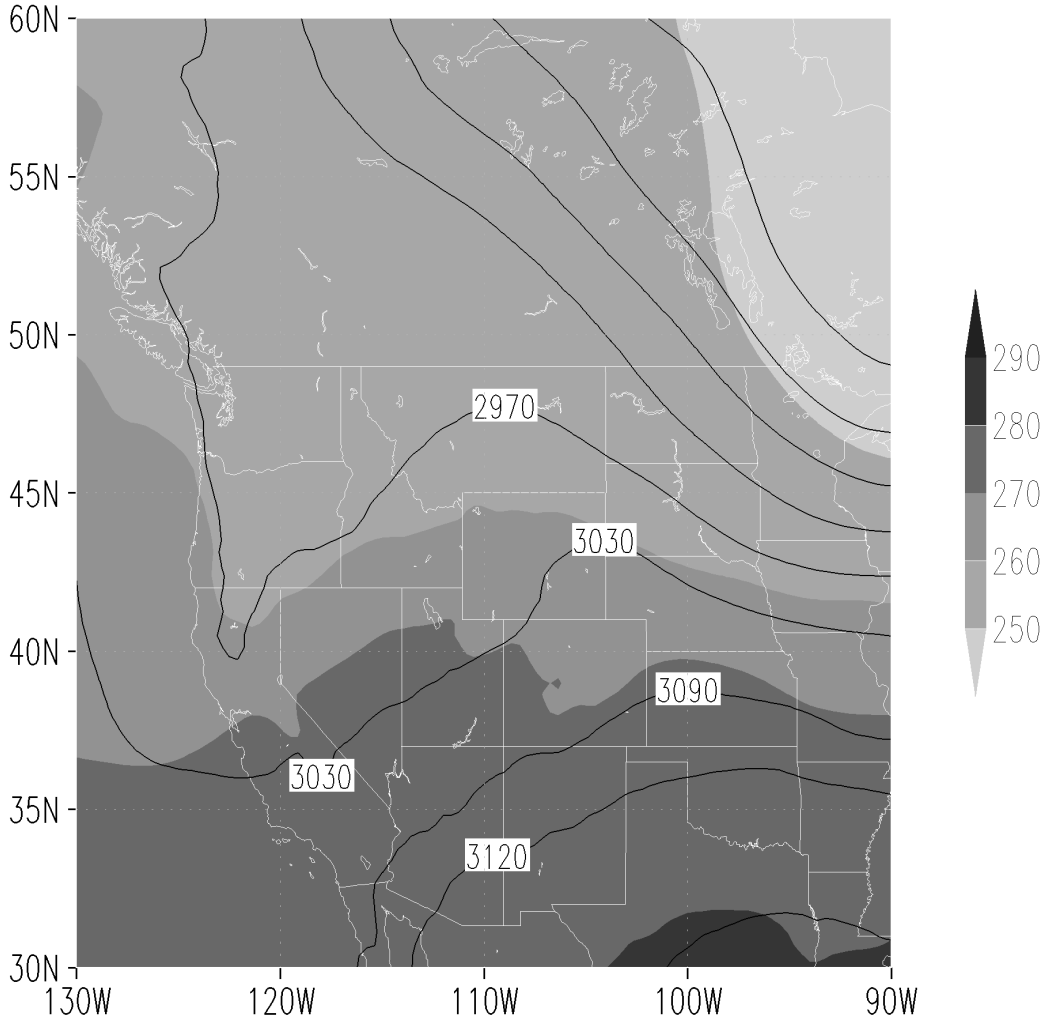

Figure 8.18: 700mb geopotential height (contours; gpm) and temperature (K) from the NARR dataset for 12:00 GMT November 30, 2007.

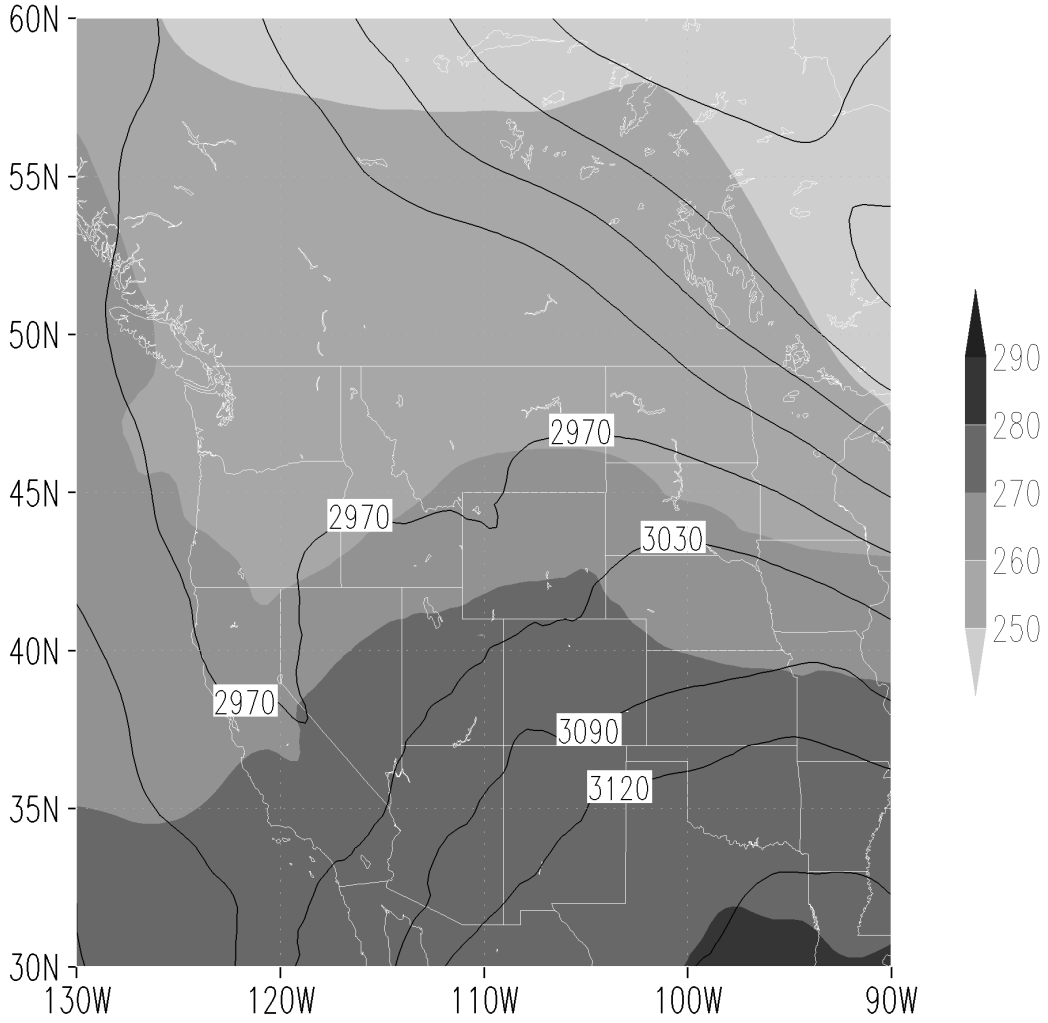

Figure 8.19: 700mb geopotential height (contours; gpm) and temperature (K) from the NARR dataset for 18:00 GMT November 30, 2007.

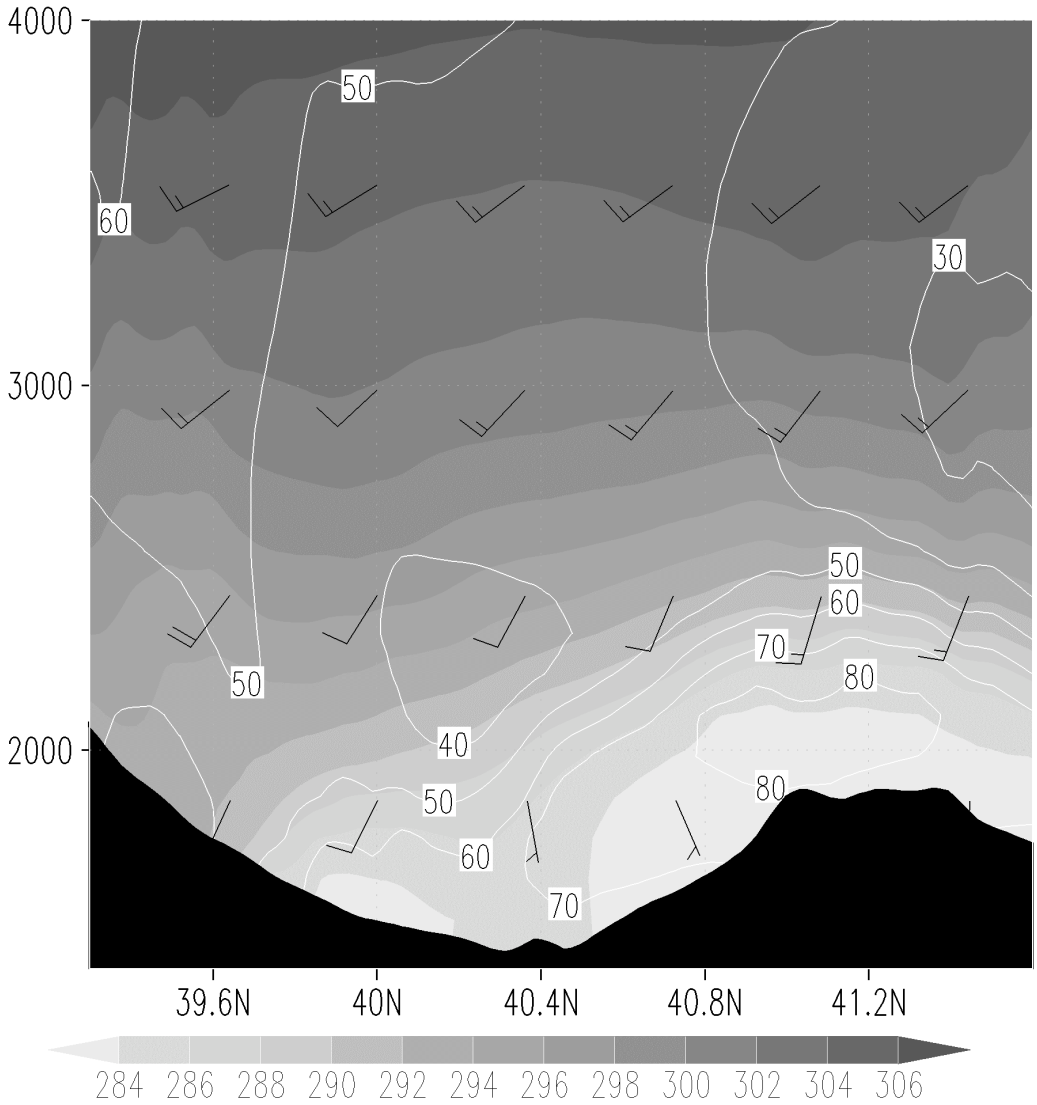

Figure 8.20: Vertical cross-section of θ (shaded; K) and RH (contours; %) for the Front Range running south to north along 104.8°W at 19:00 GMT on November 30th. Altitude on the y-axis is in meters msl.

8.2.1 Model setup

With clear conditions and southerly winds throughout the lower troposphere, particles emitted from the Front Range urban corridor are likely to be transported

northward toward Cheyenne where four of the missed approaches took place. To better accommodate the local transport of pollution in this November case, the horizontal resolution was increased in WRF/Chem and RAMS to 4km. A two-grid setup was also used for this case (Figure 8.21; Table 8.1). The outer grid does not cover the same large area as the outer

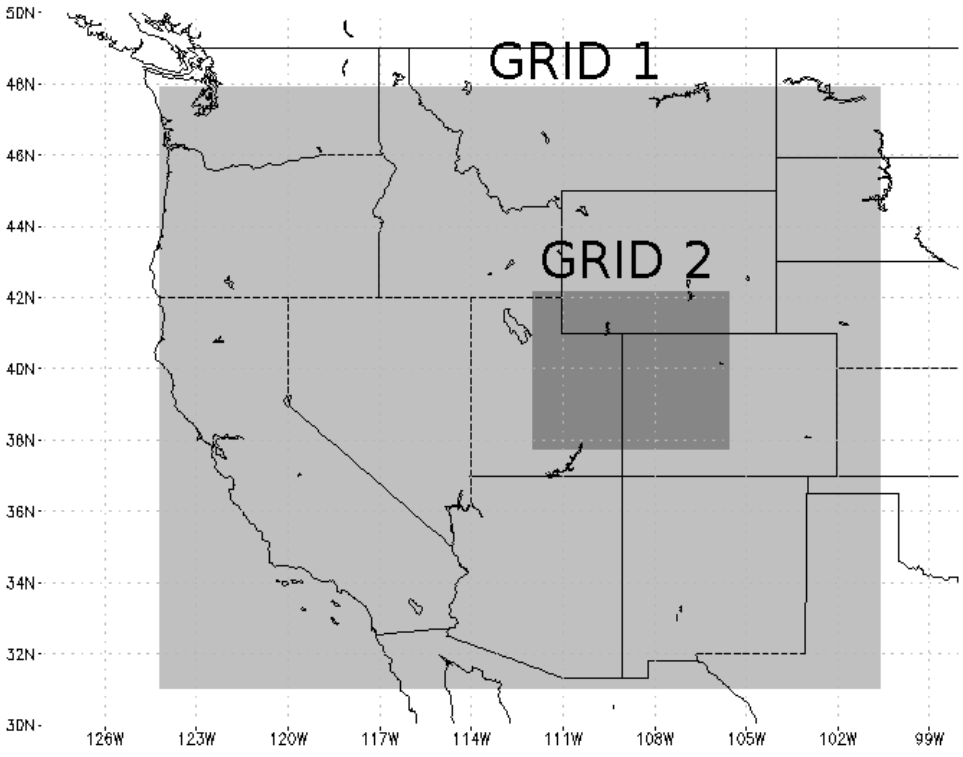

Figure 8.21: Grid locations for the ICE-L simulations. WRF/Chem and RAMS used the same horizontal grids.

grid in the previous 5-day simulation. The coverage was cut down in this case to save computation time and because emissions from local sources are expected to dominate the observations. Simulations were run on WRF/Chem for 60 hours from 12:00 GMT November 28, 2007 to 00:00 GMT December 1, 2007. This extra lead-in time allows the

model emissions and atmospheric burden of aerosols and precursor gases to spin-up, or reach a semi-steady state. Additional WRF/Chem and RAMS setup parameters are identical to the SPL simulations just described and can be found in Tables 8.2 and 8.3. All times in this and the next section will be given in GMT, with the time of interest, 19:00-21:00 GMT, corresponding to 12:00-14:00 MST.

At 19:00 GMT a substantial plume of pollution from the Front Range urban corridor was forecast by WRF/Chem to extend northward from 40˚N. The highest particle number concentrations were being transported at about 2500m msl. The plume is highly visible at 104.8˚W and is shown in a vertical cross-section of N_{cn} and accumulation mode aerosol mass concentration in Figure 8.22. Note in this cross-section that the area of greatest aerosol mass concentration is displaced from the area of greatest N_{cn}. This could be an indication that a large number of sulfate particles are being added to the WRF/Chem atmosphere at this height though the nucleation parameterization. These particles initially form with a diameter of 3nm and would not contribute significant mass to the aerosol population.

The most massive chemical components of the pollution plume were nitrate aerosol and primary carbonaceous aerosol, shown in Figures 8.23 and 8.24 respectively (also 19:00 GMT). The mass concentration of each species is plotted with the total accumulation mode aerosol mass concentration. WRF/Chem predicted less ammonium aerosol than nitrate aerosol, but the spatial variation of ammonium (Figure 8.25) closely resembles that of the nitrate aerosol. The sulfate portion of the WRF/Chem aerosol is shown in Figure 8.26. The pattern of sulfate represents a departure from the other species. The sulfate mass is a small fraction of the nitrate mass in the plume, but is the only species with significant mass above 3km msl. WRF/Chem initializes the mid and upper levels of the troposphere with a background concentration of sulfate aerosol to add to the initial fields of gas-phase

constituents. Other aerosol species are typically initialized to zero at these heights. Finally, the SOA comprises the least amount of mass compared to the other aerosol components (Figure 8.27), but its influence extends further north than the primary carbonaceous aerosol. This implies that condensation of volatile organic compounds onto existing aerosol occurred in WRF/Chem away from their major sources.

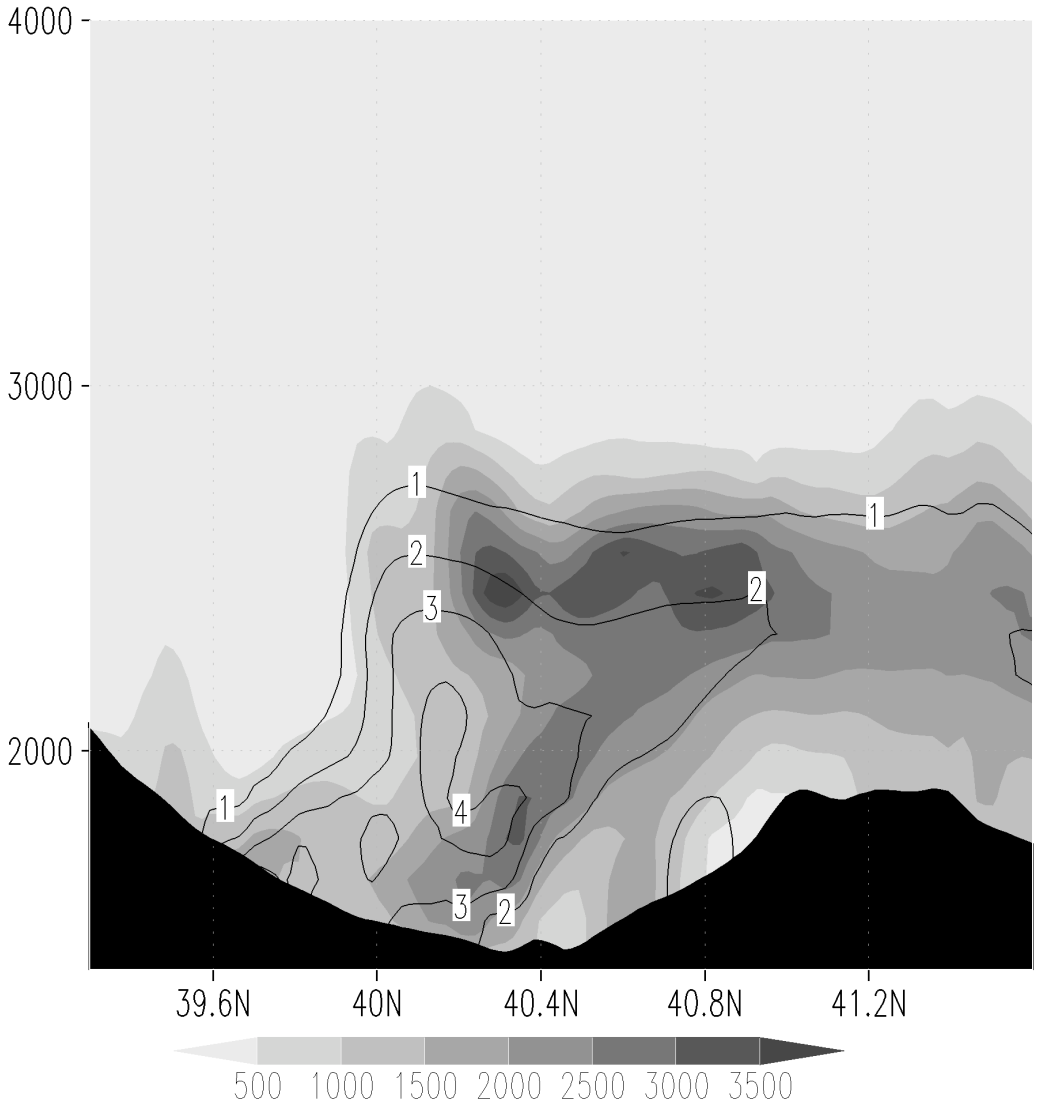

Figure 8.22: Vertical cross-section of WRF/Chem predicted N_{cn} (shaded; cm^{-3}) and accumulation mode aerosol mass concentration (contours; $\mu g/m^3$) for the Front Range running south to north along 104.8°W at 19:00 GMT on November 30th. Altitude on the y-axis is in meters msl.

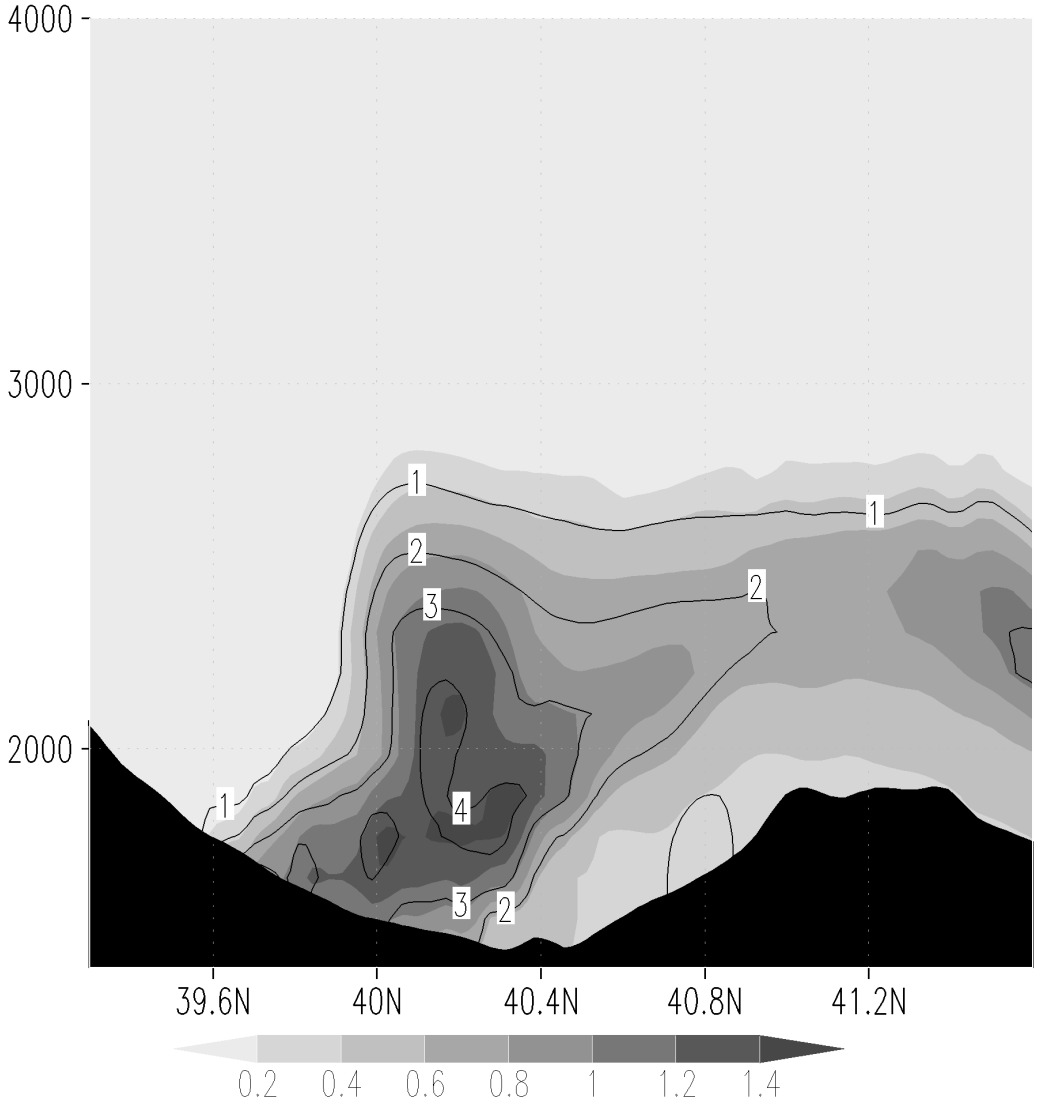

Figure 8.23: Vertical cross-section of WRF/Chem predicted nitrate aerosol mass concentration (shaded; μg/m^3) and accumulation mode aerosol mass concentration (contours; μg/m^3) for the Front Range running south to north along 104.8°W at 19:00 GMT on November 30th. Altitude on the y-axis is in meters msl.

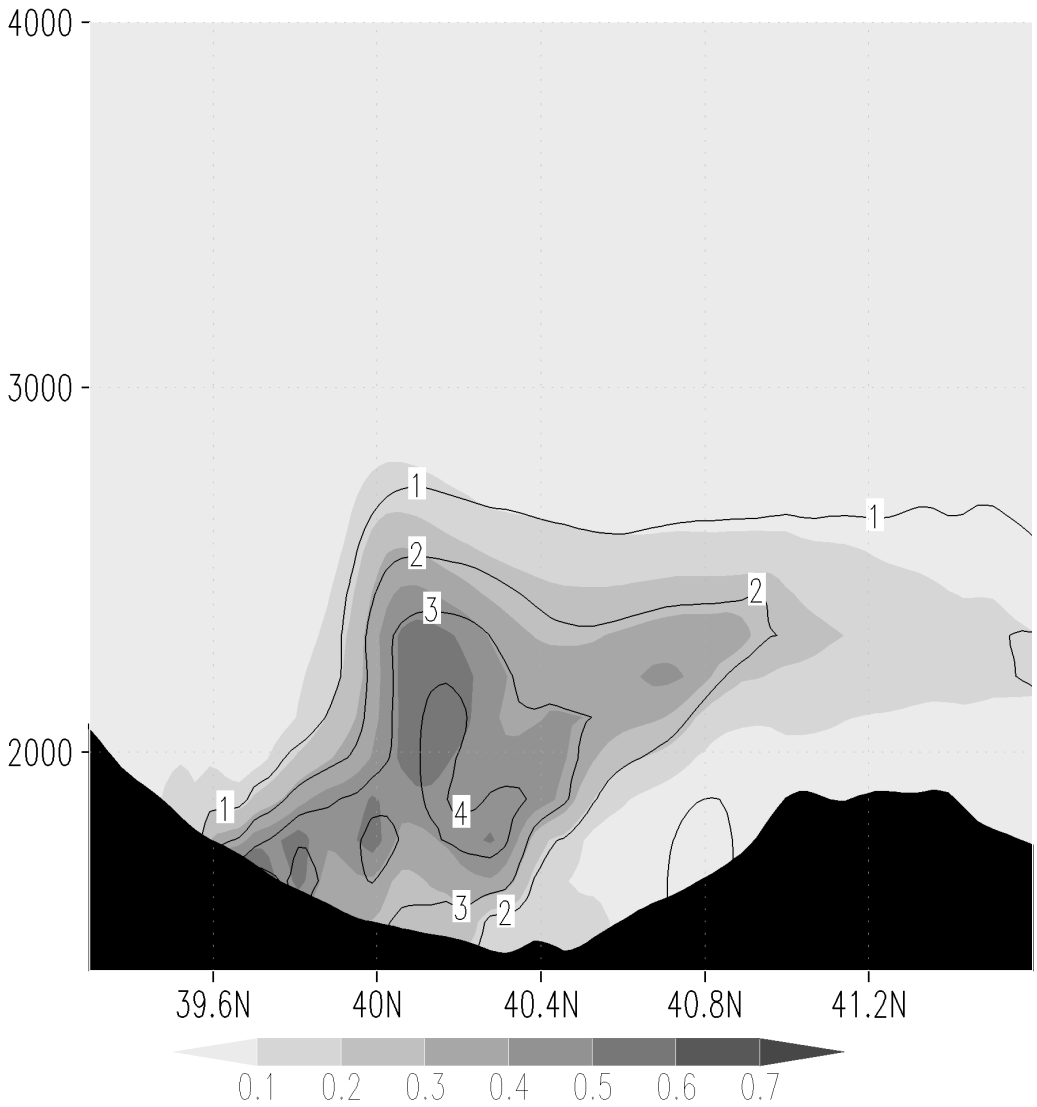

Figure 8.24: Vertical cross-section of WRF/Chem predicted primary carbonaceous aerosol mass concentration (shaded; μg/m^3) and accumulation mode aerosol mass concentration (contours; μg/m^3) for the Front Range running south to north along 104.8°W at 19:00 GMT on November 30th. Altitude on the y-axis is in meters msl.

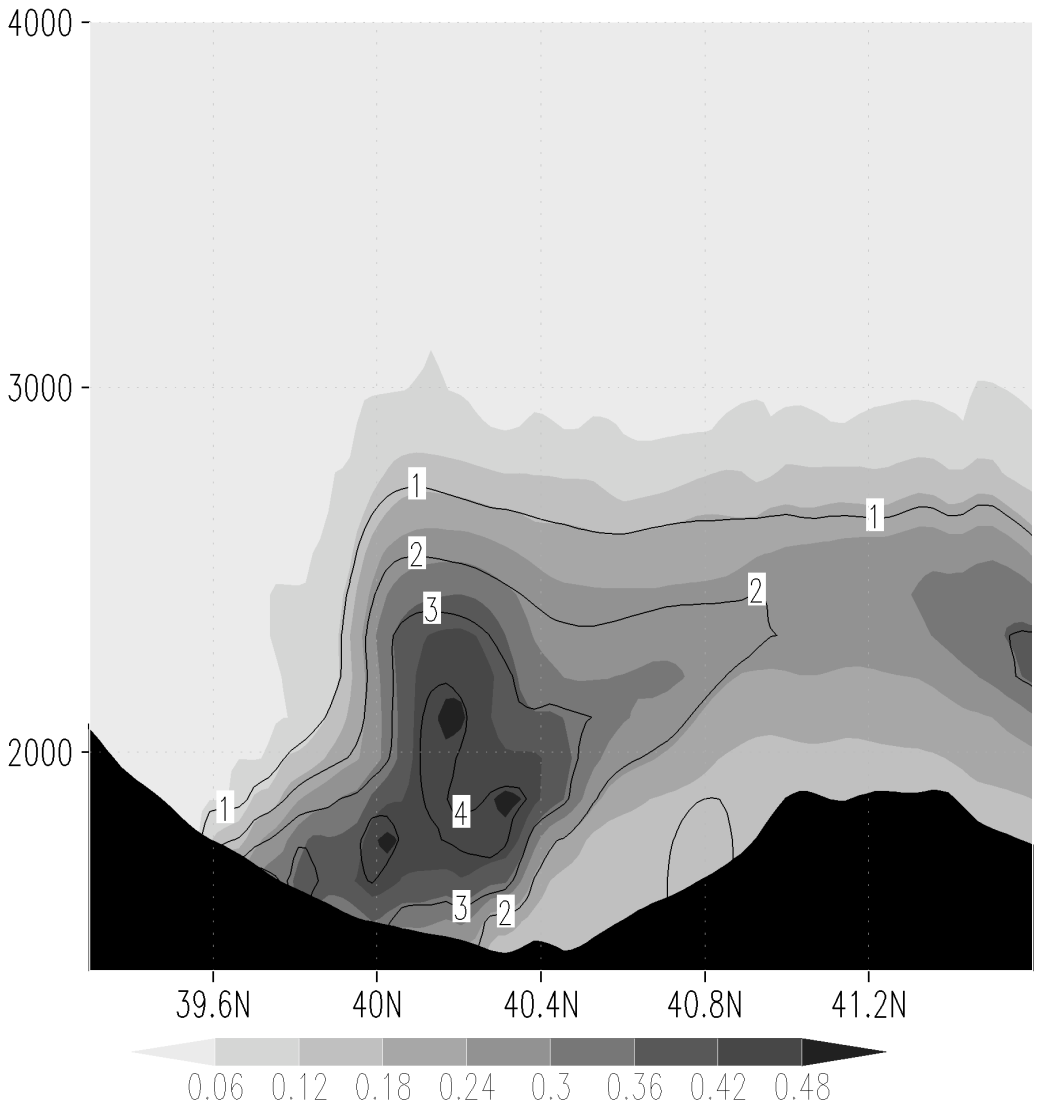

Figure 8.25: Vertical cross-section of WRF/Chem predicted ammonium aerosol mass concentration (shaded; μg/m^3) and accumulation mode aerosol mass concentration (contours; μg/m^3) for the Front Range running south to north along 104.8°W at 19:00 GMT on November 30th. Altitude on the y-axis is in meters msl.

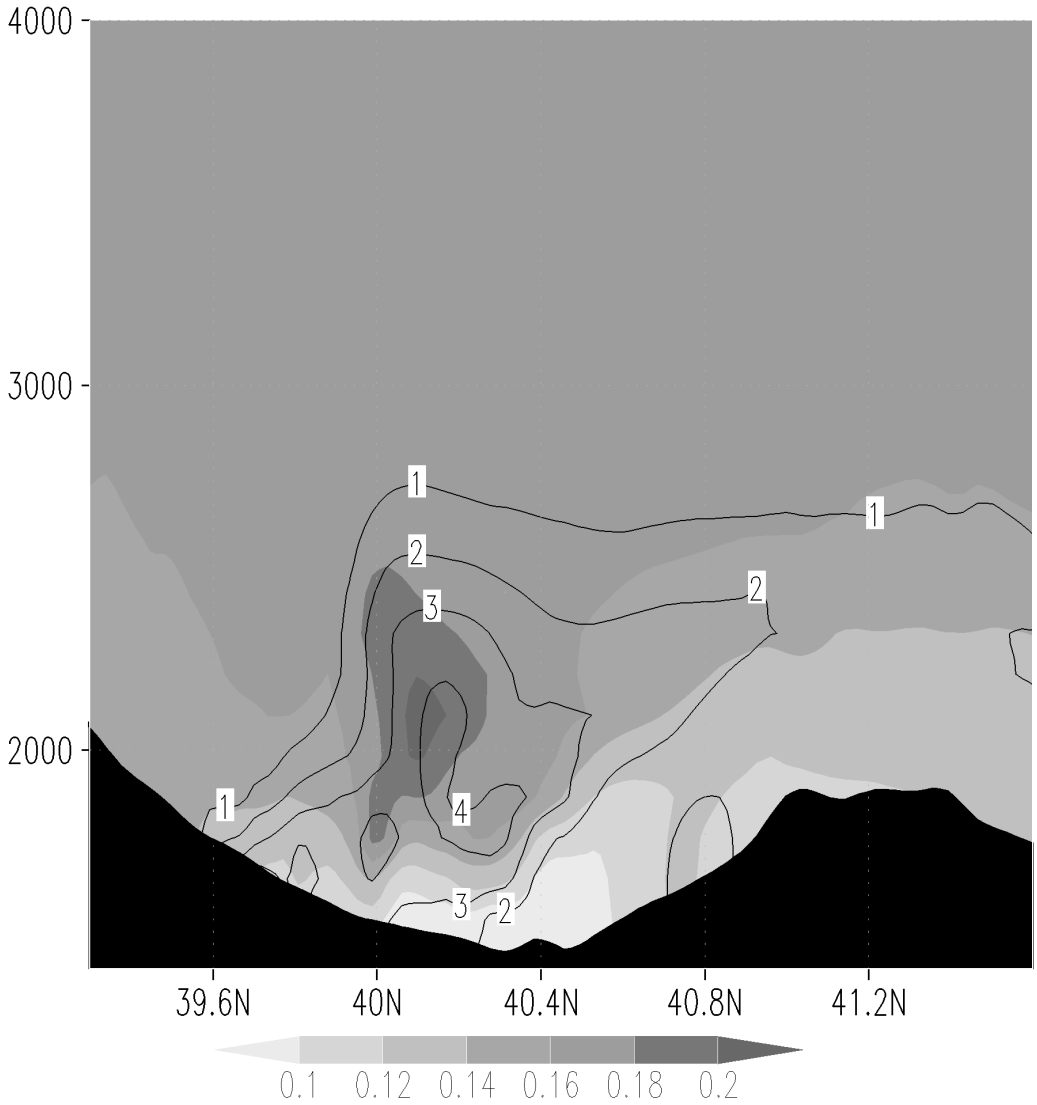

Figure 8.26: Vertical cross-section of WRF/Chem predicted sulfate aerosol mass concentration (shaded; μg/m^3) and accumulation mode aerosol mass concentration (contours; μg/m^3) for the Front Range running south to north along 104.8°W at 19:00 GMT on November 30th. Altitude on the y-axis is in meters msl.

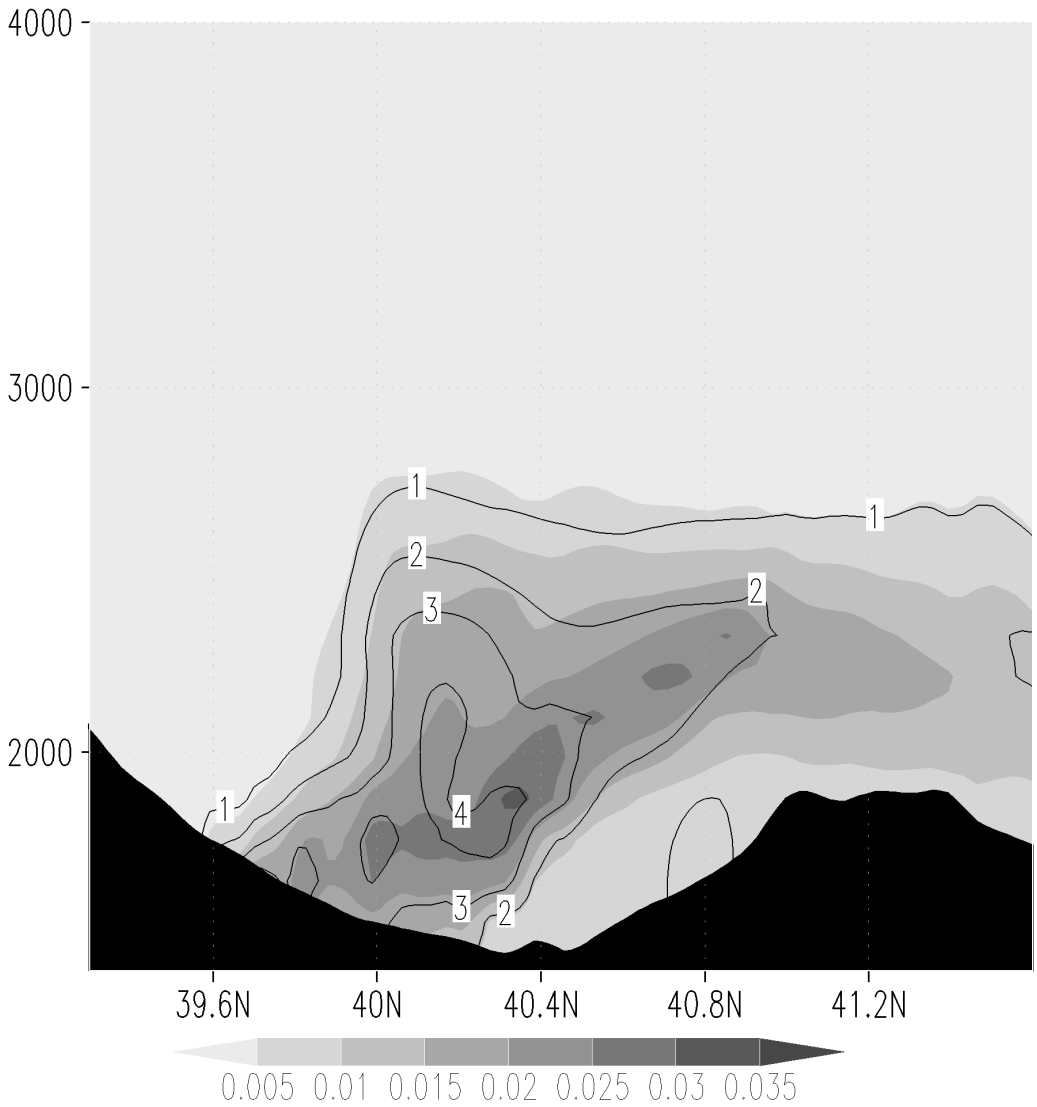

Figure 8.27: Vertical cross-section of WRF/Chem predicted SOA mass concentration (shaded; μg/m^3) and accumulation mode aerosol mass concentration (contours; μg/m^3) for the Front Range running south to north along 104.8°W at 19:00 GMT on November 30th. Altitude on the y-axis is in meters msl.

8.2.2 Model results compared to observations

The missed approach vertical profiles were all performed in or near the forecasted pollution plume but at different distances from the main sources. This provides the

WRF/Chem and RAMS coupled system with the challenge of forecasting the horizontal and vertical extent of the dispersion of particles. As a first check, Figure 8.28

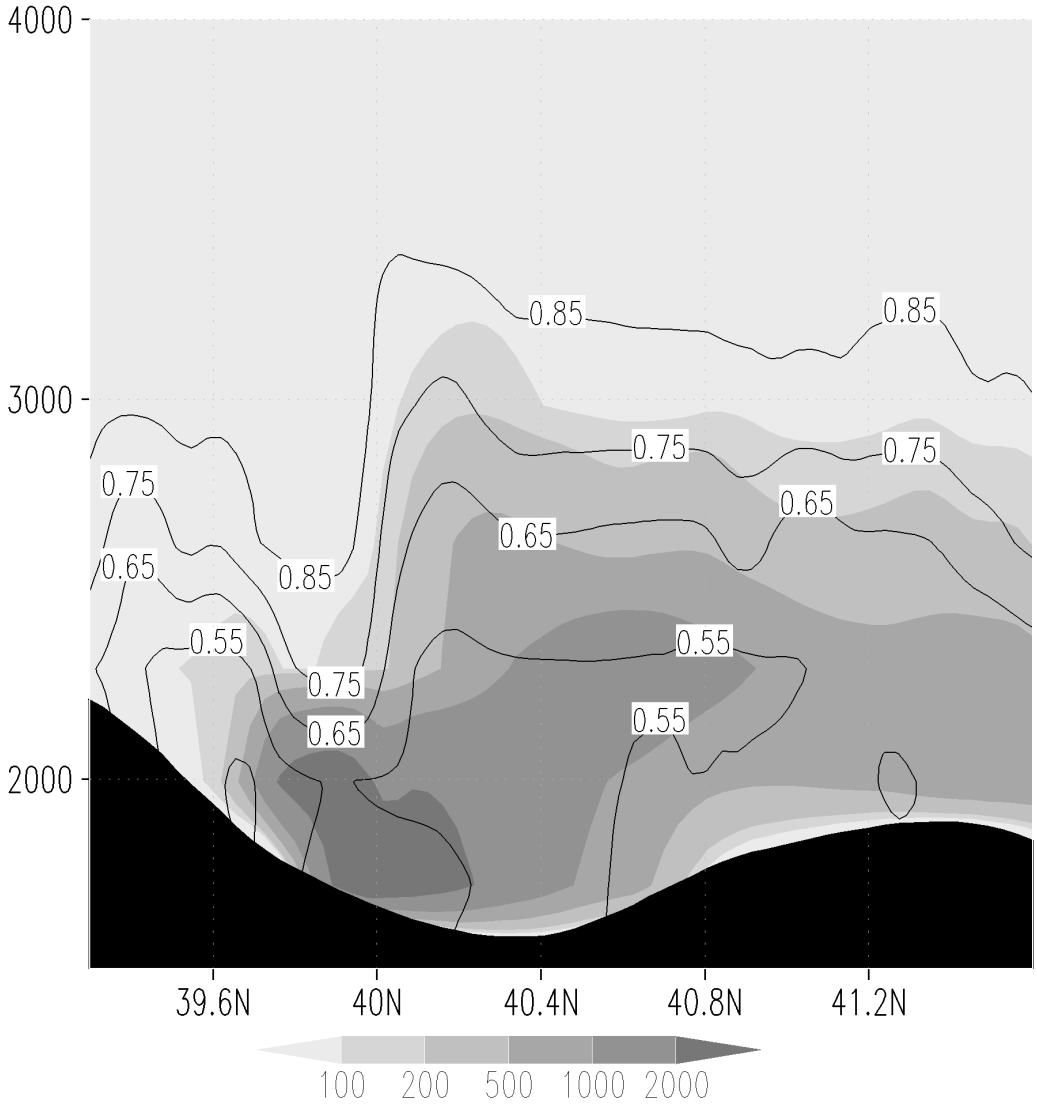

Figure 8.28: Vertical cross-section of RAMS predicted N_{ccn} (shaded; cm^{-3}) and κ (contours) for the Front Range running south to north along 104.8°W at 19:00 GMT on November 30th. Altitude on the y-axis is in meters msl.

shows the vertical cross-section of the RAMS forecast of N_{ccn} and κ at 19:00 GMT and 104.8°W. The pattern of N_{ccn} shows the northward transport from sources in the Denver

area. Note that the area of greatest N_{ccn} does not coincide with the area of greatest N_{cn} (Figure 8.22). This, again, is an indication that the N_{cn} maximum contains small, probably newly formed, particles. RAMS r_g is plotted on a vertical cross-section in Figure 8.29 and shows smaller particles sizes at the height of the N_{cn} maximum.

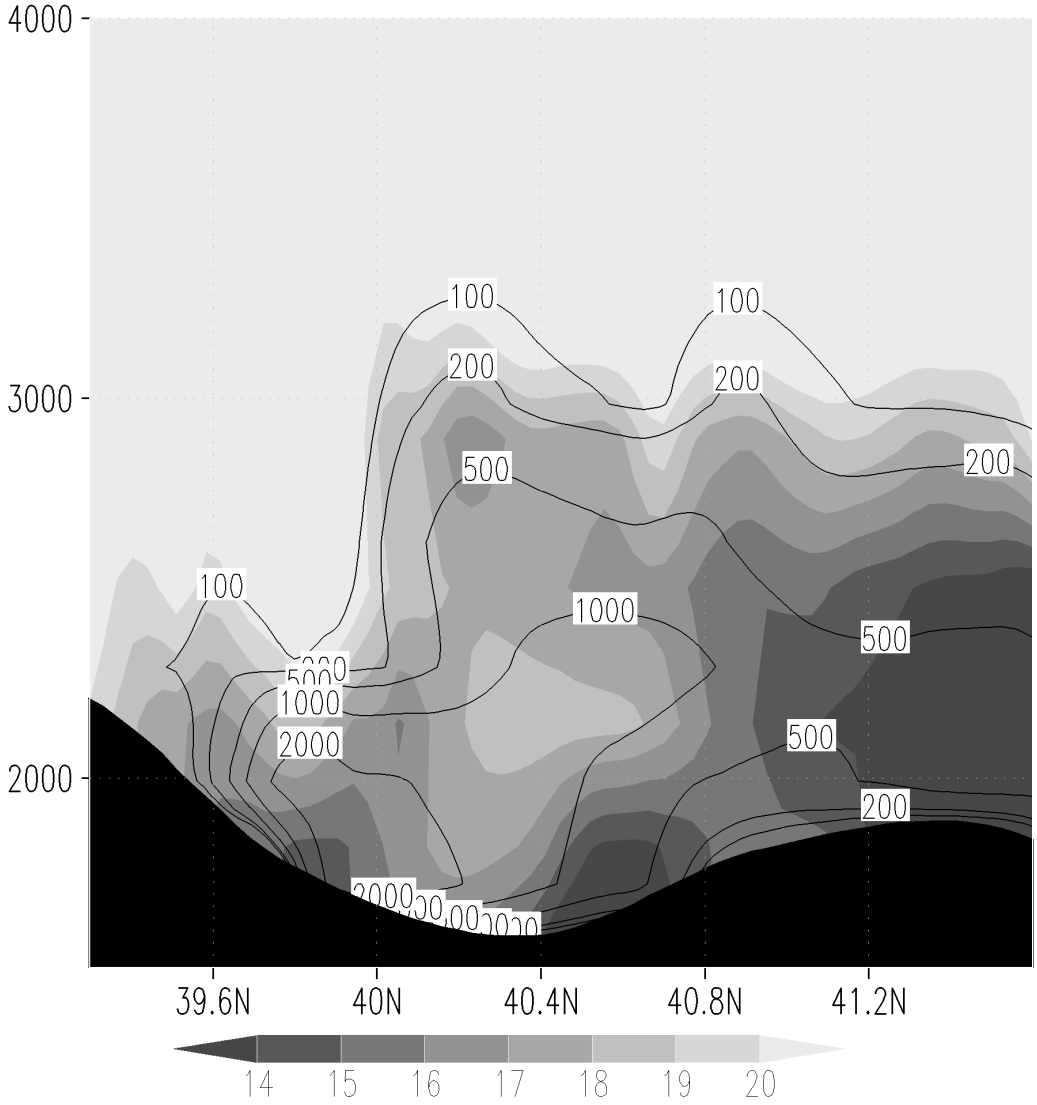

Figure 8.29: Vertical cross-section of RAMS predicted r_g (shaded; nm) and N_{ccn} (contours; cm^{-3}) for the Front Range running south to north along 104.8°W at 19:00 GMT on November 30th. Altitude on the y-axis is in meters msl.

Values of κ in Figure 8.28 are generally greater than 0.5. Above the plume, κ increases and approaches the value of pure sulfuric acid. In areas where WRF/Chem did not transport or create any aerosol mass from the surface emissions, the background sulfate is all that remains. In the absence of ammonium aerosol, all sulfate is considered to have the hygroscopicity of sulfuric acid (see Chapter 7). Elsewhere, κ exceeds typical continental values as defined by Andreae and Rosenfeld (2008). Once again, an underprediction of carbonaceous aerosols could be sustaining the high κ.

The N_{ccn} measured on all six missed approaches is compared to RAMS predictions of CCN at SS=0.4%. They are plotted as vertical profiles but note that some horizontal displacement occurs over the course of the aircraft's ascent. The RAMS profiles take this horizontal movement into account by displaying the nearest horizontal grid point to the aircraft's location at each model vertical level. Time is treated as fixed in the model profiles, although each vertical profile took less than five minutes to complete in the air. The first profile shows N_{ccn} measured as the aircraft was ascending from the Greeley airport (Figure 8.30). The observations suggest that the aircraft was initially below the elevated pollution plume and encountered higher values of N_{ccn} at around 2000m msl. RAMS captures the magnitude of the elevated plume well at this location, although it placed the layer of high N_{ccn} a few hundred meters lower than was measured.

Profiles 2 through 6 were measured during ascents to the west from the Cheyenne airport. Significant differences between model output and the ICE-L measurements of CCN are illustrated in Profile 2 shown in Figure 8.31. The aircraft apparently exited the polluted region during its ascent. This was the only profile that did not observe an elevated layer of increased N_{ccn}. This elevated layer is apparent in Profiles 3, 4, and 5, but at different altitudes (Figures 8.32 to 8.34). In all these profiles a N_{ccn} ~ 1000-1500 cm-3 in the boundary layer decreases to 500 cm^{-3} or fewer with height until reaching the pollution

plume at a height of 2350m msl (Profile 3) and 2200m msl (Profiles 4 and 5). N_{ccn} increased back to about 1000 cm^{-3} in this layer before decreasing again with height to a clean, background concentration. The differences between profiles could be due to the slightly different flight paths taken in each ascent and the different times that each was conducted. RAMS forecast a similar vertical variation in N_{ccn} with an increase from the lowest level up to 2300m msl and then a steady decrease with height above this level. Although the height of the polluted layer is not captured consistently in the model, RAMS predicts the magnitudes of N_{ccn} within the plume and especially above the plume within 30% of the observations for these profiles.

The final missed approach was carried out at Fort Collins-Loveland airport, which was the furthest west of any of the previous profiles. The model output agrees very closely with the observed N_{ccn} in the lowest 500m of the vertical profile but fails to pick up the increased number of CCN above 2200m msl observed by the C-130 (Figure 8.35). The aircraft was most likely measuring emissions that had dispersed from the Denver area as far west and north as Fort Collins. WRF/Chem and RAMS predicted the plume location too far east at this height, or, in other words, did not pick up the extent of the particle dispersion.

The skill shown here in picking up the elevated pollution layers, even with the errors in height, is important because it is a huge improvement over the previous scheme. Aerosols were, in the past, typically set to decrease linearly in number concentration with height to represent the average atmospheric profile. The WRF/Chem and RAMS system, in addition to simulating the magnitude of N_{ccn} during this case within reasonable bounds, portrayed large vertical variations in CCN that would otherwise be missed.

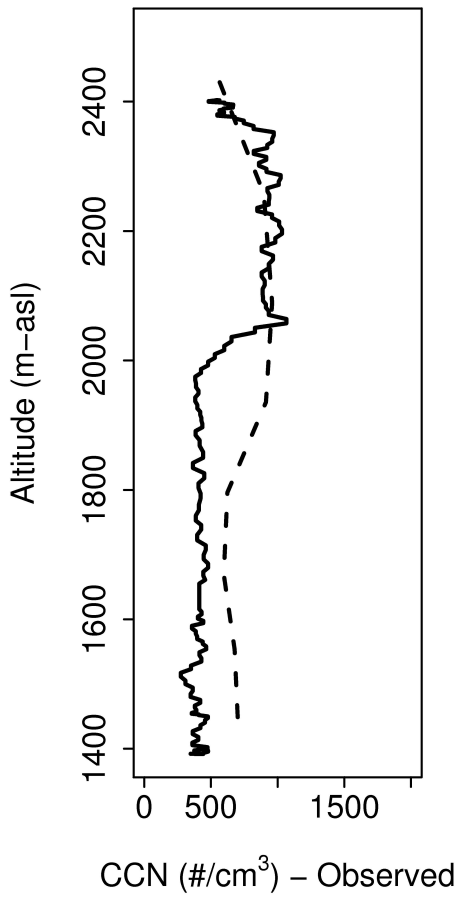

Figure 8.30: Vertical profile of N_{ccn} (SS=0.4%) observed during missed approach #1 on November 30th from the ICE-L field campaign (solid) and as predicted by RAMS for the corresponding time and positions (dashed). Altitude on the y-axis is given in meters msl.

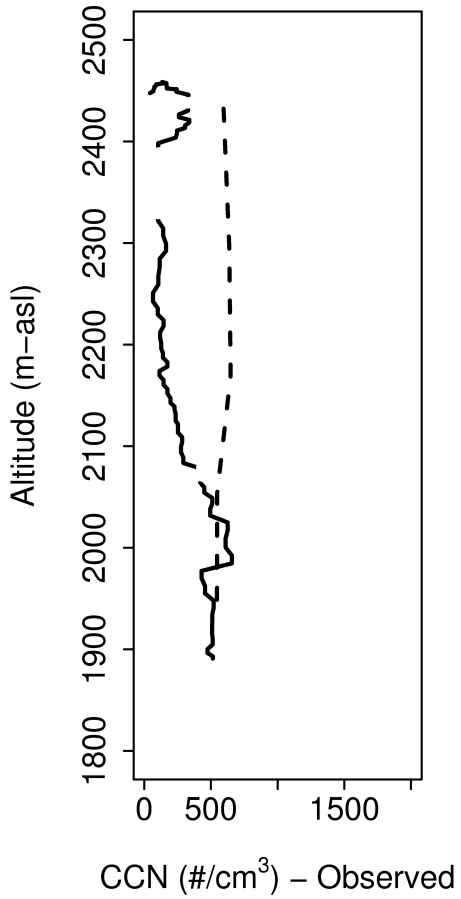

Figure 8.31: Vertical profile of N_{ccn} (SS=0.4%) observed during missed approach #2 on November 30th from the ICE-L field campaign (solid) and as predicted by RAMS for the corresponding time and positions (dashed). Altitude on the y-axis is given in meters msl.

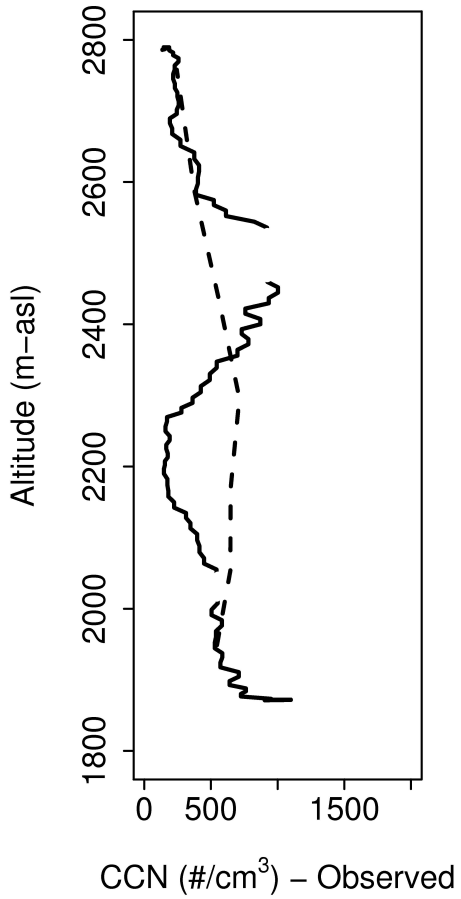

Figure 8.32: Vertical profile of N_{ccn} (SS=0.4%) observed during missed approach #3 on November 30th from the ICE-L field campaign (solid) and as predicted by RAMS for the corresponding time and positions (dashed). Altitude on the y-axis is given in meters msl.

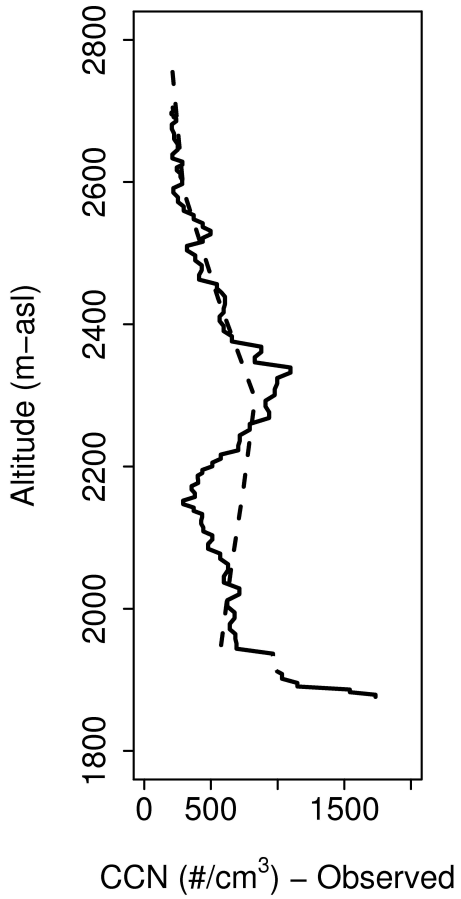

Figure 8.33: Vertical profile of N_{ccn} (SS=0.4%) observed during missed approach #4 on November 30th from the ICE-L field campaign (solid) and as predicted by RAMS for the corresponding time and positions (dashed). Altitude on the y-axis is given in meters msl.

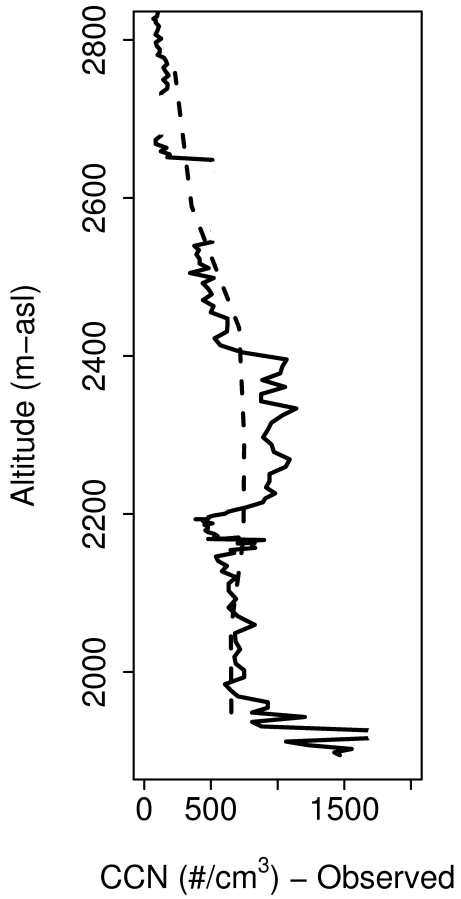

Figure 8.34: Vertical profile of N_{ccn} (SS=0.4%) observed during missed approach #5 on November 30th from the ICE-L field campaign (solid) and as predicted by RAMS for the corresponding time and positions (dashed). Altitude on the y-axis is given in meters msl.

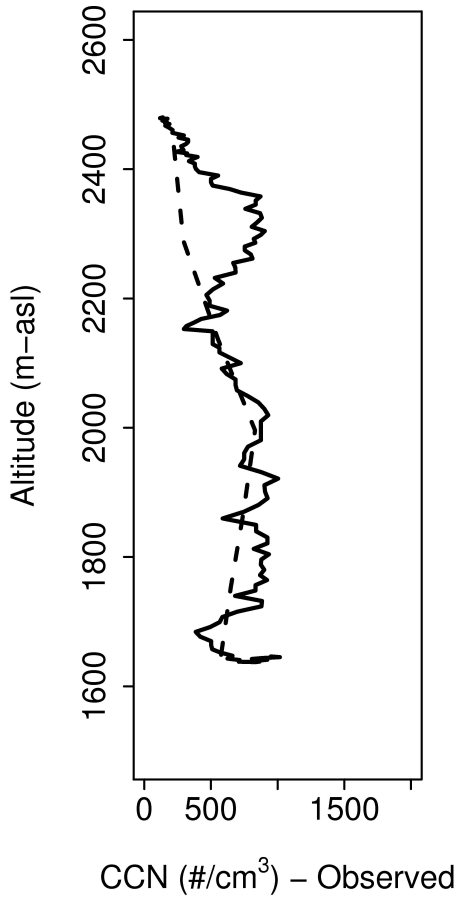

Figure 8.35: Vertical profile of N_{ccn} (SS=0.4%) observed during missed approach #6 on November 30th from the ICE-L field campaign (solid) and as predicted by RAMS for the corresponding time and positions (dashed). Altitude on the y-axis is given in meters msl.

8.3 Assessment of model performance

It is difficult to judge the skill of a model forecast when it is validated against observations from a single site or from a single case. Unfortunately, CCN observations are not widely available. The simulations described in this chapter, when compared to CCN

datasets from SPL and ICE-L, are still useful for understanding the model performance under various conditions.

Specifically, the following lessons about the performance of the new modeling system were learned:

• WRF/Chem apparently underpredicted the mass fraction of fine mode organic aerosol when the model output was compared to IMPROVE data. This may lead to a high bias in κ and in activated fraction.

• The RAMS droplet activation and CCN prediction scheme worked as expected and in accordance with the relationships proposed in Chapter 3.

• Treating dust as microphysically active could have improved the model representation of κ compared to observations. This would also have led to more accurate N_{ccn} predictions with regards to magnitude in the SPL case. Whether it is realistic to retain the internally mixed representation of the model aerosol when adding in dust is an open question. It still would not have improved the model prediction of a high CCN event on April 2nd that was not observed at SPL.

• While aerosol effects on clouds are the target subjects of this model development, cloud effects on aerosol are an important aspect of the evolution of particles in the atmosphere and are not represented in WRF/Chem. Wet scavenging in particular may have contributed to the April 2nd non-event predicted by RAMS. This issue would be resolved with online computation of aerosol processes in RAMS.

• The system as a whole generally captured the vertical variations in N_{ccn} during the ICE-L case. While this is only one case, it suggests that the model would perform well in an area dominated by anthropogenic emissions and local transport processes.

An effort was made to select cases for which the following processes would not play a large role, but it needs to be mentioned again that biomass burning, emission of DMS, isoprene, dust and sea-salt, wet deposition, and droplet nucleation were not included in WRF/Chem for these simulations. Additional uncertainty remains regarding the accuracy of the emissions inventories (Fast et al., 2006), and the assumptions about aerosol size distribution and new particle nucleation. Until the representation of these processes are included or improved, forecasts of CCN will involve large uncertainty. The simulations in this chapter have shown that the modeling system can recreate many aspects of the observed CCN to an acceptable degree.

Chapter 9

Sensitivity of predicted CCN to changes in emissions

The majority of components comprising continental aerosols have been shown to originate from anthropogenic sources (Kanakidou et al., 2005; Andreae and Rosenfeld, 2008). Since the increased aerosol concentrations impact clouds and climate, it is important to ask where the aerosols come from and which sources contribute the most to the atmospheric aerosols. Only when these sources are identified can effective control of possible adverse effects on the environment be put into action.

Several strategies for attributing ambient aerosols to particular sources have been developed, such as receptor modeling (Hegg et al., 2009) and trajectory analysis. Back-trajectory analysis is a common tool applied to aerosol source attribution problems, used in recent studies by Gunthe et al. (2009), Bougiatioti et al. (2009), Contini et al. (2010) and Medina et al. (2007), among others. Using this technique, air parcels are followed backward through time on the analyzed wind to indicate the region where the aerosol within the parcel may have originated. Aerosol composition can even be inferred from back-trajectories (e.g. VanReken et al., 2003) but these attempts to characterize source locations

and strength based on wind direction are inherently uncertain (Chapter 5; Stohl, 1998). Apart from uncertainty in the meteorological analysis itself, which can be significant (Engstrom and Magnusson, 2009), Stier et al. (2006) explain how the evolution of particles in the atmosphere is too complex to be accurately tracked using only the wind. Chemical aging of particles, phase partitioning and aerosol/cloud interactions all contribute to the changing aerosol population along the predicted back-trajectory.

To address the shortcomings associated with aerosol source attribution, Stier et al. (2006) ran global sensitivity studies in which emissions of sulfate and carbonaceous aerosol were "turned off" and compared to a reference simulation with all emissions included. This technique became available only recently with the development of integrated aerosol and microphysics models. They found that eliminating sulfates and carbonaceous aerosol emissions led to a non-additive response in the global aerosol burden, meaning that reducing emissions did not lead to a proportional reduction in aerosol burden. The non-linear response was attributed to interactive aerosol chemical and physical processes including large changes in global average aerosol lifetime of some species.

Chapman et al. (2009) used a similar strategy on a regional scale to investigate radiative effects of certain anthropogenic aerosol source types. They turned off all point sources in a northeastern United States domain and also found complex and spatially variable changes in the aerosol burden and radiative impacts. The technique of Chapman et al. (2009) and Stier et al. (2006) can also be applied to questions about the sources and major contributors to CCN populations. In this chapter, certain emissions are turned off in WRF/Chem to test the sensitivity of the CCN number concentration in western Colorado to local and distant sources in the western United States.

9.1 Model setup

For this experiment, simulations were run with the WRF/Chem and RAMS system explained in Chapter 7. A case was chosen for the sensitivity experiment to coincide with the aircraft observations of N_{cn} and N_{ccn} along the Western Slope described in Chapter 6. On December 18th, 2009, the King Air 200T was flown in clear sky from Laramie, WY to south of Cortez, CO and measured N_{ccn} at three values of SS. Recall from Chapter 6 that this day was put into the northwesterly flow category with an upper level ridge to the west and trough to the east of western Colorado. Vertical profiles were flown with the King Air 200T near Cortez, CO at 19:00 GMT and near Steamboat Springs, CO at 22:00 GMT. To focus the analysis on these times for which observations were available, WRF/Chem was run from 00:00 GMT December 16, 2009 to 00:00 GMT December 19, 2009. The 72-hour simulation time allows ample time for the model emissions to spin up.

The purpose of these simulations was to test the sensitivity of aerosols to emission changes on a regional scale. Therefore, WRF/Chem and RAMS were set up on one grid with 16km grid spacing, small enough to resolve mesoscale meteorology but large enough to cover a substantial area with reasonable computation time. The grid was centered at 41˚N and 112˚W with 130x by 100y grid points and contained the major west coast aerosol sources. Both WRF/Chem and RAMS were initialized and nudged with the NARR dataset. With the exception of the horizontal grid and meteorological nudging dataset, both models were setup identically to grid #1 in the SPL validation case and detailed in Tables 8.2 and 8.3.

With the input from the 72 hour WRF/Chem simulations, RAMS was run for 48 hours from 00:00 GMT December 17th to 00:00 GMT December 19th. Analysis files were

output every two hours of model time. The values of SS for diagnosis of N_{ccn} were set to 0.27%, 0.54%, 1.07% and 1.5% to emulate the SS_{eff} measured in the CCNC-100A.

9.1.1 Sensitivity simulations

A reference simulation was run that included the full suite of anthropogenic and biogenic emissions as defined by the NEI-2005 and MEGAN emission inventories. Five sensitivity simulations were carried out with particular aerosol species turned off, as in Stier et al. (2006), or with certain sources turned off, as in Chapman et al. (2009). The details of the excluded emissions are given for all simulations in Table 9.1. Western Slope

Table 9.1: Names and descriptions of the reference simulation and five sensitivity simulations. The emissions are removed during WRF/Chem pre-processing and Biogenic emissions are included in all simulations although their impact was negligible.

Simulation	**Description**
REF	All anthropogenic emissions included
NPS	All area emissions included Point sources eliminated between 36˚N and 41˚N, 109˚W and 106˚W
DST	Area and point emissions eliminated outside box defined by: 36˚N and 42˚N; 111˚W and 102˚W
SUL	Emissions of sulfate aerosol and SO_2 eliminated Background sulfate set to zero Background SO_2 included
NOX	Emissions of nitrate aerosol and NOx eliminated Background nitrate set to zero Background NOx included
AMM	Emissions of ammonium aerosol and NH_3 eliminated Background ammonium aerosol set to zero Background NH_3 included

point sources were turned off in the LPS simulation to test the importance of these sources for the CCN in this region as measured during ISPA-III. The area where point sources were turned off is illustrated in Figures 9.1 and 9.2. Figure 9.1 shows the magnitude of the area sources and point sources for sulfur dioxide from the NEI-2005. The concentration of point sources in northwestern Colorado and northwestern New Mexico, including several large sources, are shown in this figure. A detail of the western Colorado region is shown in Figure 9.3. Figure 9.2 shows the same image as in Figure 9.1 but with the Western Slope point sources of sulfur dioxide removed. Area emissions, such as those from transportation and agriculture, were kept in the model and, as can be seen in Figure 9.2, a few major, nearby point sources remain (notably, the Jim Bridger coal-fired power plant in southwestern Wyoming). This way the impact of the local point sources was highlighted.

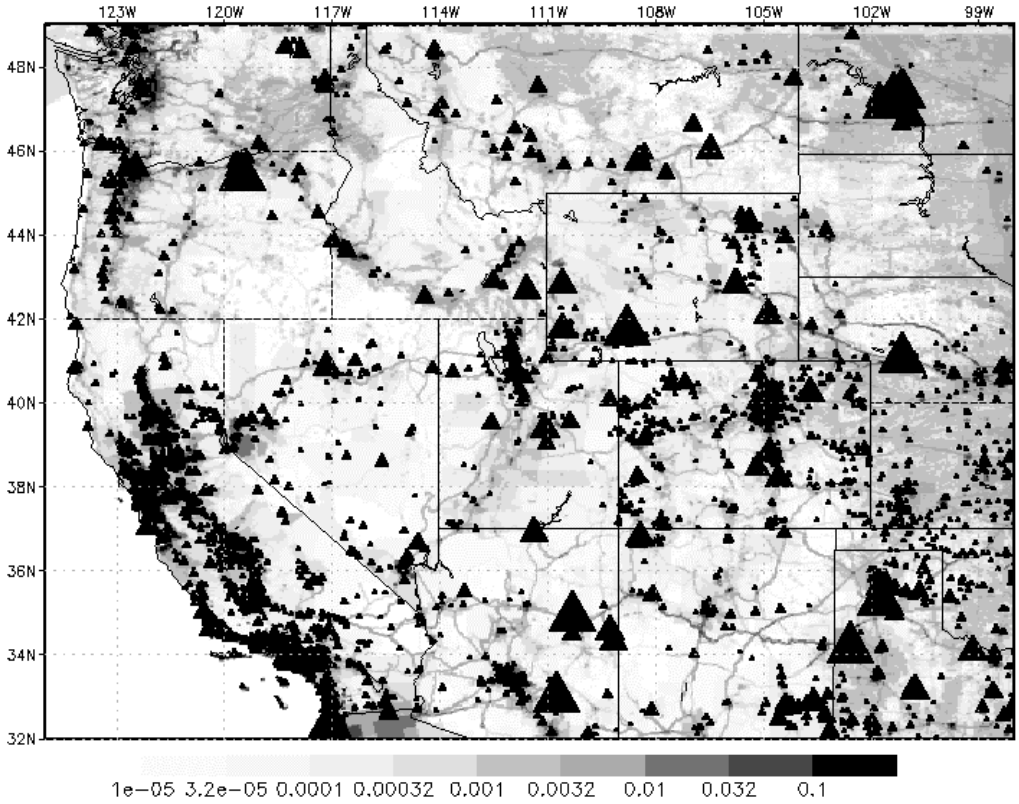

Figure 9.1: Emissions of SO_2 for the western United States from the NEI-2005. Area emissions are shaded and shown in units of short tons emitted per day from each 4km by 4km grid box. Point emissions are shown as triangles with the size of the triangle proportional to the amount of SO_2 emissions. The largest triangle size represents sources emitting over 10 short tons of SO_2 per day. Each smaller size represents an order of magnitude smaller source – 1 short ton, 0.1, 0.01 and so on.

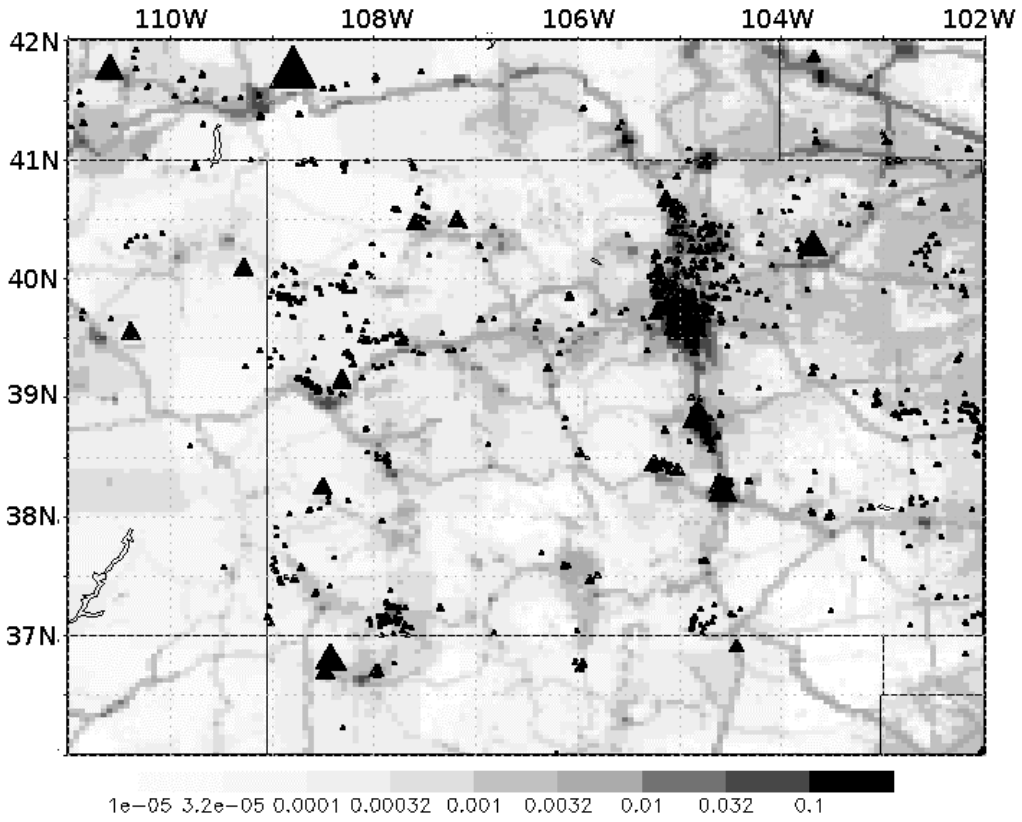

Figure 9.2: A detail of Figure 9.1.

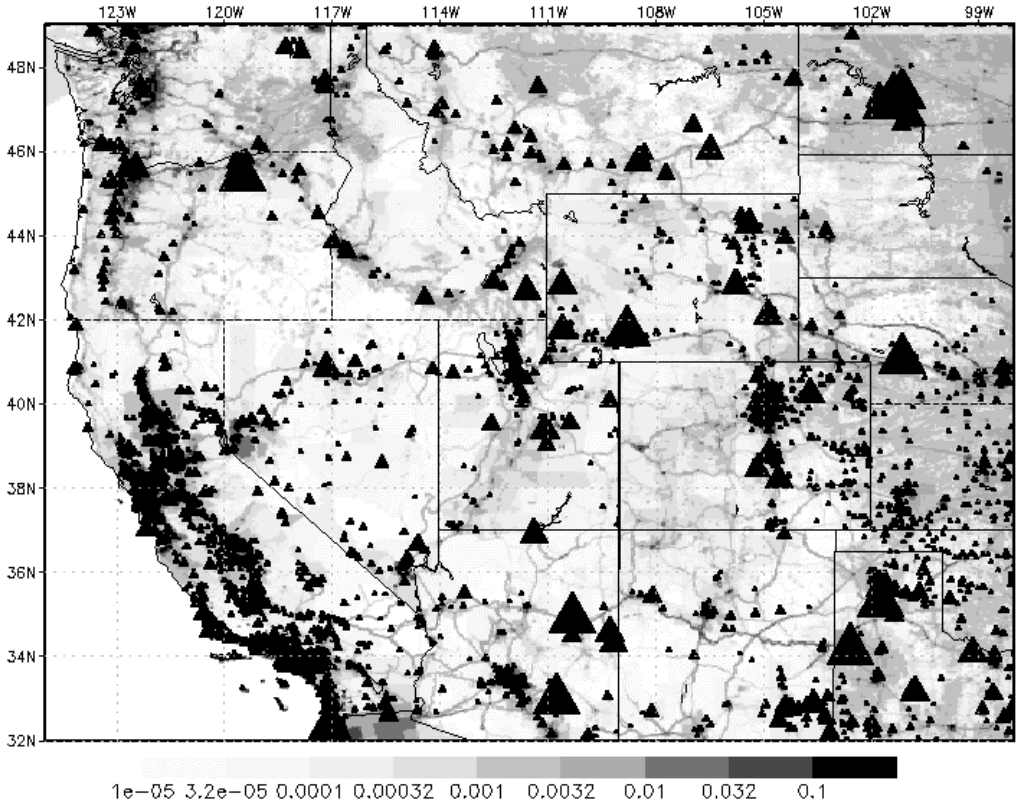

Figure 9.3: This figure shows the same emissions from Figure 9.1 with the exception of the point sources removed for the LPS simulation.

As a contrast to the LPS run, all distant emissions, including both area and point sources, were eliminated in the DST simulation. The results of these simulations are expected to be somewhat linear. In other words, by taking away large sources of aerosols and aerosol precursor gases of all species, it seems to follow that aerosol mass and N_{ccn} would be reduced proportionally. However, Chapman et al. (2009) observed a complex and highly variable response of total aerosol mass to similar emissions reductions in their experiment.

Non-linear responses to the emissions reductions are anticipated for the remaining three sensitivity simulations, SUL, NOX, and AMM. In these model runs the anthropogenic emissions of specific species are eliminated from the emissions inventory across the entire domain. Since these species are interactive in WRF/Chem, the absence of one could impact the remaining species and lead to unexpected changes in the CCN population. For example, zero emissions of ammonia (simulation AMM) will lead to an ammonia-depleted model atmosphere. As defined by Seinfeld and Pandis (2006), nitrate aerosol is prevented from forming in the acidic ammonia-depleted conditions and will likely remain in the gas phase. In addition, without ammonia aerosol mass with WRF/Chem, the sulfate aerosol will take the form of sulfuric acid, which has a much higher experimentally determined κ than ammonium sulfate. Therefore, the elimination of ammonia could lead to increases and decreases in the mass and model-predicted κ of separate species. If the overall response is a decrease in aerosol mass, less aerosol surface area may be available for condensation of organic species potentially decreasing aerosol mass, and so forth.

Throughout it is important to remember that some processes that are significant in the evolution of particles in the atmosphere are not included or are poorly represented in the WRF/Chem setup. In particular, the absence of aqueous-phase production of sulfate and tendency for underprediction of organic aerosol could impact the accuracy of the model output.

9.2 Reference simulation results

RAMS forecasts of N_{ccn} from the REF simulation are in general overpredicted compared to observations from the King Air along the Western Slope. To aid in the comparison, RAMS N_{ccn} are plotted for the western Colorado region between the hours of 12:00 GMT on December 18th and 00:00 GMT on December 19th (Figure 9.4). N_{ccn} is plotted

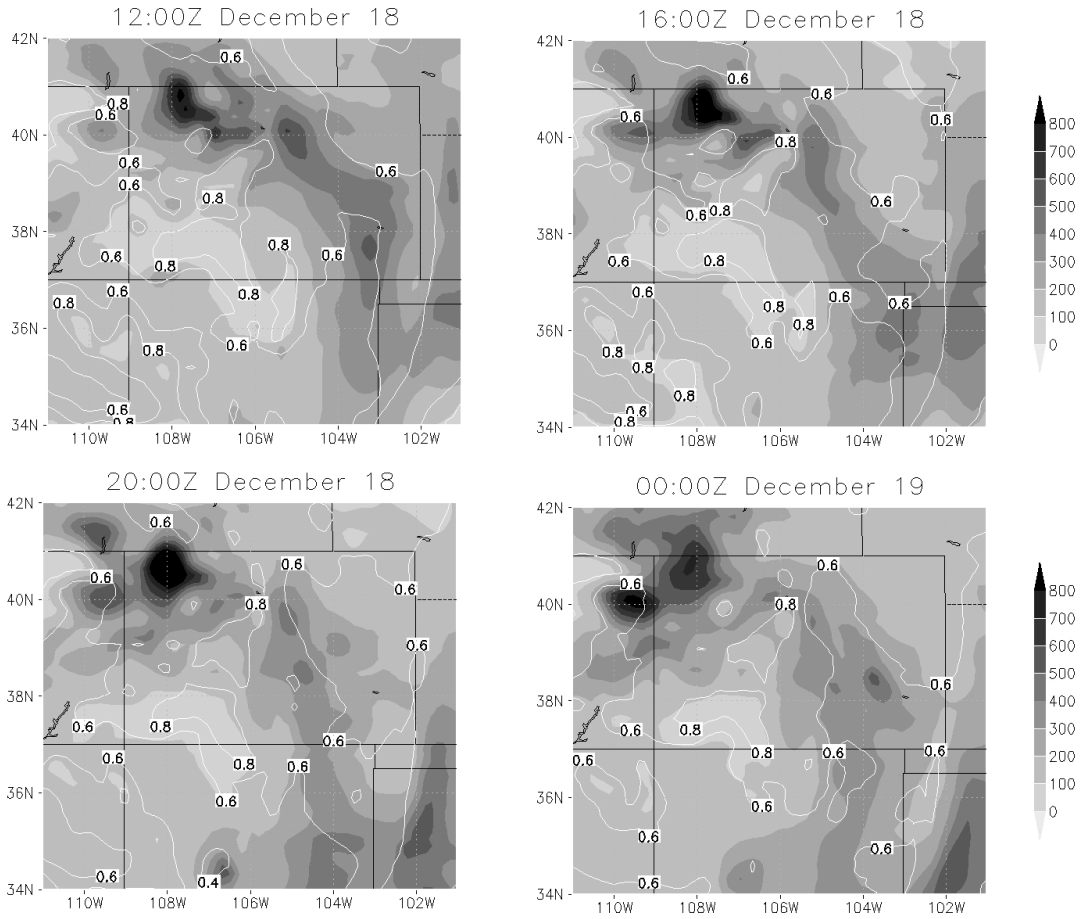

Figure 9.4: A four-panel plot of RAMS N_{ccn} at SS=0.54% (shaded; cm^{-3}) and κ (white contours) from the REF simulation. Plotted for the Western Slope region and at four times including the December 18th observations of the King Air 200T.

for SS=0.54% and at an altitude of 500m agl. This altitude is meant to correspond to the average flight level of the King Air 200T but since RAMS is plotted on a terrain-following level, the model will not exactly match up with the observation height.

Figure 9.4 shows N_{ccn}=100 to 200 cm^{-3} in southwestern Colorado for the entire 12-hour time period. These values fall within the typical range of N_{ccn} observed at this SS for northwesterly flow regimes (see Figure 6.8). Further north, the RAMS N_{ccn} increases, reaching a maximum number concentration greater than 500 cm^{-3} located to the west of SPL. These values exceed any of the observed N_{ccn} during the horizontal transects or vertical profiles on the December 18th flight. Elevated number concentrations of CCN extend to the east and south from the maximum near SPL.

RAMS κ is also plotted in the Figure 9.4 panels and, similar to the validation cases, is predicted high compared to typical continental values. These κ forecasts are especially high when compared against the particles sampled during the King Air flights, which were estimated to have very low hygroscopicity. Again, it seems reasonable to attribute overprediction of κ to a lack of organic aerosol mass predicted in WRF/Chem. The predicted κ decreases in areas where N_{ccn} increases as shown in Figure 9.4. This likely reflects areas of greater amounts of carbonaceous and ammonium aerosol from large anthropogenic sources.

9.2.1 Sensitivity study results

The effects of removing certain emissions on the CCN field are investigated by comparing the WRF/Chem and RAMS output from the sensitivity studies against the reference simulation. The results are given as area-averages in Table 9.2. Quantities of N_{ccn}, N_{cn}, and total accumulation mode aerosol mass from the RAMS forecasts are averaged over the lowest km of the model grid and for the 12 hours between 12:00 GMT December 18th to 00:00 GMT December 19th. The values were also weighted by the horizontal area represented by each grid point.

The domain-averages in Table 9.2 show that removing emissions of some species does not always lead to decreases in N_{ccn} within the modeling system. Although, accumulation mode aerosol mass decreased in all sensitivity simulations compared to REF.

Table 9.2: Model forecast domain-averaged quantities for the reference simulation and the difference between the domain averages of the reference and the sensitivity simulations. Quantities were averaged over the entire domain, weighted by grid-box area, and averaged over the lowest km of the atmosphere and 12:00 GMT December 18 and 00:00 GMT December 19. All sensitivity values are given as the percentage difference from the reference simulation with the sign of the difference marked. Positive differences are bolded. Speciated aerosol mass was derived from WRF/Chem output while the top three quantities were from RAMS.

Quantity	**Units**	**REF**					
			LPS	**DST**	**SUL**	**NOX**	**AMM**
Nccn	cm^{-3}	430	-1	-2	**+10**	-6	**+19**
Ncn	cm^{-3}	774	-1	**+5**	**+21**	-5	**+29**
Aerosol mass	$\mu g/m^3$	1.19	0	-63	-1	-19	-22
Sulfate mass	$\mu g/m^3$	0.33	-1	-36	-42	-3	**+9**
Nitrate mass	$\mu g/m^3$	0.17	0	-76	**+59**	-97	-94
Ammonium mass	$\mu g/m^3$	0.16	0	-56	-12	-31	-100
Carbonaceous mass	$\mu g/m^3$	0.23	0	-87	**+9**	-4	**+4**

The SUL and AMM simulations both resulted in increases in domain-averaged N_{ccn} of 10% and 19% over the REF N_{ccn}. The remaining LPS, DST and NOX all produced small decreases in N_{ccn}. Surprisingly, N_{cn} was increased in the DST simulation compared to REF. This is even harder to explain given that the total aerosol mass decreased in DST by more than 60% over REF indicating that the large number of particles were probably very small. It is possible that in the areas with no anthropogenic emissions in DST, the background SO_2 was able to form numerous sulfuric acid particles through nucleation. Without fresh emissions to condense onto the sulfuric acid aerosol, these particles remained small, keeping the number high but the mass low. While the mass of all aerosol species decreased in DST, sulfate decreased by the lowest percentage, which supports the given theory.

Nitrate aerosol mass underwent large changes between the SUL, NOX and AMM simulations. When NOx emissions are eliminated, almost all the nitrate aerosol mass is, not surprisingly, eliminated as well. A small fraction is produced from the background NOx concentration. When sulfur emissions are removed, nitrate aerosol increased dramatically. This probably occurred because of an increase in the availability of ammonia for formation of ammonium nitrate. The increase in nitrate was a major contributor to the aerosol mass and probably N_{ccn} in the SUL simulation. Finally, in the AMM simulation, nitrate aerosol is once again almost entirely eliminated. As explained by Seinfeld and Pandis (2006), ammonia-poor conditions tend to drive the nitrate mass to the gas phase. However, while nitrate is almost non-existent, the sulfate aerosol mass increased in AMM. With no ammonium mass, the majority of sulfate will exist as sulfuric acid and increase the domain κ. In fact, domain averaged κ was 0.80 in AMM, an 18% increase over REF. Both the increase in sulfate mass and overall hygroscopicity could explain the increase in N_{ccn} in AMM.

Ammonium aerosol mass also decreased in SUL and NOX, probably limited by the reduced amounts of acidic sulfate and nitrate to neutralize. Only small changes in carbonaceous mass were shown in SUL, NOX and AMM. It's possible the small changes resulted from changes in the available surface area of aerosol for condensation of SOA.

Table 9.3 gives the same quantities as in Table 9.2 but averaged over the Western Slope region. The differences between simulations are similar in this subset of the model domain. Again, all emissions removals led to reductions in accumulation mode aerosol

Table 9.3: Same as in Table 9.2 except that the horizontal grid average was for 36˚N to 41˚N and 109˚W to 106˚W.

Quantity	**Units**	**REF**					
			LPS	**DST**	**SUL**	**NOX**	**AMM**
Nccn	cm^{-3}	536	-6	-12	-28	-4	**+7**
Ncn	cm^{-3}	896	-5	-9	-26	-4	**+20**
Aerosol mass	$\mu g/m^3$	1.08	-10	-18	-30	-6	-16
Sulfate mass	$\mu g/m^3$	0.67	-10	-31	-66	-52	-4
Nitrate mass	$\mu g/m^3$	0.04	0	**+50**	**+275**	-88	-75
Ammonium mass	$\mu g/m^3$	0.14	0	0	-14	-7	-100
Carbonaceous mass	$\mu g/m^3$	0.04	0	0	**+25**	-25	**+50**

mass. For the Western Slope only the AMM simulation resulted in an increase in N_{ccn} over REF. The reductions in aerosol mass and N_{ccn} produced by the LPS simulation are proportionally higher on the smaller domain, as expected. It is interesting to note that the reduction in N_{ccn} caused by removing the local point sources is about half of the reduction caused by removal of distant sources. For DST both area and point sources are removed which may contribute to a greater loss in N_{ccn}, but this result still suggests that distant sources played at least as important a role as local point sources in this case.

The impact of emission changes on Western Slope CCN is further investigated with vertical profiles of RAMS N_{ccn} at the locations of the vertical stacks flown on December 18th. The profiles are plotted for the reference simulation, which is compared to the vertical stack

measurements, and all sensitivity simulations. Figure 9.5 shows these profiles for the Cortez stack that was carried out at 19:00Z on December 18th. RAMS underpredicted N_{ccn} at Cortez compared to the observations despite the high model κ (Figure 9.5a). Figure 9.5b shows the vertical profile from REF compared to that from LPS. The two profiles are almost identical which indicates that local point sources had almost no impact on N_{ccn} at this model location and time. The NOX vertical profile (Figure 9.5e) also resembled REF closely but this was likely because of the small amount of nitrate aerosol forecast and, therefore, small

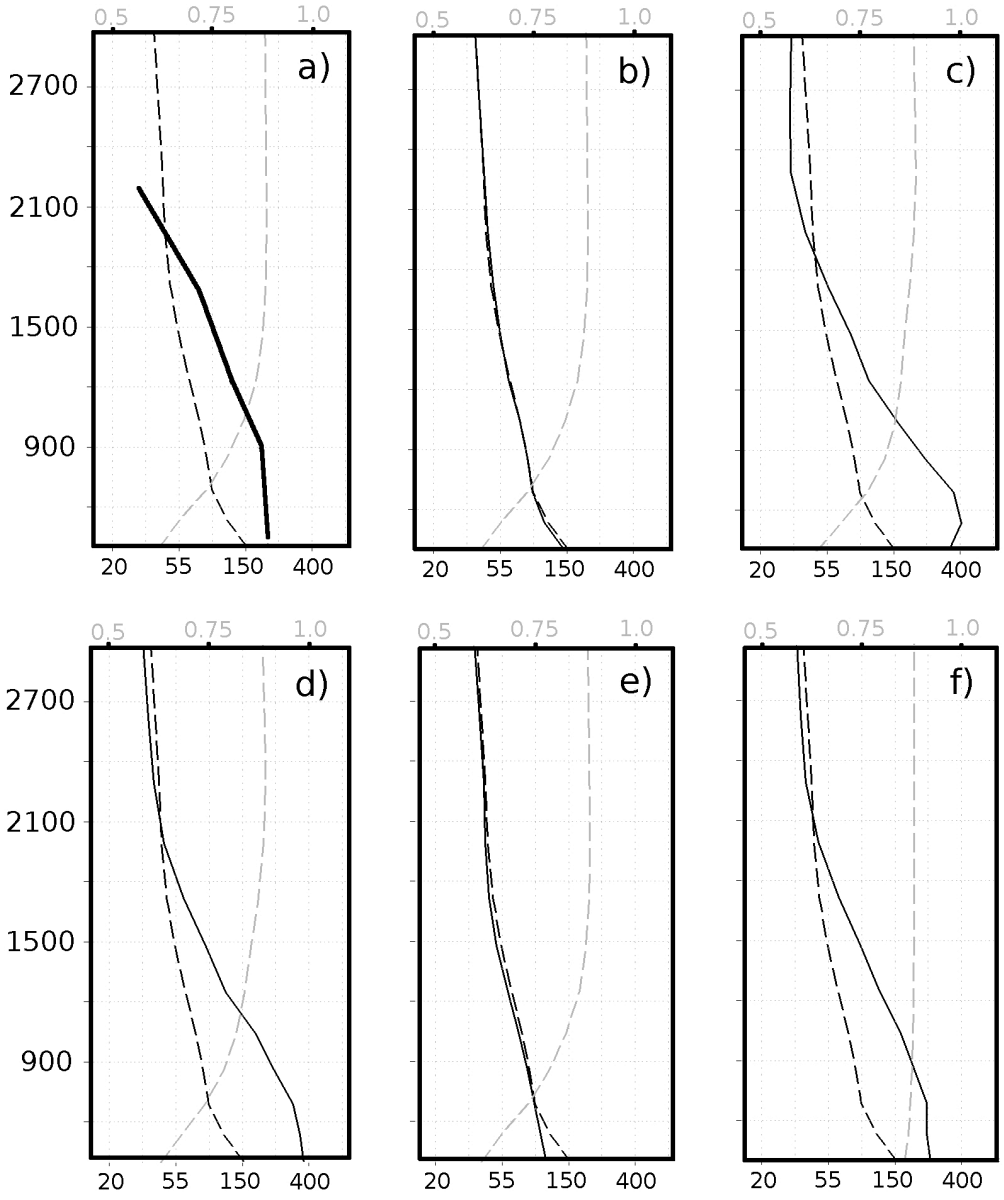

Figure 9.5: Vertical profiles of RAMS N_{ccn} at SS=0.54% (dashed black; cm^{-3}) from the REF simulation. This is plotted with N_{ccn} (solid black; cm^{-3}) and κ (dashed grey) from a) King Air observations (κ from REF), b) LPS, c) DST, d) SUL, e) NOX, and f) AMM. Altitude is in meters msl. The time and location of these profiles are 19:00 GMT December 18th at 37.4˚N and 107.7˚W to correspond to the Cortez vertical stack carried out on this day during ISPA-III.

potential impact of changing these emissions. Profiles for DST, SUL and AMM all show an increase in lower level N_{ccn} compared to REF and a small decrease above 2000m msl. Note the consistently high κ in the AMM profile (Figure 9.5f). This is an excellent example of the impact of the high proportion of aerosol assumed to act as sulfuric acid for computation of the aerosol hygroscopicity in the absence of ammonium aerosol.

The overestimated N_{ccn} in northwestern Colorado suggested by Figure 9.4 is confirmed by the profiles for the SPL stack shown in Figure 9.6. At the lowest height for which aircraft observations of N_{ccn} are available, the model overpredicts by an order of magnitude (Figure 9.6a). Higher up in the atmosphere, 1200m msl and above, the model prediction corresponds remarkably well to the observations. The LPS and SUL profiles (Figures 9.6b and 9.6d) are notable for decreases in lower level N_{ccn} compared to REF. The removal of sulfur emissions reduced the lower level κ and greatly decreased the lower level N_{ccn} both indicating that sulfur dominated the CCN in the REF simulation at this location.

For LPS, the lower level reduction in N_{ccn} and similarity to the REF profile pattern above 1100m msl suggests an upper limit for the influence of local point sources for this case. Due to this location's proximity to the local point sources, emissions had only a short time to age and rise to a higher altitude. This idea will be explored in more detail in the next section.

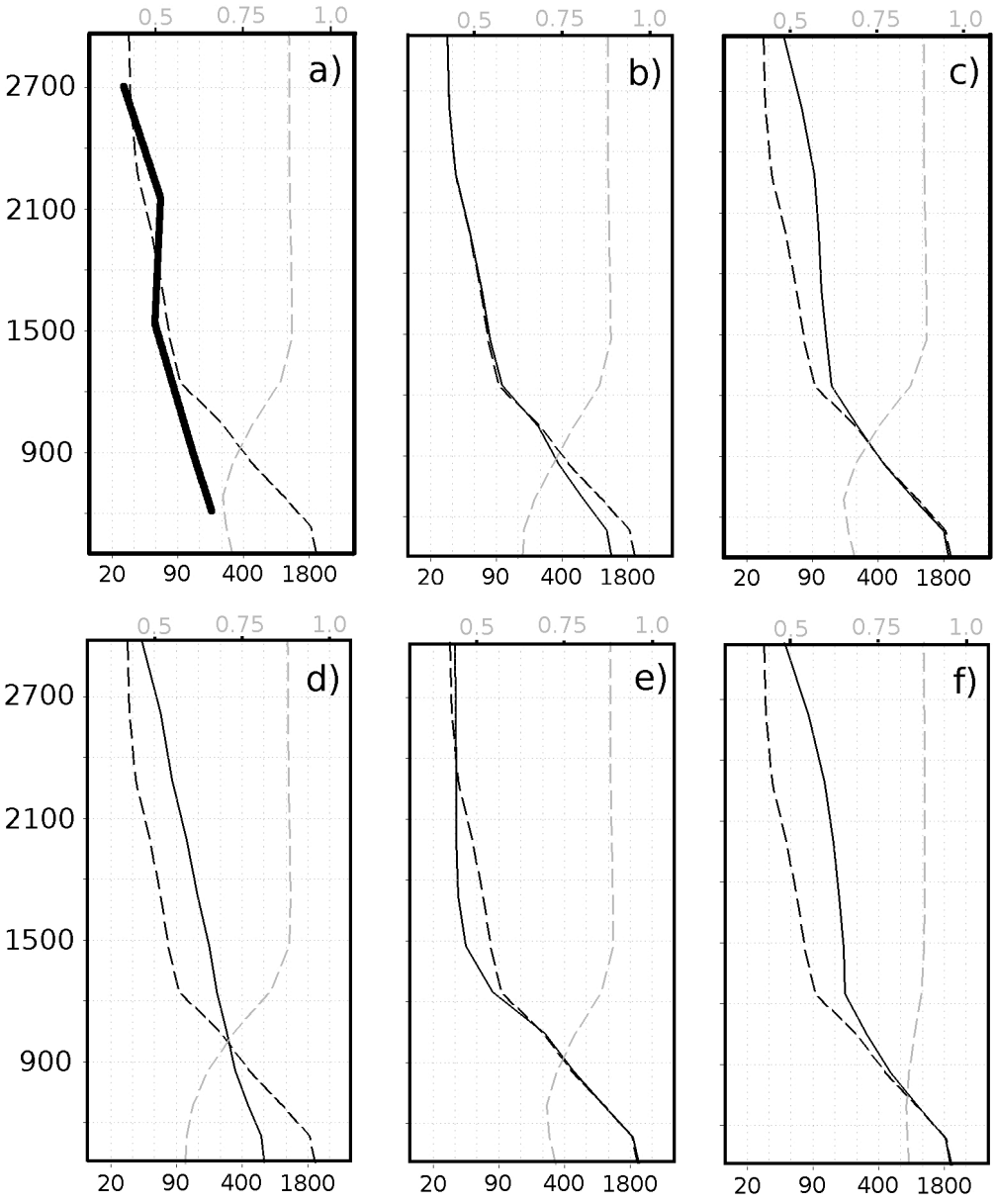

Figure 9.6: Vertical profiles of RAMS N_{ccn} at SS=0.54% (dashed black; cm^{-3}) from the REF simulation. This is plotted with N_{ccn} (solid black; cm^{-3}) and κ (dashed grey) from a) King Air observations (κ from REF), b) LPS, c) DST, d) SUL, e) NOX, and f) AMM. Altitude is in meters msl. The time and location of these profiles are 21:00 GMT December 18th at 40.5°N and 107.0°W to correspond to the Steamboat Springs vertical stack carried out on this day during ISPA-III.

9.2.2 No local point sources

The LPS simulation produced aerosols and CCN in almost identical magnitudes to REF on average across the entire domain (see Table 9.2). The impact of removing local point sources was more visible when averaged over only the local domain (Table 9.3) but still appeared to have only a small influence on the model vertical profiles show in Figures 9.5b and 9.6b. This simulation, however, warrants further investigation because local point sources, particularly in northwestern Colorado, have been linked to CCN observations at SPL (Borys et al., 2000; Borys e al., 2003). Specifically these papers suggested that large contributions to N_{ccn} from nearby point sources of sulfate aerosol led to reductions in precipitation at SPL by the mechanism described in Chapter 4. In contrast, Ward (2006) used a combination of dispersion analysis and surface observations in the Park Range and did not find a link between the local sources and orographic precipitation.

Figure 9.7 shows the proportional difference between REF and LPS N_{ccn} forecasts (SS=0.54%) in the Western Slope region for four different times and at an altitude of 400m agl. The proportional difference is defined as the (REF-LPS)/REF. The impact of specific point sources, the Craig and Hayden power plants in northwestern Colorado and the Four Corners plant in New Mexico are clearly visible as high percentage reductions in N_{ccn} for all four panels. This means that when these point sources are eliminated, proximal N_{ccn} predictions at this altitude are reduced by, at times, more than 30%. The reductions increase during the daytime hours on December 18th, which was a clear day along the Western Slope. This could indicate the impact of photolytic reactions increasing the mass of gas-phase compounds available for condensation onto existing particles or, in the case of sulfate, increase the rate of new particle formation.

The influence of the northwestern Colorado point sources can be seen stretching to the southwest through the Front Range and into New Mexico in Figure 9.7, although the magnitude of the influence is greatly reduced at these distances. Surprisingly, removing the

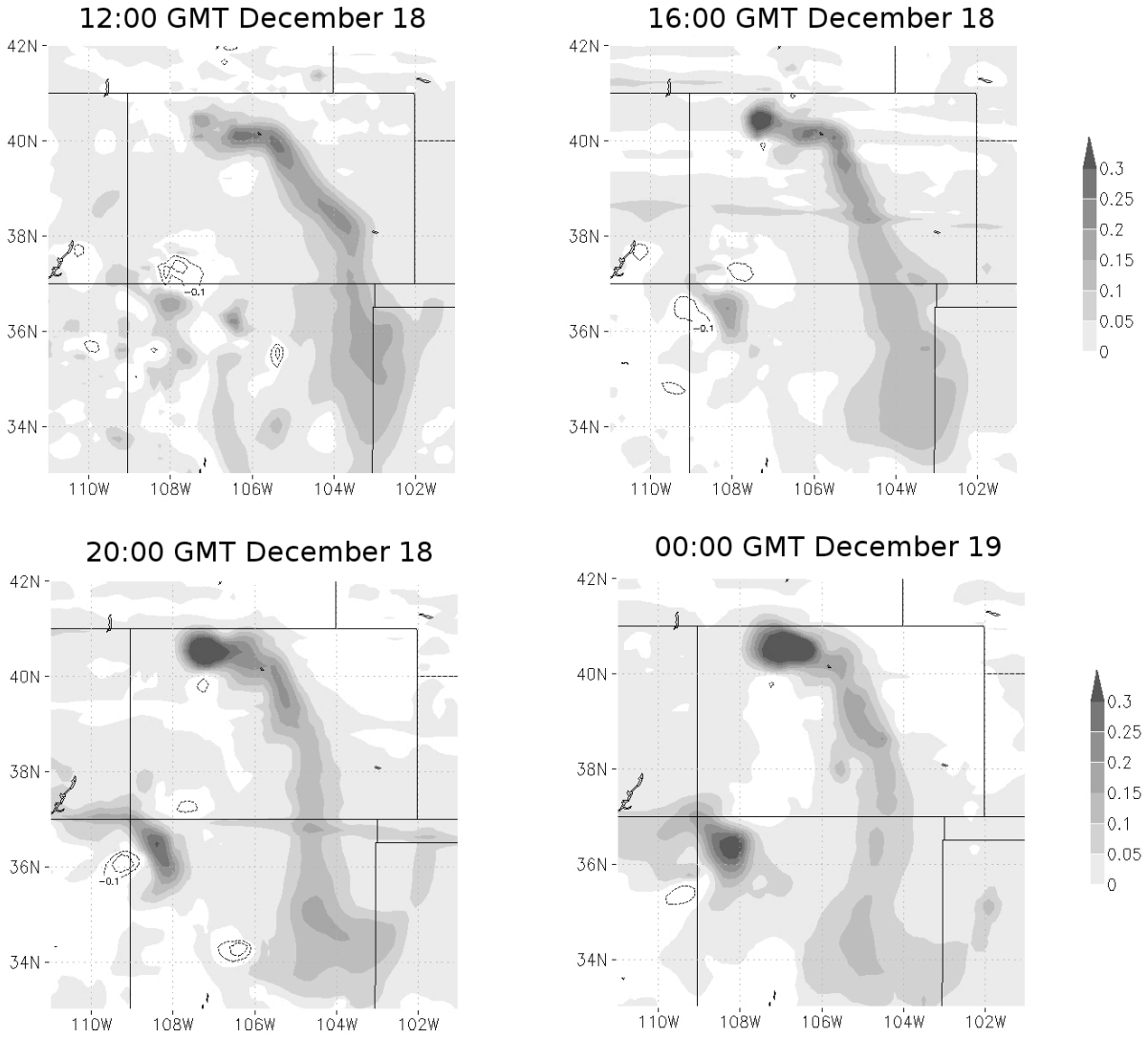

Figure 9.7: A four-panel plot of the proportional difference between the RAMS N_{ccn} forecasts of the REF and LPS simulations along the Western Slope region at an altitude of 400m agl. Positive values represent when the REF N_{ccn} was higher than the LPS N_{ccn}. The SS was 0.54%.

point sources resulted in an increase in N_{ccn} just north of the Four Corners power plant in the MVNP area for the times and altitude in Figure 9.7. It is possible that the decrease in available sulfate aerosol with the removal of the point sources allowed for an increase in nitrate and carbonaceous aerosol as was seen in Tables 9.2 and 9.3. In the small area around MVNP, the increase in these compounds overcame the loss of aerosol mass and number caused by the decrease in sulfate.

Figure 9.6b suggested that the influence of the local point sources on atmospheric CCN did not extend more than a kilometer above the ground, at least in the location where the vertical stack near SPL was performed. To investigate how the difference between REF and LPS changes with height, the same panels shown in Figure 9.7 are shown in Figure 9.8 but at an altitude of 1km agl. The maximum CCN reduction at 400m agl over the large point sources in northwestern Colorado is not evident at 1000m agl at 12:00 GMT and 16:00 GMT. Small reductions in CCN in the LPS simulation still extend southwest to New Mexico at this altitude. Larger reductions in CCN appear by the 20:00 GMT and 00:00 GMT panels east of SPL. Since 00:00 GMT is late afternoon local time, it is possible that vertical mixing occurring during the midday hours lifted some of the particles previously trapped in the boundary layer to higher model altitudes. Or perhaps this is another indication of the impact of solar radiation on aerosol aging.

These figures show that during this case the local point sources had a small but far reaching impact on the model predictions of CCN. Also, the influence of these sources, particularly the major sources in northwestern Colorado and the Four Corners region, was greatest in their immediate vicinity. Although, this local impact was limited vertically at least until late in the model simulated day. It is difficult to compare these results to those of the Chapman et al. (2009) study since they used aerosol optical depth for their analysis instead of aerosol mass. They found domain-averaged reductions in aerosol optical depth

of between 1-17% for non-cloudy areas. In percentage terms these figures match well with those realized in this study.

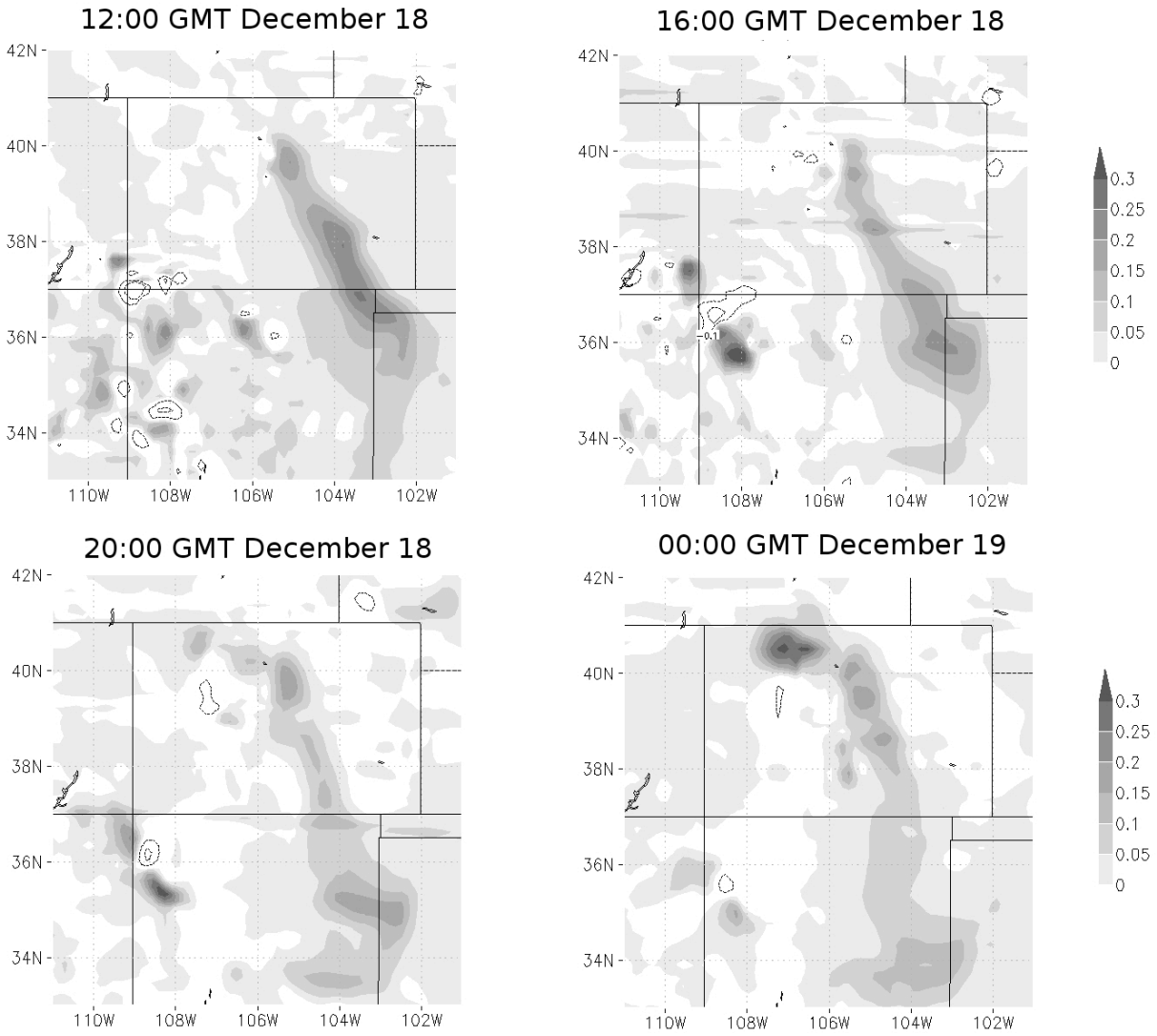

Figure 9.8: A four-panel plot of the proportional difference between the RAMS N_{ccn} forecasts of the REF and LPS simulations along the Western Slope region at an altitude of 1000m agl. Positive values represent when the REF N_{ccn} was higher than the LPS N_{ccn}. The SS was 0.54%.

9.3 Summary

The sensitivity simulations presented in this chapter provide insight into the impacts of sources of aerosol and aerosol precursor gases on the potentially cloud-active particles in the atmosphere. Removal of some emissions led to an increase in the average number concentration of particles and CCN. Ammonia emissions, for example, led to increases in both those quantities while simultaneously reducing the nitrate aerosol mass to near zero. Along the Western Slope, distant sources contributed more CCN to the local environment on the whole than the local point sources. The exception was in the immediate vicinity of major anthropogenic emitters that were shown to contribute in excess of 30% of the CCN to the surrounding area in this case, at low altitudes.

This is largely a theoretical exercise since it is unrealistic to expect anthropogenic emissions of one kind or another to be eliminated completely. Still, this method, made possible by the integration of aerosol forecasts into RAMS, can show those emissions that should be targeted for the greatest reduction in anthropogenic CCN. Perhaps the most important lesson that can be learned from this study is that the neglect of a type of aerosol or an aerosol process could potentially have far-reaching and unexpected impacts on the general accuracy of the model representation of the atmosphere.

Chapter 10

Conclusions

The aim of this study, as laid out in the introduction, was an improved understanding of the abundance and predictability of cloud-active particles in western Colorado. This topic was approached with observations and new modeling techniques that involved the integration of modules within two mesoscale modeling systems. The various conclusions from different cases and different methods described in this dissertation are put together here to form a more complete picture of the CCN in western Colorado.

10.1 Summary of results

It is helpful to review the main results of the research presented in previous chapters when drawing final conclusions. These results are listed here, ordered as they were in this dissertation:

• The RAMS droplet activation scheme was altered to include variations in aerosol hygroscopicity, represented by the κ parameter. The aerosol size representation was kept as a single-mode lognormal distribution.

• Droplet activation in the modified scheme was sensitive to changes in κ for conditions of low SS and/or low r_g. For high SS environments with particles larger than the Aitken mode, effects of hygroscopicity changes on droplet activation were inconsequential.

• This was demonstrated in simulations of a mixed-phase orographic snowstorm in the Colorado Park Range in which κ and r_g were varied. Despite the small-size particle mode observed at SPL for this case, the model predictions of SS were high enough to render aerosol composition effects on droplet number insignificant for the observed range in κ.

• These results, however, support the conclusion of Saleeby et al. (2009) that orographic clouds in this region are sensitive to changes in N_{ccn}, even if N_{ccn} is insensitive to aerosol hygroscopicity.

• CCN upwind of the Colorado mountain region was then explored with 24 days of continuous fall season observation of CCN and CN number concentration at MVNP. Sampling at SS=0.3% the project average was N_{ccn}=302 cm^{-3} and at SS=0.5% the average was N_{ccn}=481 cm^{-3}. CCN varied on a longer time scale than CN. On the whole, no conclusive relationship between N_{ccn} or N_{cn} and wind direction at the surface or aloft was discerned.

• In December, further observation of Western Slope CCN was conducted aboard the UWYO King Air platform. On average, clean conditions that varied very little with latitude were

measured along the Western Slope with N_{ccn} < 200 cm^{-3} for SS=0.27%. A CCN closure attempt resulted in overprediction of N_{ccn} indicating low hygroscopicity particles were sampled.

• Qualitatively, vertical profiles of N_{ccn} at northern and southern Western Slope locations resembled each other when collected on the same day. This suggests that CCN observations at the northern location (SPL) may be a predictor of CCN along the entire Western Slope.

• WRF/Chem forecasts of aerosol number, size and hygroscopicity were integrated into RAMS by means of nudging.

• Validation of the CCN forecasts from this integrated system showed a high bias in κ and N_{ccn} in northwestern Colorado, which could be explained in part by an underprediction of organic aerosol mass. The model performed well forecasting CCN within a plume of anthropogenic pollution along Colorado's Front Range.

• Removing emissions of specific aerosol and aerosol precursor gas species from the WRF/Chem emissions initialization led to complex and sometimes unexpected responses in model N_{ccn}.

• Removing Western Slope point sources from the model emissions resulted in a small overall decrease in regional N_{ccn}. Closer in to the large point sources (within about 50km) the decrease in N_{ccn} exceeded 30% compared to the reference simulation, but only near the surface. Small magnitude decreases in N_{ccn} were forecast to extend southward with the model wind for large distances.

10.2 Conclusions

Several conclusions about the nature of CCN flowing into the Colorado Rocky Mountains from the Western Slope can be drawn from these results. The CCN observed at SPL, MVNP, and on a line between the two sites, was characteristic of rural continental aerosol as defined by Seinfeld and Pandis (2006). For rural continental aerosols, the particle number distribution is dominated by an nuclei (Aitken) mode, particle surface area is largest in the accumulation mode, and particle mass is dictated by a small number of coarse mode particles.

According to Seinfeld and Pandis (2006), the nuclei mode receives its largest contributions of particles from local anthropogenic sources. This is difficult to reconcile with indications from both the sensitivity simulations in Chapter 9 and observations of CCN along the Western Slope in December that local sources make only minor contributions to the regional CCN field. One explanation is that number fluctuations in the nuclei mode do not impact CCN at ambient SS due to their small size. The CCN in this region would then be dependent on the aged, accumulation mode particles that are more likely to have regional or distant origins. The observations from MVNP, where N_{cn} was highly variable but N_{ccn} changed slowly and within a much smaller range, support this view. Additionally, the low activated fraction computed from the measurements suggests that a large number of the ambient particles are too small to activate droplets at the set values of SS.

Estimates of κ derived from size distribution and CCN data at SPL and from the King Air instruments indicated that low hygroscopicity aerosols were sampled and showed very little variation in this respect. This supports the characterization of western Colorado CCN

as deriving from an aged, internally mixed aerosol population. In situ measurements of particle composition are needed to confirm this hypothesis.

A major conclusion of this work is that changes in particle hygroscopicity can be neglected for purposes of modeling CCN effects on winter orographic storms in this region for two reasons. First, a small range in κ was estimated from the SPL and King Air observations, suggesting aerosol hygroscopicity in the region could be represented by a constant κ. Secondly, since updraft speeds are strong within the most important orographic storms from a water resources perspective, parcels carrying potential droplet nuclei reach high values of SS, rendering even large ranges in hygroscopicity insignificant for modification of CCN activity. In the San Juan Mountains, where liquid water content is typically higher compared to the Park Range (SPL), lower values of SS are likely to be observed for similar updraft speeds and precipitation rates. Therefore, variations in aerosol hygroscopicity may be more important in these environments, although large ranges in κ are unlikely to be observed.

In the previous chapters a new method for predicting CCN based on aerosol size, number and hygroscopicity was presented. The developed system showed some ability to forecast CCN in test cases without adding noticeable computation time to WRF/Chem or RAMS. Of course, significant time is required to produce the aerosol forecasts from WRF/Chem that were not needed using the previous scheme in RAMS. The new system will work better in cases for which organic aerosols play a small role as these tend to decrease the overall aerosol hygroscopicity and are not well represented in WRF/Chem (McKeen et al., 2007), or in most numerical models (Heald et al., 2005).

Perhaps the most important lesson to be learned from the model development work is that CCN *can* be predicted using a method similar to the one outlined in this dissertation. However, the uncertainties of these model predictions are considerable and often

unquantifiable because the current representation of atmospheric aerosol in the MADE/SORGAM configuration of WRF/Chem is far from complete. To add to the uncertainty, datasets for validation of this type of model prediction are scarce, with limited coverage in time and space. It is also important to remember that accurate representation of droplet activation is only one piece in a complex microphysical puzzle. The system presented here retains simplifications of some atmospheric processes and does not address others, such as collision-coalescence, which may be more important in the formation of precipitation and are also not well parameterized (e.g. Segal et al., 2007; Levin and Cotton, 2009). Yet, with the added capability to forecast CCN number concentration based on case-specific estimates of aerosol number, size and composition fields, the new modeling system contains a more complete representation of droplet activation compared to the existing prescribed scheme in RAMS.

10.3 Suggestions for future work

A considerable amount of additional research needs to be done on this topic both in observations and in modeling, for which the work presented here is only a first step. Questions remain concerning the chemical composition and mixing state of particles sampled upwind of the Colorado Rocky Mountains for which the ISPA-III observations could provide only speculative answers. Uncertain aerosol chemistry limits our ability to truly understand the CCN activity of ambient aerosol (Stroud et al., 2007).

An observational study that samples these aerosol characteristics could take the form of work by Cubison et al. (2008) in the Los Angeles area. They deployed two SMPS instruments and two Aerosol Mass Spectrometers (AMS), along with a DMT CCN-100 at a

surface site outside of Los Angeles. With two SMPS systems, particles could be binned by size in an extended diameter range of 3nm to 32μm, effectively capturing the entire population of cloud-active aerosols. One AMS measured the mass loadings of basic aerosol chemical species in size bins, although the size range for these measurements was narrow compared to that of the two SMPS. The second AMS was used to analyze the composition of single particles, giving a measure of the mixing state of the ambient aerosol. An identical suite of instruments could be set up at SPL (SPL already regularly operates an SMPS and CCN-100) where they would sample free-tropospheric and often cloud-base level aerosols. These observations, while on the cutting edge, are still limited in space and time and do not produce the validation datasets that model biases and errors could most effectively be evaluated against.

With regard to the modeling of CCN using WRF/Chem and RAMS, specific recommendations arise from the shortcomings of the current scheme. First, aerosol chemistry and dynamics should be set up to run online within RAMS. This would eliminate any discrepencies between the meteorology that result from using two separate models, and allow for two-way interaction between aerosols and clouds (cloud effects on aerosols). Next, dust and sea-salt need to be made microphysically active within RAMS. This task is not trivial and tests the limitations of the lookup table droplet activation scheme because of the different size ranges occupied by these species and the typical internal mixture forecasted by WRF/Chem. Dust aerosol, in particular, can act as IN in addition to their role as CCN. The prediction of IN was not addressed in this dissertation, but the integration of aerosol forecasts into RAMS will aid in the development of the existing ice crystal activation parameterization.

Accommodation of size-dependent composition for all species would be a worthwhile addition to the RAMS droplet activation scheme. This would require size-

dependent forecasts of aerosol composition, which are at this time prohibitively expensive computationally. Therefore, such a development in RAMS could be several years off, although the need has been expressed by several observational studies, notably Cubison et al. (2008).

Finally, what does this work mean in terms of recommendations for the direction of the science of aerosol/cloud interactions? To echo the recommendation of Medina et al. (2007), new datasets of CCN observations are still needed. This is now important also from a modeling perspective as forecasts of CCN are becoming available and ground truth, so to speak, is in short supply.

Although, as suggested by the work in this dissertation, CCN or CDNC forecasts could be simplified for future studies by using a prescribed aerosol composition. This is recommended for studies of environments with typically high supersaturations (SS > 0.5%) and moderate to large aerosol size distribution median radius (r_g > 0.1μm). While dependent on ambient conditions, this simplification could free up computation time for other, more influential processes in some simulations.

It is hoped that some of the methods presented here, especially the use of κ for representing the hygroscopicity of complex aerosol mixtures, will be applied in other models where less flexible systems are currently used. The purpose of the WRF/Chem and RAMS arrangement, and perhaps other systems that might be improved using this work, is future application to the range of cloud regimes that are impacted by increases in atmospheric aerosols. A better knowledge-base on the nature of cloud-active aerosols, to which this dissertation aimed to add, is essential for our understanding of the these cloud regimes and the potential for anthropogenic changes.

REFERENCES

Abdul-Razzak, Hayder and Steven J. Ghan, 2000: A parameterization of aerosol activation 2. Multiple aerosol types. *J. Geophys. Res.*, **105**, 6837-6844.

Abdul-Razzak, Hayder and Steven J. Ghan, 2002: A parameterization of aerosol activation 3. Sectional representation. *J. Geophys. Res.*, **107**(D3), doi:10.1029/2001JD000483.

Abdul-Razzak, H., S. J. Ghan, and C. Rivera-Carpio, 1998: A parameterization of aerosol activation 1. Single aerosol type. *J. Geophys. Res.*, **103**, 6123-6132.

Ackermann, Andrew S., Owen B. Toon, Jonathan P. Taylor, Doug W. Johnson, Peter V. Hobbs, and Ronald J. Ferek, 2000: Effects of aerosols on cloud albedo: evaluation of Twomey's parameterization of cloud susceptibility using measurements of ship tracks. *J. Atmos. Sci.*, **57**, 2684-2695.

Ackermann, I.J., H. Hass, M. Memmesheimer, A. Ebel, F.S. Binkowski, U. Shankar, 1998: Modal aerosol dynamics model for Europe: Development and first applications. *Atmos. Env.*, **32**, 2981-2999.

Albrecht, Bruce A., 1989: Aerosols, cloud microphysics, and fractional cloudiness. *Science*, **245**, 1227-1230.

Andreae, M. O., and D. Rosenfeld, 2008: Aerosol–cloud–precipitation interactions. Part 1. The nature and sources of cloud-active aerosols. *Earth-Sci. Rev.*, **89**, doi:10.1016/j.earscirev.2008.03.001.

Andrejczuk, M., J. M. Reisner, B. Henson, M. K. Dubey, and C. A. Jeffery, 2008: The potential impacts of pollution on a nondrizzling stratus deck: Does aerosol number matter more than type? *J. Geophys. Res.*, **113**, D19204, doi:10.1029/2007JD009445.

Antilla, T., and V.-M. Kerminen, 2007: On the contribution of Aitken mode particles to cloud droplet populations at continental background areas – a parametric sensitivity study. *Atmos. Chem. Phys.*, **7**, 4625-4637.

Arteta, J., S. Cautenet, M. Taghavi, and N. Audiffren, 2006: Impact of two chemistry mechanisms fully coupled with mesoscale model on the atmospheric pollutants distribution. *Atmos. Env.*, **40**, 7983-8001.

Barahona, D. and A. Nenes, 2007: Parameterization of cloud dropelt formation in large-scale models: Including effects of entrainment. *J. Geophys. Res*., **112**(D16), D16206, doi:10.1029/2007JD008473.

Bauer, S. E., D. Koch, N. Unger, S. M. Metzger, D. T. Shindell, and D. G. Streets, 2007: Nitrate aerosols today and in 2030: a global simulation including aerosols and tropospheric ozone. *Atmos. Chem. Phys*., **7**, 5043-5059.

Binkowski, Francis S. and Uma Shankar, 1995: The Regional Particulate Matter Model: 1. Model description and preliminary results. *J. Geophys. Res*., **100**(D12), 26,191-26,209.

Bond, T. C., D. G. Streets, K. F. Yarber, S. M. Nelson, J-H. Woo, and Z. Klimont, 2004: A technology-based global inventory of black and organic carbon emissions from combustion. *J. Geophys. Res*., **109**, D14203, doi:10.1029/2003JD003697.

Borys, R. D., D. H. Lowenthal, S. A. Cohn, and W. O. J. Brown, 2003: Mountaintop and radar measurements of anthropogenic aerosol effects on snow growth and snowfall rate. *Geophys. Res. Lett*., **30**(10), doi:10.1029/2002GL016855.

Borys, R. D., D. H. Lowenthal, and D. L. Mitchell, 2000: The relationship among cloud microphysics, chemistry, and precipitation rate in cold mountain clouds. *Atmos. Environ.,* **34**, 2593-2602.

Borys, R. D., and M. Wetzel, 1997: Storm Peak Laboratory: A research, teaching, and service facility for the atmospheric sciences. *Bull. Amer. Meteorol. Soc*., **78**(10), 2115-2123.

Boucher, Olivier and Ulrike Lohmann, 1995: The sulfate-CCN-cloud albedo effect. *Tellus*, **47B**, 281-300.

Bougiatioti, A., C. Fountoukis, N. Kalivitis, S. N. Pandis, A. Nenes, and N. Mihalopoulos, 2009: Cloud condensation nuclei measurements in the marine boundary layer of the eastern Mediterranean: CCN closure and droplet growth kinetics. *Atmos. Chem. Phys.,* **9**, 7053-7066.

Breon, Francios-Marie, Didier Tanre, Sylvia Generoso, 2002: Aerosol effect on cloud droplet size monitored from satellite. *Science*, **295**, 834-838.

Cantrell, W., G. Shaw, G. R. Cass, Z. Chowdhury, L. S. Hughes, K. A. Prather, S. A. Guazzotti, and K. R. Coffee, 2001: Closure between aerosol particles and cloud condensation nuclei at Kaashidhoo Climate Observatory. *J. Geophys. Res.-Atmos*., **106**, 28,711-28,718.

Carlton, A. G., C. Wiedinmyer, and J. H. Kroll, 2009: A review of secondary organic aerosol (SOA) formation from isoprene. *Atmos. Chem. Phys*., **9**, 4987-5005.

Chapman, E. G., W. I. Gustafson Jr., R. C. Easter, J. C. Barnard, S. J. Ghan, M. S. Pekour, and J. D. Fast, 2009: Coupling aerosol-cloud-radiative processes in the WRF-Chem model: Investigating the radiative impact of elevated point sources. *Atmos. Chem. Phys*., **9**, 945-964.

Charlson, Robert J., John H. Seinfeld, Athanasios Nenes, Markku Kulmala, Ari Laaksonen and M. Cristina Facchini, 2001: Reshaping the theory of cloud formation. *Science*, **292**, 2025-2026.

Chen, Jianjun and Robert J. Griffen, 2005: Modeling secondary organic aerosol formation from oxidation of alpha-pinene, beta-pinene and *d*-limonene. *Atmos. Environ.*, **39**, 7731-7744.

Cheng, W. Y. Y., G. Carrio, W. R. Cotton, and S. M. Saleeby, 2009: Influence of cloud condensation and giant cloud condensation nuclei on the development of precipitating trade wind cumuli in a large eddy simulation. *J. Geophys. Res.-Atmos.*, **114**, D08201, doi:10.1029/2008JD011011.

Chuang, P. Y., D. R. Collins, H. Pawlowska, J. R. Snider, H. H. Jonsson, J. L. Brenguier, Richard C. Flagan, and John H. Seinfeld, 2000: CCN measurements during ACE-2 and their relationship to cloud microphysical properties. *Tellus*, **52B**, 843-867.

Chuang, Catherine C. and Joyce E. Penner, 1995: Effects of anthropogenic sulfate on cloud drop nucleation and optical properties. *Tellus*, **47B**, 566-577.

Chung, S. H. and J. H. Seinfeld, 2002: Global distribution and climate forcing of carbonaceous aerosols. *J. Geophys. Res.*, **107**(D19), 4407, doi:10.1029/2001JD001397.

Clarke, A. D., S. R. Owens, and J. C. Zhou, 2006: An ultrafine sea-salt flux from breaking waves: Implication for cloud condensation nuclei in the remote marine atmosphere*. J. Geophys. Res.*, **111**(D6), D06292, doi:10.1029/2005JD006565.

Collett, Jeffrey L. Jr., Pierre Herckes, Sarah Youngster, and Taehyoung Lee, 2008: Processing of atmospheric organic matter by California radiation fogs. *Atmos. Res.*, **87**, 232-241.

Collett, J. L. Jr., B. Oberholzer, L. Mosimann, J. Staehelin, and A. Waldvogel, 1993: Contributions of cloud processes to precipitation chemistry in mixed phase clouds. *Water, Air and Soil Pollution*, **68**, 43-57.

Contini, D., A. Genga, D. Cesari, M. Siciliano, A. Donateo, M. C. Bove, and M. R. Guascito, 2010: Characterisation and source apportionment of PM10 in an urban background. *Atmos. Res.*, **95**, 40-54.

Cotton, William R., Bjorn B. Stevens, Graham Feingold, and Robert L. Walko, 1992: A model for simulating the Twomey effect. *Third International Cloud Modeling Workshop*, Toronto, Canada, 10-14 Aug. 1992.

Cotton, W. R., R. A. Pielke Sr., R. L. Walko, G. E. Liston, C. J. Tremback, H. Jiang, R. L. McAnelly, J. Y. Harrington, M. E. Nicholls, G. G. Carrio, and J. P. McFadden, 2003: RAMS 2001: Current status and future directions. *Meteorol. Atmos. Phys.*, **82**, 5-29.

Covert, David S., John L. Gras, Alfred Wiedensohler, Frank Stratmann, 1998: Comparison of directly measured CCN with CCN modeled from the number-size distribution in the marine boundary layer during ACE 1 at Cape Grim, Tasmania. *J. Geophys. Res.*, **103**, 16,597-16,608.

Cubison, M.J., B. Ervens, G. Feingold, K.S. Docherty, I.M. Ulbrich, L. Shields, K. Prather, S. Hering, J.L. Jimenez, 2008: The influence of chemical composition and mixing state of Los

Angeles urban aerosol on CCN number and cloud properties. *Atmos. Chem. Phys.*, **8**, 5649-5667.

DeBell, L. J., K. A. Gebhart, J. L. Hand, W. C. Malm, M. L. Pitchford, B. A. Schichtel, and W. H. White, 2006: Spatial and seasonal patterns and temporal variability of haze and its constituents in the United States: Report IV. Colorado State University, Fort Collins, CO.

Delene, D. J. and T. Deshler, 2000: Calibration of a photometric cloud condensation nucleus counter designed for deployment on a balloon package. *J. Atmos. Oceanic Technol.*, **17**, 459-467.

DeMott, P.J., D.J. Cziczo, A. J. Prenni, D. M. Murphy, S. M. Kreidenweis, D. S. Thomson, R. Borys, and D.C. Rogers, 2003: Measurements of the concentration and composition of nuclei for cirrus formation. *Proceedings of the Nat. Academy of Sciences*, **100**, No. 25, 14655-14660.

Dentener, F., S. Kinne, T. Bond, O. Boucher, J. Cofala, S. Generoso, P. Ginoux, S. Gong, J. J. Hoelzemann, A. Ito, L. Marelli, J. E. Penner, J.-P. Putaud, C. Textor, M. Schulz, G. R. van der Werf, and J. Wilson, 2006: Emissions of primary aerosol and precursor gases in the years 2000 and 1750 prescribed data-sets for AeroCom. *Atmos. Chem. Phys.*, **6**, 4321-4344.

Dudhia, Jimy and Mitchell W. Moncrieff, 1989: A three-dimensional numerical study of an Oklahoma squall line containing right-flank supercells. *J. Atmos. Sci.*, **46**(21), 3363-3392.

Dusek, U., G. P. Frank, J. Curtius, F. Drewnick, J. Schneider, A. Kurten, D. Rose, M. O. Andreae, S. Borrmann, and U. Poschl: Enhanced organic mass fraction and decreased hygroscopicity of cloud condensation nuclei (CCN) during new particle formation events. *Geophys. Res. Lett.*, **37**, L03804, doi:10.1029/2009GL040930.

Dusek, U., G.P. Frank, L. Hildebrandt, J. Curtius, J. Schneider, S. Walter, D. Chand, F. Drewnick, S. Hings, D. Jung, S. Borrmann, M.O. Andreae, 2006: Size matters more than chemistry for cloud-nucleating ability of aerosol particles. *Science*, **312**, 1375-1378.

Easter, Richard C., Steven J. Ghan, Yang Zhang, Rick D. Saylor, Elaine G. Chapman, Nels S. Laulainen, Hayder Abdul-Razzak, L. Ruby Leung, Xindi Bian, and Rahul A. Zaveri, 2004: MIRAGE: Model description and evaluation of aerosols and trace gases. *J. Geophys. Res.,* **109**, D20210, doi:10.1029/2004JD004571.

Eidhammer, Trude, Paul J. DeMott, Sonia M. Kreidenweis, 2009: A comparison of heterogeneous ice nucleation parameterizations using a parcel model framework. *J. Geophys. Res.*, **114**, D06202, doi:10.1029/2008JD011095.

Eltgroth, M. W. and P. V. Hobbs, 1979: Evolution of particles in the plumes of coal-fired power-plants .2. Numerical-model and comparisons with field measurements. *Atmos. Environ.*, **13**, 953-975.

Engstrom, A. and L. Magnusson, 2009: Estimating trajectory uncertainties due to flow dependent erros in the atmospheric analysis. *Atmos. Chem. Phys.*, **9**, 8857-8867.

Ervens, Barbara, Michael Cubison, Elisabeth Andrews, Graham Feingold, John A. Ogren, Jose L. Jimenez, Peter DeCarlo, Athanasios Nenes, 2007: Prediction of cloud condensation

nucleus number concentration using measurements of aerosol size distributions and composition and light scattering enhancement due to humidity. *J. Geophys. Res*., **112**, D10S32, doi:10.1029/2006JD007426.

Ervens, Barbara, Graham Feingold, Sonia M. Kreidenweis, 2005: Influence of water-soluble organic carbon on cloud drop number concentration. *J. Geophys. Res*., **110**, D18211, doi:10.1029/2008JD011095.

Fan, Song-Miao, Larry W. Horowitz, Hiram Levy II, and Walter J. Moxim, 2004: Impact of air pollution on wet deposition of mineral dust aerosols. *Geophys. Res. Let*., **31**, L02104, doi:10.1029/2003GL018501.

Fast, Jermone D., William I. Gustafson Jr., Richard C. Easter, Rahul A. Zaveri, James C. Bernard, Elaine G. Chapman, Georg A. Grell, and Steven E. Peckham, 2006: Evolution of ozone, particulates, and aerosol direct radiative forcing in the vicinity of Houston using a fully coupled meteorology-chemistry-aerosol model. *J. Geophys. Res*., **111**, D21305, doi:10.1029/2005JD006721 .

Feingold, Graham, 2003: Modeling of the first indirect effect: Analysis of measurement requirements. *Geophys. Res. Lett*., **30**, No. 19, 1997-2001.

Feingold, G. and A. J. Heymsfeld, 1992: Parameterizations of condensational growth of droplets for use in General-Circulation Models. *J. Atmos. Sci*, **49**, 2325-2342.

Feingold, G., W. R. Cotton, S. M. Kreidenweis, and J. T. Davis, 1999: The impact of giant cloud condensation nuclei on drizzle formation in stratocumulus: Implications for cloud radiative properties. *J. Atmos. Sci*., **56**, 4100-4117.

Feingold, G., S. M. Kreidenweis, B. Stevens, and W. R. Cotton, 1996: Numerical simulation of stratocumulus processing of cloud condensation nuclei through collision-coalescence. *J. Geophys. Res*., **101**, 21,391-21,402.

Ferek Ronald J., Dean A. Hegg, Peter V. Hobbs, Philip Durkee, and Kurt Nielsen, 1998: Measurements of ship-induced tracks in clouds off the Washington coast. *J. Geophys. Res.*, **103**(18), 23,199-23,206.

Fountoukis, Christos and Athanasios Nenes, 2005: Continued development of a cloud droplet formation parameterization for global climate models. *J. Geophys. Res*., **110**, D11212, doi:10.1029/2004JD005591.

Furutani, Hiroshi, Manuel Dall'osto, Greg C. Roberts, and Kimberly A. Prather, 2008: Assessment of the relative importance of atmospheric aging on CCN activity derived from field observations. *Atmos. Environ*., **42**, 3130-3142.

Fuzzi, S., M. O. Andreae, B. J. Huebert, M. Kulmala, T. C. Bond, M. Boy, S. J. Doherty, A. Guenther, M. Kanakidou, K. Kawamura, V.-M. Kerminen, U. Lohmann, L. M. Russell, and U. Poschl, 2006: Critical assessment of the current state of the scientific knowledge, terminology, and research needs concerning the role of organic aerosols in the atmosphere, climate, and global change. *Atmos. Chem. Phys*., **6**, 2017-2038.

Ghan, Steven J., Gina Guzman, and Hayder Abdul-Razzak, 1998: Competition between sea salt and sulfate particles as cloud condensation nuclei. *J. Atmos. Sci*., **55**, 3340-3348.

Ghan, Steven J., and Stephen E. Schwartz, 2007: Aerosol properties and processes. *Bull. Amer. Meteor. Soc*., **88**, 1059-1083.

Ginoux, P., M. Chin, I. Tegen, J. Prospero, B. Holben, O. Dubovik, and S. Lin. Sources and distributions of dust aerosols simulated with the GOCART model. *J. Geophys. Res*., **106**, 20,255-20,273.

Givati, A., and D. Rosenfeld, 2004: Quantifying precipitation suppression due to air pollution. *J. Appl. Meteor*., **44**, 1298-1315.

Grell, G.A., S.E. Peckham, R. Schmitz, S.A. McKeen, G. Frost, W.C. Skamarock, B. Eder, 2005: Fully coupled "online" chemistry within the WRF model. *Atmos. Env.*, **39**, 6957-6975.

Guenther, A., T. Karl, P. Harley, C. Wiedinmyer, P. I. Palmer, and C. Geron, 2006: Estimates of global terrestrial isoprene emissions using MEGAN (Model of Emissions of Gases and Aerosols from Nature). *Atmos. Chem. Phys.*, **6**, 3181-3210.

Gunn, Ross and B. B. Phillips, 1957: An experimental investigation of the effect of air pollution on the initiation of rain. *J. Meteor*., **14**, 272-280.

Gunthe, S. S., S. M. King, D. Rose, Q. Chen, P. Roldin, D. K. Farmer, J. L. Jimenez, P. Artaxo, M. O. Andreae, S. T. Martin, and U. Pöschl, 2009: Cloud condensation nuclei in pristine tropical rainforest air of Amazonia: size-resolved measurements and modeling of atmospheric aerosol composition and CCN activity. *Atmos. Chem. Phys. Discuss*., **9**, 3811–3870.

Gustafson, William I, Elaine G. Chapman, Steven J. Ghan, Richard C. Easter, and Jerome D. Fast, 2007: Impact on modeled cloud characteristics due to simplified treatment of unifrom cloud condensation nuclei during NEAQS 2004. *Geophys. Res. Lett*., **34**, L19809, doi:10.1029/2007GL030021.

Harrington, J. Y., 1997: The effects of radiative and microphysical processes on simulated warm and transition season Arctic stratus. Ph.D. thesis, Colorado State University, Colorado, United States, 289 pp.

Haywood, James and Olivier Boucher, 2000: Estimates of the direct and indirect radiative forcing due to tropospheric aerosols: A review. *Rev. Geophys.,* **38**, 513-543.

Heald, C. L., A. H. Goldstein, J. D. Allan, A. C. Aiken, E. Apel, E. L. Atlas, A. K. Baker, T. S. Bates, A. J. Beyersdorf, D. R. Blake, T. Campos, H. Coe, J. D. Crounse, P. F. DeCarlo, J. A. de Gouw, E. J. Dunlea, F. M. Flocke, A. Fried, P. Goldan, R. J. Griffin, S. C. Herndon, J. S. Holloway, R. Holzinger, J. L. Jimenez, W. Junkermann, W. C. Kuster, A. C. Lewis, S. Meinardi, D. B. Millet, T. Onasch, A. Polidori, P. K. Quinn, D. D. Riemer, J. M. Roberts, D. Salcedo, B. Sive, A. L. Swanson, R. Talbot, C. Warneke, R. J. Weber, P. Weibring, P. O. Wennberg, D. R. Worsnop, A. E. Wittig, R. Zhang, J. Zheng, and W. Zheng, 2008: Total observed organic carbon (TOOC) in the atmosphere: a synthesis of North American observations. *Atmos. Chem. Phys*., **8**, 2007-2025.

Heald, Colette L., Daniel J. Jacob, Rokjin J. Park, Lynn M. Russell, Barry J. Huebert, John H. Seinfeld, Hong Liao, and Rodney J. Weber, 2005: A large organic aerosol source in the free troposphere missing from current models. *Geophys. Res. Let.,* **32**, L18809, doi:10.1029/2005GL023831.

Hegg, D. A., D. S. Covert, H. H. Jonsson, and R. Woods, 2009: Differentiating natural and anthropogenic cloud condensation nuclei in the California coastal zone. *Tellus*, **61B**, 669-676.

Heymsfield, A. J., and R. M. Sabin, 1989: Cirrus crystal nucleation by homogeneous freezing of solution droplets. *J. Atmos. Sci*, **46**, 2252-2264.

Hobbs, Peter V., Jeffrey L. Stitch, and Lawrence F. Radke, 1980: Cloud-active nuclei from coal-fired electric power plants and their interactions with clouds. *J. Appl. Meteor*., **19**, 439-451.

Hodzic, A., J. L. Jimenez, S. Madronich, A. C. Aiken, B. Bessagnet, G. Curci, J. Fast, J.-F. Lamarque, T. B. Onasch, G. Roux, J. J. Schauer, E. A. Stone, and I. M. Ulbrich, 2009: Modeling organic aerosols during MILAGRO: importance of biogenic secondary organic aerosols. *Atmos. Chem. Phys*., **9**, 6946-6982.

Hong, S. Y. and H. L. Pan, 1996: Nonlocal boundary layer vertical diffusion in a Medium-Range Forecast Model. *Monthly Weather Review*, **124**(10), 2322-2339.

Hsieh, W. C., A. Nenes, R. C. Flagan, J. H. Seinfeld, G. Buzorius, and H. Jonsson, 2009: Parameterization of cloud droplet size distributions: Comparison with parcel models and observations. *J. Geophys. Res.*, **114**, D11205, doi:10.1029/2008JD011387.

Hudson, James G., 2007: Variability of the relationship between particle size and cloud-nucleating ability. *Geophys. Res. Lett*., **34**, L08801, doi:10.1029/2006GL028850.

Hyslop, Nicole P. and Warren H. White, 2008: An evaluation of interagency monitoring of protected visual environments (IMPROVE) collocated precision and uncertainty estimates. *Atmos. Environ*., **42**, 2691-2705.

Jacobson, Mark Z., Yoram J. Kaufman, and Yinon Rudich, 2007: Examining feedbacks of aerosols to urban climate with a model that treats 3-D clouds with aerosol interactions. *J. Geophys. Res*., **112**, D24205, doi:10.1029/2007JD008922.

Jiang, Hongli, Graham Feingold, and William R. Cotton, 2002: Simulations of aerosol-cloud-dynamical feedbacks resulting from entrainment of aerosol into the marine boundary layer during the Atlantic Stratocumulus Transition Experiment. *J. Geophys. Res.*, **107**(D24), 4813, doi:10.1029/2001JD001502.

Jiang, Q., and R. B. Smith, 2003: Cloud timescales and orographic precipitation. *J. Atmos. Sci.*, **60**, 1543-1560.

J. L. Jimenez, M. R. Canagaratna, N. M. Donahue, A. S. H. Prevot, Q. Zhang, J. H. Kroll, P. F. DeCarlo, J. D. Allan, H. Coe, N. L. Ng, A. C. Aiken, K. S. Docherty, I. M. Ulbrich, A. P. Grieshop A. L. Robinson, J. Duplissy, J. D. Smith, K. R. Wilson, V. A. Lanz, C. Hueglin, Y. L. Sun, J. Tian, A.

Laaksonen, T. Raatikainen, J. Rautiainen, P. Vaattovaara, M. Ehn, M. Kulmala, J. M. Tomlinson, D. R. Collins, M. J. Cubison, E. J. Dunlea, J. A. Huffman, T. B. Onasch, M. R. Alfarra, P. I. Williams, K. Bower, Y. Kondo, J. Schneider, F. Drewnick, S. Borrmann, S. Weimer, K. Demerjian, D. Salcedo, L. Cottrell, R. Griffin, A. Takami, T. Miyoshi, S. Hatakeyama, A. Shimono, J. Y Sun, Y. M. Zhang, K. Dzepina, J. R. Kimmel, D. Sueper, J. T. Jayne, S. C. Herndon, A. M. Trimborn, L. R. Williams, E. C. Wood, A. M. Middlebrook, C. E. Kolb, U. Baltensperger, D. R. Worsnop, 2009: Evolution of organic aerosols in the atmosphere, *Science*, **326**, 1525-1530.

Jirak, I. L. and W. R. Cotton, 2006: Effect of air pollution on precipitation along the front range of the Rocky Mountains, *J. Appl. Meteor. Climato*., **45**, 236-246.

Kain, J. S., and J. M. Fritsch, 1993: Convective parameterization for mesoscale models: The Kain-Fritsch scheme. *Meteor. Mon*., **46**, 165-170.

Kanakidou, M. J. H. Seinfeld, S. N. Pandis, I. Barnes, F. J. Dentener, M. C. Facchini, R. Van Dingenen, B. Ervens, A. Nenes, C. J. Nielsen, E. Swietlicki, J. P. Putaud, Y. Blakanski, S. Fuzzi, J. Horth, G. K. Moortgat, R. Winterhalter, C. E. L. Myhre, K. Tsigaridis, E. Vignati, E. G. Stephanou, and J. Wilson, 2005: Organic aerosol and global climate modeling: a review. *Atmos. Chem. Phys*., **5**, 1053-1123.

Kanakidou, M., K. Tsigaridis, F. J. Dentener, and P. J. Crutzen, 2000: Human-activity-enhanced formation of organic aerosols by biogenic hydrocarbon oxidation. *J. Geophys. Res*., **105**, 9243-9254.

Kaufman, Y. J., D. Tanre, and O. Boucher, 2002: A satellite view of aerosols in the climate system. Review. *Nature*, **419**, 215-223.

Khain, A. P., A. Pokrovsky, M. Pinsky, A. Seifert, and V. Phillips, 2004: Simulation of effects of atmospheric aerosols on deep turbulent convective clouds using a spectral microphysics mixed-phase cumulus cloud model. Part I: model description and possible applications. *J. Atmos. Sci.*, **61**, 2963-2982.

Khvorostyanov, V. I. and J. A. Curry, 2008: Kinetics of cloud drop formation and its parameterization for cloud and climate models. *J. Atmos. Sci.,* **65**, 2784-2802.

Koehler, K. A., S. M. Kreidenweis, P. J. DeMott, M. D. Petters, A. J. Prenni, and C. M. Carrico, 2009: Hygroscopicity and cloud droplet activation of mineral dust aerosol, *Geophys. Res. Lett.*, **36**, L08805, doi:10.1029/2009GL037348.

Kulmala, M., A. Laaksonen, and L. Pirjola, 1998: Parameterizations for sulfuric acid/water nucleation rates. *J. Geophys. Res*., **103**, 8301-8307.

J.-F. Lamarque, T. C. Bond, V. Eyring, C. Granier, A. Heil, Z. Klimont, D. Lee, C. Liousse, A. Mieville, B. Owen, M. G. Schultz, D. Shindell, S. J. Smith, E. Stehfest, J. Van Aardenne, O. R. Cooper, M. Kainuma, N. Mahowald, J. R. McConnell, V. Naik, K. Riahi, and D. P. van Vuuren, 2010: Historical (1850–2000) gridded anthropogenic and biomass burning emissions of reactive gases and aerosols: methodology and application. *Atmos. Chem. Phys. Discuss*., **10**, 4963-5019.

Lauer, A., J. Hendricks, I. Ackermann, B. Schell, H. Hass, and S. Metzger, 2005: Simulating aerosol microphysics with the ECHAM/MADE GCM – Part I: Model description and comparison with observations. *Atmos. Chem. Phys*., **5**, 3251–3276.

Laurent, B., B. Marticorena, G. Bergametti, J.F. Léon, and N. Mahowald, 2008: Modeling mineral dust emissions from the Sahara desert using new surface and soil developments, *J. Geophys. Res*., **113**(D14), D14218, doi:1.0.1029/2007JD009484.

Leaitch, W. R. and G. A. Isaac, 1994: On the relationship between sulfate and cloud droplet number concentrations. *J. Clim*., **7**, 206-212.

Lee, I. Y., G. Henle, and H. R. Pruppacher, 1980: A numerical determination of the evolution of cloud drop spectra de to condensation on natural aerosol-particles. *J. Atmos. Sci*., **37**(8), 1839-1853.

Lee, Taehyoung, Xiao-Ying Yu, Benjamin Ayres, Sonia M. Kreidenweis, William C. Malm, and Jeffery L. Collett Jr., 2008: Observations of fine and coarse particle nitrate at several rural locations in the United States. *Atmos. Environ*., **42**, 2720-2732.

Levin, Zev and William R. Cotton, 2009: Aerosol Pollution Impact on Precipitation, Springer, 386pp.

Levin, Zev, Eliezer Ganor, and Victor Gladstein, 1996: The effects of desert particles coated with sulfate on rain formation in the eastern Mediterranean. *J. App. Meteor*., **35**, 1511-1524.

Lin, Yuh-Lang, Richard D. Farley, and Harold D. Orville, 1983: Bulk parameterization of the snow field in a cloud model. *J. Climate Appl. Meteor*., **22**, 1065-1092.

Lohmann, U., K. Diehl, 2006: Sensitivity studies of the importance of dust ice nuclei for the indirect aerosol effect on stratiform mixed-phase clouds. *J. Atmos. Sci*., **63**, 968-983.

Lohmann, Ulrike, Johann Feichter, Catherine C. Chuang, and Joyce E. Penner, 1999: Prediction of the number of cloud droplets in the ECHAM GCM. *J. Geophys. Res*., **104**, 9169-9199.

Lynn, B., A. P. Khain, J. Dudhia, D. Rosenfeld, A. Pokrovsky, and A. Seifert, 2005: Spectral (bin) microphysics coupled with a Mesoscale Model (MM5). Part I: Model description and first results. *Monthly Weather Review*, **133**, 44-58.

Lynn, B., A. P. Khain, D. Rosenfeld, and W. Woodley, 2007: Effects of aerosols on precipitation from orographic clouds. *J. Geophys. Res*., **112**, D10225, doi:10.1029/2006JD007537.

McFiggans, G., P. Artaxo, U. Baltensperger, H. Coe, M. C. Facchini, G. Feingold, S. Fuzzi, M. Gysel, A Laaksonen, U. Lohmann, T. F. Mentel, D. M. Murphy, C. D. O'Dowd, J. R. Snider, and E. Weingartner, 2006: The effect of physical and chemical aerosol properties on warm cloud droplet activation. *Atmos. Chem. Phys*., **6**, 2593-2649.

McKeen, S., S. H. Chung, J. Wilczak, G. Grell, I. Djalalova, S. Peckham, W. Gong, V. Bouchet, R. Moffet, Y. Tang, G. R. Carmichael, R. Mathur, and S. Yu, 2007: Evaluation of several PM2.5

forecast models using data collected during the ICARTT/NEAQS 2004 field study. *J. Geophys. Res.*, **112**, D10S20, doi:10.1029/2006JD007608.

Medina, Jeessy, Athanasios Nenes, Rafaella-Eleni P. Sotiopoulou, Laura D. Cottrell, Luke D. Ziemba, Pieter J. Beckman, Robert J. Griffin, 2007: Cloud condensation nuclei closure during the International Consortium for Atmospheric Research on Transport and transformation 2004 campaign: Effects of size-resolved composition. *J. Geophys. Res.*, **112**, D10S31, (10pp).

Mellor, G. L., and T. Yamada, 1982: Development of a turbulence closure model for geophysical fluid problems. *Rev. Geophys. Space Ge.*, **20**, 851-875.

Mertes, S., F. Schroder, and A. Wiedensohler, 1995: The particle detection efficiency curve of the TSI-3010 CPC as a function of the temperature differential between saturator and condenser. *Aerosol Sci. Technol.*, **23**(2), 257-261.

Mesinger, Fedor, Geoff DiMego, Eugenia Kalnay, Kenneth Mitchell, Perry C. Shafran, Wesley Ebisuzaki, Dusan Jovic, Jack Woollen, Eric Rogers, Ernesto H. Berbery, Michael B. Ek, Yun Fan, Robert Grumbine, Wayne Higgins, Hong Li, Ying Lin, Geoff Manikin, David Parrish and Wei Shi, 2006: North American Regional Reanalysis. *Bull. Amer. Meteor. Soc.*, **87**, No 3., 343-360.

Meskhidze, Nicholas, Athanasios Nenes, William C. Conant, and John H. Seinfeld, 2005: Evaluation of a new cloud droplet activation parameterization with in situ data from CRYSTAL-FACE and CSTRIPE. *J. Geophys. Res.*, **110**, D16202, doi:10.1029/2004JD005703.

Meyers, M. P., P. J. DeMott, and W. R. Cotton, 1997: New RAMS cloud microphysics parameterization. Part II: The two-moment scheme. *J. Appl. Meteor.*, **31**, 708-721.

Meyers, M. P., R. L. Walko, J. Y. Harrington, and W. R. Cotton, 1997: New RAMS cloud microphysics parameterization. Part II. The two-moment scheme. *Atmos. Res.*, **45**, 3-39.

Ming, Yi, V. Ramaswamy, Leo J. Donner, and Vaughn T. J. Phillips, 2006: A new parameterization of cloud droplet activation applicable to general circulation models. *J. Atmos. Sci.*, **63,** 1348-1356.

Mlawer, Eli J., Steven J. Taubman, Patrick D. Brown, Michael J. Iacono, and Shepard A. Clough, 1997: Radiative transfer for inhomogeneous atmospheres: RRTM, a validated correlated-k model for the longwave. *J. Geophys. Res.*, **102**(D14), 16,663-16,682.

Muhlbauer, A., and U. Lohmann, 2008: Sensitivity studies of the role of aerosols in warm-phase orographic precipitation in different dynamical flow regimes. *J. Atmos. Sci.*, **65**, doi:10.1175/2007JAS2492.1.

Murphy, D. M., D. J. Cziczo, K. D. Froyd, P. K. Hudson, B. M. Matthew, A. M. Middlebrook, R. E. Peltier, A. Sullivan, D. S. Thomson, and R. J. Weber, 2006: Single-particle mass spectrometry of tropospheric aerosol particles. *J. Geophys. Res.*, **111**, D23S32, doi:10.1029/2006JD007340.

Mesa Verde National Park, 2005: *Geology of Mesa Verde.* National Park Service, Department of the Interior.

Nakajima, Teruyuki, Akiko Higurashi, Kazuaki Kawamoto and Joyce E. Penner, 2001: A possible correlation between satellite-derived cloud and aerosol microphysical parameters. *Geophys. Res. Letters*, **28**, No. 7, 1171-1174.

Nenes, Athanasios and John H. Seinfeld, 2003: Parameterization of cloud droplet formation in global climate models. *J. Geophys. Res.*, **108**(D14), 4415, doi:10.1029/2002JD00291.

Novakov, T., C. Rivera-Carpio, J. E. Penner and C. F. Rogers, 1994: The effect of anthropogenic sulfate aerosols on marine cloud droplet concentrations. *Tellus*, **46B**, 132-141.

O'Dowd C. D., M. H. Smith, I. E. Consterdine, and J. A. Lowe, 1997: Marine aerosol, sea-salt, and the marine sulphur cycle: A short review. *Atmos. Environ.*, **31**, 73-80.

Pang, Y., B. J. Turpin, and L. A. Gundel, 2006: On the importance of organic oxygen for understanding organic aerosol particles. *Aerosol Sci. Technol.*, **40**(2), 128-133.

Perry, Kevin D., Steven S. Cliff, and Michael P. Jimenez-Cruz, 2004: Evidence for hygroscopic mineral dust particles from the Intercontinental Transport and Chemical Transformation Experiment. *J. Geophys. Res.*, **109**, D23S28, doi:10.1029/2004JD004979.

Petters, M.D., and S.M. Kreidenweis, 2007: A single parameter representation of hygroscopic growth and cloud condensation nucleus activity. *Atmos. Chem. Phys.*, **7**, 1961-1971.

Petters, M.D., and S.M. Kreidenweis, 2008: A single parameter representation of hygroscopic growth and cloud condensation nucleus activity – Part 2: Including solubility. *Atmos. Chem. Phys.*, **8**, 6273-6279.

Petters, M. D., A. J. Prenni, S. M. Kreidenweis, and P. J. DeMott, 2007: On measuring the critical diameter of cloud condensation nuclei using mobility selected aerosol. *Aerosol Sci. Technol.*, **41**(10), 907-913.

Petters, Markus D., Anthony J. Prenni, Sonia M. Kreidenweis, Paul J. DeMott, Aiko Matsunaga, Yong B. Lim, and Paul J. Ziemann, 2006: Chemical aging and the hydrophobic-to-hydrophilic conversion of carbonaceous aerosol. *Geophys. Res. Let.*, **33**, L24806, doi:10.1029/2006GL027249.

Pierce, J. R. and P. J. Adams, 2006: Global evaluation of CCN formation by direct emission of sea salt and growth of ultrafine sea salt. *J. Geophys. Res.*, **111**, D06203, doi:10.1029/2005JD006186.

Pierce, J. R. and P. J. Adams, 2009: Uncertainty in global CCN concentrations from uncertain aerosol nucleation and primary emission rates. *Atmos. Chem. Phys.*, **9**, 1339-1356.

Pierce, J. R., K. Chen, and P. J. Adams, 2007: Contribution of primary carbonaceous aerosol to cloud condensation nuclei: processes and uncertainties evaluated with a global aerosol model. *Atmos. Chem. Phys.*, **7**, 5447-5466.

Politovich, Marcia K. and Gabor Vali, 1983: Observations of liquid water in orographic clouds over Elk Mountain. *J. Atmos. Sci*., **40**, 1300-1313.

Pruppacher, H.R., Klett, J.D., 1997: Microphysics of Clouds and Precipitation. Reidel, Dordrecht. 954 pp.

Quinn, P. K., T. S. Bates, D. J. Coffman, D. S. Covert, 2008: Influence of particle size and chemistry on the cloud nucleating properties of aerosols. *Atmos. Chem. Phys*., **8**, 1029-1042.

Radke, Lawrence F., James A. Coakley, and Michael D. King, 1989: Direct and remote sensing observations of the effects of ships on clouds. *Science*, **246**(4934), 1146-1149.

Ramanathan, V., P. Crutzen, J. Kiehl, and D. Rosenfeld, 2001: Aerosols, climate and the hydrological cycle. *Science*, **294**, 2119-2124.

Rauber, R. M., L. O. Grant, D. Feng, and J. B. Snider, 1986: The characteristics and distribution of cloud water over the mountains of Northern Colorado during wintertime storms. Part I: Temporal variations. *J. Clim. Appl. Meteorol*., **25**, 468-488.

Raymond, T. M. and S. N. Pandis, 2002: Cloud activation of single-component organic aerosols. *J. Geophys. Res*., **107**, 4787-4784.

Reutter, P., J. Trentmann, H. Su, M. Simmel, D. Rose, H. Wernli, M. O. Andreae, U. Poschl, 2009: Aerosol- and updraft-limited regimes of cloud droplet formation: influence of particle number, size and hygroscopicity on the activation of cloud condensation nuclei (CCN). *Atmos. Chem. Phys*., **9**, 7067-7080, 2009.

Richardson, Mathews S., Paul J. DeMott, Sonia M. Kreidenweis, Daniel J. Cziczo, Edward J. Dunlea, Jose L. Jimenez, David S. Thomson, Lowell L. Ashbaugh, Randolph D. Borys, Douglas L. Westphal, Gary S. Casuccio, and Traci L. Lersch, 2007: Measurements of heterogeneous ice nuclei in the western United States in springtime and their relation to aerosol characteristics. *J. Geophys. Res*., **112**, D02209, doi:10.1029/2006JD007500.

Rissman, T. A., A. Nenes, and J. H. Seinfeld, 2004: Chemical amplification (or dampening) of the Twomey effect: Conditions derived from droplet activation theory. *J. Atmos. Sci*, **61**, 919-930.

Rissman, T. A., T. M. VanReken, J. Wang, R. Gasparini, D. R. Collins, H. H. Jonsson, F. J. Brechtel, R. C. Flagan, J. H. Seinfeld, 2006: Characterization of ambient aerosol from measurements of cloud condensation nuclei during the 2003 Atmospheric Radiation Measurement Aerosol Intensive Observational Period at the Southern Great Plains site in Oklahoma. *J. Geophys. Res*., **111**, D05S11, doi:10.1029/2004JD005695.

Roberts, G. C., and A. Nenes, 2005: A continuous-flow streamwise thermal-gradient CCN chamber for atmospheric measurements. *Aerosol Sci. Technol*., **39**(3), 206-221.

Rogge, Wolfgang F., Lynn M. Hildemann, Monica A. Mazurek, and Glen R. Cass, 1996: Mathematical modeling of atmospheric fine particle-associated primary organic compound concentrations. *J. Geophys. Res*., **101**(D14), 19,379-19,394.

Rosenfeld, Daniel and Amir Givati, 2006: Evidence of orographic precipitation suppression by air pollution-induced aerosols in the western United States. *J. Appl. Meteor. and Clim*., **45**, 893-911.

Rosenfeld, D. and I. M. Lensky, 1998: Satellite-based insights into precipitation formation processes in continental and maritime convective clouds. *Bull. Amer. Meteor. Soc*., **79**, 2457-2476.

Saleeby, S. M., W. Y. Y. Cheng, and W. R. Cotton, 2007: New developments in the Regional Atmospheric Modeling System suitable for simulations of snowpack augmentation over complex terrain. *J. Weather Mod*., **39**, 37-49.

Saleeby, Stephen M., William R. Cotton, 2004: A large-droplet mode and prognostic number concentration of cloud droplets in the Colorado State University Regional Atmospheric Modeling System (RAMS). Part I: Module descriptions and supercell test simulations. *J. Appl. Meteor.*, **43**, 182-195.

Saleeby, Stephen M., and William R. Cotton, 2005: A large-droplet mode and prognostic number concentration of cloud droplets in the Colorado State University Regional Atmospheric Modeling System (RAMS). Part II: Sensitivity to a Colorado winter snowfall event. *J. Appl. Meteor*., **44**, 1912-1929.

Saleeby, S. M., and W. R. Cotton, 2008: A binned approach to cloud-droplet riming implemented in a bulk microphysics model. *J. Appl. Meteorol*., **47**, doi:10.1175/2007JAMC1664.1.

Saleeby, S. M., W. R. Cotton, D. Lowenthal, R. D. Borys, and M. A. Wetzel, 2009: Influence of cloud condensation nuclei on orographic snowfall. *J. Appl. Meteorol. Clim*., **48**, doi:10.1175/2008JAMC1989.1.

Schell, Benedikt, Ingmar J. Ackermann, Heinz Hass, Francis S. Binkowski, and Adolf Ebel, 2001: Modeling the formation of secondary organic aerosol within a comprehensive air quality model system. *J. Geophys. Res*., **106**(D22), 28,275-28,293.

Segal, Y. and A. Khain, 2006: Dependence of droplet concentration on aerosol conditions in different cloud types: Application to droplet concentration parameterization of aerosol conditions. *J. Geophys. Res*., **111**, D15204, doi:10.1029/2005JD006561.

Segal, Y., M. Pinsky, and A. Khain, 2007: The role of competition effect in the raindrop formation. *Atmos. Res*., **83**, 106-118.

Seinfeld, J. H., and S. N. Pandis, 2006: Atmospheric Chemistry and Physics, Wiley & Sons, Hoboken, New Jersey, 1203pp.

Shantz, N. C., W. R. Leaitch, L. Phinney, M. Mozurkewich, and D. Toom-Sauntry, 2008: The effect of organic compounds on the growth rate of cloud droplets in marine and forest settings. *Atmos. Chem. Phys*., **8,** 5869-5887.

Sihto, S.-L., M. Kulmala, V.-M. Kerminen, M. Dal Maso, T. Petaja, I. Riipinen, H. Korhonen, F. Arnold, R. Janson, M. Boy, A. Laaksonen, and K. E. J. Lehtinen, 2006: Atmospheric sulphuric

acid and aerosol formation: implications from atmospheric measurements for nucleation and early growth mechanisms. *Atmos. Chem. Phys*., **6**, 4079-4091.

Smagorinsky, J., 1963: General circulation experiments with the primitive equations. Part I: The basic experiment. *Mon. Weather Rev*., **125**, 1489-1506.

Smith, Michael A., 2007: Evaluation of mesoscale simulations of dust sources, sinks and transport over the Middle East. M. S. thesis, Colorado State University, Colorado, United States, 126 pp.

Smith, Steven J., Hugh Pitcher, and T. M. L. Wigley, 2001: Global and regional anthropogenic sulfur dioxide emissions. *Global and Planetary Change*, **29**, 99-119.

Snider, Jefferson R., and Jean-Louis Brenguier, 2000: Cloud condensation nuclei and cloud droplet measurements during ACE-2. *Tellus*, **52**B, 828-842.

Snider, Jefferson R., Sarah Guibert, Jean-Louis Brenguier, and J.-P. Putaud, 2003: Aerosol activation in marine stratocumulus clouds: 2. Kohler and parcel theory closure studies. *J. Geophys. Res*., **108**(D15), 8629, doi:10.1029/2002JD002692.

Snider, J. R. and M. D. Petters, 2008: Optical particle counter measurement of marine aerosol hygroscopic growth. *Atmos. Chem. Phys*., **8**, 1949-1962.

Snider, Jefferson R., Markus D. Petters, Perry Wechsler and Peter S. K. Liu, 2006: Supersaturation in the Wyoming CCN instrument. *J. Atmos. Oceanic. Technol*., **23**, 1323-1339.

Squires, P., 1958: The microstructure and colloidal stability of warm clouds. I. The relation between structure and stability. *Tellus*, **10**, 256-271.

Squires, P., and S. Twomey, 1961: The relation between cloud drop numbers and the spectrum of cloud nuclei. *Physics of Precipitation, Monograph, No. 5, Amer. Geophys. Union*., Washington, DC, 211-219.

Squires, P. and S. Twomey, 1966: A comparison of cloud nucleus measurements over central North America and the Caribbean Sea. *J. Atmos. Sci*., **23**, 401-404.

Stevens, B., W. R. Cotton, G. Feingold, and C.-H. Moeng, 1998: Large-eddy simulations of strongly precipitating, shallow, stratocumulus-topped boundary layers. *J. Atmos. Sci*., **55**, 3616-3638.

Stevens, Bjorn and Graham Feingold, 2009: Untangling aerosol effects on clouds and precipitation in a buffered system. *Nature*, **461**, doi:10.1038/nature08281.

Stier, P., J. Feichter, S. Kloster, E. Vignati, and J. Wilson, 2006: Emission-induced nonlinearities in the global aerosol system: Results from the ECHAM5-HAM aerosol-climate model. *J. Climate*, **19**, 3845-3862.

Stockwell, W.R., F. Kirchner, M. Kuhn, and S. Seefeld, 1997: A new mechanism for regional atmospheric chemistry modeling. *J. Geophys. Res*., **102**, D22, 25847-25879.

Stockwell, W. R., P. Middleton, and J. S. Chang, 1990: The second-generation regional acid deposition model chemical mechanism for regional air quality modeling. *J. Geophys. Res.*, **95**, 16,343-16,367.

Stohl, Andreas, 1998: Computation, accuracy and applications of trajectories – a review and bibliography. *Atmos. Environ*., **32**(6), 947-966.

Stokowski, David, 2005: The addition of the direct radiative effect of atmospheric aerosols into the Regional Atmospheric Modeling System (RAMS). M. S. thesis, Colorado State University, Colorado, United States, 81pp.

Stroud, Craig A., Athanasios Nenes, Jose L. Jimenez, Peter F. DeCarlo, J. Alex Huffman, Roelof Bruintjes, Elko Nemitz, Alice E. Delia, Darin W. Toohey, Alex B. Guenther, and Sreela Nandi, 2007: Cloud activating properties of aerosol observed during CELTIC. *J. Atmos. Sci*., **64**, 441-460.

Sullivan, R.C., M. J. K. Moore, M. Petters, S. M. Kreidenweis, G. C. Roberts, and K. A. Prather, 2009: Effect of chemical mixing state on the hygroscopicity and cloud nucleation properties of calcium mineral dust particles. *Atmos. Chem. Phys.*, **9**, 3303-3316.

Svenningsson, B., J. RIssler, E. Swietlicki, M. Mircea, M. Bilde, M. C. Facchini, S. Decesari, S. Fuzzi, J. Zhou, J. Monster, and T. Rosenorn, 2006: Hygroscopic growth and critical supersaturation for mixed aerosol particles of inorganic and organic compounds of atmospheric relevance. *Atmos. Chem. Phys*., **6**, 1937-1952.

Textor, C., M. Schulz, S. Guibert, S. Kinne, Y. Balkanski, S. Bauer, T. Bernsten, T. Berglen, O. Boucher, M. Chin, F. Dentener, T. Diehl, R. Easter, H. Feichter, D. Fillmore, S. Ghan, P. Ginoux, S. Gong, A. Grini, J. Hendricks, L. Horowitz, P. Huang, I. Isaksen, T. Iversen, S. Kloster, D. Koch, A. Kirkevag, J. E. Kristjansson, M. Krol, A. Lauer, J. F. Lamarque, X. Liu, V. Montanaro, G. Myhre, J. Penner, G. Pitari, S. Reddy, O. Seland, P. Stier, T. Takemura, and X. Tie, 2006: Analysis and quantification of the diversities of aerosol life cycles within AeroCom. *Atmos. Chem. Phys*., **6**, 1777-1813.

Twohy, Cynthia H., Sonia M. Kreidenweis, Trude Eidhammer, Edward V. Browell, Andrew J. Heymsfield, Aaron R. Bansemer, Bruce E. Anderson, Gao Chen, Syed Ismail, Paul J. DeMott, and Susan C. Van Den Heever, 2009: Saharan dust particles nucleate droplets in eastern Atlantic clouds. *Geophys. Res. Lett*., **36**, L01807, doi:10.1029/2008GL035846.

Twomey, S., 1959: The nuclei of natural cloud formation, Part II: The supersaturation in natural clouds and the variation of cloud droplet concentration. *Geofis. Pura. Appl.,* **43**, 243-249.

Twomey, S., 1974: Pollution and the Planetary Albedo. *Atmos. Environ.,* **8**, 1251-1256.

Twomey, S. 1977: The influence of pollution on the shortwave albedo of clouds. *J. Atmos. Sci.,* **34**, 1149-1152.

Twomey, S. and J. Warner, 1967: Comparison of measurements of cloud droplets and cloud nuclei. *J Atmos. Sci.,* **24**, 702-703.

U.S. Environmental Protection Agency, 2009: 2005 National Emissions Inventory Data & Documentation, http://www.epa.gov/ttnchie1/net/2005inventory.html.

van den Heever, Susan C., Gustavo G. Carrio, William R. Cotton, Paul J. DeMott, and Anthony J. Prenni, 2006: Impacts of nucleating aerosol on Florida storms. Part I: Mesoscale simulations. *J. Atmos. Sci*, **63**, 1752-1775.

van den Heever, S. and W. R. Cotton, 2007: Urban aerosol impacts on downwind convective storms, *J. Appl. Meteor. Climat*., **46**, 828-850.

VanReken, Timothy M., Nga L. Ng, Richard C. Flagan, and John H. Seinfeld, 2005: Cloud condensation nucleus activation properties of biogenic secondary organic aerosol. *J. Geophys. Res*., **110**, D07206, doi:10.1029/2004JD005465.

VanReken, T. M., T. A. Rissman, G. C. Roberts, V. Varutbangkul, H. H. Jonsson, R. C. Flagan, and J. H. Seinfeld, 2003: Toward aerosol/cloud condensation nuclei (CCN) closure during CRYSTAL-FACE, *J. Geophys. Res*., **108**, 4633, doi:10.1029/2003JD003582.

Virkkula, Ari, Rita Van Dingenen, Frank Raes, and Jens Hjorth, 1999: Hygroscopic properties of aerosol formed by oxidation of limonene, alpha-pinene and beta-pinene. *J. Geophys. Res.,* **104**(D3), 3569-3579.

Walko, R. L., L. E. Band, J. Baron, T. G. F. Kittel, R. Lammers, T. J. Lee, D. Ojima, R. A. Pielke Sr., C. Taylor, C. Tague, C. J. Tremback, and P. J. Vidale, 2000: Coupled atmospheric-biophysics-hydrology models for environmental modeling*. J. Appl. Meteorol.*, **34**, 994-999.

Ward, D. S., 2006: Local anthropogenic aerosol sources effect on winter clouds and precipitation in the Colorado Park Range. M. S. Thesis, Colorado State University, Colorado, United States, 108 pp.

Ward, D. S., T. Eidhammer, W. R. Cotton, and S. M. Kreidenweis, 2010: The role of the particle size distribution in assessing aerosol composition effects on simulated droplet activation. *Atmos. Chem. Phys. Discuss*., **10**, 4189-4223.

Warner, J., 1968: A reduction of rain associated with smoke from sugar-cane fires – An inadvertent weather modification*. J. Appl. Meteor*., **7**, 247-251.

Weingartner, E., H. Burtsher, and U. Baltensperger, 1997: Hygroscopic properties of carbon and diesel soot particles. *Atmos. Environ*., **31**(15), 2311-2327.

Wiacek, A., T. Peter, and U. Lohmann, 2010: The potential influence of Asian and African mineral dust on ice, mixed-phase and liquid water clouds. *Atmos. Chem. Phys. Discuss*., **10**, 4027–4077.

D. S. Wilks, 1995: Statistical methods in the atmospheric sciences, second edition. *International Geophysics Series*, **59**, Academic Press, 464pp.

Witek, Marcin, L., Piotr J. Flatau, Patricai K. Quinn, and Douglas L. Westphal, 2007: Global sea-salt modeling: Results and validation against multicampaign shipboard measurements. *J. Geophys. Res*., **112**, D08215, doi:10.1029/2006JD007779.

Xue, Huiwen and Graham Feingold, 2006: Large-eddy simulations of trade wind cumuli: Investigation of aerosol indirect effects. *J. Atmos. Sci*., **63**, 1605-1623.

Zhang, Renyi, Inseon Suh, Jun Zhao, Dan Zhang, Edward C. Fortner, Xuexi Tie, Luisa T. Molina, and Mario J. Molina, 2004: Atmospheric new particle formation enhanced by organic acids. *Science*, **304**, doi:10.1126/science.1095139.

Zhang, Y., 2008: Online-coupled meteorology and chemistry models: history, current status, and outlook. *Atmos. Chem. Phys.*, **8**, 2895-2932.

Zhang, Y., R. C. Easter, S. J. Ghan, and H. Abdul-Razzak, 2002: Impact of aerosol size representation on modeling aerosol-cloud interactions. *J. Geophys. Res*., **107**(D21), 4558, doi:10.1029/2001JD001549.